RELATIONSHIPS BETWEEN OPTO-ELECTRONIC PROPERTIES, MOLECULAR STRUCTURE AND MORPHOLOGY IN FULLERENE CONTAINING SOLAR CELLS.

Daniel Fernández Pinto

Dipòsit Legal: T 66-2016

Daniel Fernández Pinto

Relationships between opto-electronic properties, molecular structure and morphology in fullerene containing solar cells

Ph.D Thesis

Supervised by Dr. Emilio Palomares Gil and Dr. Carles Bo Jané

Institut Català d'Investigació Química – Universitat Rovira i Virgili

UNIVERSITAT ROVIRA I VIRGILI

Tarragona, July 2015

UNIVERSITAT ROVIRA I VIRGILI

ICIQ
Institut Català d'Investigació Química

FAIG CONSTAR que aquest treball, titulat "Relationships between opto-electronic properties, molecular structure and morphology in fullerene containing solar cells", que presenta Daniel Fernández Pinto per a l'obtenció del títol de Doctor, ha estat realitzat sota la meva direcció al ICIQ.

HAGO CONSTAR que el presente trabajo, titulado "Relationships between opto-electronic properties, molecular structure and morphology in fullerene containing solar cells", que presenta Daniel Fernández Pinto para la obtención del título de Doctor, ha sido realizado bajo mi dirección en el ICIQ.

I STATE that the present study, entitled " Relationships between opto-electronic properties, molecular structure and morphology in fullerene containing solar cells ", presented by Daniel Fernández Pinto for the award of the degree of Doctor, has been carried out under my supervision at the ICIQ.

Tarragona, 28-JUL-2015

El/s director/s de la tesi doctoral
El/los director/es de la tesis doctoral
Doctoral Thesis Supervisor/s

Emilio Palomares Gil

Carles Bo Jané

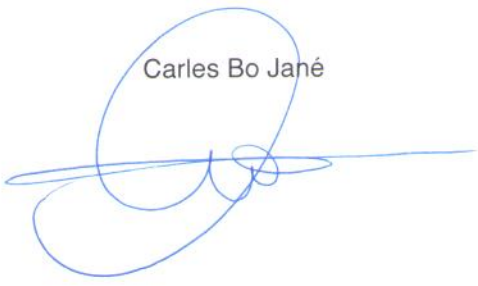

To my mother.

General Table of Contents

Acknowledgements

A PhD thesis is no easy feat. It requires dedication, hard work, patience and support. Since my first 3 month stay at ICIQ as a summer fellow in 2009 I have found all of them present within the people that make up this wonderful community. My supervisors, Carles and Emilio, have been a great source of inspiration for me through the years. They have both provided different and invaluable views during my thesis with their distinct and complimentary research styles. They are both remarkable researchers and human beings who offered me financial, personal and academic support whenever it was needed along the way. I deeply thank both of them for supporting me and giving me the opportunity to have had them as my supervisors.

The postdocs at the lab also provided fundamental moral and academic support for me through this thesis. I would have never been able to get all this work done without the incredibly insightful discussions and teachings of John, Josep, Vijay, Aurelien and Georgiana. From them Aurelien played the most critical role in my formation as a researcher with an amazing grasp of the scientific method and a pulchritude and dedication to research that would be praised by Thomas Kuhn himself. From him I learned that the quality of our experiments and the depth of our observations have more weight than the number of publications we get to write.

My fellow lab mates were also amazing to be with and always helped the long experiments seem shorter. I would like to thank Laia, James, Lydia, Nuria, Jose, Alba, Ivan, Taye, Ilario, Toni, Werther, Cristina and Sofia for always being there when I needed them, for having patience in explaining concepts and for having patience with the endless versions and bugs within the software programs I wrote through the years. Although I became friends with some more than others – as we always tend to do – I will never forget any of you through the years. Those of you

who drove me to the airport have a very special place in my heart (only true friends do that!).

I would also like to thank all the people within research support that also played a pivotal role in the development of my thesis. I would especially like to thank Fernando and Javi who besides helping me with my research goals also became my friends through the years. Obviously no thanks would be complete without mentioning the three wonderful secretaries I met within the two research groups I worked in – Eva, Bea and Núria – who helped me through the endless bureaucratic ordeals that one must deal with when being in a foreign country.

This PhD was a very challenging and yet enjoyable experience that wouldn't have been possible without all the above and possibly many more people who I have forgot to mention. To all those of you who made this experience possible, my deepest and sincerest thanks.

Motivation and aim of this thesis

As it will be discussed throughly in the beginning of the introductory chapter, organic solar cells have a real possibility to eventually replace or compliment single crystal silicon technology in the production of usable electrical power for humanity. The lower cost and significantly easier fabrication of organic solar cells gives them a large competitive advantage over silicon solar cells provided that problems dealing with device lifetimes and large scale module efficiencies can be solved.

In order to improve device efficiencies and reach these goals it is important to make critical advances in the understanding of how these devices work and how the materials within them interact. It is the main aim of this thesis to contribute to these developments in order to enhance our current understanding of the materials within organic solar cells, how changing them affects device properties and how they can be potentially improved to enhance device performance. We seek to answer fundamental questions within the field dealing with the opto-electronic behavior of the devices and develop models that can lead to the finding of new materials.

This is a summary of all the chapters contained within this thesis as well as their main objectives:

Chapter 1. This chapter contains an introduction to the general concepts that are used throughout the thesis. Herein we explain the basics of solar cell characterization, organic solar cell structures, organic solar cell operating mechanisms, performance limiting factors, ideal donor properties and other device materials. We also perform a detailed overview of the diketopyrrolopyrrole family of organic donor molecules as a significant portion of this thesis is based on developments involving this molecule family.

Chapter 2. In this chapter we go through the computational methods used for the creation of predictive models used in chapter 6 of this thesis. This chapter seeks to be a collection of practical resources for anyone who wishes to reproduce the computational exercise carried out in this thesis. The chapter contains a detailed explanation of the entire database building process as well as scripts used for the

building of the statistical models used.

Chapter 3. Through this chapter we explain the experimental techniques used to characterize the devices and molecules used within this thesis. We explain the experiments used for opto-electronic characterization including transient absorption spectroscopy, photo-induced transient photo-voltage, photo-induced charge-extraction and photo-induces transient photo-current. Some experiments used for single molecule characterization such as cyclic voltammetry and UV-vis spectroscopy are also explained.

Chapter 4. This is the first experimental chapter of this thesis. Herein we explored the changes in device performance associated with changes in the fullerene acceptor in DPP$(TBFu)_2$ small molecule solar cells. We tested 3 different diphenylmethano fullerenes and used a wide array of different characterization techniques in order to understand why the fullerenes show different performance and open circuit voltages even though their electronic structure is largely the same.

Chapter 5. In the second experimental chapter we decided to explore the relationship between morphology and structure in a large family of DPP donor molecule derivatives using $PC_{71}BM$ as an electron acceptor. We optimized all devices to obtain the best possible performance and then used a variety of opto-electronic techniques, microscopies and X-ray diffraction experiments to understand how the different changes in the molecular structure affected the nanomorphology and device performance. By using all these information we were able to draw a complete picture of how different modifications affected device performance and what the limiting factors to device efficiency were in each different case.

Chapter 6. This chapter focuses on the generation of statistical models for the prediction of electrical properties in small molecule organic solar cells. We built a large database from published experiments with electrical device properties (Voc, Jsc, FF and PCE), associating all these properties to molecular 2D and 3D

structures for donor molecules. We then used these structures to obtain 2D and DFT descriptors that were used to create models that attempted to predict the best electrical properties that could be obtained with a given donor molecule structure.

Chapter 7. In this chapter we performed experiments to build lead halide perovskite solar cells containing fullerenes ($PC_{71}BM$ and C_{60}) as acceptor materials. We attempted to use a hot casting process for the deposition of the pervoskite material to gain greater control over film morphology. We then carried out the photo-physical characterization of these devices in order to understand how they differ from perovskite devices built using mesoporous titanium dioxide.

Chapter 8. This chapter contains a brief summary of all the results from previous chapters as well as the main conclusions of this thesis.

Chapter 1

Introduction

Table of Contents

Solar power

The sun provides the surface of the world with more than $1.4x10^5$TW of power, with around $3.5x10^4$TW of this power being usable. With human society consuming less than 18 TW of energy (as of 2012) the sun is an obvious candidate for the replacement of all energy sources used by humanity.[1] The process to do so is already well underway with the cost of photo-voltaic energy now down to 0.5 USD per peak Watt[2] and solar installations in the US already surpassing the 17GW mark and projections showing this contribution to grow to 250GW by 2030 and 2900 GW by 2050.[3] The use of highly efficient solar panels and solar concentrator plants will allow for the eventual total replacement of human energy needs within this century.[4]

All current medium to large scale solar panel installations rely on the use of monocrystalline silicon (c-Si), polycrystalline silicon, amorphous silicon, cadmium-telluride (CdTe) or copper-iondium-gallium-selenide (CIGS) with c-Si modules taking around 90% of the current market share an all other technologies currently accounting for less than 10% of all installed capacity.[5] Crystalline silicon technology has the advantage of having large efficiencies[6] and being able to leverage the silicon wafer production of the computer industry. Efficiencies of more than 20% on mass produced 100-μm thick c-Si panels are already possible while an exponential drop in costs will continue.[7]

However the silicon industry still has several problems with both sustainability and environmental impact as the production of crystalline silicon is both resource intensive and polluting.[8] This is bound to change in the future as lower cost and environmentally sustainable methods for silicon production are developed.[2,9] Further decreases in c-Si wafer thickness with increases in power density will also help improve the environmental impact of c-Si solar panel production.[10]

Following these ideas it is difficult to image that any technology will ever surpass silicon for the construction of large scale photo-voltaic arrays since any competing

technology would need to improve over the average lifetime USD/W of current c-Si solar cells, a mature technology already benefiting from economies of scale. However organic solar cells, which use polymer or small molecule photo-active materials, have very low production costs both from lower raw material costs and simpler and massively scalable production techniques (such as roll-to-roll processing).[5,11–17] Cost analysis reveals that organic solar cells can beat the average lifetime USD/W of current c-Si technology with an efficiency above only 2% and a lifetime of 3 years with efficiencies above 5% and lifetimes of 3-5 years making them competitive against current coal and gas power generation.[18] This means that a move towards organic solar cells in the long term is not only possible but may be inevitable as device lifetimes and mass produced module efficiencies improve further.

To make this technology competitive it is therefore fundamental to work on improved polymer and small molecule materials, improved device contacts and better device fabrication techniques. This should lead to the increase in module efficiencies and lifetimes that is required for the competitiveness of organic solar cell technology with crystal silicone solar cells or similar solar energy conversion technologies.

Solar Cell Characterization

Generally solar cells are characterized by creating what is commonly denominated as an I-V Curve (Figure 1).[19] In an I-V curve the device is put under a given solar illumination standard (generally the 1.5AM standard)[20] and a voltage source is used to apply different levels of reverse bias to the device and measure the device's current response. This measurement allows us to determine the power response (product of applied bias and produced current) for the device at different levels of applied bias, allowing us to determine the power production curve for the device and therefore the maximum power conversion efficiency for the device (PCE). By using this curve we can also determine the open circuit voltage (Voc) which is the voltage given by the device when the applied reverse

bias is able to cancel out all the current generated by the device, the short circuit current (Isc) which is the current response of the device when the applied bias is zero and the fill factor (FF) for the device which is the product of the current and applied bias at maximum power divided by the product of the Isc and the Voc. Generally current values (I) are converted to current density values (J) by dividing the current by the device's active area in order to be able to easily compare between devices with different sizes.

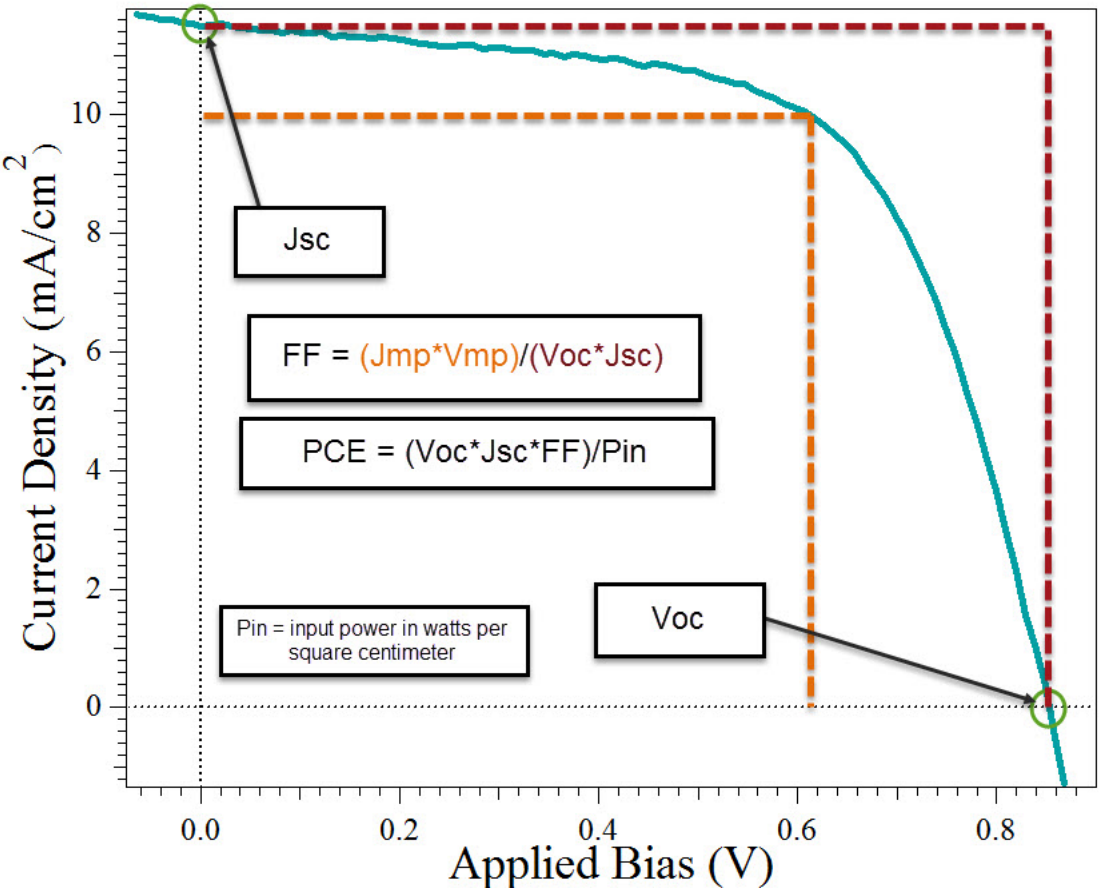

Figure 1. A sample I-V curve showing how to obtain the Voc, Jsc, FF and PCE .

Organic Solar Cells

Device Structure

Organic solar cells are built using the general structure showed in Figure 2.[21] Light enters the device through the glass, charges are generated within the photo-active layer and are then collected in the transparent conductive material and metal contacts. In general the transparent conductive material used in lab-scale organic solar cells is 300-500μm thick ITO (Indium Tin Oxide) due to it being easily patterned, hard to scratch, chemically resistant, temperature resistant and very transparent.[22] The metals used are generally aluminum, silver or gold, although metal combinations such as Ca/Ag are also common. These metals are used due to their work functions, high conductivities and ability to be deposited using thermal evaporation, the main technique used for back-contact deposition in lab-scale organic solar cells.[23]

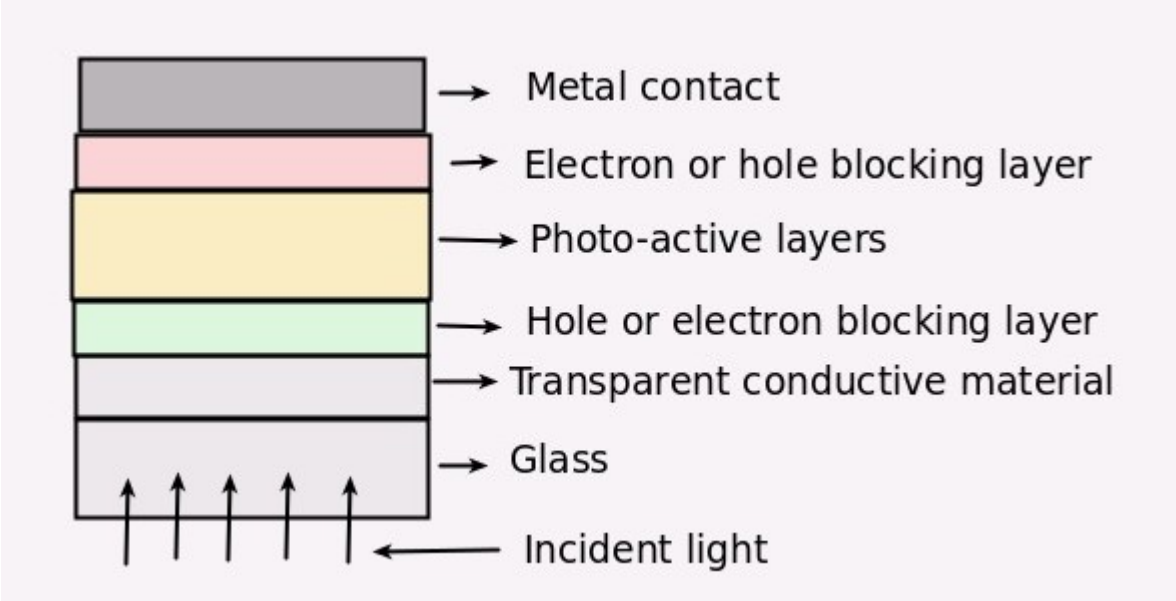

Figure 2. General structure for organic solar cells. This structure includes inverted as well as normal geometry organic solar cells. It does not include top illumination type devices.

The actual configuration of the cell depends on the work function alignment between the conductive transparent material and metal contact. If the desired

back-contact metal has a high work function (Gold at 4.46eV or silver at 4.47eV for example[24]) then it is common to construct the cells in a way that makes the Fermi-level gradient move from low to high values such that the device will be made with an ITO|Hole blocking layer|Photo-active layers|Electron blocking year| metal contact structure. This structure is called an inverted structure and is most commonly desired when vacuum evaporation of the metal contacts wants to be avoided, such as in roll-to-roll fabrication procedures.[25]Most commonly devices in lab setups are produced using a configuration where a low work function metal is used as the back-contact, implying the use of an ITO|electron blocking layer| Photo-active layers|hole blocking layer|metal contact structure, this is usually referred to as a "normal geometry". It is also worth mentioning that configurations involving top-illumination or top and bottom illumination with transparent back-contacts also exist, but their use is much less common.[26]

The most critical aspect pertaining to device structure is the configuration of the photo-active layer(s). In an organic solar cell the photo-active layer is made up of a donor molecule and an acceptor molecule and these molecules can be either mixed together within a single layer or placed within two separate layers. The first type of device is called a bulk-heterojunction (BHJ) structure while the second is a bi-layer structure (Figure 3). Most attention has focused on the development of devices with a BHJ structure as higher efficiencies are generally achievable in this configuration with current lab records above the 10% power conversion efficiency mark.[27–29]

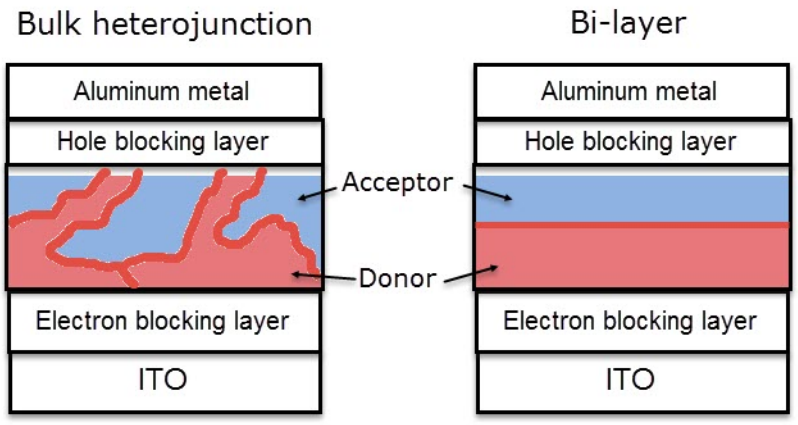

Figure 3. Images showing the structure of bulk heterojunction and bi-layer organic solar cells with normal geometry configurations.

The use of selective contacts (hole and electron blocking layers) is also of special importance in improving the efficiency of organic solar cells. The electron blocking layer, which is most commonly PEDOT:PSS, helps to decrease surface roughness, improve Fermi level alignment and charge recombination[30–33] while layers that go on top of the active layer help protect the active layer from damage by the evaporated cathode, also changing the energy level alignment by forming dipole moments with the active layer and/or cathode structures[34]. It is worth mentioning that the layers that go above the active layer in a normal geometry often do not play the role of “hole blocking layers” but instead are simply “cathode buffer layers” that help improve the Fermi level alignment between the active layer and the metal cathode without effectively blocking holes in the process. The most commonly used “cathode buffer layer” material is LiF[23,35] while other organic cathode buffer materials that act as hole blocking layers can also be used[36–39]. Another useful strategy to form a cathode buffering layers is to include additives such as PEG within the active layer blend which might spontaneously form a cathode buffering layer upon deposition.[40]

Basic Operating Principles

In organic solar cells incident electromagnetic radiation in the solar spectrum is converted into useful electrical energy by taking advantage of a charge separation process generated by the coupling of an organic electron donor and an organic electron acceptor. In the simplest model for these devices (Figure 4) an excitation of the donor molecule by a photon generates an exciton (a mobile excited state) within the donor material which then separates into two charge carriers (an electron-hole pair, often called polarons) within the donor/acceptor interface. These polarons then migrate through the donor and acceptor domains and are collected at the device contacts, generating the device's current. We can therefore think about the entire process as following these steps[41]:

1. Exciton generation by incident radiation
2. Exciton movement towards a donor/acceptor interface
3. Generation of charge carriers from excitons
4. Movement of charge carriers to the contacts

The efficiency of our solar cells are therefore limited by problems that arise within each one of these steps. The exciton generation by incident radiation is limited by the molar extinction coefficient of the donor molecule at each different wavelength. An ideal molecule should be able to absorb all photons within the solar spectrum which means that its molar extinction coefficient should be high enough to absorb all photons from solar radiation.

Since the dielectric constants of organic semiconductor materials are so low (typically 2-4), charge separation of excitons into charge carriers can only happen at the donor/acceptor interface.[42] Due to this reason excitons generated within the donor material must be able to reach a donor/acceptor interface in order to be able to yield charge carriers (electron-hole pairs). However the excitons have a relatively low lifetime and generally can only diffuse for around 5-25nm before decaying back to the ground state[43] reason why it is very important for donor/acceptor interfaces to always be reachable within this distance inside the device. This is one of the main reasons why bulk-heterojunction devices present such a significant improvement over most bi-layer structures; the much larger presence of donor/acceptor interfaces facilitates the charge separation process in much thicker films while bi-layers cannot be made thicker than the exciton diffusion length, since only a single donor/acceptor interface is present between the two layers.

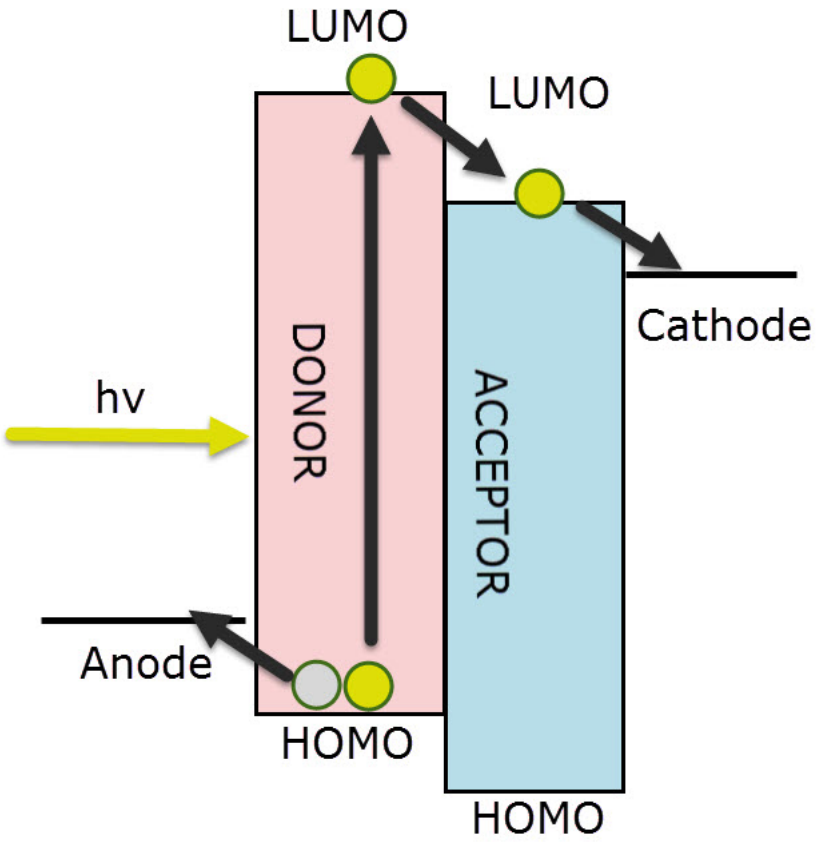

Figure 4. Image showing a conceptual model for the movement of electrons (yellow circles) and holes (grey circle) in organic solar cells.

When excitons reach the donor/acceptor interface they must then be converted to free charge carriers. When the electron-hole pairs are first generated the low dielectric constant for the materials implies a large Coulomb binding energy that may difficult the separation of the electron-hole pairs. If the charge carriers are unable to escape this Coulomb binding energy then they recombine, a process that is known as geminate recombination. If the pairs are able to overcome this binding energy then they turn into free carries and can proceed to move towards the device contacts. The dissociation efficiency for the electron-hole pair depends on the initial separation distance and the strength of the applied electric field.[42] Experimental evidence now suggests that the successful charge separation in organic solar cells receives a significant contribution from above-gap excitations where the excess photon energy converts to hot interfacial charge

transfer states that effectively contribute to polaron creation.[44,45] It has also been shown that charge separation does not need to happen exactly at the donor/acceptor interface but can happen even dozens of angstroms away from it.[46] An exciton dissociation model based on a field-dependent tunnel process has been showed to be consistent with experimental observations in organic bi-layer devices.[47]

After successful charge separation has happened the free charge carries must then reach the electrodes in order for the device to operate. The driving force for this movement is provided by the device's built-in electric field. The holes travel through the donor phase while the electronics travel through the acceptor phase. A charge carrier can then recombine with another charge carrier with opposite charge from a different generation event at a donor/acceptor interface as it moves towards the contacts. This recombination process is known as non-geminate recombination. The effectiveness of this charge transport process depends mainly on the electron and hole mobilities of the two phases and the morphology of the donor/acceptor blend.[48] Free charge carriers must be able to both move fast enough towards the contacts (high mobility) and be able to actually reach the contacts (adequate morphology). These charge carries can also recombine with excitons via an Auger recombination process.[49] It is also possible for carriers to recombine through inter-facial defect states that can trap electron/holes and therefore allow for recombination.[50]

Limiting Factors

All the different processes that can limit the efficiencies of organic solar cells are currently well known. Experiments to evaluate geminate/non-geminate recombination, mobility and morphology have already concluded that device efficiencies are mostly limited by absorption coefficients and bimolecular recombination.[48-51] This implies that an improvement in organic solar cell efficiencies to reach the 15-20% mark can only be achieved by either having molecules that have higher molar extinction coefficients with broader spectral

absorptions and/or molecules that generate better morphologies that can lead to higher charge carrier mobilities. Multiple donor and tandem solar cell approaches have already showed some success in eliminating the first problem[27,52,53] while the search for ways to accurately control morphology still seems elusive. Although several attempts have been made to attempt to describe rules for the creation of donor materials for organic solar cells[54–58] none of these approaches has been able to successfully allow for the design of highly efficient donor materials. Highly efficient donors with adequate morphologies have been found mainly through exhaustive trial and error processes, guided by the experience of different researchers within the field. The adequate prediction and understanding of morphology in bulk-heterojunction solar cells therefore remains a challenge in the filed of organic photo-voltaics.

Materials

Small Molecule Donors

Donor materials in organic solar cells are usually divided between polymers and small molecules. The field of small molecule organic photo-volatics (SM-OPV) has seen a significant surge during the past several years due to the important advantages that small molecules have over polymers as donor materials. Small molecules can be obtained in high purity, their properties can be determined using *in silico* methods, they can be designed and prepared using a variety of synthetic methods and they can be produced in large quantities.[41,59,60] There are now several reports of small molecule solar cells achieving device efficiencies above 9%, with some of them reaching efficiencies above the 10% mark.[27,61,62] This shows that small molecule solar cells can achieve the same level of performance as the most highly efficient polymer solar cells.

Donor molecule requirements

A suitable small molecule donor for an organic solar cell must fulfill some minimum characteristics to be able to generate charge separation within a photo-

voltaic device. Furthermore, some of these characteristics need to have optimum values in order for the donor molecules to have a good level of performance. These are the minimum requirements for a molecule to work well within a bulk-heterojunction organic solar cell:

- Soluble in the same casting solvent as the acceptor. Since active layer films in bulk-heterojunction solar cells are prepared through spin coating, a donor molecule needs to be soluble in the same solvents as the acceptor in order to be casted into a film.
- The donor molecule needs to be nonreactive towards the acceptor. If the molecule reacts with the acceptor then it is not possible to create a bulk-heterojunction device using the intended donor/acceptor mixture.
- The LUMO level of the donor needs to be higher than the LUMO level of the acceptor. More precisely it is required that the quasi-Fermi level of the donor be higher than the quasi-Fermi level of the acceptor material within the casted donor-acceptor domains.
- High molar extinction coefficients across a broad absorption spectrum. The molecule needs to have strong absorptions in order to be able to convert a significant portion of the solar spectrum into excitons. Low molar extinction coefficients or narrow absorptions lead to sub-optimal performance.
- Optimum balance in surface tension between donor molecules and acceptor molecules. An ideal donor materials needs to have a balanced surface tension between its own molecules and the acceptor material in order to generate domains with a suitable morphology to facilitate charge transport across the device.
- High charge carrier mobility. A suitable donor needs to have a significantly large hole mobility within its casted domains such that free charge carriers can be transported efficiently towards the electrodes. The magnitude of the charge mobility needs to be of the same order of magnitude as that of the acceptor domains.

Diketopyrrolopyrrole donors

The Diketopyrrolopyrrole (DPP) core (Figure 5) has been used since the 1970s in the manufacture of high performance pigments.[63,64] The large molar absorption coefficients, easy synthesis and highly tunable properties (via the 4 positions available for substitution within the molecule) made it an excellent candidate for research in organic solar cells.

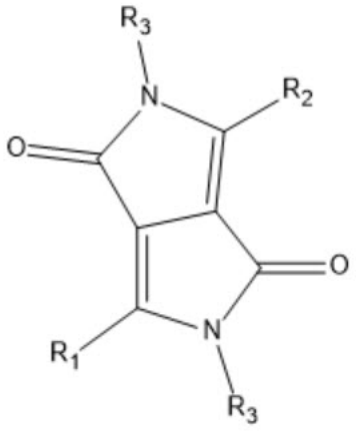

Figure 5. A schematic representation of the diketopyrrolopyrrole (DPP) core. The R1 and R2 positions are generally used to incorporate donor or acceptor moieties while the R3 positions are generally used to incorporate alkyl chains to increase molecule solubility .

The DPP core has been used as a building block for the construction of donor polymers in organic solar cells solar cells.[65–67] However the first reports of the use of DPP cores in the production of small molecule organic solar cells came in 2009 when an efficiency of 4.4% was realized using a DPP core functionalized with a thiopene-benzofuran moiety and 2-ethyl-hexyl side chains (Figure 6). The fabricated device used $PC_{71}BM$ as an acceptor.[68] This DPP molecule showed a very high molar extinction coefficient with a particularly good phase separation and electron mobility, one of the best performance marks for small molecule solar cells at the time.

During the following year there were not many developments in the use of DPP in

donor molecules but there were significant developments in the use of DPP molecules with electron withdrawing groups as electron acceptors within organic solar cells.[69,70]

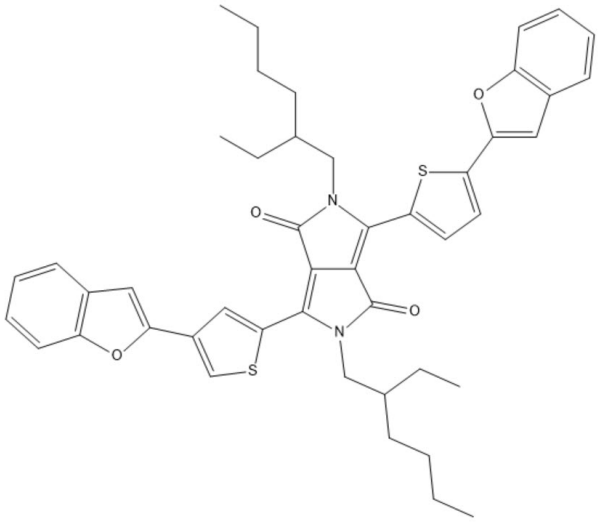

Figure 6. Representation of the DPP donor molecule that achieved devices with a 4.4% efficiency in 2009 using $PC_{71}BM$ as an acceptor. The thiophene-benzofuran donors help increase the molecule's absorption coefficient and charge mobility while the 2-ethylhexyl chains increase solubility.

In 2011 there started to be additional advances in the field with the publication of a 4.1% efficiency using a DPP core functionalized with C2-pyrene and 2-ethyl-hexyl moieties. The success of the C2-pyrene functionalization was attributed to a much larger hole mobility thanks to the pi-pi interactions while the molar extinction coefficient was significantly lower than that of the previously reported thiophene-benzofuran functionalized DPP core.[71] An efficiency of 4.06% was also reported using a molecule containing two DPP cores, using a naptho[2,3-b:6,7-b]dithiophene (NDT) bridge between the DPP substitutions.[72] This last molecule used $PC_{61}BM$ as an acceptor so potentially higher efficiencies would have been obtained with $PC_{71}BM$.

In 2012 there were several new publication dealing with DPP core donors. New donors using CN and nitro groups were published with a 3.34% efficiency using

substituted $PC_{61}BM$ derivatives. In this case the highest efficiency, better than with normal $PC_{61}BM$, was obtained using a $PC_{61}BM$ derivative that contained the same CN and nitro moieties as the donor molecule, hinting at the importance of donor/acceptor interactions in enhancing the performance of small molecule devices.[73]

At almost the same time another paper was published using a donor containing two DPP cores separated by a phenyl pi bridge, achieving a large voltage of +0.93V and an efficiency of 4.01% with $PC_{71}BM$. The addition of the phenyl bridge between the DPP cores significantly increased the device Voc while increasing the Jsc and the fill factor due to a improvement in the domain separation characteristics of the device. While the directly linked and thiophene separated devices showed poor performance the much more favorable steric qualities of the phenyl separated molecule yielded better devices.[74]

In 2013 there were significant advances to move above the 4.4% performance mark with the use of DPP core containing molecules with four separate papers achieving better efficiencies during this year. The first paper used a donor molecule built using a sync porphyrin functionalized with two DPP molecules, achieving an efficiency of 4.78% thanks to the addition of a pyridine additive within the casting process. This further hints at the importance of morphology tuning in DPP devices as the addition of the pyridine had important implications in the phase separation of the porphyrin molecule within the devices (due to the Zinc-pyridine interactions).[75]

The next paper achieved a PCE of 5.79% within devices built using $PC_{61}BM$. The new donor molecule contained two DPP cores linked by a 5-alkylthiophene-2-yl substituted benzodithiophene. Success in this case was attributed to the better alignment of the molecular orbitals with those of PC61BM and the higher electron mobility of the molecule compared with previously published DPP based donor molecules. The very high molar absorption coefficient of this molecule also played a pivotal role in achieving a very high current density.[76]

Another efficiency above 5% was achieved using a donor molecule built by two DPP molecules separated by a benzene-dithiol bridge. In this case an efficiency of 5.29% was achieved after very judicious optimization of the devices by changing the casting solvent from chloroform to ortho dichlorobenzene and using di-iodo-octane (DIO) as a process additive.[77] A different paper showing an efficiency of 4.78% achieved these results using a single DPP core functionalized with extensive oligothiophene chains and using DIO as a process additive.[78]

From the 4 papers published in 2013 that used DPP donors with efficiencies above 4.4% it became clear that the use of processing additives was a viable strategy to increase device performance. However the 5.79% efficiency achieved without the use of any processing additives still showed that it was possible to generate much better PCE values by having a favorable molecular design that did not require the use of processing additives for the formation of an adequate morphology.

In 2015 there were also significant advances in the development of DPP containing donor molecules with the publication of two papers showing donors used within devices with efficiencies surpassing 6%. After the publication of a paper with notions for rational design of DPP oligomers (reaching a 5.4% efficiency)[79] another paper showing a new donor molecule with a D-A-D-A-D-A-D motive was published with a 7% efficiency.[80] In this case rather than an effect from additives the increase in PCE was achieved by attempting solvent annealing using different organic solvents. The best results for this molecule were achieved using THF solvent annealing.

The best result for DPP containing donor molecules up to 2015 came from the use of a DPP containing porphyrin (Figure 7), obtaining a device performance of 8.08%.[53] The structure of this porphyrin is remarkably similar to that of the 2013 paper achieving a 4.78% efficiency with the only difference that the porphyrin is substituted with a thiophene-2-ethyl-hexyl moiety rather than the octyl-ether containing phenyl subsituents used before. The active layer was also subjected to a pyridine based treatment, improving performance from a 5.89% to the 8.08% PCE that was finally achieved. The dramatic changes in efficiency achieved by

changing the porphyrin substituents points to the incredibly sensitive fine-tuning of donor-acceptor interactions that must be carried out to achieve high PCE values.

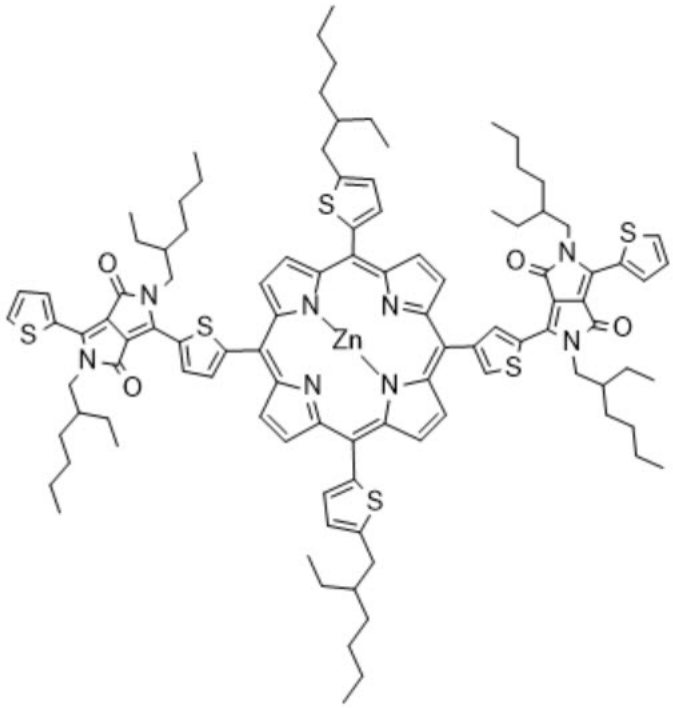

Figure 7. Schematic representation of the DPP donor molecule used in the devices with the highest reported efficiency for DPP donors as of 2015. The molecule yielded devices with a PCE of 8.08% due to its wide absorption spectra, high molar absorption coefficient and very high hole mobilities.

Donors containing the DPP core have been able to reach some of the highest efficiencies to date in small molecule organic solar cells. An improved understanding of the molecule features necessary to obtain high mobilities, increase and broaden light absorption and of the optimization processes necessary to obtain favorable morphologies has led to an increase from a 4.4% efficiency achieved in 2009 to the 8.08% value achieved in 2015.

Fullerene Acceptors

Fullerenes have been used rather ubiquitously as acceptors within organic solar

cells. This is due to the fact that fullerenes have many properties that make them ideal for this job. The LUMO level of most fullerenes is below the LUMO of commonly used donors and the electron mobility in fullerenes is very high (in the order of 10^{-2} $cm^2V^{-1}S^{-1}$)[81]. Moreover fullerenes can be easily functionalized and this allows for a fine control over their solubility and phase separation properties.[82]

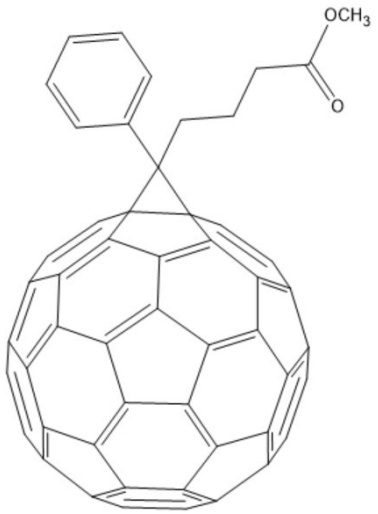

Figure 8. Schematic representation of the $PC_{61}BM$ fullerene, the most commonly used acceptor in organic solar cells.

Besides the above fullerenes also have other properties that make them hard to replace in organic solar cells. It has been recently shown that the existence of low lying excited state in fullerene anions lead to a ten-fold increase in charge separation while not affecting charge recombinations rates.[83]

Although $PC_{61}BM$ (Figure 8) and $PC_{71}BM$ are the most commonly used fullerenes in organic solar cells, there are other fullerenes that can yield better results when coupled with certain donor molecules. Diphenylmethano fullerenes, Diels-Adler aducts of C_{60} and Indene-C(60) bisadduct derivaties have showed improved results against $PC_{61}BM$ in polymer solar cells.[84–86] Other fullerene derivatives with better solubilities and higher lying LUMO orbitals have also been proposed as improvements to $PC_{61}BM$ in polymer solar cells.[87]

Lead Halide Pervoskite

During the past few years lead halide pervoskites ($PbCH_3NH_4I_3$) have become a leading material in the development of new solar cells. This material produces highly efficient devices thanks to its large dielectric constant, large charge mobility, broad absorptions and large absorption coefficient. In addition lead halide perovskites are cheap to produce and their fabrication methods are relatively simple.[88,89]

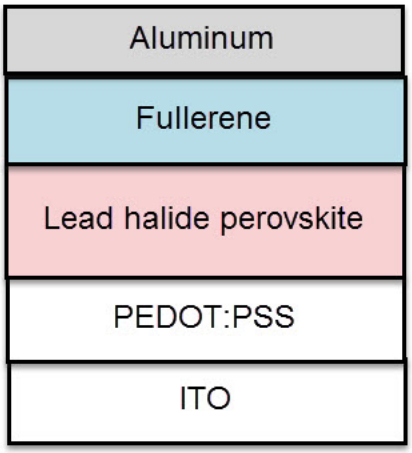

Figure 9. Schematic representation of the device structure for solar cells where the a lead halide perovskite layer replaces an organic donor material.

Perovskites can be used as a replacement for donor materials in traditional organic solar cells with devices prepared in a bi-layer structure where the pervoskite phase replaces the layer where the organic donor is traditionally placed (Figure 9). Devices built in this manner using $PC_{61}BM$ or C_{60} as electron acceptors have already showed efficiencies surpassing the 10% mark. [90–97]

However perovskite containing solar cells do not behave in the same way as traditional organic solar cells due to the special qualities of the perovskite material.[98] For example while charge separation happens only at donor/acceptor interfaces in organic solar cells due to the low dielectric constant of organic materials charge separation in perovskite solar cells occurs in the bulk of the material due to its large dielectric constant. Factors limiting device performance in

fullerene containing pervoskite solar cells are still not fully understood although film uniformity has been showed to play an important role.[99] There are also currently no studies using transient techniques addressing the recombination dynamics of fullerene containing pervoskite solar cells.

Bibliography

(1) Hosenuzzaman, M.; Rahim, N. A.; Selvaraj, J.; Hasanuzzaman, M.; Malek, A. B. M. A.; Nahar, A. *Renew. Sustain. Energy Rev.* **2015**, *41*, 284–297.

(2) Andrews, R. N.; Clarson, S. J. *Silicon* **2015**, *7* (3), 303–305.

(3) Fthenakis, V. *Proc. IEEE* **2015**, *103* (3), 283–286.

(4) Mathews, J. A.; Hu, M.-C.; Wu, C.-Y. *Renew. Sustain. Energy Rev.* **2015**, *46*, 275–281.

(5) Meillaud, F.; Boccard, M.; Bugnon, G.; Despeisse, M.; Hänni, S.; Haug, F.-J.; Persoz, J.; Schüttauf, J.-W.; Stuckelberger, M.; Ballif, C. *Mater. Today* **2015**.

(6) Green, M. A.; Emery, K.; Hishikawa, Y.; Warta, W.; Dunlop, E. D. *Prog. Photovoltaics Res. Appl.* **2015**, *23* (1), 1–9.

(7) Terheiden, B.; Ballmann, T.; Horbelt, R.; Schiele, Y.; Seren, S.; Ebser, J.; Hahn, G.; Mertens, V.; Koentopp, M. B.; Scherff, M.; Müller, J. W.; Holman, Z. C.; Descoeudres, A.; Wolf, S. De; de Nicolas, S. M.; Geissbuehler, J.; Ballif, C.; Weber, B.; Saint-Cast, P.; Rauer, M.; Schmiga, C.; Glunz, S. W.; Morrison, D. J.; Devenport, S.; Antonelli, D.; Busto, C.; Grasso, F.; Ferrazza, F.; Tonelli, E.; Oswald, W. *Phys. status solidi* **2015**, *212* (1), 13–24.

(8) Aman, M. M.; Solangi, K. H.; Hossain, M. S.; Badarudin, A.; Jasmon, G. B.; Mokhlis, H.; Bakar, A. H. A.; Kazi, S. . *Renew. Sustain. Energy Rev.* **2015**, *41*, 1190–1204.

(9) Marchal, J. C.; Krug III, D. J.; McDonnell, P.; Sun, K.; Laine, R. M. *Green Chem.* **2015**, *17* (7), 3931–3940.

(10) Branham, M. S.; Hsu, W.-C.; Yerci, S.; Loomis, J.; Boriskina, S. V; Hoard, B. R.; Han, S. E.; Chen, G. *Adv. Mater.* **2015**, *27* (13), 2182–2188.

(11) Livi, F.; Søndergaard, R. R.; Andersen, T. R.; Roth, B.; Gevorgyan, S.; Dam, H. F.; Carlé, J. E.; Helgesen, M.; Spyropoulos, G. D.; Adams, J.; Ameri, T.; Brabec, C. J.; Legros, M.; Lemaitre, N.; Berny, S.; Lozman, O. R.; Schumann, S.; Scheel, A.; Apilo, P.; Vilkman, M.; Bundgaard, E.; Krebs, F. C. *Energy Technol.* **2015**, *3* (4), 423–427.

(12) Angmo, D.; Krebs, F. C. *Energy Technol.* **2015**, n/a – n/a.

(13) Vilkman, M.; Apilo, P.; Välimäki, M.; Ylikunnari, M.; Bernardi, A.; Po, R.; Corso,

G.; Hast, J. *Energy Technol.* **2015**, *3* (4), 407–413.

(14) Cheng, P.; Bai, H.; Zawacka, N. K.; Andersen, T. R.; Liu, W.; Bundgaard, E.; Jørgensen, M.; Chen, H.; Krebs, F. C.; Zhan, X. *Adv. Sci.* **2015**, *2* (6), n/a – n/a.

(15) Liu, W.; Shi, H.; Andersen, T. R.; Zawacka, N. K.; Cheng, P.; Bundgaard, E.; Shi, M.; Zhan, X.; Krebs, F. C.; Chen, H. *RSC Adv.* **2015**, *5* (45), 36001–36006.

(16) Lucera, L.; Kubis, P.; Fecher, F. W.; Bronnbauer, C.; Turbiez, M.; Forberich, K.; Ameri, T.; Egelhaaf, H.-J.; Brabec, C. J. *Energy Technol.* **2015**, *3* (4), n/a – n/a.

(17) Sivula, K. *J. Phys. Chem. Lett.* **2015**, *6* (6), 975–976.

(18) Mulligan, C. J.; Bilen, C.; Zhou, X.; Belcher, W. J.; Dastoor, P. C. *Sol. Energy Mater. Sol. Cells* **2015**, *133*, 26–31.

(19) Carson, J. A. *Solar Cell Research Progress*; Nova Publishers, 2008.

(20) Riordan, C.; Hulstron, R. In *IEEE Conference on Photovoltaic Specialists*; IEEE; pp 1085–1088.

(21) *Organic Solar Cells: Fundamentals, Devices, and Upscaling*; CRC Press, 2014.

(22) Ginley, D.; Hosono, H.; Paine, D. C. *Handbook of Transparent Conductors*; Springer Science & Business Media, 2010.

(23) *Organic Solar Cells: Materials and Device Physics*; Springer Science & Business Media, 2012; Vol. 19.

(24) Bolz, R. E. *CRC Handbook of Tables for Applied Engineering Science*; CRC Press, 1973.

(25) Hau, S. K.; Yip, H.-L.; Jen, A. K.-Y. *Polym. Rev.* **2010**, *50* (4), 474–510.

(26) Patil, B. R.; Shanmugam, S.; Teunissen, J.-P.; Galagan, Y. *Org. Electron.* **2015**, *21*, 40–46.

(27) Liu, Y.; Chen, C.-C.; Hong, Z.; Gao, J.; Yang, Y. M.; Zhou, H.; Dou, L.; Li, G.; Yang, Y. *Sci. Rep.* **2013**, *3*, 3356.

(28) Liu, C.; Yi, C.; Wang, K.; Yang, Y.; Bhatta, R. S.; Tsige, M.; Xiao, S.; Gong, X. *ACS Appl. Mater. Interfaces* **2015**, 150220090109002.

(29) Kan, B.; Li, M.; Zhang, Q.; Liu, F.; Wan, X.; Wang, Y.; Ni, W.; Long, G.; Yang, X.; Feng, H.; Zuo, Y.; Zhang, M.; Huang, F.; Cao, Y.; Russell, T. P.; Chen, Y. *J. Am. Chem. Soc.* **2015**, 150304052305008.

(30) Greiner, M. T.; Helander, M. G.; Wang, Z.-B.; Tang, W.-M.; Lu, Z.-H. *J. Phys.*

Chem. C **2010**, *114* (46), 19777–19781.

(31) Nardes, A. M.; Kemerink, M.; de Kok, M. M.; Vinken, E.; Maturova, K.; Janssen, R. A. J. *Org. Electron.* **2008**, *9* (5), 727–734.

(32) VITORATOS, E.; SAKKOPOULOS, S.; DALAS, E.; PALIATSAS, N.; KARAGEORGOPOULOS, D.; PETRAKI, F.; KENNOU, S.; CHOULIS, S. *Org. Electron.* **2009**, *10* (1), 61–66.

(33) Park, S.; Tark, S. J.; Kim, D. *Curr. Appl. Phys.* **2011**, *11* (6), 1299–1301.

(34) Qi, B.; Zhang, Z.-G.; Wang, J. *Sci. Rep.* **2015**, *5*, 7803.

(35) Brabec, C. J.; Shaheen, S. E.; Winder, C.; Sariciftci, N. S.; Denk, P. *Appl. Phys. Lett.* **2002**, *80* (7), 1288.

(36) Liu, Y.; Page, Z.; Duzhko, V.; Emrick, T.; Russell, T. *APS March Meet. 2015* **2015**.

(37) Yang, E. Y.; So, B. M.; Chung, C. M.; Oh, S. Y. *J. Nanosci. Nanotechnol.* **2012**, *12* (1), 760–763.

(38) Tsuji, H.; Yokoi, Y.; Sato, Y.; Tanaka, H.; Nakamura, E. *Chem. Asian J.* **2011**, *6* (8), 2005–2008.

(39) Tsuji, H.; Ota, Y.; Furukawa, S.; Mitsui, C.; Sato, Y.; Nakamura, E. *Asian J. Org. Chem.* **2012**, *1* (1), 34–37.

(40) Deckman, I.; Obuchovsky, S.; Moshonov, M.; Frey, G. L. *Langmuir* **2015**, *31* (24), 6721–6728.

(41) Heremans, P.; Cheyns, D.; Rand, B. P. *Acc. Chem. Res.* **2009**, *42* (11), 1740–1747.

(42) Blom, P. W. M.; Mihailetchi, V. D.; Koster, L. J. A.; Markov, D. E. *Adv. Mater.* **2007**, *19* (12), 1551–1566.

(43) Lunt, R. R.; Giebink, N. C.; Belak, A. A.; Benziger, J. B.; Forrest, S. R. *J. Appl. Phys.* **2009**, *105* (5), 053711.

(44) Grancini, G.; Maiuri, M.; Fazzi, D.; Petrozza, A.; Egelhaaf, H.-J.; Brida, D.; Cerullo, G.; Lanzani, G. *Nat. Mater.* **2013**, *12* (1), 29–33.

(45) Shen, X.; Han, G.; Fan, D.; Xie, Y.; Yi, Y. *J. Phys. Chem. C* **2015**, *119* (21), 11320–11326.

(46) Caruso, D.; Troisi, A. *Proc. Natl. Acad. Sci. U. S. A.* **2012**, *109* (34), 13498–13502.

(47) Petersen, A.; Ojala, A.; Kirchartz, T.; Wagner, T. A.; Würthner, F.; Rau, U. *Phys. Rev. B* **2012**, *85* (24), 245208.

(48) Heeger, A. J. *Adv. Mater.* **2014**, *26* (1), 10–27.

(49) Proctor, C. M.; Kuik, M.; Nguyen, T.-Q. *Prog. Polym. Sci.* **2013**, *38* (12), 1941–1960.

(50) Cowan, S. R.; Banerji, N.; Leong, W. L.; Heeger, A. J. *Adv. Funct. Mater.* **2012**, *22* (6), 1116–1128.

(51) Bartesaghi, D.; Pérez, I. D. C.; Kniepert, J.; Roland, S.; Turbiez, M.; Neher, D.; Koster, L. J. A. *Nat. Commun.* **2015**, *6*, 7083.

(52) Yang, Y. (Michael); Chen, W.; Dou, L.; Chang, W.-H.; Duan, H.-S.; Bob, B.; Li, G.; Yang, Y. *Nat. Photonics* **2015**, *9* (3), 190–198.

(53) Gao, K.; Li, L.; Lai, T.; Xiao, L.; Huang, Y.; Huang, F.; Gao, K.; Li, L.; Lai, T.; Xiao, L.; Huang, Y.; Huang, F.; Peng, J. **2015**.

(54) O'Boyle, N. M.; Campbell, C. M.; Hutchison, G. R. *J. Phys. Chem. C* **2011**, *115* (32), 16200–16210.

(55) Zhou, H.; Yang, L.; You, W. *Macromolecules* **2012**, *45* (2), 607–632.

(56) Scharber, M. C.; Mühlbacher, D.; Koppe, M.; Denk, P.; Waldauf, C.; Heeger, A. J.; Brabec, C. J. *Adv. Mater.* **2006**, *18* (6), 789–794.

(57) Aguirre, J. C.; Hawks, S. A.; Ferreira, A. S.; Yee, P.; Subramaniyan, S.; Jenekhe, S. A.; Tolbert, S. H.; Schwartz, B. J. *Adv. Energy Mater.* **2015**, *5* (11), n/a – n/a.

(58) Poelking, C.; Andrienko, D. *J. Am. Chem. Soc.* **2015**, *137* (19), 6320–6326.

(59) Lin, Y.; Li, Y.; Zhan, X. *Chem. Soc. Rev.* **2012**, *41* (11), 4245–4272.

(60) Mishra, A.; Bäuerle, P. *Angew. Chemie Int. Ed.* **2012**, *51* (9), 2020–2067.

(61) Zhang, Q.; Kan, B.; Liu, F.; Long, G.; Wan, X.; Chen, X.; Zuo, Y.; Ni, W.; Zhang, H.; Li, M.; Hu, Z.; Huang, F.; Cao, Y.; Liang, Z.; Zhang, M.; Russell, T. P.; Chen, Y. *Nat. Photonics* **2014**, *9* (1), 35–41.

(62) Kan, B.; Li, M.; Zhang, Q.; Liu, F.; Wan, X.; Wang, Y.; Ni, W.; Long, G.; Yang, X.; Feng, H.; Zuo, Y.; Zhang, M.; Huang, F.; Cao, Y.; Russell, T. P.; Chen, Y. *J. Am. Chem. Soc.* **2015**, *137* (11), 3886–3893.

(63) Qu, S.; Tian, H. *Chem. Commun. (Camb).* **2012**, *48* (25), 3039–3051.

(64) Edwin B. Faulkner, R. J. S. *High Performance Pigments*; John Wiley & Sons,

2009.

(65) Li, W.; Furlan, A.; Roelofs, W. S. C.; Hendriks, K. H.; van Pruissen, G. W. P.; Wienk, M. M.; Janssen, R. A. J. *Chem. Commun. (Camb).* **2014**, *50* (6), 679–681.

(66) Dou, L.; You, J.; Yang, J.; Chen, C.-C.; He, Y.; Murase, S.; Moriarty, T.; Emery, K.; Li, G.; Yang, Y. *Nat. Photonics* **2012**, *6* (3), 180–185.

(67) Liu, F.; Gu, Y.; Wang, C.; Zhao, W.; Chen, D.; Briseno, A. L.; Russell, T. P. *Adv. Mater.* **2012**, *24* (29), 3947–3951.

(68) Walker, B.; Tamayo, A. B.; Dang, X.-D.; Zalar, P.; Seo, J. H.; Garcia, A.; Tantiwiwat, M.; Nguyen, T.-Q. *Adv. Funct. Mater.* **2009**, *19* (19), 3063–3069.

(69) Karsten, B. P.; Bijleveld, J. C.; Janssen, R. A. J. *Macromol. Rapid Commun.* **2010**, *31* (17), 1554–1559.

(70) Sonar, P.; Ng, G.-M.; Lin, T. T.; Dodabalapur, A.; Chen, Z.-K. *J. Mater. Chem.* **2010**, *20* (18), 3626.

(71) Lee, O. P.; Yiu, A. T.; Beaujuge, P. M.; Woo, C. H.; Holcombe, T. W.; Millstone, J. E.; Douglas, J. D.; Chen, M. S.; Fréchet, J. M. J. *Adv. Mater.* **2011**, *23* (45), 5359–5363.

(72) Loser, S.; Bruns, C. J.; Miyauchi, H.; Ortiz, R. P.; Facchetti, A.; Stupp, S. I.; Marks, T. J. *J. Am. Chem. Soc.* **2011**, *133* (21), 8142–8145.

(73) Sharma, G. D.; Mikroyannidis, J. A.; Sharma, S. S.; Roy, M. S.; Justin Thomas, K. R. *Org. Electron.* **2012**, *13* (4), 652–666.

(74) Lee, J. W.; Choi, Y. S.; Jo, W. H. *Org. Electron.* **2012**, *13* (12), 3060–3066.

(75) Li, L.; Huang, Y.; Peng, J.; Cao, Y.; Peng, X. *J. Mater. Chem. A* **2013**, *1* (6), 2144–2150.

(76) Lin, Y.; Ma, L.; Li, Y.; Liu, Y.; Zhu, D.; Zhan, X. *Adv. Energy Mater.* **2013**, *3* (9), 1166–1170.

(77) Huang, J.; Zhan, C.; Zhang, X.; Zhao, Y.; Lu, Z.; Jia, H.; Jiang, B.; Ye, J.; Zhang, S.; Tang, A.; Liu, Y.; Pei, Q.; Yao, J. *ACS Appl. Mater. Interfaces* **2013**, *5* (6), 2033–2039.

(78) Wang, H.; Liu, F.; Bu, L.; Gao, J.; Wang, C.; Wei, W.; Russell, T. P. *Adv. Mater.* **2013**, *25* (45), 6519–6525.

(79) Yin, Q.-R.; Miao, J.-S.; Wu, Z.; Chang, Z.-F.; Wang, J.-L.; Wu, H.-B.; Cao, Y. *J.*

Mater. Chem. A **2015**, *3* (21), 11575–11586.

(80) Wang, J.-L.; Wu, Z.; Miao, J.-S.; Liu, K.-K.; Chang, Z.-F.; Zhang, R.-B.; Wu, H.-B.; Cao, Y. *Chem. Mater.* **2015**, *27* (12), 150609134530004.

(81) Bartelt, J. A.; Lam, D.; Burke, T. M.; Sweetnam, S. M.; McGehee, M. D. *Adv. Energy Mater.* **2015**, n/a – n/a.

(82) *Progress in High-Efficient Solution Process Organic Photovoltaic Devices*; Yang, Y., Li, G., Eds.; Topics in Applied Physics; Springer Berlin Heidelberg: Berlin, Heidelberg, 2015; Vol. 130.

(83) Liu, T.; Troisi, A. *Adv. Mater.* **2013**, *25* (7), 1038–1041.

(84) Riedel, I.; von Hauff, E.; Parisi, J.; Martín, N.; Giacalone, F.; Dyakonov, V. *Adv. Funct. Mater.* **2005**, *15* (12), 1979–1987.

(85) He, Y.; Chen, H.-Y.; Hou, J.; Li, Y. *J. Am. Chem. Soc.* **2010**, *132* (4), 1377–1382.

(86) Sieval, A. B.; Treat, N. D.; Rozema, D.; Hummelen, J. C.; Stingelin, N. *Chem. Commun. (Camb).* **2015**, *51* (38), 8126–8129.

(87) He, Y.; Li, Y. *Phys. Chem. Chem. Phys.* **2011**, *13* (6), 1970–1983.

(88) Leo, K. *Nat. Nanotechnol.* **2015**, *10* (7), 574–575.

(89) Park, N.-G. *Mater. Today (Oxford, U. K.)* **2014**, *18* (2), Ahead of Print.

(90) Yoon, W.; Boercker, J. E.; Lumb, M. P.; Tischler, J. G.; Jenkins, P. P.; Walters, R. J. In *2014 IEEE 40th Photovoltaic Specialist Conference (PVSC)*; IEEE, 2014; pp 1577–1580.

(91) Hu, L.; Peng, J.; Wang, W.; Xia, Z.; Yuan, J.; Lu, J.; Huang, X.; Ma, W.; Song, H.; Chen, W.; Cheng, Y.-B.; Tang, J. *ACS Photonics* **2014**, *1* (7), 547–553.

(92) Ryu, S.; Seo, J. W.; Shin, S. S.; Kim, Y. C.; Jeon, N. J.; Noh, J. H.; Seok, S. Il. *J. Mater. Chem. A* **2015**, *3* (7), 3271–3275.

(93) Kim, H.-B.; Choi, H.; Jeong, J.; Kim, S.; Walker, B.; Song, S.; Kim, J. Y. *Nanoscale* **2014**, *6* (12), 6679.

(94) You, J.; Hong, Z.; Yang, Y. M.; Chen, Q.; Cai, M.; Song, T.-B.; Chen, C.-C.; Lu, S.; Liu, Y.; Zhou, H.; Yang, Y. *ACS Nano* **2014**, *8* (2), 1674–1680.

(95) Liu, X.; Yu, H.; Yan, L.; Dong, Q.; Wan, Q.; Zhou, Y.; Song, B.; Li, Y. *ACS Appl. Mater. Interfaces* **2015**.

(96) Bai, Y.; Yu, H.; Zhu, Z.; Jiang, K.; Zhang, T.; Zhao, N.; Yang, S.; Yan, H. *J. Mater.*

Chem. A **2014**.

(97) Min, J.; Zhang, Z.-G.; Hou, Y.; Ramirez Quiroz, C. O.; Przybilla, T.; Bronnbauer, C.; Guo, F.; Forberich, K.; Azimi, H.; Ameri, T.; Spiecker, E.; Li, Y.; Brabec, C. J. *Chem. Mater.* **2015**, *27* (1), 227–234.

(98) O'Regan, B. C.; Barnes, P. R. F.; Li, X.; Law, C.; Palomares, E.; Marin-Beloqui, J. M. *J. Am. Chem. Soc.* **2015**, 150318153052006.

(99) Wen, X.; Sheng, R.; Ho-Baillie, A. W. Y.; Benda, A.; Woo, S.; Ma, Q.; Huang, S.; Green, M. A. *J. Phys. Chem. Lett.* **2014**, *5* (21), 3849–3853.

Chapter 2

Computational Methods

Table of Contents

Introduction

This chapter will describe the computational methods used within Chapter 6 of this thesis for the construction of a donor molecule database intended for the creation of statistical models for the prediction of experimental electrical properties in small molecule organic solar cells using a donor/$PC_{60}BM$ bulk-heterojunction architecture.

This section includes scripts that might be useful for anyone trying to reproduce or further the computational results achieved within this work. The scripts allow for the efficient batch processing of the database molecules and the efficient extraction of information into a usable database form. The scripts used for the construction of the final statistical models are also included within this chapter.

Database Construction

Molecule structure addition

The first step to add molecules to the database was to obtain their structure in a format that was suitable for further processing by the programs used for the calculation of 2D and 3D descriptors. This was achieved by converting the molecules to the Simplified Molecular-Input Line-Entry System (SMILES) format[1] from general organic notation using the ChemDraw Ultra v12.0 software[2].

The molecules were drawn as shown in Figure 1 and then converted using the “Copy As SMILES” option within the software. This process had to be done manually but there are currently important advances in automatic structure extraction from text that could be used in the future to gather this information.[3]

After the SMILES structure information was obtained the line was saved within a file containing an integer code which was unique to each molecule (for example 124.smi) . The experimental electrical properties for that molecules were also added to a csv file using the same code for future reference. We took care to

make the codes continous such as if 120 molecules were added we would have codes from 1 to 120.

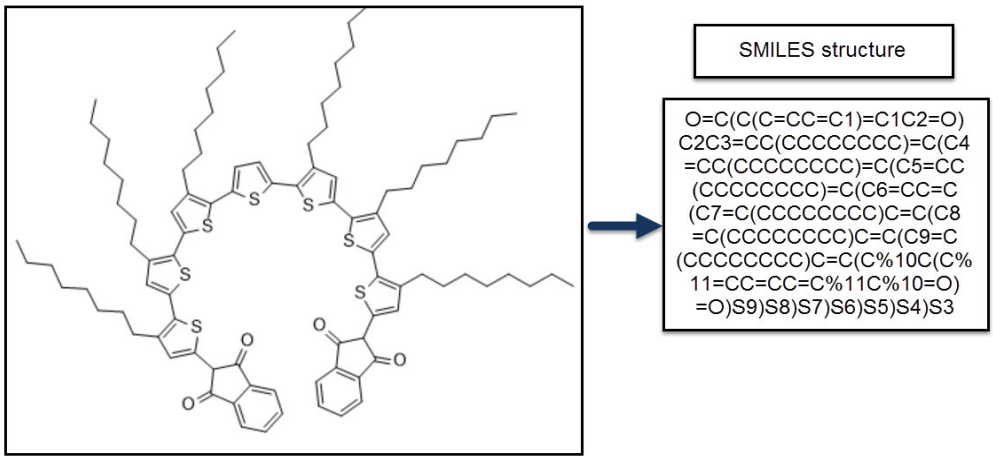

Figure 1. Sample molecular structure drawn in ChemDraw and then converted to the SMILES structure format.

Additional Structure Files

We generated 2D chemical descriptors using the PaDEl-descriptor software.[4] However this program does not recognize the SMILES format natively and it is therefore necessary to generate mol2 format files so that the molecules within the database can be used to generate descriptors. To create these mol2 files we used the OpenBabel software[5] and the SMILES format files generated before.

Additionally the mol2 and SMILES files have no 3D structure so in order to generate 3D structures to be used in the calculation of electronic properties we also had to convert our SMILES files to the XYZ format. We created these two file conversions in batch by using the code in Script 1. The MOLECULE_COUNT variable can be changed to the desired number of molecules to be converted. The script should be executed from the folder where all the SMILES structure files are located.

```
#!/usr/bin/python
import subprocess
import sys
import os

def main():

    MOLECULE_COUNT = 200

    for i in range(1,MOLECULE_COUNT+1):
        if os.path.exists(str(i)+ ".smi"):
            print "running {0}".format(str(i))
            os.system("babel -ismi " + str(i)+ ".smi -omol2 " + str(i)+ ".mol2")
            os.system("babel -ismi " + str(i)+ ".smi -oxyz " + str(i)+ ".xyz
--gen3d")

if __name__ == "__main__": main()
```

Script 1. Script used to convert files from SMILES to mol2 and XYZ format in batch.

However this automatic molecule conversion did not yield adequate 3D structures for all molecules. Some molecules, particularly those with 12-carbon or longer alkyl group chains had problems in the generation of the 3D structure (overlapping atoms for example) due to this reason we still had to correct or manually generate many molecules using the Gabedit software.[6] It is therefore important to manually check all generated structures to ensure that they not do not suffer from this type of problems.

2D Descriptor Generation

Once the correct structures were established we proceeded to generate 2D descriptors using the PaDEL-descriptor software. In order to do this we placed all mol2 structure files within a separate folder (mol2StructureFolder) and then used the PaDEL command line program.

---

java -jar PaDEL-Descriptor.jar -2d -usefilenameasmolname -detectaromaticity -descriptortypes usedDescriptors.xml -dir mol2StructureFolder -file

outputDescriptors.csv

Script 2. Command used to generate the descriptors from the mol2 files. The descriptors are output to a file called "outputDescriptors.csv". The PaDEL-descriptor software folder should be added to the system path.

There are many of these descriptors that either cannot be calculated (calculation is never finished) or generate errors (NaN, inifinity values) when calculated over mol2 files that contain no information on 3D structure. For this reason we had to reduce the number of calculated descriptors and use some internal PaDEL program options to allow for the calculations to finish successfully for all molecules within our database. The descriptor configuration used is placed within a configuration file (usedDescriptors.xml).

```
<Root>
    <Group name="2D">
        <Descriptor name="AcidicGroupCount" value="false"/>
        <Descriptor name="ALOGP" value="false"/>
        <Descriptor name="AminoAcidCount" value="false"/>
        <Descriptor name="APol" value="false"/>
        <Descriptor name="AromaticAtomsCount" value="true"/>
        <Descriptor name="AromaticBondsCount" value="true"/>
        <Descriptor name="AtomCount" value="false"/>
        <Descriptor name="AutocorrelationCharge" value="false"/>
        <Descriptor name="AutocorrelationMass" value="false"/>
        <Descriptor name="AutocorrelationPolarizability" value="true"/>
        <Descriptor name="BasicGroupCount" value="false"/>
        <Descriptor name="BCUT" value="false"/>
        <Descriptor name="BondCount" value="true"/>
        <Descriptor name="BPol" value="true"/>
        <Descriptor name="CarbonTypes" value="true"/>
        <Descriptor name="ChiChain" value="false"/>
        <Descriptor name="ChiCluster" value="false"/>
        <Descriptor name="ChiPathCluster" value="false"/>
        <Descriptor name="ChiPath" value="false"/>
        <Descriptor name="Crippen" value="false"/>
        <Descriptor name="EccentricConnectivityIndex" value="true"/>
        <Descriptor name="EStateAtomType" value="false"/>
        <Descriptor name="ExtendedTopochemicalAtom" value="false"/>
        <Descriptor name="FMF" value="false"/>
        <Descriptor name="FragmentComplexity" value="true"/>
        <Descriptor name="HBondAcceptorCount" value="false"/>
        <Descriptor name="HBondDonorCount" value="false"/>
        <Descriptor name="HybridizationRatio" value="true"/>
        <Descriptor name="IPMolecularLearning" value="false"/>
        <Descriptor name="KappaShapeIndices" value="true"/>
```

```
        <Descriptor name="KierHallSmarts" value="true"/>
        <Descriptor name="LargestChain" value="true"/>
        <Descriptor name="LargestPiSystem" value="true"/>
        <Descriptor name="LongestAliphaticChain" value="true"/>
        <Descriptor name="MannholdLogP" value="false"/>
        <Descriptor name="McGowanVolume" value="false"/>
        <Descriptor name="MDE" value="true"/>
        <Descriptor name="MLFER" value="false"/>
        <Descriptor name="PetitjeanNumber" value="true"/>
        <Descriptor name="RingCount" value="false"/>
        <Descriptor name="RotatableBondsCount" value="true"/>
        <Descriptor name="RuleOfFive" value="false"/>
        <Descriptor name="Topological" value="true"/>
        <Descriptor name="TPSA" value="false"/>
        <Descriptor name="VABC" value="false"/>
        <Descriptor name="VAdjMa" value="true"/>
        <Descriptor name="Weight" value="true"/>
        <Descriptor name="WeightedPath" value="false"/>
        <Descriptor name="WienerNumbers" value="true"/>
        <Descriptor name="XLogP" value="false"/>
        <Descriptor name="ZagrebIndex" value="true"/>
    </Group>
    <Group name="3D">
        <Descriptor name="CPSA" value="false"/>
        <Descriptor name="GravitationalIndex" value="false"/>
        <Descriptor name="LengthOverBreadth" value="false"/>
        <Descriptor name="MomentOfInertia" value="false"/>
        <Descriptor name="PetitjeanShapeIndex" value="false"/>
        <Descriptor name="WHIMUnity" value="false"/>
        <Descriptor name="WHIMMass" value="false"/>
        <Descriptor name="WHIMVolume" value="false"/>
        <Descriptor name="WHIMEneg" value="false"/>
        <Descriptor name="WHIMPolar" value="false"/>
    </Group>
    <Group name="Fingerprint">
        <Descriptor name="Fingerprinter" value="false"/>
        <Descriptor name="ExtendedFingerprinter" value="false"/>
        <Descriptor name="EStateFingerprinter" value="false"/>
        <Descriptor name="GraphOnlyFingerprinter" value="false"/>
        <Descriptor name="MACCSFingerprinter" value="false"/>
        <Descriptor name="PubchemFingerprinter" value="true"/>
        <Descriptor name="SubstructureFingerprinter" value="false"/>
        <Descriptor name="SubstructureFingerprintCount" value="false"/>
        <Descriptor name="KlekotaRothFingerprinter" value="false"/>
        <Descriptor name="KlekotaRothFingerprintCount" value="false"/>
    </Group>
</Root>
```

Script 3. Contents of the usedDescriptors.xml file used to generate chemical descriptors that could be calculated correctly for all molecules within the database.

DFT Descriptor Generation

We also obtained electronic structure (HOMO-1, HOMO, LUMO and LUMO+1 energies) and COSMO-RS descriptors (σ-profile) using the ADF 2013 software[7]. To do this we performed the following steps for all molecules within the database:

1. Create a new folder for the molecule's calculations.
2. Optimize the geometry at a BP86/TZP level of theory.
3. Rename the TAPE21 file created to opt_moleculeID.t21
4. If the optimization finished successfully then perform a single point energy calculation as suggested in the ADF manual for COSMO-RS calculations at the optimized geometry.
5. Rename the TAPE21 file created to cosmo_moleculeID.t21
6. Generate the coskf format files from the cosmo_moleculeID.t21 file using the cpkf ADF tool.
7. Generate the cosmo format files from the coskf format file using the kf2cosmo tool. The cosmo format files contain the sigma profile information.
8. Generate orbital energy information from the cosmo_moleculeID.t21 file using the adfreport tool.
9. Copy the resulting orbital energy and cosmo files to a folder containing all molecule results. Copy the final XYZ to a folder containing all final geometries.

In order to perform this fairly complicated process in a manner as simple as possible we created python scripts to automate each one of these steps individually and then a master script that automated the entire process. All individual process scripts have a command parameter -i which determines the ID of the molecule they need to process. For example the geometry optimization script (runGeometryOpt) can be called to carry out the geometry optimization of molecule 110 by using the command “python runGeometryOpt.py -i 110”. The

process scripts created are the following (actual script code can be found within Appendix 1):

- **runGeometryOpt** : Sets up and executes a geometry optimization for a given molecule.
- **runCOSMO** : Sets up and runs a single point calculation using the last point of a converged geometry optimization.
- **runADFK:** generates a coskf file from the tape21 file created from a single point energy run.
- **runSigma:** Uses the coskf file to generate a cosmo file containing the σ-profile for a molecule.
- **CheckProcess:** This script executes the entire process highlighted before for all molecules within the database using the 4 scripts mentioned before. The script automatically detects converged geometry runs and the step of the process where each molecule is located.

To use these scripts a work folder is created and all python script files are placed inside of it. We also create three folders within this work folder called “allXYZ”, “allFinalXYZ” and “allCosmo”. All molecule XYZ files are then placed inside the “allXYZ” folder and the checkProcess script is executed. The script creates folders for each new molecule and begins by running optimizations. The checkProcess script can then be executed within a cron job (every day for example) until all the molecules are processed. Each time the CheckProcess script is executed it will also give information about the number of molecules that have converged and will show inputs for geometry optimization and COSMO-RS runs.

Finally when all the cosmo and orbital energy files have been added to the resulting folder we used a python script to append all this information into a csv file format that was easy to manipulate and use to load data into R. The end result is a csv file that contains all σ-profile and orbitals energy descriptors with the information for one molecule per row.

```
#!/usr/bin/python
import subprocess
import sys
import os
import csv

def main():

    convergedCount = 0
    MOLECULE_COUNT = 200
    allSigmaProfiles = []

    columnHeaders = []
    columnHeaders.append("name")

    for i in range(0,51):
        columnHeaders.append("Sigma_"+str(i+1))

    columnHeaders.append("HOMO")
    columnHeaders.append("LUMO")
    columnHeaders.append("LUMO1")
    columnHeaders.append("HOMO1")

    allSigmaProfiles.append(columnHeaders)

    for i in range(1, MOLECULE_COUNT+1):
        filename = "allCosmo/cosmo_" + str(i) + ".cosmo"
        filename_info = "MOLECULE_" + str(i) + "/cosmo_" + str(i) + ".info"
        if os.path.exists(filename) and os.path.exists(filename_info):
            filecontent = list(csv.reader(open(filename, 'rb'), delimiter='\t'))
            startParsing = False
            sigmaProfile =[]
            geometry = []
            sigmaProfile.append(i)
            startParsingGeometry = False

            for item in filecontent:
                if "$cosmo_energy" in item:
                    startParsingGeometry = False
                if startParsingGeometry:
                    geometry.append(item[0])
                if "$coord_car" in item:
                    startParsingGeometry = True
                if startParsing:
                    sigmaProfile.append(float(str(item[0][10:])))
                if "$sigma_profile" in item:
                    startParsing =True

            filecontent = list(csv.reader(open(filename_info, 'rb'),
delimiter='\t'))

            for item in filecontent:
                if "Orbitals" not in item and len(item)>1:
                    energy = float(item[2])
                    sigmaProfile.append(energy)
```

```
            finalGeometry = []
            finalGeometry.append(str(len(geometry)))
            finalGeometry.append("This is an XYZ file")
            for item in geometry:
                finalGeometry.append(item)

            csvfile = open('allFinalXYZ/final_'+ str(i)+'.xyz', 'wb')
            for item in finalGeometry:
                csvfile.write("%s\n" % item)

            allSigmaProfiles.append(sigmaProfile)

    csvfile = open('allCosmoResults.csv', 'wb')
    writer = csv.writer(csvfile)
    writer.writerows(allSigmaProfiles)


if __name__ == "__main__": main()
```

Script 4. Python script used for formatting and appending of σ-profile and orbitals energy descriptors into a single csv file. The final file produced is named "allCosmoResults.csv".

Despite the fact that this process generated good results for a significant number of molecules there were several times were geometry runs had to be stopped and manually restarted due to issues with the geometry optimization process. Some molecules were also never attempted due to the fact that their calculation was not computationally feasible at the level of theory used (molecules with more than 200 atoms, molecules with metal centers, etc).

Model Generation

We performed our model generation using the R statistical analysis software and its random forest library.[8,9] These are the steps that were carried out for the generation of each model:

1. Load the output csv files containing 2D or DFT descriptors and experimental electrical properties into R (one molecule descriptors and experimental results per row).
2. Eliminate column containing molecule ID values

3. Randomly split data into an 85% training set and a 15% testing set such that the values for the variable to be predicted are homogeneously distributed between both sets.
4. Eliminate columns for other experimental variables that will not be predicted by this model.
5. Train the random forest model using the training set.
6. Calculate the mean square error in predictions within the testing set using the trained model.
7. If the generated model gave the smallest error up until now from all the models tested then save this model.
8. Repeat steps from 3 to 7 a total of two thousand times.
9. Create graphs and additional predictions using the final model created.

In the above manner we generated models that contained the largest possible generalization (lowest error within the testing set) as the model building process is repeated across many different training/testing set splits. This is necessary in order to avoid the generation of a poor model from a poorly chosen training/testing set split. The 2000 loop count is however arbitrary as potentially larger values can be used if a deeper search for better generalization is desired. However we did not find that larger counts led to any significant additional drop in testing set errors.

```
library(randomForest)
library(caret)
library(e1071)
library(corrgram)
library(ggplot2)
library(rpart)

mydata = read.csv("PathToResultsFile.csv")
mydata$name <- NULL

maxError = 1000
```

```
for (i in 1:2000){
  trainIndex <- createDataPartition(mydata$PCE, p = 0.85, list = FALSE, times = 1)

  Train <- mydata[trainIndex, ]
  Test <- mydata[-trainIndex, ]

  Train$V <- NULL
  Train$FF <- NULL
  Train$J <- NULL

  r0 = randomForest(formula = PCE ~ ., data = Train, importance = TRUE, ntree=2000,
scale = TRUE)
  error = (sum((predict(r0, Test)-Test$PCE)^2)/length(Test$PCE))
  print(maxError)

  if (error < maxError){
    maxError = error
    r1 <- r0
    PCETrain <- Train
    PCETest <- Test
  }

}

p <-ggplot()
p <- p + geom_point(size=3, aes(x=PCETrain$PCE ,y=predict(r1, PCETrain),
colour="Training set"))
p <- p + geom_point(size=5, aes(x=PCETest$PCE  ,y=predict(r1, PCETest),
colour="Testing set"))
p <- p + ylab("Predicted PCE (%)")
p <- p + xlab("Experimental PCE (%)")
p <- p + theme(axis.title.y = element_text(size = rel(1.5)))
p <- p + theme(axis.title.x = element_text(size = rel(1.5)))
p <- p + theme(axis.text.x = element_text(angle = 45, hjust = 1))
p <- p + theme(panel.background = element_rect(colour = "black"))
p <- p + geom_abline(intercept = 0, slope = 0)
p <- p + opts(legend.position = c(0.9, 0.1))
p

imp <- data.frame(row.names(importance(r1, 1)), importance(r1, 1)[,c("%IncMSE")],
stringsAsFactors=FALSE)

colnames(imp)<-c("name","importance")

p <-ggplot(data=imp, aes(x=reorder(imp$name, imp$importance), y=imp$importance))
p <- p + geom_bar(stat='identity')
p <- p + ylab("Variable Importance")
p <- p + xlab("Variable Names")
p <- p + theme(axis.title.y = element_text(size = rel(1.5)))
p <- p + theme(axis.title.x = element_text(size = rel(1.5)))
p <- p + theme(axis.text.x = element_text(angle = 90, hjust = 1))
p <- p + theme(panel.background = element_rect(colour = "black"))
p <- p + geom_abline(intercept = 0, slope = 0)
p <- p + opts(legend.position = c(0.9, 0.1))
p
```

Script 5. Sample R script used for model generation and model result plotting. In this case a model for the PCE is constructed.

It is also true that other model types implemented in R (such as support vector machines or logistic regressors) can be used in the same script by changing the "r0 = randomForest..." line to whatever model is desired. The R machine learning implementations are fairly inter-compatible so testing of the same process using different machine learning algorithms should be straightforward.

The parameters for the random forest model (such as the number of trees used) can also be changed in the above script in order to obtain different results. The train/testing set split can also be modified to any desired value, although values lower than 80% are generally too low to provide meaningful generalization (at least for our tested database size).

Bibliography

(1) Anderson, E.; Veith, G. D.; Weininger, D. *SMILES, a Line Notation and Computerized Interpreter for Chemical Structures*; U.S. Environmental Protection Agency, Environmental Research Laboratory, 1987.

(2) Mills, N. *J. Am. Chem. Soc.* **2006**, *128* (41), 13649–13650.

(3) Southan, C.; Stracz, A. *J. Cheminform.* **2013**, *5* (1), 20.

(4) Yap, C. W. *J. Comput. Chem.* **2011**, *32* (7), 1466–1474.

(5) O'Boyle, N. M.; Banck, M.; James, C. A.; Morley, C.; Vandermeersch, T.; Hutchison, G. R. *J. Cheminform.* **2011**, *3* (1), 33.

(6) Allouche, A.-R. *J. Comput. Chem.* **2011**, *32* (1), 174–182.

(7) Te Velde, G.; Bickelhaupt, F. M.; Baerends, E. J.; Fonseca Guerra, C.; van Gisbergen, S. J. A.; Snijders, J. G.; Ziegler, T. *J. Comput. Chem.* **2001**, *22* (9), 931–967.

(8) R Core Team. R: A Language and Environment for Statistical Computing, 2013.

(9) Breiman, L. *Mach. Learn. 45* (1), 5–32.

Chapter 3

Experimental Methods

Table of Contents

Introduction

This chapter will focus on the description of the experimental methods used to perform the opto-electronic characterization of films and devices through this thesis. This chapter will not include details on device fabrication as these details will be explained on each individual experimental chapter. We leave the description of fabrication procedures to subsequent chapters since device fabrication procedures can vary significantly between device types and are better understood in the context of each chapter. We therefore reserve this section for characterization techniques that are universally applied to all studied devices and films.

First we will go through experiments used to characterize photo-active materials and photo-active material thin films and we will then go into the experiments used for the opto-electronic characterization of finished devices.

Active layer characterization

UV-Visible spectroscopy

We obtained UV-Visible spectra from active layer films and donor molecule solutions in order to better understand the absorption characteristics of the materials and how they change through different post-processing steps. These UV-Visible spectra measurements were performed using a Shimadzu UV 2401PC spectrophotometer, using double beam optics, a photomultiplier detector and deuterium/tungsten light sources. For the determination of molar extinction coefficients for small molecules calibration curves at different molecule concentrations in dichloromethane were measured (0.1-1.0 absorption) and the extinction coefficient was obtained using the Beer-Lambert law. Some measurements were also carried out using a Shimadzu UV-1700 spectrophotometer.

The steady state emission measurements for donor material thin films and

solutions, as well as the fluorescence life-time measurements were carried out using an Edinburgh Instrument LifeSpec II spectrometer. The spectrometer used a time-correlated single photon counting technique with a picosecond pulsed laser source at 475nm.

Using the intersection of the normalized absorption and fluorescence spectra we were able to calculate the optical band-gap for the studied materials which was used in conjunction with HOMO or LUMO level data derived from electrochemical measurements in order to calculate an approximation of the HOMO and LUMO levels of the materials.

Cyclic voltammetry measurements

We also carried out an electrochemical characterization of all donor molecules and fullerenes included within this thesis. These measurements were performed in order to obtain experimental values for the HOMO and/or LUMO levels taking advantage of the presence of reversible oxidation and reduction reactions for the molecules under study.

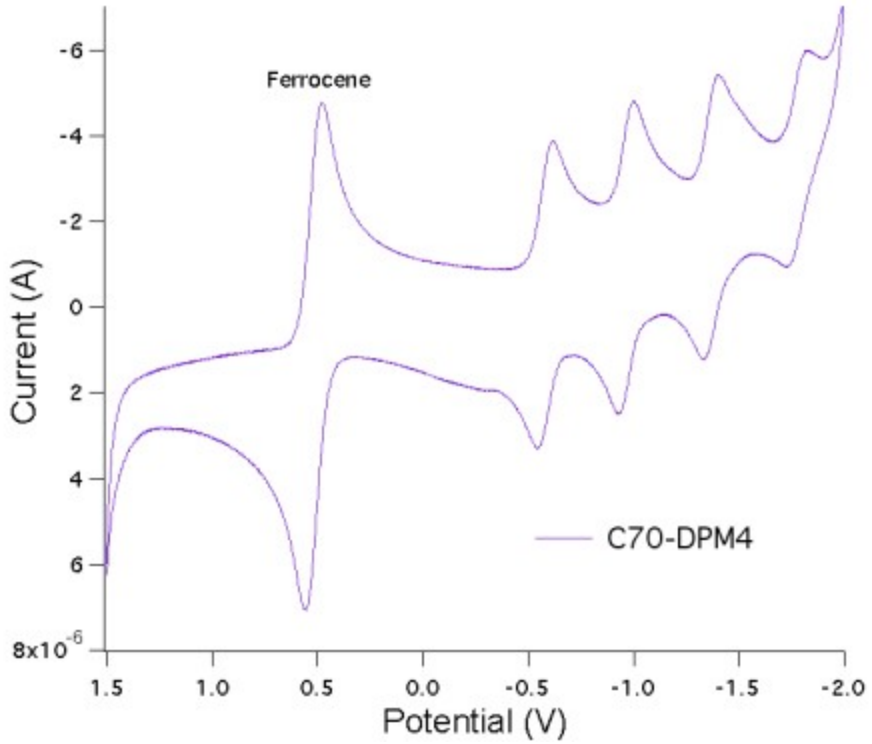

Figure 1. Sample cyclic-voltammetry measurement for the C_{70}-DPM4 molecule

used in Chapter 5.

Cyclic voltammetry measurements were carried out using a PARSTAT 22273 potentiostat (Princeton Applied Research). The measurements were made using solutions that contained a 0.1M tetrabuthylammonium hexafluorophosphate support electrolyte and the molecule under study in a concentration of approximately 1.0 mM in dry dichloromethane. We used an Ag/AgCl standard electrode as reference, a platinum wire working electrode and a platinum mesh counter electrode. Solutions were degassed briefly using Ar (10-30 seconds) before measuring since degassing for prolonged periods of time was not possible due to the volatility of the solvent used for the measurements. In the case of fullerenes degassing was particularly critical since measurements towards negative potentials are more deeply affected by the presence of atmospheric oxygen within the solution. Ferrocene was also used as an internal standard in order to more accurately measure the standard oxidation or reduction potentials for the devices.

Using the measure oxidation/reduction potential for the materials and the value attributed to the Ferrocene/Ferrocenium standard potential we can then establish values for the HOMO/LUMO levels according to the following equations[1]:

$$E_{HOMO} = -\left(E_{Oxidation} + 4.8\,eV\right) \qquad \text{(Equation 1)}$$

$$E_{LUMO} = -\left(E_{Reduction} + 4.8\,eV\right) \qquad \text{(Equation 2)}$$

Since most molecules do not have reversible oxidation and reduction reactions we often have to extrapolate either the HOMO or the LUMO by using the optical bandgap measurement obtained from the normalized fluorescence and UV-Vis spectra under dilute concentrations (0.1-0.01mM).[2]

$$E_{bandgap} = 1242/\lambda_{onset} \qquad \text{(Equation 3)}$$

$$E_{HOMO} = E_{LUMO} - E_{bandgap} \qquad \text{(Equation 4)}$$

$$E_{LUMO} = E_{HOMO} + E_{bandgap} \qquad \text{(Equation 5)}$$

It is worth mentioning that the above is a significant approximation because it

assumes that the electronic and optical bandgaps are the same. This can be a false assumption if the HOMO→LUMO transition is forbidden, a case in which the direct HOMO/LUMO bandgap cannot be measured using classic UV-Visible spectroscopy techniques. However for all molecules within our studies the HOMO→LUMO transition is allowed and therefore we assume this extrapolation to be a good approximation of the molecules' actual electronic structure.[3]

Laser Transient Absorption Sepctroscopy

The Laser Transient Absorption Spectroscopy technique (L-TAS) is a technique that measures transmission differences of a photo-active material film that is exposed to a laser perturbation. The sample is exposed to a predetermined wavelength (2nm slit) of generally visible light (400-700nm) and is then perturbated by a laser probe (1ns) of a fixed wavelength (PTI GL-3300 N_2 laser) that generates additional polarons within the material. If the polarons absorb the wavelength that the film is being exposed to and their molar extinction coefficient at that wavelength is significantly different than that of the molecules in their base state then the polaron generation caused by the laser probe will cause a change in the absorption of the film that will decay as a function of time. The laser probe must also be energetic enough to be able to generate enough polarons within the material. Using a laser probe in the absorption maximum of the studied film is recommended.

The absorption is measured using a photodetector based on a 3mm diameter silicon photodiode connected to a pre-amplifier (80ns and 10MHz) and a main amplifier that controls the DC offset and high/low pass filters. The decay is then received by a TDS 2022 Tektronic oscilloscope.

This measurement therefore gives direct information about polaron lifetimes since the decay lifetime for the change in absorption caused by the laser probe is directly proportional to this value. This means that the L-TAS measurement can give important information about non-geminate recombination, since it can

measure the polaron lifetime in organic donor-acceptor blends.

This measurement is also limited by the fact that the excitons need to have a sufficiently different molar extinction coefficient at the used wavelength than the molecules in their base state. For molecules like fullerenes this usually involves moving into the infrared spectrum (900-1000nm) where the absorption for the fullerene radical anions are generally located.

When measuring the L-TAS it is therefore useful to measure the polaron delta absorption spectrum by performing L-TAS measurements at different incident wavelengths and recording the amplitude in order to measure decay lifetimes at the highest possible signal-to-noise ratio.

Device Characterization

Current-Voltage characterization

The electric properties of our devices were obtained by measuring current-voltage (I-V) curves using a Sun 200 Solar Simulator (150W, ABET Technologies) and a Keithley 2400 digital source meter. Appropriate filters were used to simulate the AM 1.5G spectrum[4]. To perform this measurement devices were placed under 1 sun light intensity and the Keithley source meter was then used to apply different voltages while the current response was recorded.

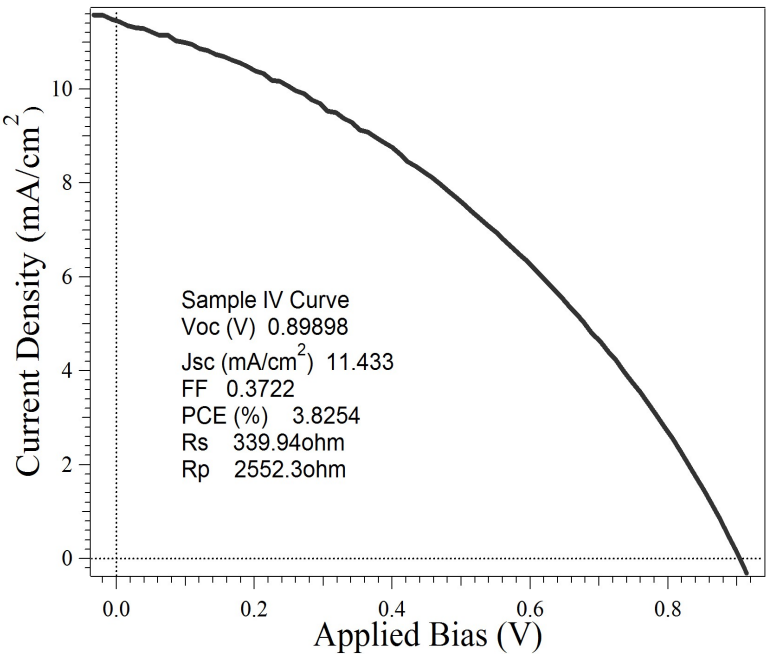

Figure 2. Sample I-V curve and electric properties for a solar cell measured under forward bias and a 1 Sun light intensity.

Device I-V curves were also measured at different light intensities by using different filters (80%, 50%, 12% and 5% of 1 Sun). These filters were placed directly on top of the devices measured under 1 sun. Devices were always measured under a nitrogen atmosphere using an air-tight holder with a Quartz window. Light intensity calibration (at 100 mW cm^{-2}) was performed for each substrate using an NRLE certified monocrystalline silicon photodiode.

In the case of small molecule organic solar cells all devices were measured under what is generally described as “forward bias”, where the I-V curve is constructed by first applying a negative potential and then moving towards a positive potential region. In the case of perovskyte containing solar cells the devices were also measured under reverse bias conditions were the potential moves from positive values towards negative values. This is necessary in the case of pervoskyte solar cells due to the hysteresis characteristics commonly present for these devices.[5]

Incident Photon-to-Current Conversion Efficiency

We also measured the incident photon to current conversion efficiency (IPCE) for our devices using a home-built system. The IPCE measures the percentage of photons that can be converted to collected charges at a given wavelength and is therefore a key property in determining the light harvesting efficiency of a device. The IPCE can be calculated from the wavelength, incident power and incident wavelengths by using Equation 7.

$$IPCE = \frac{I_{SC}}{P} . \frac{1240}{\lambda} .100 \qquad \text{(Equation 7)}$$

In this experiment a 150 W oriel Xenon lamp with a motorized monochromator

(2nm slit) was used to generate the incident light coupled with a Keithley 2400 digital source meter that was used to measure the device current at each different wavelength. The current measured was averaged over an integration time of 5 seconds in order to obtain a reliable measurement due to the low signal to noise ratio at the power levels reached by devices when irradiated by a single wavelength. The setup was calibrated using a diode with a well known IPCE profile

Charge mobility measurements

We measured hole and electron mobility for our donor/acceptor organic bulk heterojunction active layers using the Space Charge Limited Current (SCLC) model. In this model devices containing two hole blocking or electron blocking layers are prepared (Figure 3) and the I-V curve for the devices is measured up to potential levels that are large enough for the I-V current response to be linear and equal between dark and applied light bias. When this happens the device is considered to be within the space charge limited regime where current is mainly limited by charge mobility within the photo-active layer.

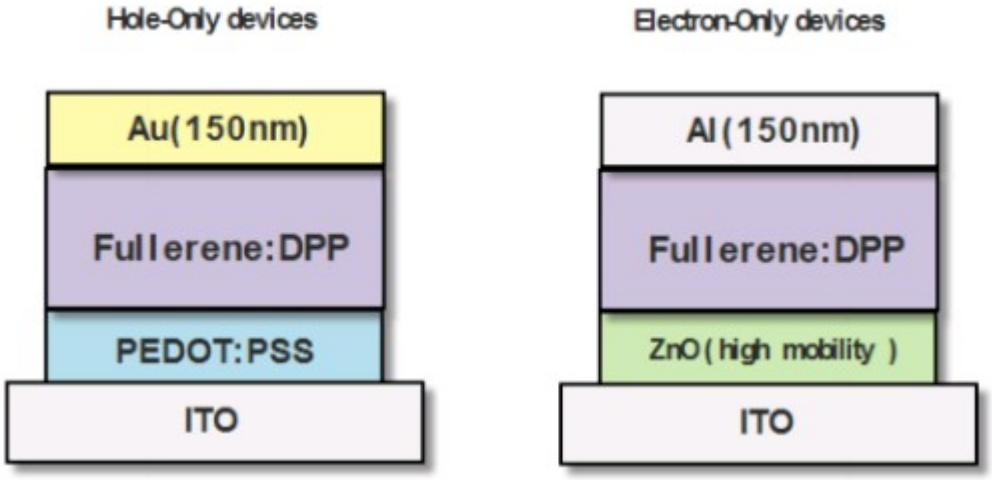

Figure 3. Device geometry for hole only and electron only devices used to measure electron and hole mobilities taking advantage of the SCLC model.

When devices reach the SCLC regime we can determine mobility using the Murgatroyd equation (Equation 6)[6]. It is worth noting that we cannot use the basic

Mott-Gurney law to determine charge mobility for our devices as the large potentials at which the SCLC regime is reached in our case causes the electric field to also have an influence on charge mobility. In the Murgatroyd equation the charge mobility (μ) is related with the charge limited current (J_{SCLC}), the difference between the potential and the built-in potential (V_{eff}=V-V_{bi}), the device thickness (d), the Poole-Frenkel parameter (β) and the product of vaccum and relative permittivities ($\varepsilon = \varepsilon_0 \varepsilon_r$). We fitted the above equation to our measured I-V data using the Igor Pro software (WaveMetrics, Inc. Lake Oswego, OR, USA).

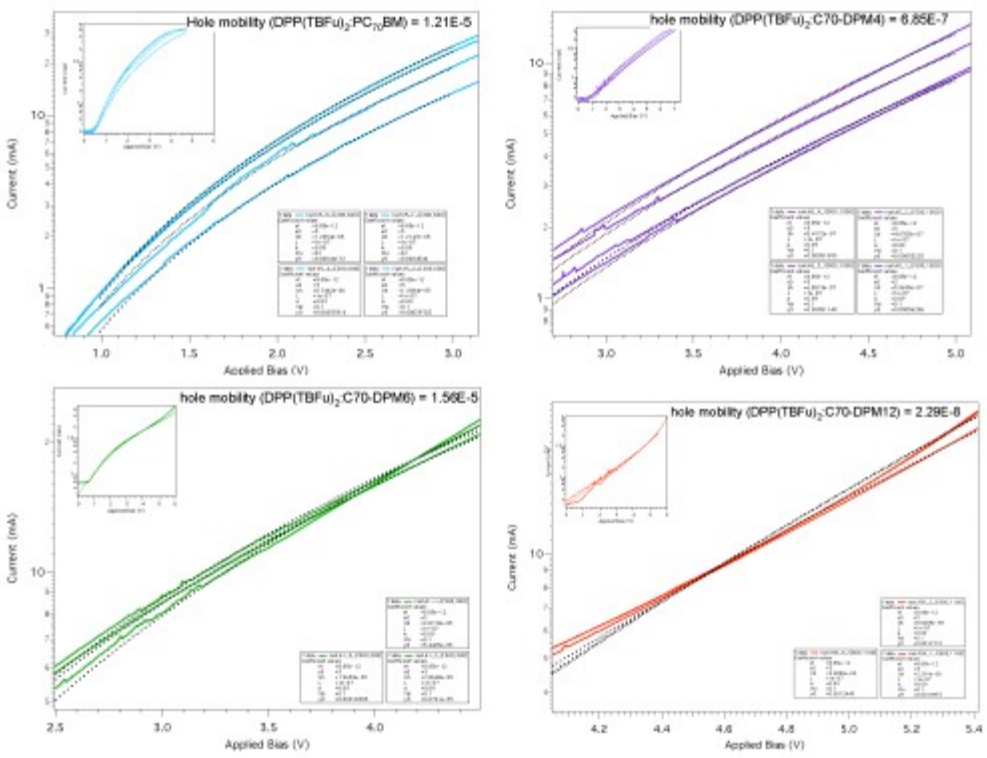

Figure 4. Sample hole mobility measurements for 4 different devices.

$$J_{SCLC} = \frac{9}{8}\varepsilon\mu\frac{V_{eff}}{d^3}\exp\left(\frac{0.89\beta\sqrt{V\,eff}}{\sqrt{d}}\right) \qquad \text{(Equation 6)}$$

Mobility measurements were also repeated several times for each active layer blend in order to ensure that the measurements were reproducible (as seen in Figure 4). This was necessary since the increase in temperature caused by the

large voltage and current values applied to the devices often caused changes that could render the measurements inaccurate. By measuring several times we ensured the the obtained values for the devices were accurate and not a consequence of some unintended changes within the active layers.

It is also worth mentioning that SCLC measurements cannot be easily applied to perovskite containing devices since the heat generation at higher potentials causes the perovskite active layer to irreversibly change. The SCLC measurement technique is therefore not appropriate to measure charge mobility in this type of devices.

Photo-induced Charge Extraction

The photo-induced charge extraction experiment measures the total charge accumulated within a device at a given level of applied light bias.[7–10] In this experiment a device is placed under a defined light intensity until the device reaches the steady state (constant voltage). When this happens the light source is powered off and the device is then connected to a known resistance (50 Ω) which drains any charges stored within the solar cell. When the device is drained the voltage decay as a function of time is measured and recorded using an oscilloscope. Since the integral of the voltage decay as a function of time divided by the resistance is equal to the charge in Coulombs we can therefore determine the amount of accumulated charges within the device. By repeating the experiment using different levels of applied bias we can determine the charges accumulated by the device in the steady state at different light intensities. We also perform the experiment under dark conditions in order to determine the level of charges expected from electrical noise.

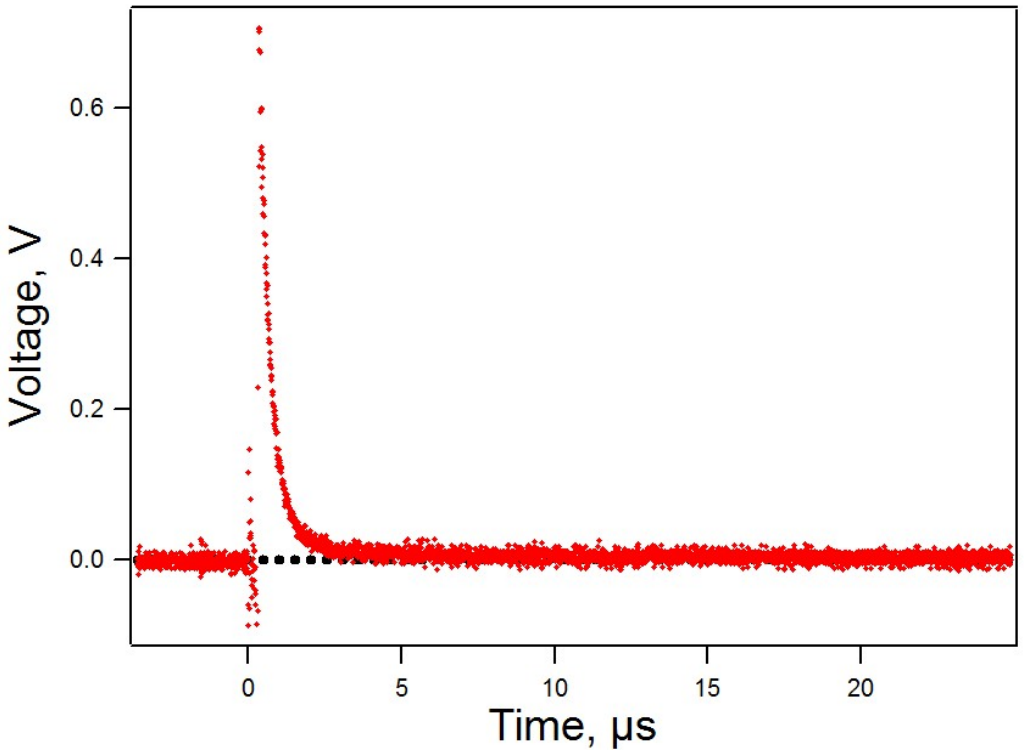

Figure 5. Sample charge extraction voltage decay results. You can see how the decay reaches the 0 line after less than 20 microseconds.

The experiment assumes that charge recombination for the device at short circuit conditions is zero. For this reason it is important to measure the Jsc for the device at different light intensities and ensure that the relationship between the Jsc and light intensity is linear. Another important consideration is that the voltage decay must reach the zero line in order for all the charges within the device to be considered as extracted. When studying new devices it is important to measure the CE under different time windows to ensure that potential has indeed decayed to zero.

In our case the charge extraction setup is built using a LED ring built from LUXEON(R) Lumileds to generate the applied bias and a DC power supply that is able to regulate the LED light intensity from 1 sun to dark. The discharge signal across the 50 Ω resistance is then measured with a Yokogawa DLM2000 oscilloscope.

Photo-Induced Transient Photovoltage

The Photo-Induced Transient Photovoltage (PI-TPV or TPV) experiment measures the changes in voltage associated with the generation of additional charge carriers created by a laser perturbation within a device that has reached the steady state at a given applied light bias.[8,11–13] It is analogous to an L-TAS experiment except that in this case we are measuring the voltage response of the device rather than the change in absorption given by the generation of charge carriers within an active layer film. In the TPV experiment the laser perturbation generates an increase in the voltage associated with the generation of additional charge carriers and the decay of this voltage perturbation towards the steady state voltage is associated with the recombination of these charge carriers within the device. In contrast with the L-TAS experiment, the TPV experiment accounts for all possible recombination processes within the device, including recombination processes associated with the contacts which are not present within the L-TAS experiment.

The TPV experiment assumes that the number of charges generated by the perturbation is small relative to the number of charges generated in the steady state so this requires the magnitude of the voltage perturbation caused by the laser pulse to be small. Generally perturbations below 20mV are used for the measurement although the magnitude of the perturbation at constant light intensity will increase as the applied light bias is reduced (as the number of charge carriers in the steady state becomes lower). For this reason the TPV experiment often demands an adjustment of the laser intensity as the light intensity changes in order to maintain the perturbation below 20 mV.

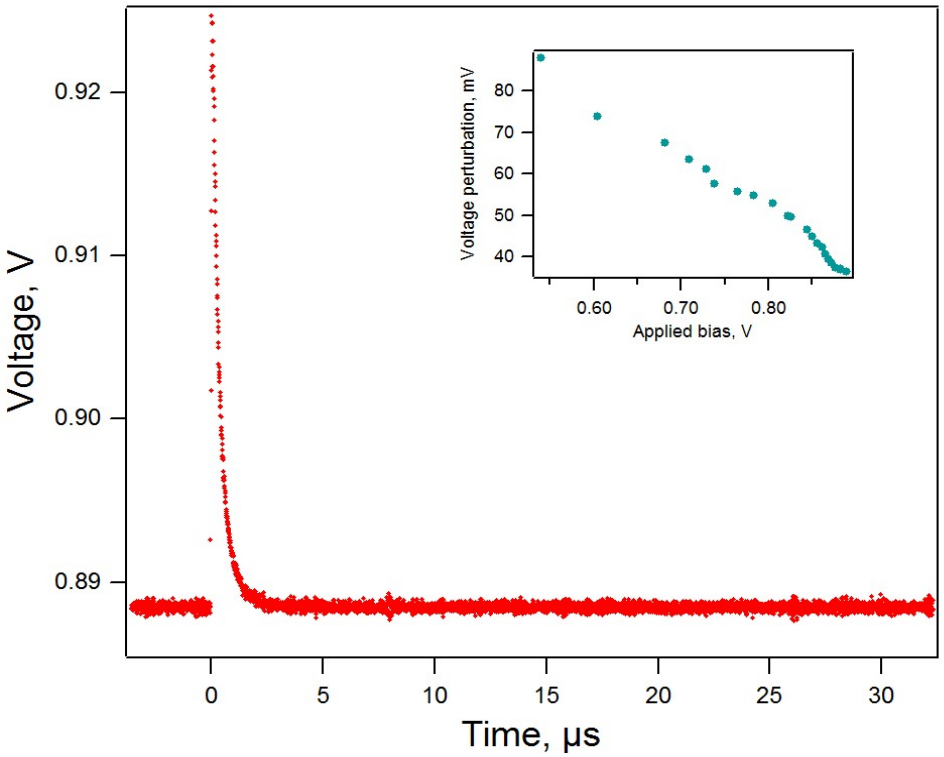

Figure 6. Sample TPV decay. Inset plot shows voltage perturbation as a function of applied light bias at constant laser intensity. You can see how the magnitude of the perturbation increases as the light intensity decreases.

In our TPV experiment the light bias is applied using the same LED ring used in the CE experiments. The perturbation was created using an N2 laser with a 50ns pulse. The wavelength of the lase pulser was chosen so that it matched the active layer absorption maximum as closely as possible. The voltage decay after each laser pulse was recorded using a Yokogawa DLM2000 oscilloscope. The laser trigger pulse was done every 1.5 seconds and each final measurement was created using the average of 30 different decay measurements.

Photo-Induced Transient Photocurrent

The last technique used to characterize our devices is the Photo-Induced Transient Photocurrent (PI-TPC or TPC) experiment. This experiment involves three separate measurements that allow us to deduce the charge density for a device at a given

level of applied bias. In the first step a laser perturbation is applied to a device connected to a 50Ω resistance in the dark and the voltage decay from this perturbation is recorded using an oscilloscope. The same measurement, with the same laser intensity, is repeated for the device at the level of applied light bias where we want to measure charge density. We then perform a normal TPV measurement at the exact same laser intensity at a desired applied light bias level.

$$N_{dark} = \frac{\int TPC_{dark}(V)dt}{50\Omega} \qquad \text{(Equation 8)}$$

$$dC_i = \frac{N_{dark}}{\Delta V_i} \qquad \text{(Equation 9)}$$

The first measurement, TPC_{dark}, gives us a decay whose integral divided by the resistance corresponds to the amount of charges (N_{dark}) generated by the laser perturbation within the device. The second measurement, TPC_{light} ,is used to confirm that charges generated in the steady state at the light intensity where we want to measure charge density (N_{light}) do not change the amount of charges generated by the laser perturbation. In this sense N_{dark} should be equal to N_{light}. The TPV measurement at the same light and laser intensity then gives us the voltage increase caused by the perturbation.

Since we know the voltage increase (ΔV_i) at a given light intensity (I) and we know the amount of charges generated (N_{dark}) we can therefore calculate the differential capacitance for that applied light bias (dC_i) using equation 9. By carrying out TPV measurements under different light biases at constant laser intensity and then integrating the differential capacitance at each light bias as a function of the steady state voltage we can obtain the charge density for the devices at each given light intensity.

The TPC measurement is therefore an indirect method to measure charge density within a device since it relies on the use of differential capacitance in order to calculate charge density. The TPC measurement has the advantage that it only

measures chemical capacitance while the charge extraction experiment measures all accumulated charges within a device, including those accumulated by the geometric capacitance of a solar cell.

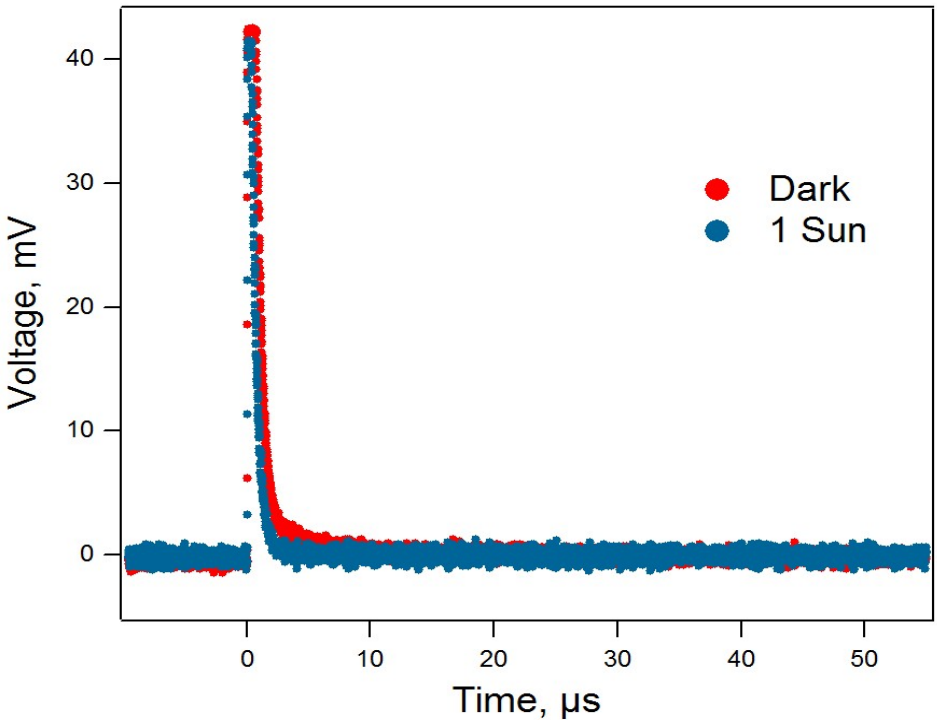

Figure 7. Sample TPC measurements under dark and 1 sun light intensities. The charge results are 0.86nC and 0.54nC respectively. In this case the TPC cannot be used to calculate charge densities at this level of light bias due to the significant difference between both charges.

An important inconvenient of the TPC measurement is that it relies heavily on the fact that the laser perturbation must be constant between TPC/TPV experiments in order for the measurement to be accurate. For each change in laser intensity the TPC_{dark} and TPC_{light} measurements need to be recorded again, as changes in laser intensity change the number of charges that are generated by the perturbation. Laser reproducibility is therefore quite critical for the TPC experiment.

Our TPC experiment uses the same LED setup and laser source used for our TPV experiments. The same setup for short circuting the device through the 50Ω

resistance is also used. Measurements are also made using the same Yokogawa DLM2000 oscilloscope.

Bibliography

(1) LEONAT, L.; SBÂRCEA, G.; BRÂNZOI, I. V. *U.P.B Sci. Bull, Ser. B* **2013**, *75* (3), 111–118.

(2) D'Andrade, B. W.; Datta, S.; Forrest, S. R.; Djurovich, P.; Polikarpov, E.; Thompson, M. E. *Org. Electron. physics, Mater. Appl.* **2005**, *6* (1), 11–20.

(3) Hu, D.; Shen, F.; Liu, H.; Lu, P.; Lv, Y.; Liu, D.; Ma, Y. *Chem. Commun. (Camb).* **2012**, *48* (24), 3015–3017.

(4) ASTM G173 - 03(2012) Standard Tables for Reference Solar Spectral Irradiances: Direct Normal and Hemispherical on 37° Tilted Surface http://www.astm.org/Standards/G173.htm (accessed Jul 2, 2015).

(5) Unger, E. L.; Hoke, E. T.; Bailie, C. D.; Nguyen, W. H.; Bowring, A. R.; Heumuller, T.; Christoforo, M. G.; McGehee, M. D.; Heumüller, T. *Energy Environ. Sci.* **2014**, *7* (11), 3690–3698.

(6) Bisquert, J.; Montero, J. M.; Bolink, H. J.; Barea, E. M.; Garcia-Belmonte, G. *Phys. status solidi* **2006**, *203* (15), 3762–3767.

(7) Credgington, D.; Hamilton, R.; Atienzar, P.; Nelson, J.; Durrant, J. R. *Adv. Funct. Mater.* **2011**, *21* (14), 2744–2753.

(8) Koops, S. E.; Barnes, P. R. F.; O'Regan, B. C.; Durrant, J. R. *J. Phys. Chem. C* **2010**, *114* (17), 8054–8061.

(9) O'Regan, B. C.; Durrant, J. R. *Acc. Chem. Res.* **2009**, *42* (11), 1799–1808.

(10) Shuttle, C. G.; Maurano, A.; Hamilton, R.; O'Regan, B.; de Mello, J. C.; Durrant, J. R. *Appl. Phys. Lett.* **2008**, *93* (18), 183501.

(11) Shuttle, C. G.; O'Regan, B.; Ballantyne, A. M.; Nelson, J.; Bradley, D. D. C.; de Mello, J.; Durrant, J. R. *Appl. Phys. Lett.* **2008**, *92* (9), 093311.

(12) Hamilton, R.; Shuttle, C. G.; O'Regan, B.; Hammant, T. C.; Nelson, J.; Durrant, J. R. *J. Phys. Chem. Lett.* **2010**, *1* (9), 1432–1436.

(13) O'Regan, B. C.; Scully, S.; Mayer, A. C.; Palomares, E.; Durrant, J. *J. Phys. Chem. B* **2005**, *109* (10), 4616–4623.

Chapter 4

Small molecule BHJ solar cells based on DPP(TBFu)$_2$ and diphenylmethanofullerenes (DPM): Linking morphology, transport, recombination and crystallinity.

Table of Contents

Motivation

The field of solution processed bulk-heterojunction (BHJ) solar cells has been widely dominated by polymer or small molecule donors and fullerene based acceptors[1]. Of these fullerene acceptors, the phenyl-butyric acid methyl ester substituted series ($PC_{60}BM$ and $PC_{70}BM$) have been by far the most commonly used. However, the ease of functionalization of the conjugated fullerene core has driven the search for new alternatives as the fullerene properties can be easily tuned by varying the functional groups while retaining the core's electronic properties. Particularly, it is well known that solubility, processability and HOMO-LUMO level positioning can be tuned by adequate chemical functionalization. Numerous alternatives have been published to date[2], but surprisingly only few structures have given better power conversion efficiencies (PCEs) than devices made with their methyl esters counterparts.[2a,3] These new acceptors have shown to have a strong effect on the crystallization process of the donor polymer domains, in polymer-based OSC devices, and can in some cases significantly impair device function.[4]

A diphenylmethano[60]fullerene (C_{60}-DPM) derivative bearing two lateral C_{12} aliphatic chains has been studied by others[5] and us in polymer-based devices.[4b] Although the experimental HOMO-LUMO levels of this new fullerene derivative where essentially similar to those of $PC_{60}BM$, it was shown to induce some distinct changes in the device performance. These properties were explained by the fact that C_{60}-DPM12 affects the crystallinity of the P3HT donor domains.[4b,5b] Similarly to polymer-based solar cells, the properties of SM-BHJ OSC have shown to be dependent on the crystallinity of the donor domains, and probably to a much greater extent. It has been demonstrated that in such type of devices crystalline growth of donor domains is either promoted or impeded depending on the type of fullerene used in the active layer blend.[6] The crystallite's growth seems to be related to the ratio of aliphatic over the aromatic carbons of the fullerene derivative, so that an optimum size of alkyl chain is required to promote donor's crystallite growth.[6a]

Based on our previous work on the use of solvent annealing to control the thin film nanomorphology[6b] we describe herein the preparation of solar cells devices based on a small molecule DPP(TBFu)2 donor and a series of C_{70}-DPM fullerene derivatives bearing alkyl chains of a different length, varying from 4, 6 to 12 carbons (**Figure 1**) with the aim to learn more about the relation between nanocrystalline domains in the photo-active layer and the device performance under working conditions. The presence of alkyl chains in the fullerene is expected to promote changes on the thin film nanomorphology that may also induce changes on (a) device performance and (b) charge transfer reactions at the materials interface. We have carried out a thorough characterization of the devices, in order to understand how the effect of fullerene substitution impacts the crystallinity and how this change in crystallinity is influencing the electronic transport and recombination properties of the devices.

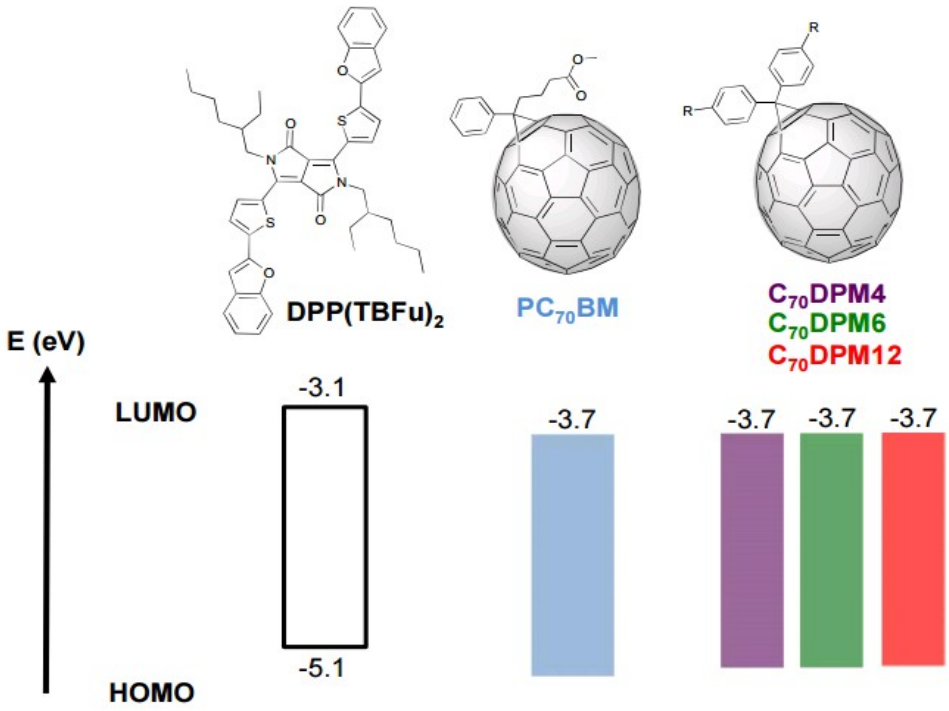

Figure 1.

Molecular structure of the DPP(TBFu)$_2$ donor and the C70-DPM series of fullerene used in the study, with their experimental HOMO and LUMO levels derived from cyclic voltametry and UV-Visible/steady-state emission measurements.

The effect of the different C_{70}-DPM fullerenes on the crystallinity of the donor domains has been investigated both quantitatively and qualitatively

using 1D and 2D X-Ray diffraction on active layers films. Space Charge Limited Current (SCLC) electron and hole charge carrier mobilities were measured and matched to the trend observed for the difference in crystallinity of the devices made out from the different C_{70}-DPM derivatives. Transient absorption spectroscopy (TAS) on active layer films and charge carrier recombination measurements carried out on complete devices using the transient photocurrent/transient photovoltage technique (CE/TPV) combined with ideality factor analysis provided insights on difference in band structure and energetic defects brought about by the C_{70}-DPM series respect to the $PC_{70}BM$ acceptor.

Device Fabrication

DPP(TBFu)2 was purchased from Lumtec Ltd. (Lumtec Ltd. Taiwan) and was used without further purification. DMP fullerenes derivatives were synthesised as described by Martin et al.1 PC70BM was purchased from Solenne (Solenne BV, the Netherlands). High purity (HPLC gradient grade, 99.9%) CHCl3 was used for the active layer deposition. The solvent was dried with activated molecular sieves and kept in a sealed bottle with silver foil prior to use. Aluminium (99.999%) and LiF (99.995%) were purchased from Sigma-Aldrich.

Pre-patterned Indium Tin Oxide (ITO) 5 Ohm/square (PSiOTec, Ltd., UK) sodalime glass substrates were first rinsed with acetone to remove the residual photoresist layer. The substrates were then placed in a teflon holder and sequentially sonicated in acetone (1 × 10 min) and isopropanol (2 × 10 min), and finally dryed under a flow of Nitrogen. The ITO substrates where ozone-treated in a UV-ozone cleaner for 30 mins in ambient atmosphere, and subsequently coated in air with a layer of filtered (0.45 mm, cellulose acetate) solution of Poly(3,4-ethylenedioxythiophene) : poly(styrenesulfonate) (PEDOT:PSS, HC Starck Baytron P) (4500 rpm 30 seconds followed by 3500 rpm 30 seconds). The PEDOT:PSS film was dried at 120 ºC under inert atmosphere for 15 min. Active layers were spin-coated (8000 rpm) in air over the PEDOT:PSS layer from a 20 mg/ml (total concentration) solution of DPP(TBFu)2 and PC71BM (6:4 w/w ratio). The approximate thickness of the active layer was 80 nm.

The solvent annealing step was carried out straight after deposition of the active layer by exposing the films to a saturated vapour of solvent in a closed vessel. The vessel (100 ml) was filled with 5 ml of CH2Cl2 and left sealed for 10 min. prior to the SVA step to ensure the atmosphere was saturated with solvent. The substrates were exposed to the solvent vapours from 15 seconds to several minutes by placing them in the solvent vessel. The cathode layer was deposited by thermal evaporation in an ultra high vacuum chamber (1x10-6 mbar). Metals were evaporated through a shadow mask leading to devices with an area of 9 mm2. LiF (0.6 nm) and Al (100 nm) were deposited at a rate of 0.1 Å/s and 0.5-1 Å/s respectively. Following fabrication, the films were maintained under a Nitrogen atmosphere and stored in the dark until used.

Results and Discussion

The crystallinity of donor domains in SM-BHJ devices has shown to be of capital importance to obtain good devices characteristics. In a previous study from our group we demonstrated that crystallite growth was very significantly enhanced in active layer blends of DPP(TBFu)$_2$:PC$_{70}$BM compared to films of pristine DPP(TBFu)$_2$ SM donor. The enhancement of crystallite growth then attributed to the presence of PC$_{70}$BM in the blend motivated us to investigate on the influence of fullerene functionalization on crystal growth of donor domains in SM-BHJ devices. To do so we employed a well-known structure depicted in Figure 2, where the active layers consisted of blend of DPP(TBFu)$_2$ and three different fullerene derivatives to which solvent annealing (with CH_2Cl_2) was applied as a post-deposition treatment. Such treatment has shown to promote crystal growth in active layers made out of small molecule:fullerene blends , particularly in devices using the DPM’s fullerenes. Prior to study the crystallinity of the different blends devices were fabricated with each C$_{70}$-DPM derivative and PC$_{70}$BM for reference purposes, and optimised for donor/acceptor (D/A) ratio, active layer thickness and annealing time. This provided a broad trend in the J-V characteristics, where both FF and JSC are seen to decrease relative to the alkyl chain length of the fullerene (**Figure 2**).

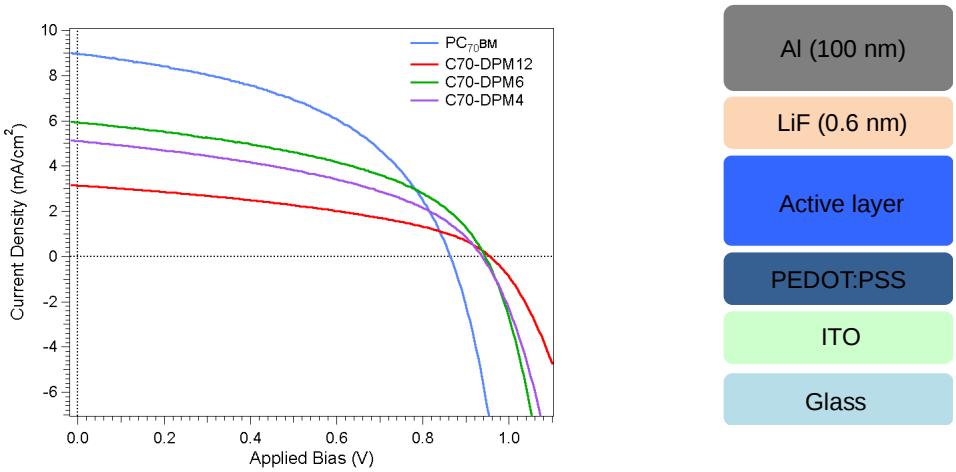

Figure 2. *J-V characteristics of solar cell devices fabricated with $PC_{70}BM$ and the C70-DPM series acceptors. These curves represent the average performance of devices made under optimized conditions.*

Device active layer	V_{OC} (V)	J_{SC} mA/cm^2	FF	PCE (%)	μ hole	μ electron
DPP(TBFu)$_2$:$PC_{70}BM$	0.858	8.97	0.47	3.64	1.2 (+/- 0.2) x 10^{-5}	1.6 (+/- 0.2) x 10^{-5}
DPP(TBFu)$_2$:C_{70}-DPM4	0.933	5.10	0.43	2.06	6.9 (+/- 1.0) x 10^{-7}	1.5 (+/- 0.8) x 10^{-5}
DPP(TBFu)$_2$:C_{70}-DPM6	0.944	5.92	0.45	2.55	1.6(+/- 0.3) x 10^{-5}	9.0 (+/- 0.8) x 10^{-7}
DPP(TBFu)$_2$:C_{70}-DPM12	0.954	3.13	0.41	1.21	2.3 (+/- 0.5) x 10^{-8}	2.4 (+/- 0.5) x 10^{-7}

Table 1. *Hole and electron mobility values for devices with active layers made with C_{70}-DPM fullerene series and $PC_{70}BM$.*

The V_{OC} is however consistently higher in devices made out of C70-DPM fullerenes (**Table 1**). The physics undermining such feature will be expounded below. The decrease in J_{SC} is corroborated by IPCE measurement showing a decrease in the overall IPCE value (**Figure 3b**) over the all range of the visible region. Interestingly the shape of the IPCE is similar in all fullerene derivatives showing that the contribution of each wavelength to the photocurrent is not altered by the fullerene substitution.

The change in the UV-Vis absorption measured (**Figure 3a**) in active layers prepared using conditions of optimised devices follows a previously described trend where the appearance of blue shifted absorption bands

typical of aggregation features is observed in all cases.[6b,7] The slight variation in the intensity of the bands is attributed to the slight difference in device thickness and D/A ratio in the blends.

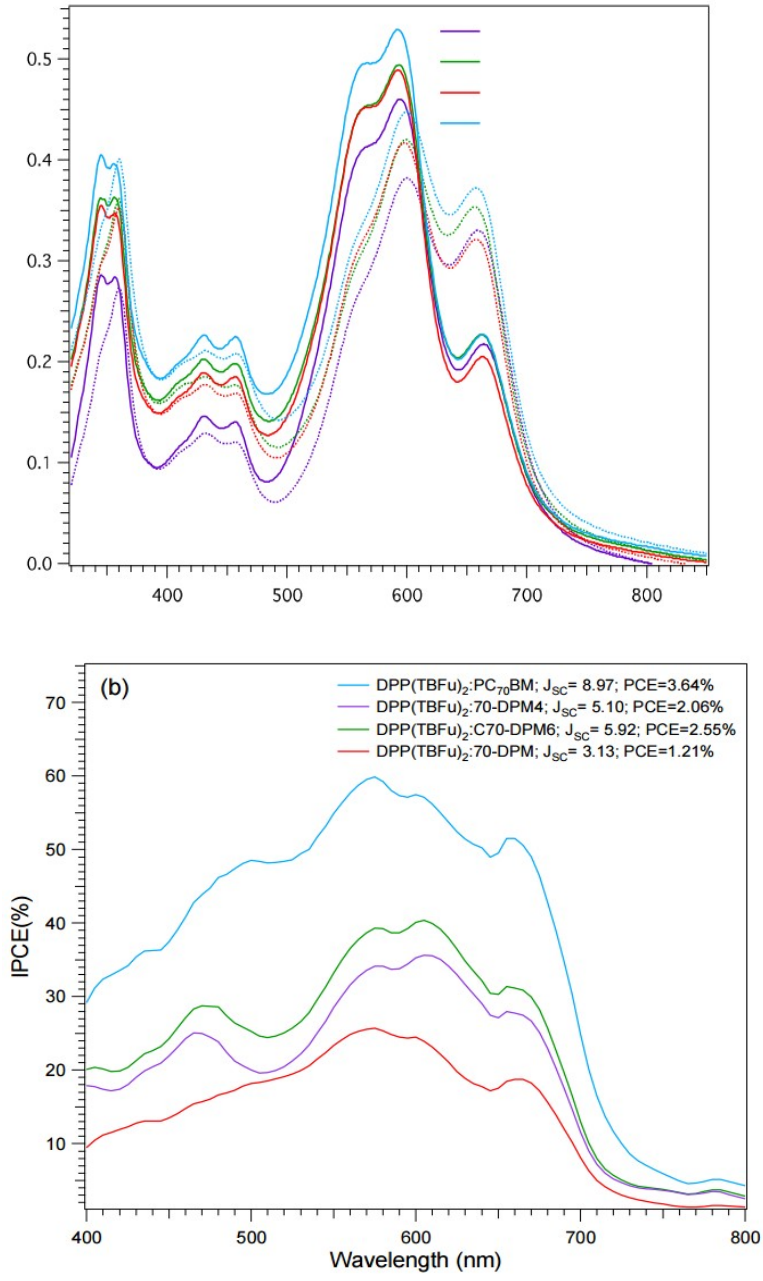

***Figure 3**. a) UV-Visible absorption spectra of CH_2Cl_2 solvent-annealed (solid line) and non-annealed (dotted line) DPP(TBFu)$_2$:fullerene active layers films. b) IPCE curves of solar cell devices whose J-V characteristics are shown in **Figure 2**.*

This aggregation characteristic in the solid state had been related to a crystallization process and well characterised using XRD experiments.[6b] Similarly, we first utilised out-of-plane grazing incidence XRD (GIXRD) setup with area detector to obtain qualitative information on the

orientation of crystallites of donor in the active layer. Measuring those same films with a point detector in reflection mode allowed us for a quantitative analysis. The area detector images taken from active layers prepared on glass substrates in the same conditions as optimised devices, are in agreement with previously reported results, with the appearance of the same diffraction spot upon annealing in all active layers at 2θ=6.1º with interplanar spacing of 14.5 Å attributed to the crystalline domains of the donor material. This confirms the formation of crystalline domains of donor molecules in the bulk for all C_{70}-DPM fullerenes (**Figure 4**).[6b,7] The texture in the different films shows a rather similar trend as in the reference DPP(TBFu)$_2$:PC$_{70}$BM where the crystallites adopt a rather homogenous orientation. However, the appearance of additional well resolved Debye rings superimposed on the main diffraction spot in the case of C_{70}-DPM6 and C_{70}-DPM12 active layer is strong evidence for the presence of two different populations of crystallites, one very well oriented and the other randomly oriented.

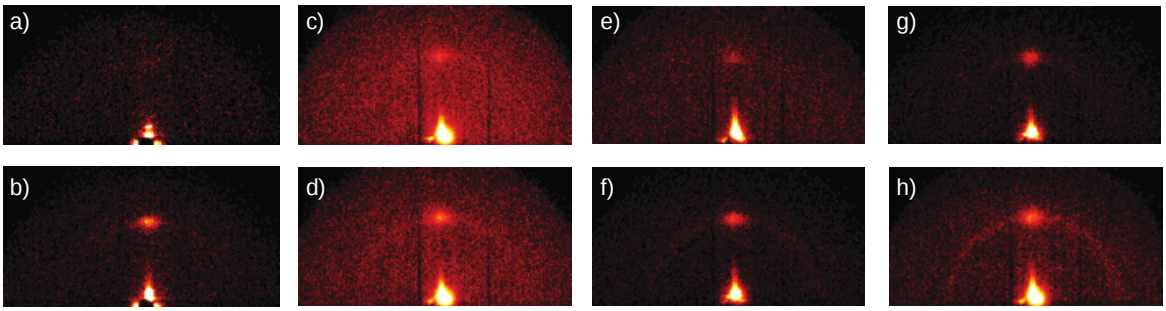

Figure 4. *Area detector image in the out-of-plane direction of non annealed and solvent annealed films of a) and b) DPP(TBFu)$_2$:PC$_{70}$BM blend (t_a= 60 sec.) c) and d) DPP(TBFu)$_2$:C70-DPM4 blend (t_a= 60 sec.) e) and f) DPP(TBFu)$_2$:C70-DPM6 blend (t_a= 60 sec.) g) and h) DPP(TBFu)$_2$:C70-DPM12 blend (t_a= 60 sec.) obtained in reflexion mode with an incident angle of ω=0.5º at a distance of 30 cm.*

The point detector diffractograms (**Figure 5**) confirm the crystalline growth triggered by SVA, and, using the diffraction peak parameters such as the FWHM and integrated area an approximate relative quantification was possible. However due to the out-of-plane set up limitation only the fraction of oriented crystallites could be quantified. Out of that fraction the

data show that the bigger crystallites grow when $PC_{70}BM$ is part of the blend and the crystallite size decrease upon increasing the alkyl chain length in the case of C70-DPM fullerenes. It appears that crystalline growth is very much limited in the C70-DPM-based devices and crystallite size remains in the range of those in pristine $DPP(TBFu)_2$ films[6b] as seen by the values of FWHM in **Figure 5**. The integrated area of the diffraction peaks accounts for a larger fraction of crystalline material in the active layers of C_{70}-DPM4 and DMP6 relative to $PC_{70}BM$, where the value integrated area is greater for C_{70}-DPM4 and C_{70}-DPM6 while the lowest value is seen for C_{70}-DPM12.

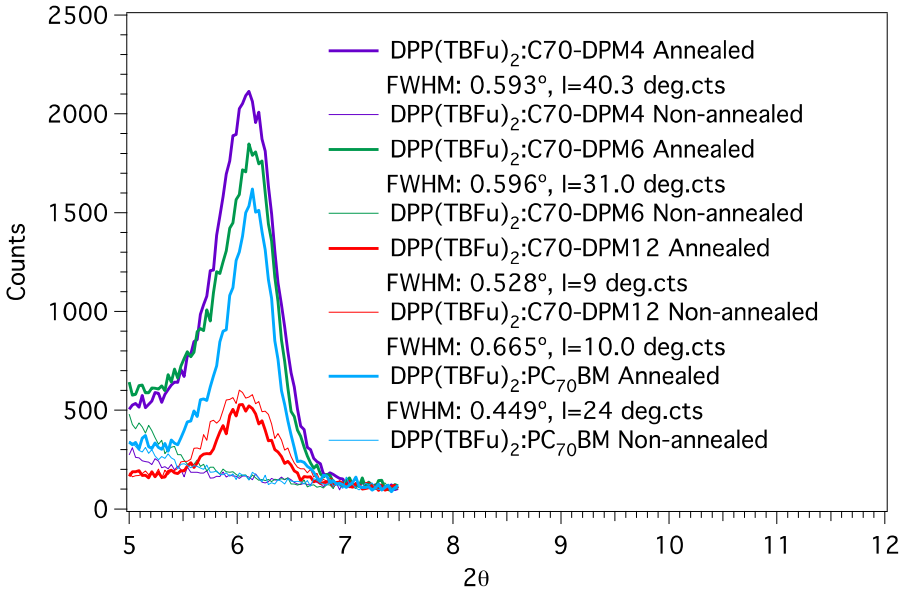

Figure 5. *Point detector diffractograms of annealed and non-annealed active layers taken in reflexion mode. The peak parameters are reported in the legend.*

The AFM images of un-annealed and annealed devices **(Figure 6)** corroborate the crystallisation process characterised by X-ray diffraction, nonetheless some striking differences were seen between the fullerene blends studied. The active layers of C_{70}-DPM6 and $PC_{70}BM$ fullerenes display a rather flat morphology with smooth surface when un-annealed as seen by the RMS roughness value, while those of C_{70}-DPM4 and C_{70}-DPM12 display very large “aggregate-like” features giving rise to much higher roughness values. Interestingly, all layers rearrange to a very similar morphology upon SVA, with roughness value in the same range for

all active layers, showing the effect of SVA in providing thermodynamic freedom by locally dissolving molecules and allowing them to rearrange at the nanoscale.[8]

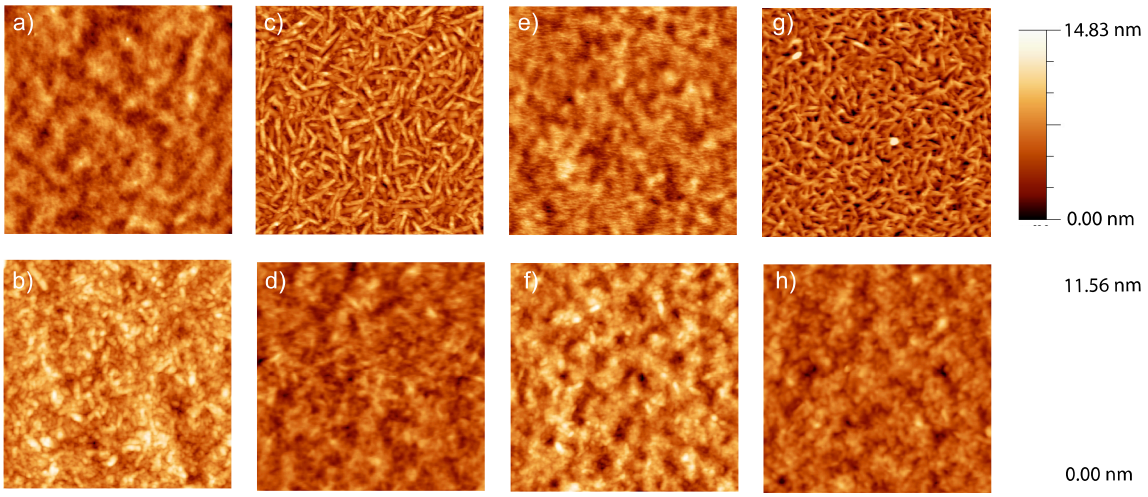

Figure 6. *2D AFM micrographs non annealed (5×5 μm) and solvent annealed (2×2 μm) films of a) and b) DPP(TBFu)$_2$:PC$_{70}$BM blend (t_a= 60 sec.) c) and d) DPP(TBFu)$_2$:C70-DPM4 blend (t_a= 60 sec.) e) and f) DPP(TBFu)$_2$:C70-DPM6 blend (t_a= 60 sec.) g) and h) DPP(TBFu)$_2$:C70-DPM12 blend (t_a= 60 sec.).*

The formation of large domains in C$_{70}$-DPM4 and C$_{70}$-DPM12 films before the annealing process (**Figure 6 c) and g**)) may stem from the high level of incompatibility between the donor and these two acceptors. A presumably strong repulsion interaction in solution between these fullerenes and the donor molecule could lead to a strong segregation upon the fast drying conditions of the spin coating processing of the active layer. Subsequently when the active layers are submitted to SVA, thermodynamic freedom is brought to the system for it to equilibrate in such a manner that the interface energy lowers leading to a more or less rapid growth of crystalline donor domains very much limited by the magnitude of the interactions between the different materials at their interface. Analogously to crystalline growth on a macroscopic scale, the surface energy of the crystallites is believed to increase proportionally to the rate of crystallite growth and will eventually define the size of the final crystallites. In the case of the active layers studied herein the surface

energy is believed to be directly related to the crystallite/amorphous-material[9] interaction, thus explaining the difference in crystallinity of the active layers made with the different fullerene derivatives. Varying the SV annealing time supposedly allows trapping the morphology in this equilibration path, affording active layers with different crystallite size and different crystalline volume as previously demonstrated. It is likely that the solvent in the SVA step merely acts as a 'catalyst' in the sense that it lowers the activation energy of the process, which would otherwise happen on a much slower time scale. Such hypothesis is supported by the fact that some of the active layers made with C_{70}-DPM derivatives show a tendency to 'self-anneal', whereby a non-annealed film of the active layer undergoes a colour change consistent with crystalline growth within a mater of hours. Thus the faint diffraction peaks observed in non-annealed films in **Figure 4** (picture c, e, g) are simply arising from that self-annealing process. Those peaks are not observed in the point detector diffractogram as this data could be acquired just a few hours after active layer deposition. For the case of C_{70}-DPM12-based active layer the diffraction peak appears in the point detector data of the un-annealed film as the kinetics of self-annealing at room temperature are much faster than for the active layers of other fullerenes. Evidence for this process is provided in **Figure 7** where the change in the UV-Vis absorption characteristics of DPP(TBFu)$_2$:C_{70}-DPM12 active layer left at 40ºC, in air was monitored over a week time and shows the appearance of the characteristic blue shifted bands assigned to the crystallisation of donor domains within hours.

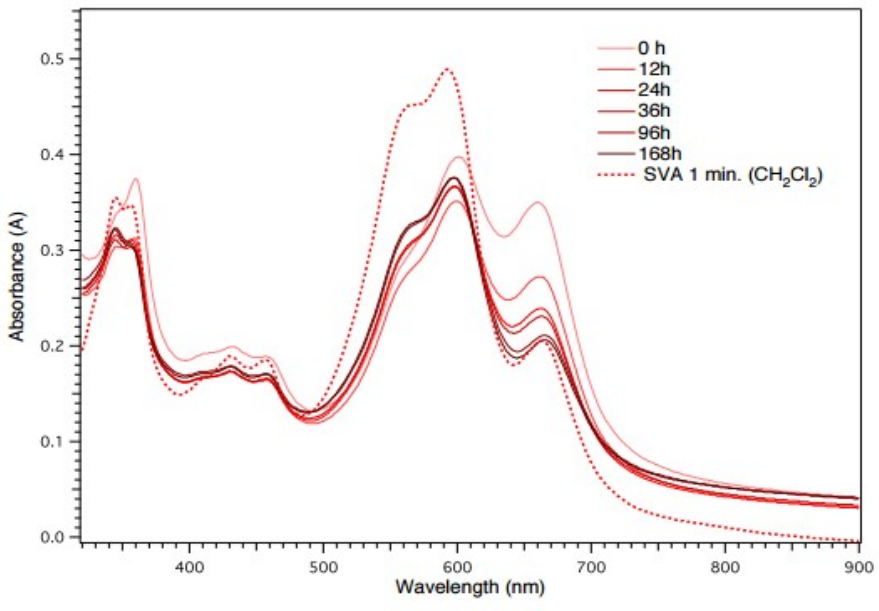

Figure 7*. UV-Vis spectra of initially un-annealed DPP(TBFu)$_2$:C70-DPM12 left in ambient air at 40ºC recorded at different time intervals showing the self annealing process. The intensity of the original red shifted absorption band gradually decreases while the blue shifted band related to crystalline phase increases in intensity.*

As previously demonstrated the crystallinity features explained above are reflected in the device's characteristics. The crystallite size is much related to the FF factor of the devices, a trend that is roughly followed in the present case.

Additionally, the difference in crystallinity of the active layer could have a significant impact on the D/A interface and thus on polaron pair generation and recombination. Such change in polaron pair generation could be a potential explanation for the difference in the IPCE value observed between the devices made with the different fullerene derivatives and could therefore be related to the J_{SC} of the devices. Transient absorption spectroscopy provides for a practical method to approximately quantify the generation yield of polaron pairs that have escaped the CT coulombic attraction. By comparing the intensity of the decay transients of the different active layers where the laser pulse is held at a constant distance from the substrate and at constant power one can obtain valuable information of the efficiency of the overall charge generation process since the magnitude of the polaron light absorption is proportional to the density of generated polarons in the blend film[10]. Therefore, TAS was measured on samples of DPP(TBFu)$_2$:fullerene blends deposited on glass substrates and annealed in a vapour of CH_2Cl_2 similarly to optimised devices. The films were probed with an incident laser pulse with wavelength of 580 nm and the transients recorded at a wavelength of 990 nm the absorption maximum of the DPP(TBFu)$_2$ polaron absorption band, determined from the reference sample of DPP(TBFu)$_2$:$PC_{70}BM$ active layer film (**Figure 8b**). Interestingly the decays of all blend film show strong similarities in both intensity of the signal and decay life-time, the slight difference in signal intensity being attributed to the slight difference in absorption of the films

(see **Figure 8a**). Therefore the data suggests a similar polaron generation yield.

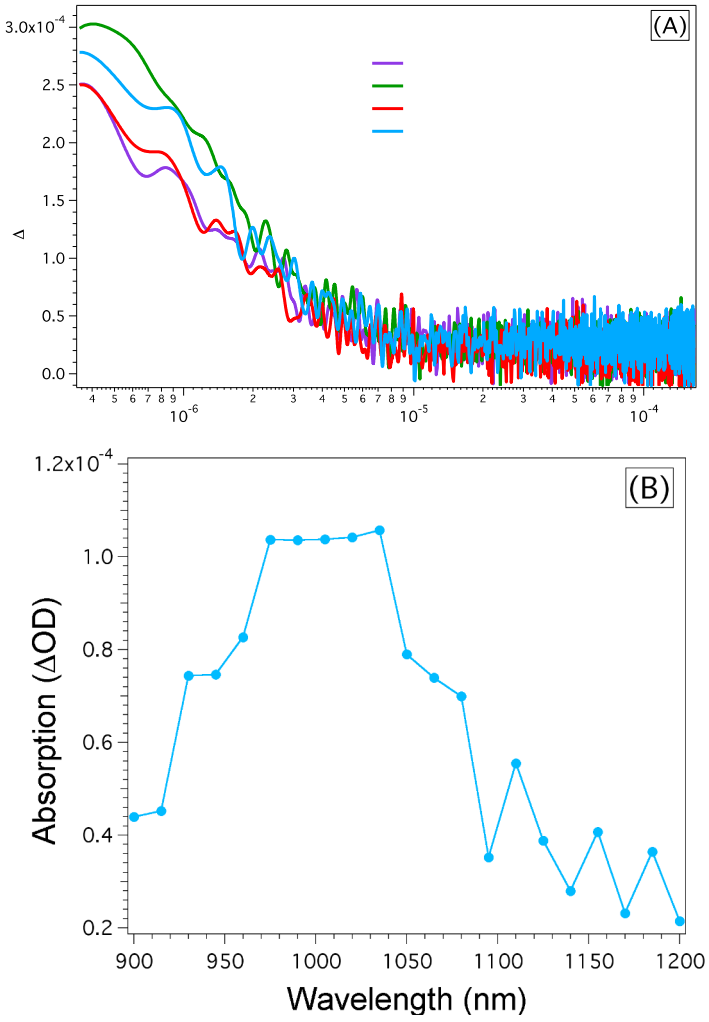

Figure 8. *a) Transient Absorption decays of DPP(TBFu)$_2$:fullerene films. Laser probe was set at 580 nm. b) Transient absorption spectra of DPP(TBFu)$_2$:PC$_{70}$BM blend films at 1 μs after the laser excitation (probe at 580 nm)*

It should be noted, however, that the generation yield measured in blend films from the TAS measurement does not take into account the presence of electrodes as in complete devices, which could potentially contribute to the CT (charge transfer) separation yield, although the internal field in open circuit condition –i.e. the conditions of the TAS measurements– could be negligible. In the present case the structure of the complete devices being similar and varying only from their active layers, the effect of the electrodes is expected to have a similar contribution on the CT separation yield in all the devices and thus are not expected to induce any change in the overall free polaron pair generation in devices one respect to the other. Consequently, since a similar density

of free polaron pairs are generated in all devices it could be assumed the differences in the devices' characteristics, particularly J_{SC}, is likely to be principally left to charge collection properties.

To address this issue, space charge limited current (SCLC) hole and electron carrier mobilities were measured on all devices. Hole and electron only devices, were fabricated according to standard reported procedures, and the SCLC region was recorded by sweeping the forward bias to large values of potential (see SI). Hole and electron SCLC could not be fitted to the conventional Mott-Gurney equation, nonetheless it was fitted to a field dependent mobility equation. **Table 1** shows that the values of the zero field mobilities, from which electron mobilities for DPM-based acceptor are in good agreement with values reported for polymer and small molecule blends.[7, 12]

Electron mobility is seen to be higher for devices made using C_{70}-DPM6 and $PC_{70}BM$ while the value decreases significantly for devices C_{70}-DPM4 and C_{70}-DPM12. The mobility results also show an important difference between the C_{70}-DPM4 and C_{70}-DPM12 fullerenes as in the case of C_{70}-DPM4 only hole mobility is slightly reduced while in the case of C_{70}-DPM12 both hole and electron mobilities are of lower magnitudes. The hole mobility of C_{70}-DPM6 and $PC_{70}BM$ have a very similar value, showing that the limiting factor in the case of C_{70}-DPM6 appears to be solely electron mobility. It seems clear from these results that the drop in performance of devices made with C_{70}-DPM fullerene derivatives is partly explained by a difference in crystalline size and crystalline volume of the donor's material domains inducing a change in hole mobility, but also –equally as important– by a decrease in electron mobility inherent to the functionalization of the fullerene derivative. Therefore, although the active layer incorporating C70-DPM4 and C70-DPM6 fullerenes account for a higher volume of donor's crystallites respect to $DPP(TBFu)_2$:$PC_{70}BM$, and that polaron pair generation is of similar magnitude, J_{SC} remains below that of devices incorporating $PC_{70}BM$ in their active layer, in agreement with the lower electron mobilities measured for C70-DPM4 and C70-DPM6.

Now we turn on to the study of the V_{OC}, which origin is generally thought of being proportional to the difference between the LUMO energy level of the acceptor and the HOMO level of the donor. However, in the present case the LUMO level of the fullerene are not shown to vary with chemical functionalization and the experimental difference in V_{OC} between the different devices is more likely to be determined by recombination kinetics.[13] In order to identify how the latter contributes to V_{OC} and to some extent to the shape of the *J-V* characteristics, a qualitative recombination study was carried out using a well-established charge extraction and transient photovoltage method.[13a,14] The CE measurements allow measuring the average charge density at open circuit in the devices. **Figure 9a** shows the plot of the charge density (*n*) *vs.* open circuit voltage obtained from CE for the all devices corrected for the electrode capacitance (see SI). The data shows to be in good agreement with the charge density being of similar magnitude in all measurements the charge density reaching about 2 x 10^{16} charges/cm^3 at values close to V_{OC} similarly to what has been reported earlier for such type of devices.[13a,14i] All data display a similar trend where the total charge is seen to increase almost linearly with V_{OC} up to a certain value where the variation becomes exponential a feature that has been observed earlier in SM BHJ and SM bilayer devices linked with the lower thickness of the active layer respect to polymer based devices.[13a,14g,14i,15] However, the exponential variation over the higher values of charge density (greater light bias) is consistent with previous results and is evidence of charges accumulated in the bulk of the device.

Device active layer	V_{OC} (V)	n_0	γ	β	ϕ
$DPP(TBFu)_2$:PC_{70}BM	0.858	7.5×10^{14}	3.5	22.9	7.4
$DPP(TBFu)_2$:C70-DPM4	0.933	4.5×10^{14}	3.8	21.7	5.4
$DPP(TBFu)_2$:C70-DPM6	0.944	4.8×10^{14}	3.7	20.9	5.4
$DPP(TBFu)_2$:C70-DPM12	0.954	2.6×10^{14}	4.2	19.7	4.7

Table 2: *Values of recombination parameters derived from CE /TPV measurements for devices with active layers made with C70-DPM fullerene series and $PC_{70}BM$.*

The plots of *n vs.* V_{OC} fitted single exponentials of the form of **Equation 1**, analogously to the splitting of the quasi-Fermi levels in intrinsic semiconductors, where the value of γ (from ≈3.8V^{-1} for $DPP(TBFu)_2$:DPM4 to ≈4.2 V^{-1} for $DPP(TBFu)_2$:C70-DPM12, see **Table 2**) is lower than that expected for ideal semiconductors as previously described, an effect that has been attributed to the presence of an exponential tail of trap states extending into the band gap of the active layer.

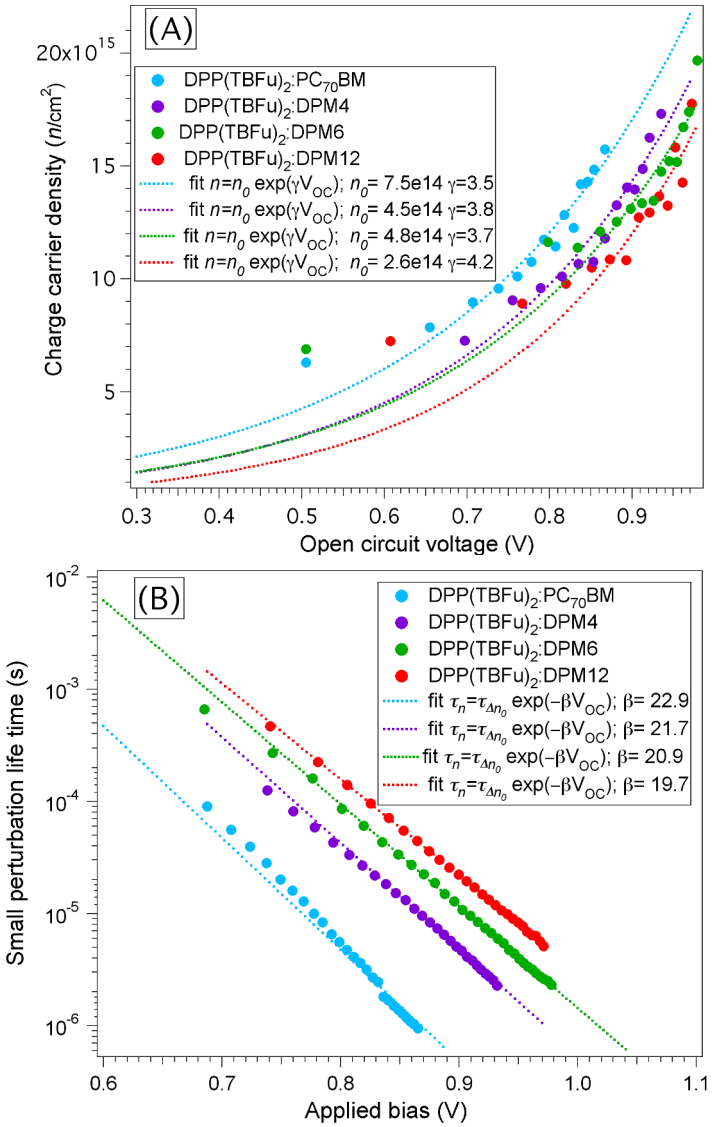

Figure 9*. A) Comparison of the charge density (n) as a function of the open circuit voltage determined from CE measurement. B) Carriers lifetime measured using TPV as a function of device open circuit voltage.*

The carriers life time (τ_n) versus open circuit voltage (V_{OC}) plot for all the devices is shown in **Figure 9b**, where the curves were fitted to single exponential decays of the form of **Equation 2**.

$$n = n_0 e^{\gamma Voc} \qquad \textbf{Equation 1}$$

$$\tau_{\Delta n} = \tau_0 e^{-\beta Voc} \qquad \textbf{Equation 2}$$

$$\frac{dn}{dt} = -kn^{\phi} \qquad \textbf{Equation 3}$$

$$\tau_{\Delta n} = \tau_{\Delta n0} n^{-\phi} \qquad \textbf{Equation 4}$$

The plots in **Figure 9a** and **Figure 9b** were combined as shown in **Figure 10a** and used to determine the overall order of recombination, defined by **Equation 3**, where ϕ is obtained by fitting the curve of the small perturbation carrier life time *tau vs. n* to a power law of the form of **Equation 4**. Interestingly the recombination order varies significantly from device to device, with unexpectedly high values (ϕ = 8.4) for the devices displaying lower V_{OC}. Such high values, as opposed to a value of 2, which is to be expected in a strictly bimolecular recombination process in the case of Langevin type recombination, have been measured several times in earlier reports,[14h, 16c, 16d, 17] and were attributed to recombination through trap states in the band gap of the active layer materials.[17] Therefore the non-geminate recombination process is described as an essentially bimolecular process where the recombination coefficient is allowed to be charge dependent accordingly to the presence of trap states in the band gap. [14c, 14e, 14h]

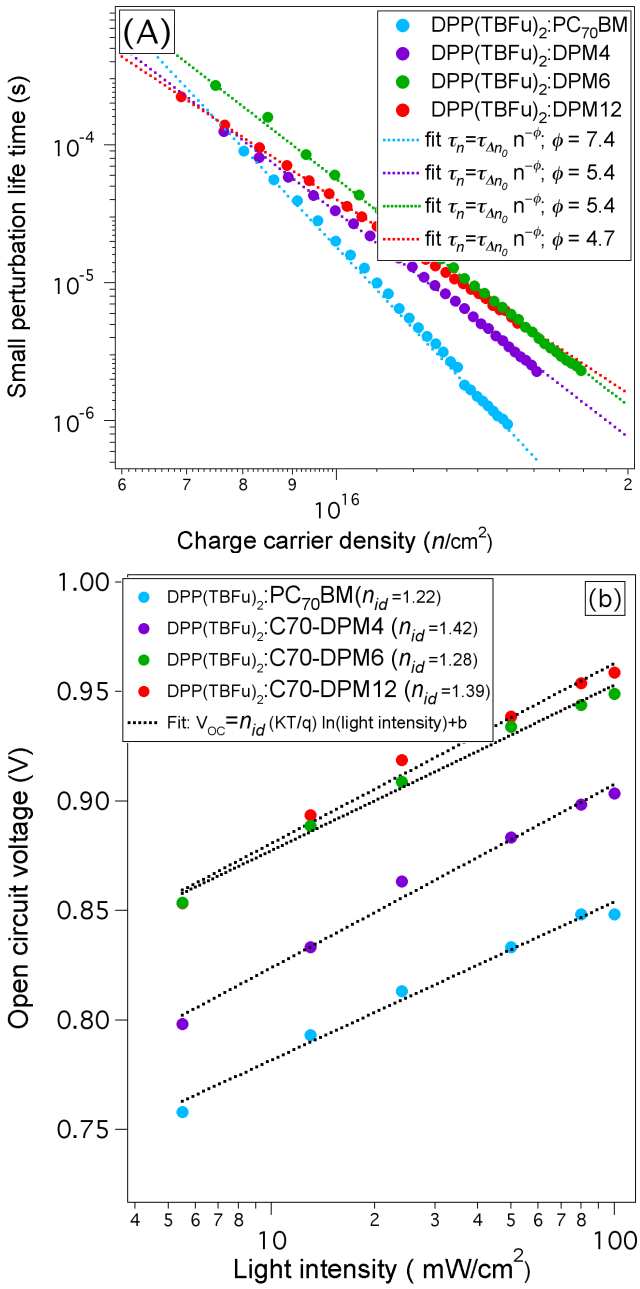

***Figure 10**. a) Small perturbation carrier life time vs. open circuit voltage plot for devices made with the C70-DPM series and reference DPP(TBFu)2:PC70BM blends. Curves are fitted to mono-exponential decays, whose parameters are reported in **Table 2**. b) Open circuit voltage vs light intensity for all devices used in this work.*

It is interesting to note that the devices made with DPM4 and DPM6 derivatives all show a similar apparent recombination order of about 5 and that devices made with DPP(TBFu)$_2$:PC$_{70}$BM blends have a higher recombination order (7.4). Nevertheless, the recombination life times measured through CE/TPV correspond to a total charge carrier

recombination and therefore it is difficult to attribute the experimental reaction order (ϕ) obtained using this method to a specific recombination mechanism. Indeed it has been showed, that, especially in thin active layers as in our case, surface recombination or doping can have a very significant influence on the apparent recombination order[18]. To gain more insight on this matter we calculated the ideality factor (n_{id}) of all devices as defined in **Equation 5** by fitting the V_{OC} *vs* Light bias plot to a logarithmic function as depicted in **Figure 10b**. The values of n_{id} obtained are in the range of expected value for thin devices (d<100 nm) where surface recombination is significant and where a moderate concentration of deep traps is present. Given that the thickness is similar in all the devices, the lower n_{id} for devices made with $PC_{70}BM$ would then be explained by a higher mobility as observed experimentally. In the case of DPM-based devices the higher n_{id} would be consistent with a slightly higher density of deep trap states, corroborated by the lower apparent recombination order, and consistent with lower crystallinity of the active layer. Those deeper traps could be the result of the presence of a population of disorientated $DPP(TBFu)_2$ crystallites in the case of DPM-based devices (*vide supra*) creating inhomogeneous crystallites boundaries. The presence of a higher population of oriented crystallites in DPM4 and DPM6-based devices respect to the $PC_{70}BM$-based ones does not compensate for the defects brought by the disoriented fraction since although the total crystalline volume is greater, the crystallites are smaller in size thus generating more boundaries than in $PC_{70}BM$-based active layer. The slopes of the n vs applied bias plots combined with the recombination lifetime follow the trend observed for the Voc of the devices. That is, the devices with broader DOS (qualitatively estimated through the parameter γ in the n vs applied bias plot) and faster recombination kinetics display the lowest Voc as in the $PC_{70}BM$ or DPM-based devices, whereas the opposite trend is exemplified by $DPP(TBFu)_2$:DPM12 devices. A similar trend had been observed in polymer-based OSC devices comprising C_{70}-DPM fullerene derivatives, whereby the HOMO-LUMO energy levels of the fullerenes derivatives could not explain the difference in the experimental Voc.

Conclusion

The present study has allowed the in-depth understanding of the very limiting factors to PCE in small molecule BHJ devices based on DPP(TBFu)2. By using an extensive set of characterisation techniques we have been able to obtain important insights into the morphological changes induced by different fullerene acceptors on the active layer of DPP(TBFu)2-based BHJ devices. First X-Ray diffraction and AFM have shone light on the kinetics of the crystalline growth triggered by SVA in the active layers, demonstrating that the fullerene acceptors have a strong impact on the quantity and size of crystallites of donor material formed. A broad trend could be drawn where the crystalline features decrease with longer alkyl chain functionalization of the fullerenes. Subsequently, transient absorption spectroscopy revealed that those changes in crystallinity have an apparently insignificant effect on polaron pair generation; however hole mobility was very significantly affected as measured by SCLC. Additional data on electron mobility showed that the fullerene functionalization is critical in providing high electron mobility and that excessive alkyl chain length functionalising group leads to extremely low mobilities.

Finally data on non-geminate recombination kinetics obtained by CE/TPV methods provided important qualitative information on the variation of the band structure and the recombination kinetics of the devices incorporating the different fullerenes. Indeed, although all fullerene derivatives showed very similar LUMO levels the change in crystallinity they cause on the donor domains and their intrinsic solid-state band properties, induce a significant change on the hole/electron averaged DOS distribution and on the non-gemination recombination order. Such changes explain the difference in Voc observed experimentally. Additionally, simple ideality factor comparison between devices allowed withdrawing information on the band structure difference brought about by the different fullerenes.

All in all, this study provided important insights for the design of new fullerene-based acceptors, whereby, to provide improved devices' characteristics not only should they display the highest possible electron mobility, but as importantly, must interact with the donor in a favourable manner in order to induce the formation of large and numerous donor

crystallites in the active layer. The nature of such type of weak interaction is currently being investigated in the laboratory. 95

Bibliography

(1) a) C. J. Brabec, S. Gowrisanker, J. J. M. Halls, D. Laird, S. Jia and S. P. Williams, Adv. Mater., **2010**, 22, 3839; b) C. Deibel and V. Dyakonov, Rep. Prog. Phys., **2010**, 73, 096401; c) W. Cai, X. Gong and Y. Cao, Sol. Energy Mater. Sol. Cells, **2010**, 94, 114; d) H.-L. Yip and A. K. Y. Jen, Energy Environ. Sci., **2012**, 5, 5994; e) P. M. Beaujuge and J. M. J. Fréchet, J. Am. Chem. Soc., **2011**, 133, 20009; f) J. L. Delgado, P. A. Bouit, S. Filippone, M. A. Herranz and N. Martin, Chem. Commun., **2010**, 46, 4853.

(2) a) C.-Z. Li, H.-L. Yip and A. K. Y. Jen, J. Mater. Chem., **2012**, 22, 4161; b) B. Walker, C. Kim and T.-Q. Nguyen, Chem. Mater., **2011**, 23, 470; c) A. Mishra and P. Bäuerle, Angew. Chem., Int. Ed., **2012**, 51, 2020; d) Y. Lin, Y. Li and X. Zhan, Chem. Soc. Rev., **2012**, 41, 4245.

(3) a) Y. He, H.-Y. Chen, J. Hou and Y. Li, J. Am. Chem. Soc., **2010**, 132, 1377; b) G. Zhao, Y. He and Y. Li, Adv. Mater., **2010**, 22, 4355; c) Y. He, G. Zhao, B. Peng and Y. Li, Adv. Funct. Mater., **2010**, 20, 3383.

(4) a) F. C. Jamieson, E. B. Domingo, T. McCarthy-Ward, M. Heeney, N. Stingelin and J. R. Durrant, Chem. Sci., **2012**, 3, 485; b) A. SánchezDíaz, M. Izquierdo, S. Filippone, N. Martin and E. Palomares, Adv. Funct. Mater., **2010**, 20, 2695; c) J. H. Choi, K.-I. Son, T. Kim, K. Kim, K. Ohkubo and S. Fukuzumi, J. Mater. Chem., **2010**, 20, 475.

(5) a) I. Riedel, E. von Hauff, J. Parisi, N. Martín, F. Giacalone and V. Dyakonov, Adv. Funct. Mater., **2005**, 15, 1979; b) G. Garcia-Belmonte, P. P. Boix, J. Bisquert, M. Lenes, H. J. Bolink, A. La Rosa, S. Filippone and N. Martin, J. Phys. Chem. Lett., **2010**, 1, 2566.

(6) a) A. Tamayo, T. Kent, M. Tantitiwat, M. A. Dante, J. Rogers and T.- Q. Nguyen, Energy Environ. Sci., **2009**, 2, 1180; b) A. Viterisi, F. Gispert-Guirado, J. W. Ryan and E. Palomares, J. Mater. Chem., **2012**, 22, 15175.

(7) B. Walker, A. B. Tamayo, X.-D. Dang, P. Zalar, J. H. Seo, A. Garcia, M. Tantiwiwat and T.-Q. Nguyen, Adv. Funct. Mater., **2009**, 19, 3063.

(8) J. Vogelsang, J. Brazard, T. Adachi, J. C. Bolinger and P. F. Barbara, Angew. Chem., Int. Ed., **2011**, 50, 2257.

(9). Here amourphous-material referes to either the amorphous fraction of donor material in the active layer or most importantly to the fraction of suposedely amorphous fullerene domains. 10. T. M. Clarke, A. Ballantyne, S. Shoaee, Y. W. Soon, W. Duffy, M. Heeney, I. McCulloch, J. Nelson and J. R. Durrant, Adv. Mater., **2010**, 22, 5287.

(11) a) J. Bisquert, J. M. Montero, H. J. Bolink, E. M. Barea and G. Garcia-Belmonte, phys. stat. sol. (a), **2006**, 203, 3762; b) J. M. Montero and J. Bisquert, Solid-State Electron., **2011**, 55, 1.

(12) E. von Hauff, V. Dyakonov and J. Parisi, Sol. Energy Mater. Sol. Cells, **2005**, 87, 149.

(13) a) D. Credgington and J. R. Durrant, J. Phys. Chem. Lett., **2012**, 3, 1465; b) A. Maurano, R. Hamilton, C. G. Shuttle, A. M. Ballantyne, J. Nelson, B. O'Regan, W. M. Zhang, I. McCulloch, H. Azimi, M. Morana, C. J. Brabec and J. R. Durrant, Adv. Mater., **2010**, 22, 4987; c) G. GarciaBelmonte and J. Bisquert, Appl. Phys. Lett., **2010**, 96, 113301.

(14) a) C. G. Shuttle, A. Maurano, R. Hamilton, B. O'Regan, J. C. de Mello and J. R. Durrant, Appl. Phys. Lett., **2008**, 93, 183501; b) C. G. Shuttle, B. O'Regan, A. M. Ballantyne, J. Nelson, D. D. C. Bradley and J. R. Durrant, Phys. Rev. B, **2008**, 78, 113201; c) R. Hamilton, C. G. Shuttle, B. O'Regan, T. C. Hammant, J. Nelson and J. R. Durrant, J. Phys. Chem. Lett., **2010**, 1, 1432; d) F. C. Jamieson, T. Agostinelli, H. Azimi, J. Nelson and J. R. Durrant, J. Phys. Chem. Lett., **2010**, 1, 3306; e) A. Maurano, R. Hamilton, C. G. Shuttle, A. M. Ballantyne, J. Nelson, B. O'Regan, W. Zhang, I. McCulloch, H. Azimi, M. Morana, C. J. Brabec and J. R. Durrant, Adv. Mater., **2010**, 22, 4987; f) D. Credgington, R. Hamilton, P. Atienzar, J. Nelson and J. R. Durrant, Adv. Funct. Mater., **2011**, 21, 2744; g) D. Credgington, Y. Kim, J. Labram, T. D. Anthopoulos and J. R. Durrant, J. Phys. Chem. Lett., **2011**, 2, 2759; h) A. Maurano, C. C. Shuttle, R. Hamilton, A. M. Ballantyne, J. Nelson, W. Zhang, M. Heeney and J. R. Durrant, J. Phys. Chem. C, **2011**, 115, 5947; i) D. Credgington, F. C. Jamieson, B. Walker, N. Thuc-Quyen and J. R. Durrant, Adv. Mater., **2012**, 24, 2135; j) G. F. A. Dibb, F. C. Jamieson, A. Maurano, J. Nelson and J. R. Durrant, J. Phys. Chem. Lett., **2013**, 4, 803.

(15) A. Sanchez-Diaz, R. Pacios, U. Munecas, T. Torres and E. Palomares, Org. Electron., **2011**, 12, 329.

(16) a) M. P. Eng, P. R. F. Barnes and J. R. Durrant, J. Phys. Chem. Lett., **2010**, 1, 3096; b) C. G. Shuttle, R. Hamilton, J. Nelson, B. C. O'Regan and J. R. Durrant, Adv. Funct. Mater., **2010**, 20, 698; c) C. G. Shuttle, R. Hamilton, B. C. O'Regan, J. Nelson and J. R. Durrant, Proc. Natl. Acad. Sci. USA, **2010**, 107, 16448; d) D. Spoltore, W. D. Oosterbaan, S. Khelifi, J. N. Clifford, A. Viterisi, E. Palomares, M. Burgelman, L. Lutsen, D. Vanderzande and J. Manca, Adv. Energy. Mater., **2013**, 3, 466.

(17) a) R. C. I. MacKenzie, T. Kirchartz, G. F. A. Dibb and J. Nelson, J. Phys. Chem. C, 2011, 115, 9806; b) T. Kirchartz, B. E. Pieters, J. Kirkpatrick, U. Rau and J. Nelson, Phys. Rev. B, **2011**, 83, 115209.

(18) T. Kirchartz and J. Nelson, Phys. Rev. B, **2012**, 86, 165201.

Chapter 5

Understanding the limiting factors of optimized Small molecule-bulkheterojunction organic solar cells from an experimental perspective.

Table of Contents

Motivation

Small Molecules are attracting increasing interest for Bulkheterojunction Solar cell devices. Recent records of power conversion efficiency (PCE) of over 8% have demonstrated that small molecules, when suitably designed can match and even exceed the performance of polymer-based BHJ OSCs.[1] This is of paramount importance as SMs have the advantage over polymers to be easily synthesised and isolated as pure entities rather than as polydisperse mixtures of different chain length molecules. However, if polymers benefit from their long conjugated back bone to provide for solid state packing and enhanced carrier transport, small molecules can only rely on week intermolecular interactions to lead to highly crystalline active layer to provide enhanced transport properties. Consequently, SMs have shown, to date, mixed results and highly efficient donor SMs are often discovered serendipitously rather than through rational design. Despite considerable worked published on SM-BHJ, so far no precise relationship as been established between donor structure and *J-V* characteristics.[2]

Herein we report on the photovoltaic properties of five diketopyrrolopyrrole (DPP)-based donor molecules in SM-BHJ solar cell devices characterised extensively in order to provide a link between the donor structure and the devices *J-V* characteristics. The chemical structure of these derivatives comprises the DPP bisthiophene group functionalized with ethylhexyl alkyl chains as the central unit. The lateral end groups have been varied, first by inducing subtle changes from the original DPP(TBFu)$_2$ benzofuran moiety,[3] then substituting donor end groups by electron acceptors, and finally using a bulky arylamine group. The aim was to obtain a wider understanding on the key parameters responsible for the *J-V* characteristics evolution of SM-BHJ devices taking the largest possible variables into account. Amongst these variables band gaps, HOMO-LUMO levels, light

absorption, crystalline packing in the solid state, crystal-forming properties in films, charge carrier mobility and charge carrier recombination were assessed and interrelated. We relied on a myriad of characterisation techniques such as by UV-Vis, emission and cyclic voltammetry, X-ray diffraction (XRD), AFM, transient photovoltage charge carrier lifetimes measurements to provide information on optical properties of the active layers, morphological features and recombination kinetics. This allowed us to propose a mechanism for the solvent vapour annealing assisted formation of crystalline domains of donor molecule in the active layer blend, as well as relating those features with the *J-V* characteristics of the devices.

Results

It has been widely demonstrated that often the subtlest changes in the molecular structure of SM-donor, greatly influence the performance of SM-BHJ devices and thus donors with very similar photophysical properties often show very different photovoltaic conversion characteristics.[4] Several studies have attempted to draw a trend between the donor's molecular structure and devices characteristic by varying the chemical structure of the donor. If the change in structure has generally be shown to affect the overall crystallinity of the active layer,[4a, 4b, 4f-i, 4k, 4l, 4n] little is known about the mechanisms governing crystallite growth in active layers of SM-BHJ devices and how the resulting microstructure limit the overall efficiency of the devices. Thus the aim herein has been to rationally design a small series of DPP derivatives in order to shine light on the energetics of microstructure formation and to demonstrate how the changes occasioned by the donors' chemical structure indirectly impact on all aspects of the *J-V* characteristics in a very significant manner. Five donors were designed in such way to induce changes in the morphology of the active layer however inducing as little changes as possible in the photophysical properties (eg. HOMO-LUMO, and

band gap energies). The five derivatives were designed as follow: some subtle structural changes were introduced in the original DPP(TBFu)$_2$ structure, by, first removing the phenyl group of the benzofuran moiety (structure **1**) and substituting the oxygen atom for a sulphur (structure **2**)[4e, 4l] to asses the effect of conjugation length and week interactions on the solid state packing. A second class of derivatives incorporate electron-withdrawing groups (**4** and **5**) to assess the effect of weakly polarisable atoms in interfering with crystalline growth in the active layers. Finally the last derivative (**3**) incorporates a large tetragonal triarylamine group with long alkyl chains aiming at disrupting any π-π stacking interaction in the solid state and to asses its effect on morphology (Figure 1a).

The synthesis of the derivatives was carried out by two different methods. Compound **3**, **4** and **5** were synthesised through palladium mediated Suzuki coupling of a commercially available dibrominated DPP intermediate while compound **1** and **2** were synthesised through the direct alkylation of the respective DPP cores (see SI).

Solar cell devices were fabricated using a reported structure,[5] whose active layer was made out of a blend of PC$_{70}$BM and the Donor derivative (Figure 1b). The active layer of each donor:PC$_{70}$BM blend was deposited by spin coating of the solution of the blend from $CHCl_3$ and subsequently submitted to a solvent vapour annealing step in CH_2Cl_2 before deposition of the cathode (LiF/Al). SVA was chosen over thermal annealing as it has demonstrated superior ability in controlling the crystallisation process of this type of donor molecules in SM-BHJ-based devices.[5-6] Devices were optimised for the PC$_{70}$BM:Donor ratio, active layer thickness and SVA time (see SI).

Photophysical properties

The optical properties of all donors were characterised by UV-Vis absorption and emission spectra. HOMO and LUMO energy levels were calculated from cyclic voltammetry (see SI). Figure X shows the

HOMO-LUMO energy levels alignment of each DPP derivatives respect to $PC_{70}BM$. It can be seen that the donors have a very similar band gap centred around 2 eV. Donor **3** deviates slightly from this value having a band gap of 1.9 eV. The UV-Vis absorption spectra of all the derivatives show very similar features with maximum absorption in the range of 590 nm and 650 nm, and onsets of absorption located around 700 nm except for **5** whose absorption extends up to 750 nm.

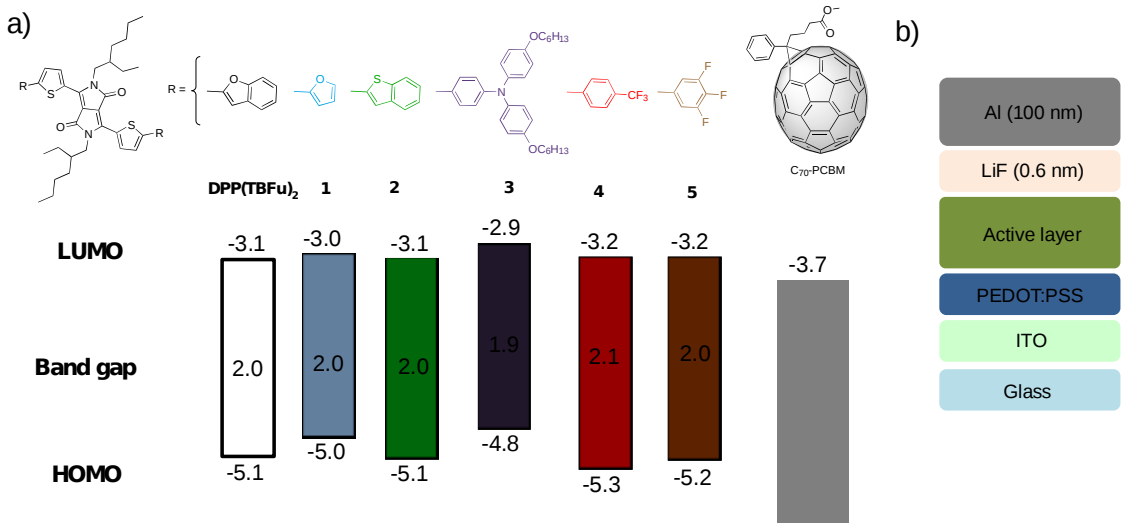

Figure 1. *a) Chemical structure of diketopyrrolopyrrole derivatives used for this study and their HOMO-LUMO and band gap energy derived from cyclic voltametry measurements and UV-Vis/emission measurements. The LUMO and band gap of $PC_{70}BM$ measured in the same conditions is shown as comparison. b) Solar cell architecture used in this study.*

Interestingly, all derivatives, show the same features as the original $DPP(TBFu)_2$ donor in active layer films, that is three main absorption bands of roughly equal intensity centred around 600 nm (Figure 2a). The relative intensity of these bands was shown to change very significantly upon SVA for $DPP(TBFu)_2$, a trend followed by all derivatives (Figure 2b). Derivatives **1** and **4** show a similar increase of the blue shifted bands. Derivatives **2**, **3** and **4** display a rather less significant change upon annealing. Contrary to the other derivatives the intensity of the absorption band in the annealed active layer films remains similar to that of the non-annealed films, however the bands'

shapes become much sharper. Such changes in absorption properties in the films induce a noticeable colour change especially for the derivatives **2**, **4**, and **5**.

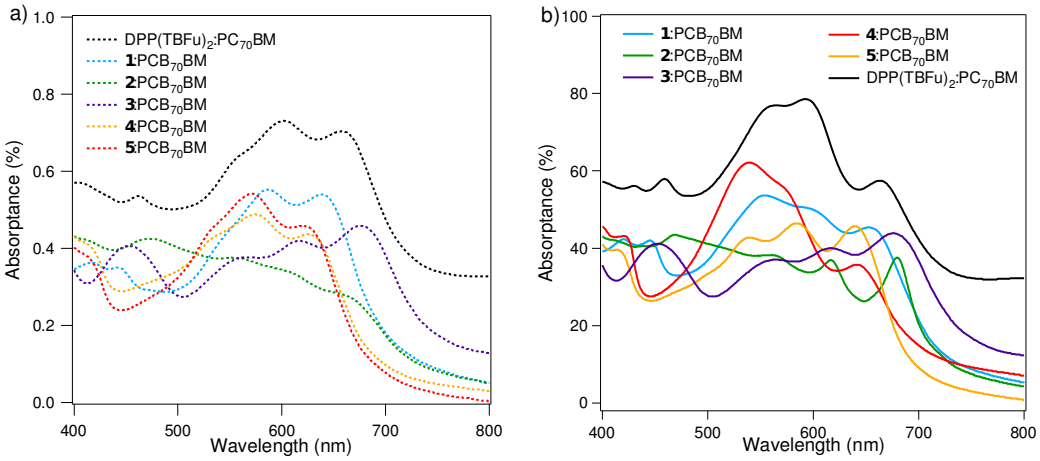

Figure 2. *UV-Vis absorption spectra of active layers made out of DPP derivative and PC70BM blends in optimum device conditions. a) Non-annealed films, b) CH_2Cl_2-Solvent vapour annealed films.*

Photovoltaic properties

Solar cell devices were fabricated using the same structure for all DPP donor derivatives (Figure 1b). The devices were optimised for D/A ratio, for active layer thickness and for solvent annealing time. The *J-V* characteristics evolution of the devices upon solvent annealing follows a similar trend as previously observed with $DPP(TBFu)_2$, where short circuit current density (J_{SC}) increases with annealing time up to a maximum value and decreases with longer annealing time.[6c, 7] Concomitant with this decrease of J_{SC} an increase of FF is usually observed. It is interesting to note that FF are fairly low in all devices with values ranging from 40 to 55%, although devices of derivative **2**, similarly to $DPP(TBFu)_2$[7] have seen his FF improve to 66% when long annealing times were applied (Figure SX). However this is not without a very significant decrease in J_{SC}, bringing the overall efficiency below

1%. Interestingly, the V_{OC} of the devices do not follow a trend, and only relates to the HOMO-LUMO energies of the derivatives with limited accuracy (Table 1). The J_{SC} show values ranging from 1 mA/cm^2 to almost 9 mA/cm^2 for the commercial DPP(TBFu)$_2$ reference donor which are corroborated with the EQE measurements (Figure 3).

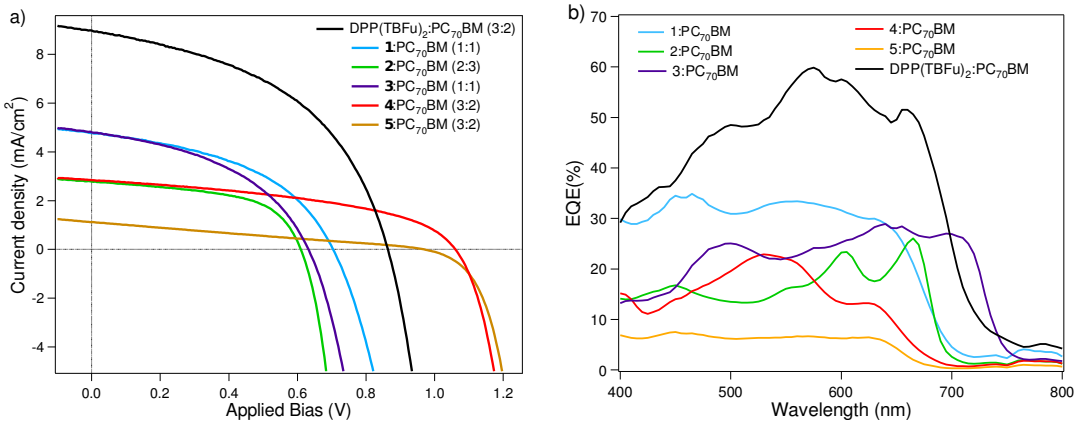

Figure 3. a) J-V characteristics of solar cell devices fabricated with DPP series donors and $PC_{70}BM$. These curves represent the average performance of devices made under optimized conditions. b) Corresponding EQE spectra.

The drop in J_{SC} observed for devices of donor **2** annealed for longer time (Figure SX) confirms a previously described trend for solvent annealed DPP-based OSCs whereby the SVA-induced crystal growth affects the interfacial area resulting in lower J_{SC}.[5] As such, crystallite size is very likely to play a significant role in determining the J_{SC} of the different derivatives. However, before investigating on the crystalline properties of the active layers, it is important to notice the very significant change in the absorption intensity between the active layers. Such difference cannot solely be attributed to a difference in absorption coefficient of the donors as these values are situated in a similar range as that of DPP(TBFu)$_2$ for donors **1**, **2** and **4** as seen in Table 1. Donor **3** has a much higher absorption coefficient than DPP(TBFu)$_2$ while that of **5** is significantly lower. In fact, the absorbance of the active layer is limited, to an important extent, by the layer's thickness, as seen in Table 1, resulting from the active

layer thickness optimisation and by the D/A ratio resulting from the D/A ratio optimization.

Derivative	D/A ratio	Annea-ling time	Abs. Coeff. (sol.)	Active layer thickness (nm)	Integrated absor-ptance area	% area respect to DPP(TBfu)$_2$	Theoretic-al J_{SC}	Experimen-tall J_{SC}
1	**1:1**	1 min	55220 (±394)	110	138	63	5,7	4,8
2	**2:3**	75s	49825 (±625)	85	120	55	4,9	2,8
3	**1:1**	4 min	96617 (±717)	95	129	59	5,3	4,8
4	**3:2**	6 min	49240 (±315)	95	130	60	5,3	2,8
5	**3:2**	90s	20869 (±305)	80	110	50	4,5	1,1
DPP(TBFu)$_2$	**3:2**	1 min	65964 (±301)	75	218	100	9,0	9,0

Table 1. Photophysical parameters of DPP derivatives in solution and of Derivatives:$PC_{70}BM$ blends in the solid state.

A simple comparison of optical parameters allowed estimating the J_{SC} loss related to the absorption of the active layers. The Absorptance spectra of all the active layers were integrated respect to the wavelength over the 400 to 900 nm. It was reasoned that if the derivatives blends experience similar D/A electron transfer kinetics and geminate recombination kinetics to that of the reference DPP(TBFu)$_2$ blend, the J_{SC} would be expected to be proportional to the fraction of the active layer absorption integral. Table 1 shows that active layers of derivative **1** and **3** follow this theoretical trend fairly accurately however that of derivative **2**, **4** and **5** is far off.

Relative IQE (rIQE) measurements give an approximation of the ability of each active layer to efficiently convert photons into electrical charge.[8] As seen in Figure 4, devices of derivative **1** and **3** show a similar overall value of rIQE as that of reference DPP(TBFu)$_2$ device

(approx. 70 % on average), implying that all three active layers convert photon to free charge carriers with similar efficiency. This confirms the fact that the J_{SC} produced by derivatives **1** and **3** is mostly limited by the absorption capacity of the active layers relative to the DPP(TBFu)$_2$ reference. The offset between calculated and experimental J_{SC} could be attributed to a slight difference in geminate recombination kinetic and exciton diffusion length respect to the reference DPP(TBFu)$_2$ device. Derivative **4** and **5** on the other hand show a much lower rIQE than the latter derivatives, corroborating the larger offset in experimental and theoretical J_{SC} as seen in Table 1. This is evidence of additional losses being responsible for the lower experimental J_{SC} than expected from absorption properties of the active layer. Derivative **2** shows an intermediate behaviour where the rIQE reaches that of the reference DPP(TBFu)$_2$ device for two wavelengths whereas dropping bellow 50% for the rest of the spectrum.

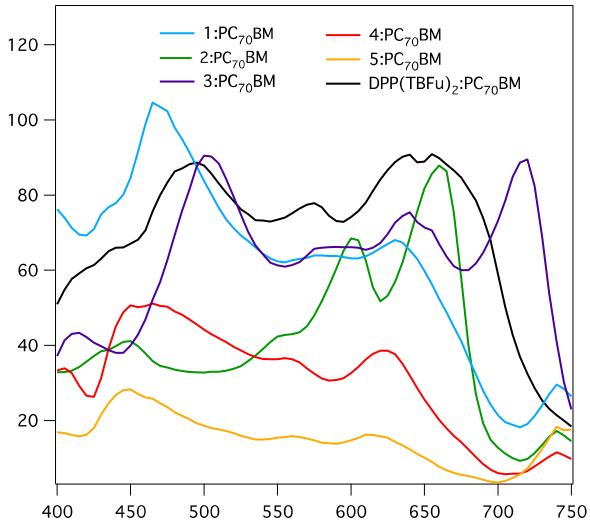

Figure 4. Relative IQE (rIQE) spectrum of devices made with the DPP derivatives. The rIQE spectrium have been calculated from the EQE and absorptance spectrum of the devices as rIQE = EQE/absorptance.

Consequently, the above results give an indication on the losses occasioned by the decrease in absorption of the active layers, due only partially to a decrease in absorption coefficient of the derivatives respect to DPP(TBFu)$_2$, but more importantly, by the active layer thickness and D-A composition. The optimum thickness and D/A ratio are established experimentally and correspond to the value providing the optimum compromise between strong absorption, fast carrier transport, and slow recombination kinetics leading to the overall highest PCE for a given system. The hole mobility values measured on hole only devices (Table 2) corroborates this assumption with values in the same range for devices of derivative **1** to **4** and values in the range of 10^{-10} V/cm.s for derivative **5**.

Morphological characterisation

The optimum active layer thickness is itself indirectly determined by morphological parameters conferring enhanced transport properties to the blend. The formation of the D/A interface is indeed, one of such parameters, which can qualitatively be monitored by photoluminescence (PL) measurement.[9] Figure 5 depicts the PL spectra of active layer films of the donor:PC$_{70}$BM blends deposited on quartz substrates using the same conditions as is OSC devices. A relative increase in emission is observed in most cases upon annealing, which is indicative of the formation of segregated domains of donor and acceptor, and therefore of a modification of the D/A interfacial area. Although, quantification between blends is not possible, it is interesting to note that both fluorinated derivatives, **4** and **5**, show significant photoluminescence intensity even when the layers are not annealed, indicating some type of segregation being present in the non-annealed state.

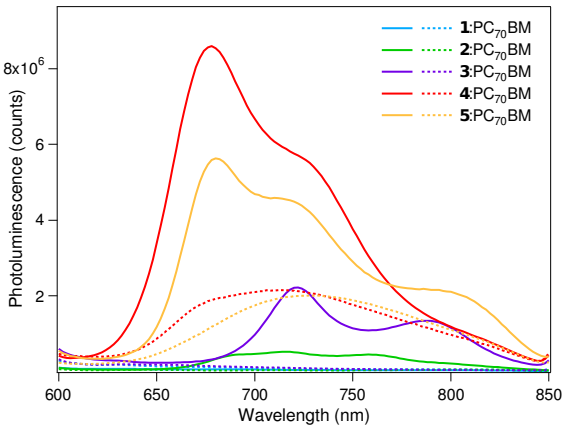

Figure 5. Photoluminescence spectra of active layers made of DPP derivatives and $PC_{70}BM$. The spectra of the non-annealed layers are shown in dotted lines, those of the annealed active layers in solid lines.

To obtain more information on the morphology of the active layers conventional X-ray diffraction (XRD), and GIXRD (Grazing incidence XRD) measurements on the active layers of each donor:$PC_{70}BM$ blend was carried out. First, conventional diffractograms in the Bragg-Brentano configuration were recorded in the out of plane direction. Figure 6 shows the diffractograms of each active layer annealed in conditions of optimised devices and annealed for 10 minutes. All donors show a propensity to form crystalline domains in active layers upon annealing, as seen by the presence of a diffraction peak at low 2θ angle in all the annealed layers, and an additional weak peak from the same family of diffraction plane in the case of derivative **3**. These peaks at small 2θ value are characteristic of pure DPP donor crystallites and,[4l, 7, 10] as previously demonstrated, cannot be attributed to $PC_{70}BM$ crystallites. Although PCBM has been shown to form crystalline domains in some solvent annealed active layers,[6e] those domains were extremely small (<2 nm) and PCBM remains most often largely amorphous in blends of SM-BHJ solvent annealed active layers, at least in our measurement conditions (low energy X-ray incident beam).[7] The shape and size of the diffraction peaks,

however, advocates for different crystallization kinetics between the donors. Scherer analysis (see SI for details) of the peaks' full width at half maximum (FWHM) revealed that donor **3** and **4** have the ability to grow crystallites of considerably greater size, at least in the out of plane direction, respect to the other derivatives. The greatest attainable crystallite size in active layers of **3** and **4** is in the same range as the layer thickness, being 67 and 90 nm respectively, while it is in the range of 10 nm for derivative **1**, **2** and **5**. In most cases both the size of the crystallites and the total crystalline volume is seen to increase with annealing time as previously observed in SM-BHJ devices.[6c, 7] However, the increase is almost insignificant in the case of derivative **2** and **5**. Derivative **1** is the only derivative that show the opposite trend on the size evolution of the crystallites over the annealing time, [11] however the crystalline volume is seen to increase greatly upon longer annealing times.

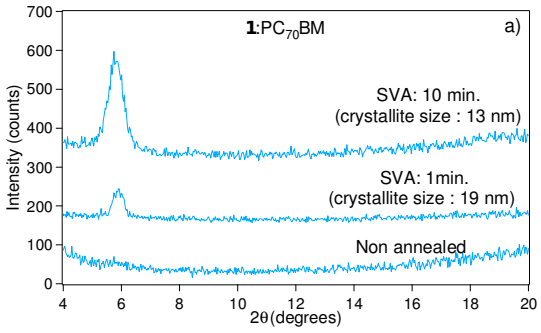

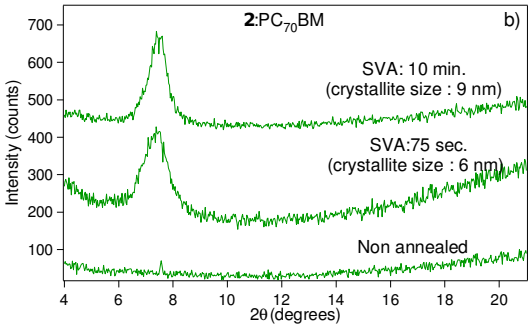

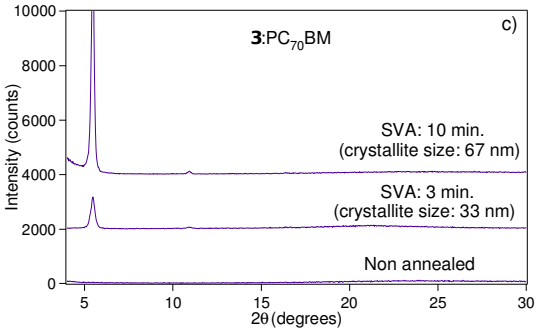

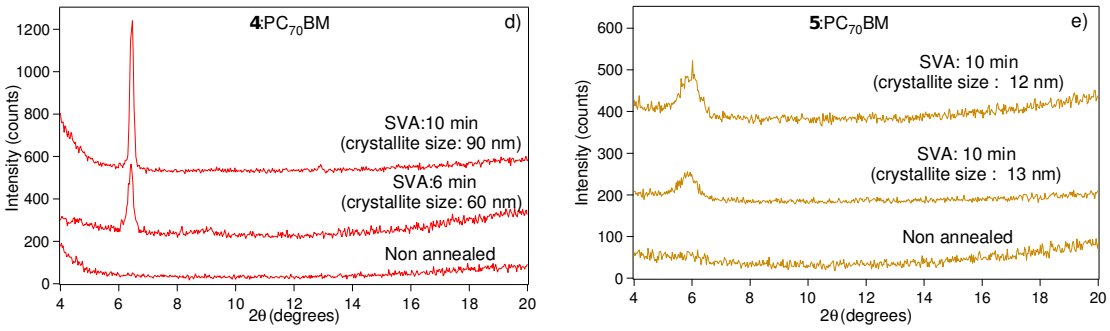

Figure 6. Bragg-Brentano point detector diffractograms of solvent vapour annealed (CH_2Cl_2) and non annealed active layers

Additional 2D diffraction patterns recorded in GIXRD mode reveals that the crystallites have a high degree of orientation respect to the substrate surface as seen by the presence of very narrow diffraction rings (Figure 7). Derivative **3** show the least degree of texture along the out-of-plane direction whereas all the other derivatives show to be highly oriented (See CHI cuts graphs for texture quantification, Figure SX). It can be additionally extrapolated that crystallites of derivative **2** and **4** have an extremely high degree of orientation, in the out-of-plane direction as well, as seen by the apparent weak signal intensity at low ω angles compared to that of the point detector 1D diffractograms (see Figure SX for additional GIXRD images).[12]

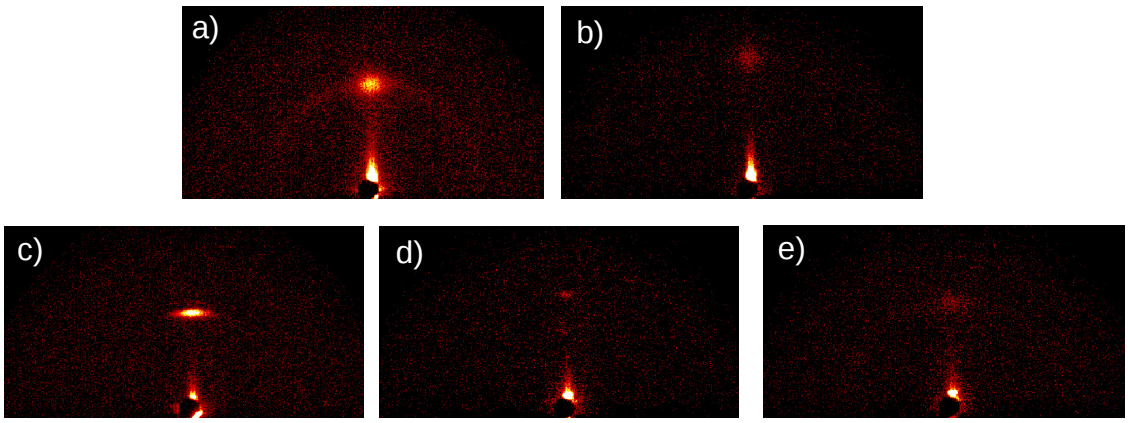

*Figure 7. Out of plane GIXRD images of active layers. Recorded at a 30 cm distance from the sample with ω =0.5º, the incident beam angle with respect to the substrate, a) **1**:$PC_{70}BM$; b) **2**:$PC_{70}BM$; c) **3**:$PC_{70}BM$; d) **4**:$PC_{70}BM$; e) **5**:$PC_{70}BM$.*

To gain additional evidence on the distribution and shape of the crystallites, AFM analysis of the active layers was carried out. Images were recorded on as cast and on annealed active layers from optimised devices. First, the change of morphology, derived from RMS roughness between the non-annealed and annealed devices confirms the trend observed in the XRD measurements. That is, an increase in roughness upon SVA, characteristic of crystallite growth within the active layer,[6b-d, 7] is observed for active layers of derivative **1**, **2** and **3** (Figure 8 and 9). In the case of derivatives **4** and **5** the un-annealed active layers show an unexpectedly high overall roughness value and a granular relief pattern, which likely stem from the fast drying conditions of the spin coating processing. The domains remain amorphous as seen in the XRD diffractograms, however the strong contrast difference in phase images (figure 8i and 8j) suggest that the granular pattern is consistent with segregated domains of donor and acceptor materials. This further confirms the unusually high PL emission intensity of non-annealed active layers of **4** and **5** as seen in Figure 4.

Upon exposing the active layers to solvent vapour of CH_2Cl_2 a clear change is noticed in the topology images consistent with the XRD measurements where molecules are seen to rearrange into pure crystalline domains of donor.

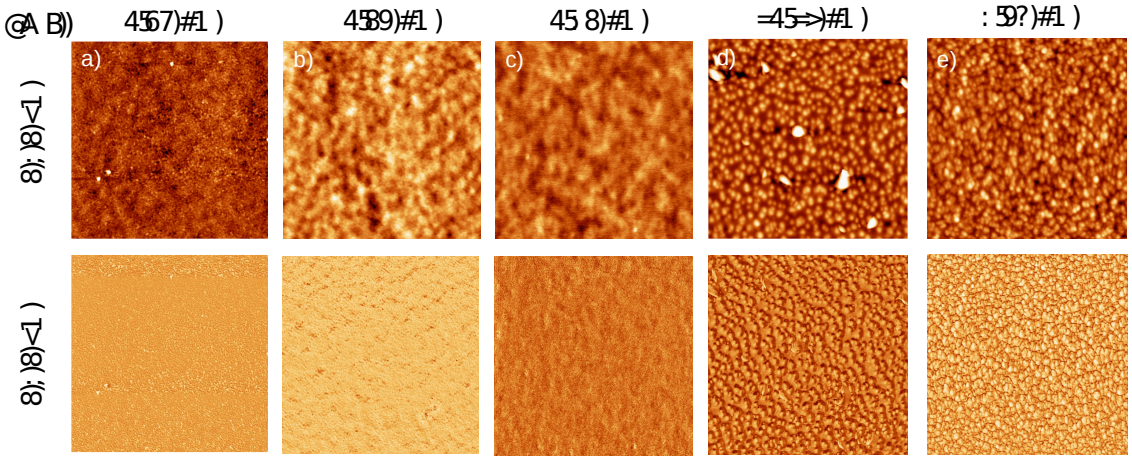

*Figure 8. AFM topology (top) and phase (bottom) images of un-annealed active layers of devices made from each donor derivative. a) **1**:$PC_{70}BM$; b) **2**:$PC_{70}BM$; c) **3**:$PC_{70}BM$; d) **4**:$PC_{70}BM$; e) **5**:$PC_{70}BM$.*

This rearrangement process is observed in most active layers and is seen to lead to very different morphologies. It is interesting to note that derivative **4** and **5** although having a similar chemical structure have a very different behaviour towards crystalline growth. Figure 9d, show the unusual formation of micrometre size, although few, sheet-like domains attributed to crystalline domains of pristine donor as it follows the evidence of unusually large crystallites in the out-of-plane direction (in the order of magnitude of the active layer's thickness) from XRD diffractogram (Figure 6). The contrast difference in the AFM phase image confirms the pristine nature of the crystallites (Figure 9d, bottom image). Conversely the fluorinated analogue **5**, show no morphological change through SVA by AFM, a trend also confirmed by XRD, which indicate very limited crystalline volume as seen by the weak diffraction peak in Figure 6e. The case of derivative **1**, **2** and **3** is rather different than the fluorinated derivatives. Derivative **1** and **2**, although forming crystallites of moderate size as seen in XRD, show a homogenous distribution within the active layer. Crystallites are seen embedded in the $PC_{70}BM$ matrix as demonstrated by the featureless phase images (Figure 9a and b, bottom images). Films of derivative **3** show a much higher roughness than the latter derivatives consistent with the presence of larger crystallites as measured by XRD.

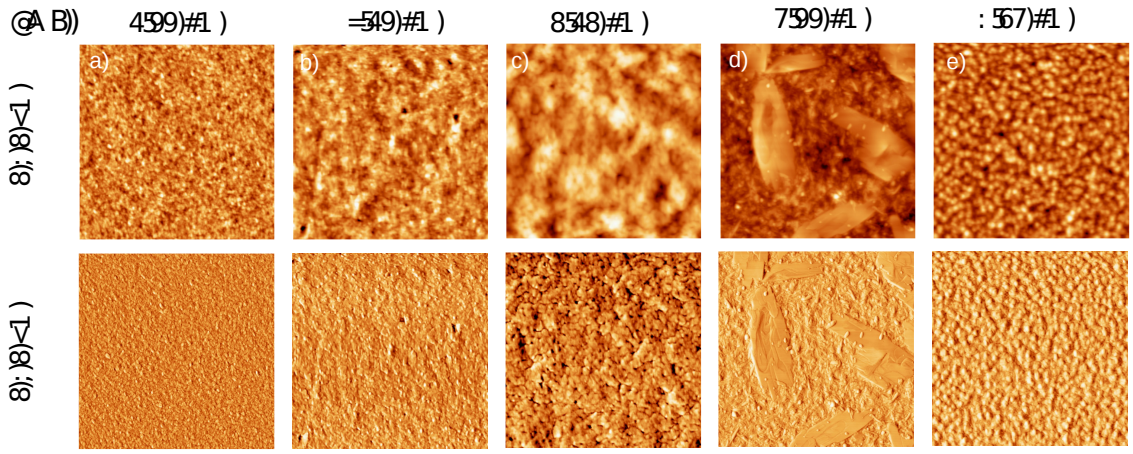

Figure 9. AFM topology (top) and phase (bottom) images of annealed active layers of devices made from each donor derivative. a) ***1****:$PC_{70}BM$; b)* ***2****:$PC_{70}BM$; c)* ***3****:$PC_{70}BM$; d)* ***4****:$PC_{70}BM$; e)* ***5****:$PC_{70}BM$.*

Molecular packing in crystallites of donor

Conventional XRD and GIXRD measurements in combination with AFM images allowed drawing fairly precise information of the active layers morphology at the nanoscopic scale as well as obtaining some insights on the kinetics of crystallisation of the SMs donor in the blend. To complete the analysis, we further investigated on the donors' packing in the crystalline domains using a recently published method which relies on the comparison of diffractograms of "powdered" active layers with XRD single crystal structures.[13] Single crystals of donors were grown in a range of different conditions to obtain as many polymorphic structures as possible for each derivative. Single crystal structures of at least one polymorph have been obtained for each derivative (Figure SX). The powdered layer method, consisting of depositing large area active layers on glass substrates, and measuring powder diffraction allows for accurate crystalline phase determination of the donors crystallites in the active layer, which would not otherwise be possible due to the limited amount of peaks present in the diffractogram of active layers. The

lack of diffraction peaks is both the result of limited crystallite size and high degree of texture. The analysis, which rely on diffractogram comparison using least-square profile refinement routines allowed confirming that molecules of derivatives **1** and **2** pack, in crystalline domains of active layers, in the same crystalline phases as that of their respective single crystals (Figure 10 and 11). The calculated diffractograms of the corresponding single crystal structures fit well enough for unambiguous phase assignment.

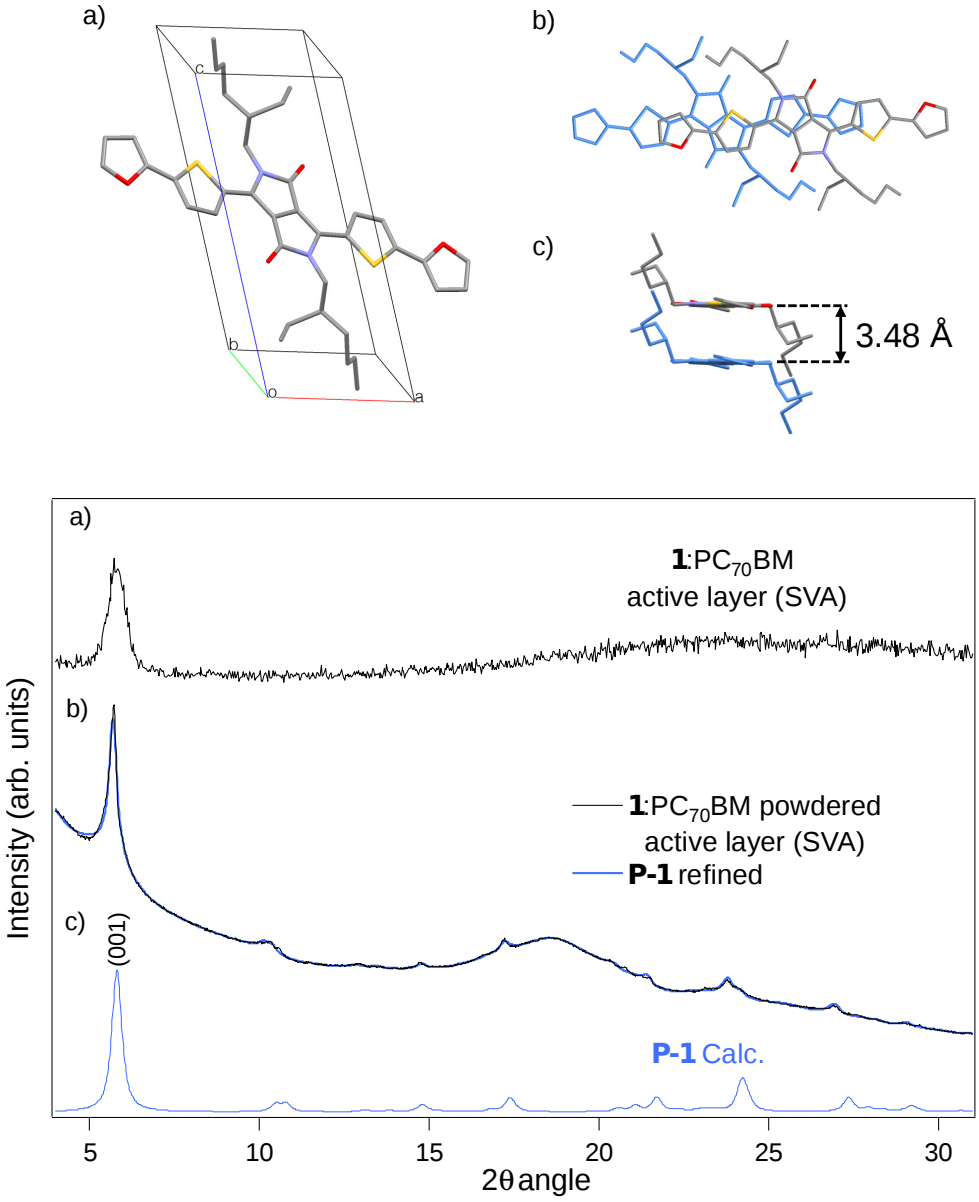

*Figure 10. X-Ray crystal structure of derivative **1**; Space group P-1 a) unit cell depicted side view of the (001) plane; b) Top and c) side view of the molecules stacks. Powdered active layer analysis; d) Active layer point detector diffractogram,*

e) Powder active layer diffractogram and superimposed refined diffractogram from the X-ray single crystal structure; f) calculated diffractogram (100 K) from the X-Ray single crystal structure.

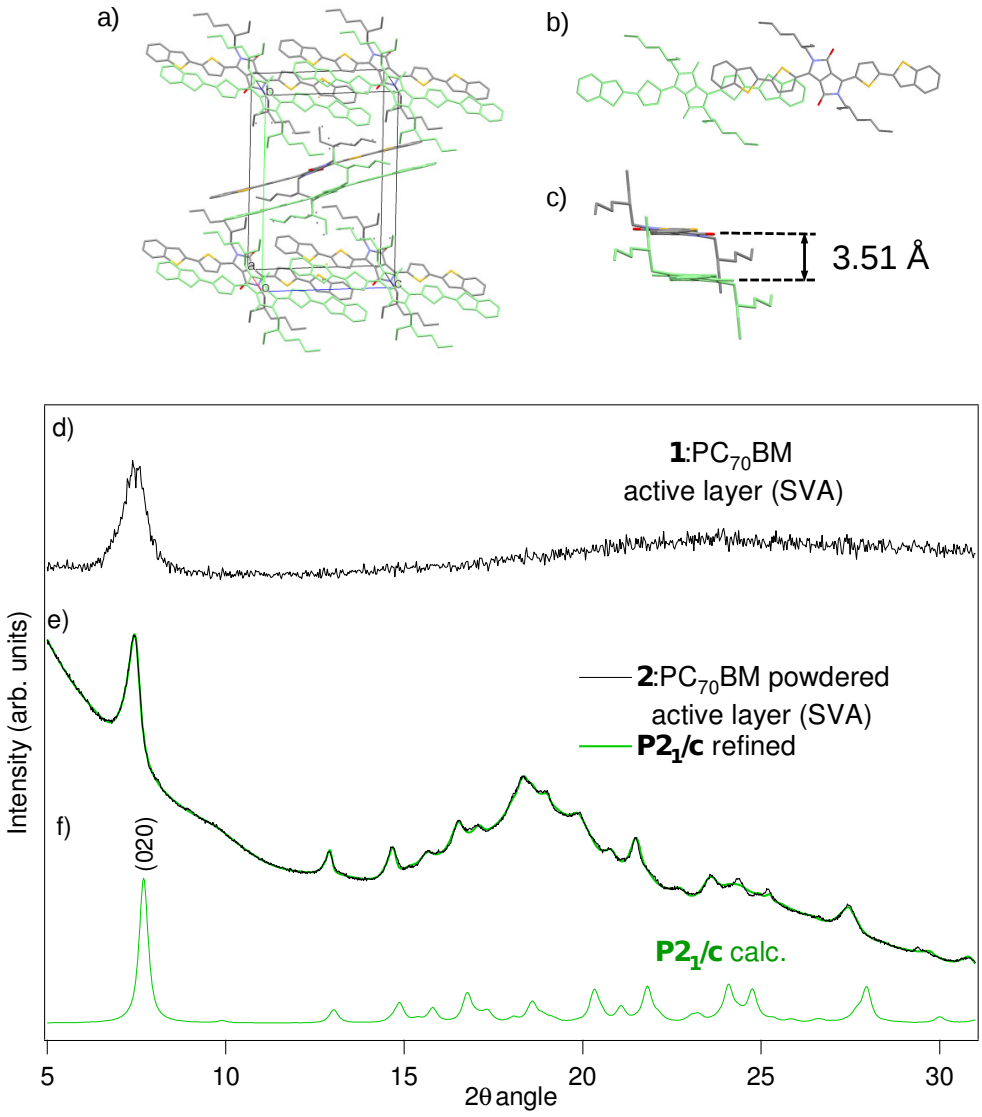

*Figure 11. X-Ray crystal structure of derivative **2** (hydrogens were omitted for clarity); Space group $P2_1/c$ a) unit cell depicted side view of the (020) plane; b) Top and c) side view of the molecules stacks. Powdered active layer analysis; d) Active layer point detector diffractogram, e) Powder active layer diffractogram and superimposed refined diffractogram from the X-ray single crystal structure; f) calculated diffractogram (100 K) from the X-Ray single crystal structure.*

The powdered active layer's diffractograms of blends of derivative **3**, **4** and **5** did not match those calculated from their respective single

crystal data structure, thus confirming that donor molecules in crystallites of the active layer are packed in a different phase as that of the single crystal (Figure SX). Unfortunately no additional crystal polymorphs that could provide for a better match could be isolated. Nonetheless, packing information from derivative **1** and **2** combined with GIXRD provides valuable information on the orientation of such packing (or orientation of the crystallites) respect to the substrate surface. That is, active layers and powdered layers diffractogram comparison lead to the deduction that crystallites of derivative **1** in active layers have a preferred orientation (deduced from GIXRD) with their (001) plane parallel to the surface (Figure 10a). The same analysis applies to derivative **2**, which shows to be oriented with its (020) plane parallel to the surface (Figure 11a). Importantly, powdered layer diffractogram profile refinement from derivative **2**, required the inclusion of anisotropic peak broadening parameters to provide for better profile shape refinement (see SI for details). This results in assuming that the crystallites of derivative **2**, grow with their unit cell parameter **b** and **c** significantly larger than parameter **a**. The implications of such feature will be expounded in the discussion section. The main morphological features derived from the above XRD and AFM measurements are shown in simplified cartoons in figure 12.

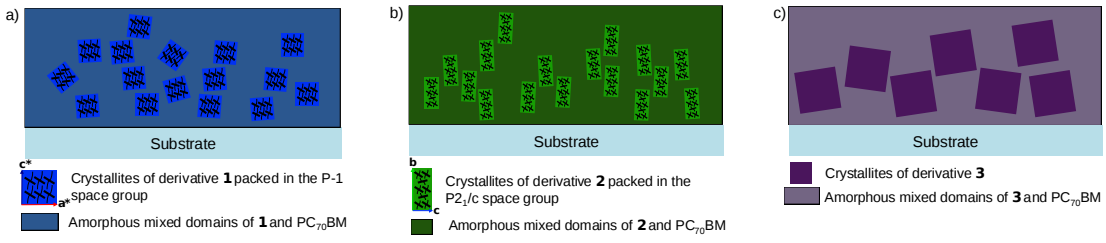

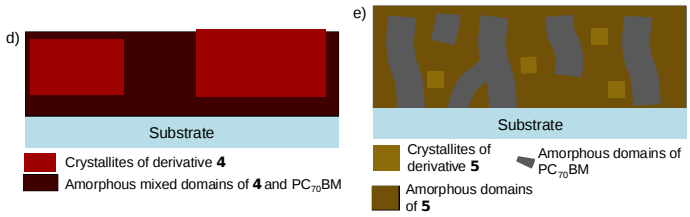

*Figure 12. Schematic representation of active layers in optimized conditions (side view) of a) derivative **1** showing partially oriented crystallites of **1** in the P-1 phase (the direction of the arrangement is represented respect to the reciprocal lattice whose a* and c* direction are represented by the red and blue arrows) b) derivative **2** showing uniformly oriented size-anisotropic crystallites of **2** in the $P2_1/c$ phase (the direction of the arrangement is represented respect to the crystal lattice whose **b** and **c** direction are represented by the green and blue arrows); c) derivative **3** showing partially oriented large crystallites of **3**; d) derivative **4** showing highly oriented outsized crystallites of **4**; e) derivative **5** showing scarce oriented crystallites of **5** embedded in segregated amorphous region of **5** resulting from spin-coating-induced demixing.[14]*

Crystalline growth

Although phase segregation in some polymer-$PC_{70}BM$ has been suggested to occur *via* a spinodal decomposition (demixing) mechanism,[15] the large and poorly intermixed morphologies formed in some of our solvent vapour annealed SM-PCBM active layers (especially derivative **3** and **4**) advocate for a different crystallite growth mechanism. It is likely that spinodal decomposition occurs in the early stages of active layer drying during spin coating resulting in the uniformly segregated, though amorphous, domains of donor and acceptor, as well exemplified by active layers of derivatives **4** and **5** (see AFM images, figure 8).[15f, 16] The low miscibility of the donors with the fullerene presumably enhanced by the Fluorine atoms in the case of **4** and **5**, (note on London dispersion forces) would allow the system to enter a spinodal region upon the fast drying conditions of the spin coating process. In the subsequent SVA step, the crystallization of donor molecules from the amorphous active layer blend matrix would then occur *via* a homogeneous or heterogeneous nucleation and growth mechanism as previously suggested.[15b] The experimental conditions would provide sufficient undercooling for the homogeneous nucleation process to be kinetically favoured as the SVA is carried out

at room temperature, well below the melting temperature of the blend. However it is very likely that heterogeneous nucleation dominates the process. This is supported by the fact that the crystallinity of the active layer (the total crystalline volume) has previously been shown to be highly dependent on the type and roughness of the substrate the active layer is deposited onto.[13, 17] In the heterogeneous nucleation mechanism the free energy change of the transformation is simply a linear scaling of the free energy change of the homogenous nucleation for the same system as described in equation 1. The scaling factor, dependent on the contact angle (ψ) between the nucleus and the surface from where the crystal is grown is in our case deemed to be similar since all the active layers where deposited on the same ITO/PEDOT:PSS substrate. It is thus omitted in the following study.

equation 1

The free energy change for a homogenous process implying spherical nuclei of radius r is described by equation 2.

$$\Delta G_{Hetero} = \Delta G_{Homo} f(\psi)$$ **equation 2**

Accordingly, ΔG(r) is seen to be dependent on three energy parameters: ΔG_C corresponding to the bulk free energy difference of crystal formation, intrinsic to each material polymorphic crystalline phase; γ corresponding to the interfacial energy (or energy arising from the interface between the nucleus composed of pure donor molecules and the D/A amorphous matrix); and ΔG_E the elastic free energy change due to the strain arising from the growth of a particle in the solid matrix. The latter two energy terms act as a barrier to nucleation. The profile shape of the free energy change of the

transformation for a given system is seen to proceed through a maximum value (activation energy) determining the critical nucleus size (r*) to be achieved for crystallite growth to become favourable (when $d\Delta G(r)/dr=0$; ΔG^*).[18]

Consequently, for a given active layer, r* and ΔG^* will be determined by the intrinsic ability of the donor molecule to arrange in a thermodynamically stable crystalline phase (maximising ΔG_C and minimizing γ) in the amorphous D/A blend. The interfacial contribution to nucleus growth dominates at small nucleus sizes while the volumetric one ($\Delta G_C + \Delta G_E$) dominates at large nucleus size. Following experimental evidence it appears that SVA act as to lower the G_E contribution resulting presumably in lower G* than in thermal annealing methods. This is supported by the fact that crystallization occurs at low temperatures (typically RT) as opposed to the thermal annealing process, and that crystals of a macroscopic size are commonly grown from thin layers through SVA,[19] the solvent saturated atmosphere allowing molecule dislocation over micrometre distances.

The formation of one preferential polymorphic structure is, to some extent, explained on grounds of change in free energy of crystal formation (ΔG_C), which is expected to vary from one crystalline phase to the other. However, the formation of the final crystalline phase in the active layer could proceed through a complex energetic path, including the formation of greater ΔG_C intermediate polymorphic nuclei, rearranging towards less energetically favoured crystalline phase providing for lower interfacial energy able to compensate the lower ΔG_C of that new hypothetical polymorph.[20] This implies that the resultant crystalline phase is not necessarily the most thermodynamically stable, i.e. the one leading to the larger difference in crystal formation free energy.

Once nuclei with size superior to r* have formed the rate of crystallite growth rate is limited by the diffusion of donor molecule from the bulk

(the mixed D/A amorphous phase) to the interface and transfer of donor molecule from the vicinity of the nucleus to the interface.

To provide an insight into the energetics of the crystallites' growth, contact angle measurements were carried out on non-annealed active layers of all derivatives. The surface free energy (SFE) measured through this technique provides a relative quantification of the interfacial energy γ of the amorphous fraction of the active layers in the early stage of the growth (r=0, Figure 13). The measurements were carried out with a three solvent system (see SI for details). The polar and dispersive fractions of the SFE are reported on Table 3. As expected, the polar fraction shows a very similar contribution for all derivatives due to the highly apolar nature of the components of the active layer. However the dispersive SFE, which is assumed to satisfactorily model the interaction between the surface and hydrophobic molecules such as the donors, is seen to vary significantly from derivative to derivative. Active layers of derivative **2** displays the highest value of SFE while **4** displays the lowest value. To provide for a qualitative analysis of the ΔG_C contribution we derived the free energy change of crystallisation $\Delta_{crys}G$ for derivative **1** and **2** from the enthalpy of fusion ($\Delta_{fus}H$) of pure crystalline powder samples of **1** and **2** in the P-1 and $P2_1/c$ phases respectively. The $\Delta_{fus}H$ of the powders was derived from the specific heat capacity of the materials measured by differential scanning calorimetry (DSC) (see SI for powder characterisation, DSC curves and $\Delta_{fus}H$ and ΔG_C calculation). The calculated values of $\Delta_{crys}G$ show that the formation of crystallites of **2** in the $P2_1/c$ phase is thermodynamically more favourable ($(\Delta_{crys}G(\mathbf{2}\text{-}P2_1/c) < \Delta_{crys}G(\mathbf{1}\text{-}P\text{-}1)$) than the formation of crystallites of **1** in a P-1 phase (Table 2). We then use these values as a relative indicator to draw a hypothetical energy profile of the nucleation process. That is, neglecting the ΔG_E contribution, the experimental SFE and $\Delta_{crys}G$ show that the interfacial energy (γ) for nuclei formation in active layer of **1** and **2** and their associated bulk crystalline free

energy change profile (ΔG_C) are likely to adopt the shape of that in Figure 13. The higher ΔG_C contribution compensate for the higher interfacial energy experienced by nuclei of derivative **2** during crystalline growth in the amorphous matrix of the active layer. This results in r^*_2 being inferior to r^*_1 and in the formation of nuclei of **1** being kinetically favoured respect to **2** ($\Delta G^*_1 < \Delta G^*_2$).

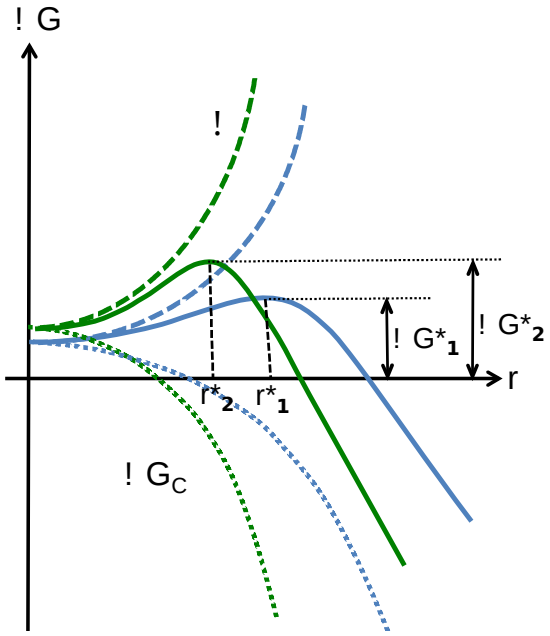

*Figure 13. Hypothetical energetic profile of donors' nucleation in active layers of derivatives **1** and **2**.*

This model is in good agreement with the XRD experimental evidence (figure 6), where the rate of nucleation is seen to be relatively slow for derivative **2**, with virtually no increase in overall crystalline volume over 10 min. of SVA, while nucleation is seen to proceed faster in the case of derivative **1** showing a great increase in crystalline volume after 10 min. of SVA. The fact that small crystallites are produced in active layers of derivative **2** and bigger ones in the case of derivative **1** follow the assumption of r*2<r*1. In both cases the very little increase, or no increase at all,[21] in crystallite size is related to the rate of crystallite growth which is deemed very slow respect to the rate of

nucleation. Therefore, the increase of crystalline volume in the active layer is seen to be dominated by nucleation kinetics.

Derivative	Average disperse (J)	Average polar (J)	Total average (J)	$\Delta_{crys}G$ (crystaline phase)
1	20.8	3.4	24.2	-23.6 KJ/mol (P-1)
2	29.2	1.7	30.9	-42.9 KJ/mol ($P2_1/c$)
3	22.7	1.9	24.6	-
4	16.1	1.8	18.0	-
5	24.2	1.1	25.3	-

*Table 2. Average surface free energy of the non-annealed active layers and crystallisation free energy change of powders of derivative **1** (P-1) and **2** ($P2_1/c$). The blend composition and the deposition condition of the active layer are the same as those of optimised devices (see table 1 and SI).*

Unfortunately the missing information on crystalline phase in active layers of derivative **3**, **4** and **5** did not allow for a similar energetic quantification as for derivatives **1** and **2**.

However following the above observations, it can be estimated from XRD and AFM data (*vide supra*) that the rates of nucleation and growth are rather balanced in the case of derivative **3**. That is, the observed increase in crystalline volume and crystallite size confirms that both nucleation and growth are kinetically favoured.

The case of derivative **4** exemplifies the trend where, contrary to derivative **1**, the growth rate is faster than the nucleation rate as seen by the presence of a small number though very large crystallites. Derivative **5** on the other hand, display both slow rates of nucleation and growth. The rather extreme difference in behaviour between the latter two derivatives is most probably explained on grounds of energy change of crystallization (ΔG_C). That is, it is very likely that derivative **5** will see its solid state packing energetics greatly affected by the presence of 6 very weekly polarisable atoms homogeneously distributed around its conjugated core leading to a small free energy change of crystallisation unable to cope with the interfacial free

energy contribution in the nucleation process. These two derivatives additionally point out to the impact of donor's chemical structure on the initial demixing step, providing active layers with different SFEs. The low SFE inherited from the spin coating parameters (speed, spinning time and acceleration) as well as the D/A ratio are accountable in the case of **4** for the growth of extremely large crystallites.

Additional to the influence of the interface energy on crystallite growth is the propensity of crystallites to grow along a specific crystallographic direction. This is exemplified by derivative **2**, whose 'powdered' layer diffractogram suggests that growth occurs preferentially along the (010) direction, implying that the largest side of the crystallites is oriented perpendicularly to the surface as demonstrated with the GIXRD images.

Non-geminate recombination

Finally, In order to identify how the morphological features contribute to the V_{OC} and to some extent to the shape of the *J-V* characteristics, a qualitative recombination study was carried out using a well-established charge extraction and transient photovoltage method (see SI for experimental details).[22] The CE measurements allow measuring the average charge density at open circuit in the devices. The corresponding plots of the charge density (*n*) *vs.* V_{OC} of all the devices are shown in figure 14a. The charge density *n* was corrected for the electrode capacitance (see SI). The data shows to be in good agreement with the charge density being of similar magnitude in all measurements, reaching about 2 x 10^{16} charges/cm^3 at values close to V_{OC} similarly to what has been reported earlier for such type of devices.[22i, 22j] For all the devices the total charge is seen to fit an exponential increase, evidence of charges accumulated in the bulk of the device. The plots of *n vs.* V_{OC} were fitted to single exponentials of

the form of Equation 3 (see Table 3) consistent with an exponential tail of trap states extending into the band gap of the active layer.[23]

$$n = n_0 e^{\gamma Voc} \qquad \textbf{Equation 3}$$

$$\tau_{\Delta n} = \tau_0 e^{-\beta Voc} \qquad \textbf{Equation 4}$$

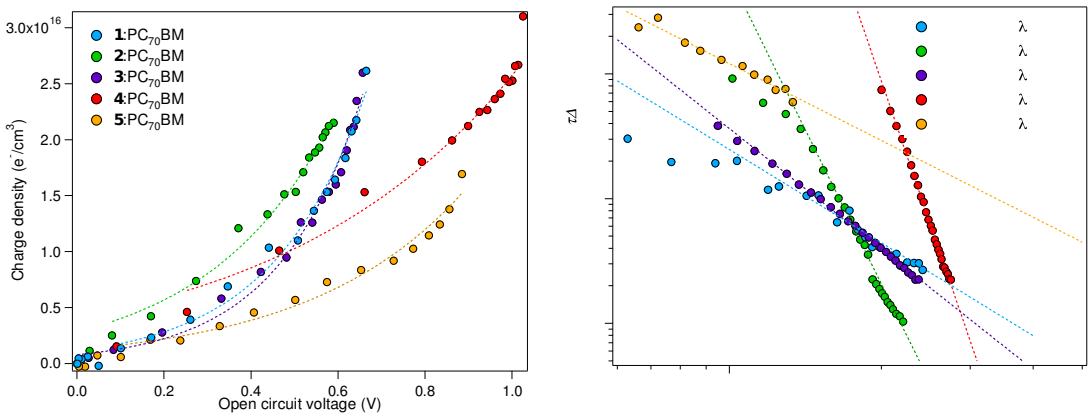

Figure 14. a) Comparison of the charge density (n) as a function of the open circuit voltage determined from CE measurement. The curves are fitted to an exponential grow of the form $n=n_0e^{(\gamma VOC)}$ (dotted line) whose parameters are reported in Table 3. b) Small perturbation carrier life time *vs.* Charge carrier density plot. The charge carrier density was calculated from the exponential fittings of figure a). Curves are fitted to power law decays of the form $\tau_{\Delta n}=\tau_{\Delta n0}\, n^{-\lambda}$, whose parameters are reported in Table 3.

The carriers life time *(tau)* versus open circuit voltage (V_{OC}) plot for all the devices is shown in Figure SX, where the curves were fitted to single exponential decays of the form of Equation 4.

The overall order of recombination ϕ, defined by Equation 5, can be approximated to $\phi = \lambda+1$, in our TPV experimental conditions ($\Delta n << n$).[22h] The parameter λ is obtained experimentally by fitting the curve of the small perturbation carrier life time $\tau_{\Delta n}$ *vs.* n to a power law of the form of Equation 6.

$$\frac{dn}{dt} = -kn^{\phi}$$ Equation 5

$$\tau_{\Delta n} = \tau_{\Delta n0} n^{-\lambda}$$ Equation 6

First, the overall small perturbation life times are in good agreement with the trend of experimental V_{OC} for all derivatives' devices. That is, derivatives **4** and **5** leading to higher V_{OC} display an overall longer carrier lifetime, while derivative **1**, **2** and **3** show much shorter lifetime. Life times of derivatives **2**, are shown to be the shortest accordingly the trend observed for the V_{OC}.

Derivative	VOC theoretical	VOC	ΔVOC	ΔVOC (%)	JSC	FF	PCE (%)	m hole
1	1.0	0.702	0.30	30	4.77	45	1.52	1.25 x 10-6
2	1.1	0.608	0.50	44	2.78	55	0.93	1.28 x 10-8
3	0.8	0.628	0.17	21	4.80	44	1.32	8.5 x 10-8
4	1.3	1.06	0.30	18	2.84	45	1.34	6.3 x 10-8
5	1.2	0.964	0.24	19	1.11	25	0.27	6.9 x 10-10
DPP(TBFu)2	1.1	0.858	0.25	22	8.97	48	3.64	5.3 x 10-4 to 2 x 10-5

Table 3. *J-V* characteristics parameters of all devices

Interestingly the recombination order varies significantly from device to device, with unexpectedly high values (ϕ = 11.8). Such high values, as opposed to a value of 2, which is to be expected in a strictly bimolecular recombination process in the case of Langevin type recombination, have been measured several times in earlier reports,[22h, 23c, 23d, 24] and were attributed to recombination through trap states in the band gap of the active layer materials.[24] Therefore the non-geminate recombination process is described as an essentially bimolecular process where the recombination coefficient is allowed to be charge dependent accordingly to the presence of trap states in the

band gap.[22c, 22e, 22h] It has recently been demonstrated that such high values of ϕ are likely the result of predominant surface recombination as expected for very thin (<100 nm) active layers.[25] This is in very good agreement with the morphological data expounded above whereby device of derivative **4**, which displays an abnormally high recombination order, is seen to form extremely large domains of pure donor contacting with the top metal cathode thus inducing increased surface recombination kinetics. The consequence of morphology-induced high recombination order is further exemplified in figure SX, where the V_{OC} of the device is seen practically invariant of light illumination. Hence, the fast decrease in charge carrier lifetime respect to charge carrier density, expressed by ϕ, is consistent with a limited hole and electron quasi-Fermi level splitting with increasing light biases. A very similar trend is observed for derivative **1**, whose high recombination order correlates with the small variation of V_{OC} respect to light illumination (Figure SX). However, in this case, rather than being due to donor domains contacting directly with the cathode, it may be the result of the inhomogeneity of electrons and holes concentration along the active layer thickness,[25] expected to be more prominent as devices of derivative **1** have shown to grow preferentially along the surface normal. Devices made with derivatives **1** and **3** have a similar recombination order whereas devices of derivative **5** show a much lower recombination order of 2, consistent with very low mobility semiconductors where recombination is limited by the probability of encounter of electrons and holes. Importantly, the recombination data is in good agreement with the trend of V_{OC}, whereby the experimental V_{OC} in each device is lowered respect to the theoretical value from a magnitude roughly proportional to the mean recombination lifetimes around 1SUN illumination light bias. That is, devices in which charge carrier lifetimes are slower at high charge carrier density (corresponding to approx. 1SUN illumination) show the smallest offset between their

theoretical V_{OC} and experimental one (ΔV_{OC} (%), Table 3) and *vice versa*. Then, device of derivative **2**, displaying the fastest kinetics under 1 SUN illumination bias resulting from the high recombination order show the largest offset between its theoretical V_{OC} and experimental one. Devices of derivative **4** and **5**, exemplify the opposite trend, where the offset is seen to be the smallest, despite device of **4** having a very high recombination order.

Overall, the mean small perturbation lifetime at low light bias is consistent with the predicted D/A interfacial area derived from the crystallite size and hole mobility values. That is, charge carriers in devices of derivative **2** exhibit a significantly longer lifetime at low illumination biases than derivative **1** whose morphological features have been shown similar to **2** (similar crystallite size). The difference in mean lifetime at low bias may then be related to the difference in hole mobility shown to be more than one order of magnitude higher in devices of derivative **1**. Conversely, the extremely low mobility in devices of derivative **5** is responsible for the slow recombination life times at low light bias regardless of the presence of fairly intermixed D/A domains. The slow recombination life times at low light bias of derivative **4** could on the contrary be attributed to the reduced D/A interfacial area. The case of derivative **3** is rather difficult to rationalise solely by morphological aspects. The small offset between theoretical and experimental V_{OC} is presumably due to a narrower DoS distribution as extrapolated from charge extraction measurements (i.e the position of the CE curve of derivative **3** (figure Xa), which is shifted toward higher voltages than expected from the experimental device's V_{OC} suggest the population of higher energy states in the tail of the DoS than derivative **1**). The faster-than-expected recombination lifetimes from the hole mobility may be due to some degree of anisotropy in hole mobility, implying that hole mobility is significantly higher in the direction parallel to the substrate than in the direction of charge extraction. This seems a fair assumption given the very high

degree of orientation of the crystallites of donors in the active layer and a potential high anisotropicity in the christalline packing of **3** in the solid state (see X-ray structure of **3**, Figure SX).

Discussion

Several key structural characteristics could be related to the solar cell device performance of each derivative. First of all, a very simple quantitative analysis of the absorption properties of each derivative active layer demonstrated how much the thinness of SM-BHJ active layers is a limitation to light absorption and thus to photocurrent generation. The slight decrease in the absorption coefficient of the donor derivatives **1**, **2** and **4** does not account for the decrease in absorption intensity of the active layers. Additional to active layer thickness the D/A ratio and donor molecular weight play a significant role in determining the absorption capacity of the final active layer. The main challenge resides in the fact that none of these parameters can be directly controlled, as the D/A ratio and active layer thickness are the result of devices optimization. To each optimum D/A ratio is associated a set of transport properties, which will eventually limit the active layer to a thickness that provides a compromise between strong absorption, fast transport and slow recombination kinetics. This effect is well exemplified in our study where most of the devices having gone D/A and thickness optimization resulted in a similar hole mobility while spanning a range of different thicknesses and active layer crystallinity features. Finally, the molecular weight directly impacts on the actual quantity of donor present in the active layer. For a given weight ratio of D/A, the absorption is directly dependent of the mole quantity of donor respect to the acceptor depend on its molecular weight. Consequently, donor **3** whose absorption coefficient is almost twice as high as donor **1**, does not provide for the expected stronger absorption in active layer films (at the same D/A ratio and

similar thickness) due to the molecular weight of **3** being more than twice that of **1**.

Transport properties are acquired upon formation of crystalline domains in the active layer. The ability of donors to form crystallites of considerable size from the amorphous D/A blend is central to obtaining devices with enhanced *J-V* characteristics. An insight into the thermodynamics governing the process has been given. The ability of the donor to crystallise in the active layer is principally governed (at least in SVA-treated active layers) by ΔG_C and γ. Both factors are intrinsic to the donor's structure and are greatly affected by subtle changes in its chemical structure. As such, donors with subtle differences in their structure as **4** and **5** provide active layers with extremely different crystallization energetic impacting on the overall crystallinity. The miscibility of the donor with the acceptor in the solid state is important to determine the energetics of the active layer prior to the nucleation and growth process.(note) That is, the magnitude of the donor/acceptor demixing occurring in the early stages of the active layer's deposition is of capital importance to the following crystallite growth occurring during the annealing step as the latter is directly impacted by the surface energetics resulting from the earlier A/D demixing.[15b, 15d] This phenomenon certainly explains the differences in morphology and crystalinity observed upon changes in deposition conditions (spin coating solvent, speed and acceleration) in earlier reports.[13, 26] The SVA time optimization, by allowing crystallites to grow to a determined size, establishes a trade off between hole mobility and high D/A interface. Importantly, SVA, thickness and D/A ratio parameters are indirectly related since changes in the D/A ratio will impact the energetics of crystallite growth, which in turn will impose a limitation on the maximum attainable thickness itself determined by the maximum attainable hole mobility is such crystalline state.

Provided that mobility is sufficiently high, the final D/A interfacial area resulting from these optimization processes will further limit the device's characteristics from the absorption properties of the active layers. Low interfacial area will limit the J_{SC} but provide less V_{OC} losses though reduced non-geminate recombination kinetics, as exemplified by donor **4**. Conversely, the higher interfacial area in devices of derivative **1** corroborates the higher experimental losses in V_{OC}, while the J_{SC} losses (respect to the absorption properties of the active layers) are minimal. Derivatives **2** and **3** are intermediate cases between the latter two extremes, where subtle morphological parameters (such as the crystallite shape anisotropy and presumed narrow DoS distribution) induce additional losses (high V_{OC} losses in derivative **2**) or unexpected loss compensation (lower-than-expected V_{OC} losses from recombination kinetics in derivative **3**). The rather low J_{SC} in derivative **2** arising from the low photon-to-charge conversion efficiency at lower wavelengths might stem from low hole mobility. Derivative **5** illustrates the case where crystallite growth is not seen to occur with sufficient magnitude providing very low hole mobility limiting J_{SC} even further than in derivative **2**.

If the experimental lifetime correlates the loss in V_{OC} respect to the theoretical maximum, the correlation between recombination and FF often observed in polymer-based devices is not observed herein. The negligible field dependency on charge generation displayed by polymer-based devices [27] is usually not as insignificant in SM-BHJ devices[28] due to charge delocalisation (especially hole) occurring on short distances and mostly in crystalline domains. It thus makes sense to assume that the higher FF observed in devices of derivative **2**, are the results of larger hole delocalisation distance in the direction of charge extraction resulting from donors crystallite shape anisotropy, the non-recombination kinetics having little influence on the shape of the *J-V* curve (FF).[28] This is further supported by the fact that FF is seen to increase up to 66% (with no significant concomitant

increase in V_{OC}) with increasing crystallite size promoted by longer SVA times (Figure SX), favouring charge extraction at low internal field.

Finally, the packing pattern of donor molecules in the crystalline domain is expected to have a significant influence on the transport properties. The 'powdered' layer method provided for precise information on the crystalline phase of the crystalline domains for active layers of derivative **1** and **2**. In the case of derivative **1** molecules pack in a low symmetry P-1 space group with molecules stacked uniformly over a long range. Derivative **2** packs in the $P2_1/c$ space group, in a herringbone fashion. As seen from Figure 10 and 11 a significantly higher transfer integral could be expected in crystals of derivative **1** in the direction perpendicular to the π-delocalised backbone plane due to apparent ampler π-π stacking and slightly shorter stacking distances than in crystals of derivative **2**. The lower symmetry packing of derivative **1** induces continuous stacking in the three directions of space, while the herringbone arrangement in the case of derivative **2** implies a discontinuity in the arrangement. These parameters are likely to impact on the electronic properties of the active layers comprising such derivatives, and may likely be the reason for higher hole mobility in devices of derivative **1** (Table 3).

As previously demonstrated, mobility in organic materials often display a high degree of anisotropy, which is directly related to the packing pattern in the solid state.[29] As such, the orientation of the solid-state packing arrangement respect to the substrate is likely to play a very important role in the hole mobility properties in the bulk. Low symmetry "slipped stacked" patterns as that of derivative **1**, have shown to lead to highly anisotropic mobility with the highest value perpendicular to the π-π stacks. Herringbone arrangements usually lead to less anisotropy as "hopping" is allowed in different directions of space. Our experimental observations are consistent

with these assumptions. As an example, derivative **1** which forms highly oriented crystallites respect to the out-of-plane direction with their π-π stacked backbone oriented, to a fair extent, perpendicular to the direction of charge collection are seen to give rise to the highest SCLC mobility.

Conclusion

To conclude, we employed a myriad of characterisation techniques in order to best relate the devices' characteristics of SM-BHJ with the morphological features of the active layers induced by the donors' structure. We demonstrated that subtle changes in the donor's structure have a strong impact on the devices' characteristics. As such, predicting the characteristics of SM-BHJ devices from the donor's chemical structure may remain a very challenging task. However our study pointed out some basics requirements to be taken into account when designing new donors for SM-BHJ. Most importantly, it is imperative that the donor is able to grow numerous monodisperse nanometre-sized crystallites of donors inside the D/A amorphous matrix. Additionally, the strong propensity of SM donors' crystallites to adopt a uniform orientation in active layers of OSC devices as seen in the present study and others, is a key parameter in determining the transport properties in the bulk. That is, crystallites with uniform orientation have been proved to lead to higher mobility in organic material due to faster intragrain charge hopping.[30] However to have a positive impact, the orientation has to match the direction of faster transport in the crystallites. In this respect the solid-state packing of the donor molecule plays the major role. While, extensively π-π-stacked units could provide for fast charge hopping in the direction perpendicular to the stacks, it usually implies that hopping is reduced in the remaining directions of space. This anisotropy feature is usually reduced in higher symmetry packing patterns.

Consequently, if a donor is seen to pack in a low symmetry crystalline phase it is essential that the crystallite be oriented in the direction of higher mobility. A higher symmetry arrangement could be more forgiving.

All these inter-related properties are extremely difficult to predict as crystallization of SMs stems from week intermolecular interactions between donors, which are easily disrupted in the complex environment of SM-BHJ active layers (*e.g*. the presence of fullerene). As a first step towards the understanding of crystallite formation in SM active layers we proposed that crystalline growth in active layers occurs *via* a nucleation and growth mechanism, at least when the SVA post-deposition treatment is applied, and as such a balance between the bulk energy of growing crystal and the interface energy is necessary to favour the growth of homogenous crystallites. Such property is as well difficult to predict, but could be thought of being controlled for instance by the use of supramolecular binding motifs[31] or through extensive computational simulations.[32]

Finally some aspects of the absorption properties of the donor have been clarified; although no concrete design rules could be identified, other than maximising the absorption coefficient of the donor, since the main factor limiting the absorption of the active layers is the active layer thickness whose maximum is indirectly limited the transport and recombination properties given by the above morphological parameters.

Then it appears that the PCE improvement in SM-BHJ from rational design is rather limited and may rely on empirical design, unless some supramolecular interactions could be put into use to control the crystallisation of donor in active layers. An alternative to the BHJ structure could lie in the PiN structure described by Matsuo *et al.*[33] which has been largely unexplored to date although having shown great promise in controlling the crystalinity (size, shape, shape

dispersity and packing phase) of the active layer using a stepwise deposition and morphology formation process.

Bibliography

1. a) V. Gupta, A. K. K. Kyaw, D. H. Wang, S. Chand, G. C. Bazan and A. J. Heeger, *Scientific Reports*, **2013**, 3; b) A. K. K. Kyaw, D. H. Wang, V. Gupta, J. Zhang, S. Chand, G. C. Bazan and A. J. Heeger, *Adv. Mater.*, **2013**, 25, 2397; c) A. K. K. Kyaw, D. H. Wang, D. Wynands, J. Zhang, N. Thuc-Quyen, G. C. Bazan and A. J. Heeger, *Nano Lett.*, **2013**, 13, 3796; d) Y. Liu, C.-C. Chen, Z. Hong, J. Gao, Y. Yang, H. Zhou, L. Dou and G. Li, *Sci. Rep.*, **2013**, 3; e) D. H. Wang, A. K. K. Kyaw, V. Gupta, G. C. Bazan and A. J. Heeger, *Adv. Energy. Mater.*, **2013**, 3, 1161; f) J. Zhou, Y. Zuo, X. Wan, G. Long, Q. Zhang, W. Ni, Y. Liu, Z. Li, G. He, C. Li, B. Kan, M. Li and Y. Chen, *J. Am. Chem. Soc.*, **2013**.
2. a) Y. Li, Q. Guo, Z. Li, J. Pei and W. Tian, *Energy Environ. Sci.*, **2010**, 3, 1427; b) Y. Lin, Y. Li and X. Zhan, *Chem. Soc. Rev.*, **2012**, 41, 4245; c) A. Mishra and P. Baeuerle, *Angew. Chem., Int. Ed.*, **2012**, 51, 2020; d) Q. L. Huang and H. X. Li, *Chin. Sci. Bull.*, 2013, 58, 2677; e) Y. Chen, X. Wan and G. Long, *Acc. Chem. Res.*, **2013**, 46, 2645.
3. B. Walker, A. B. Tamayo, X.-D. Dang, P. Zalar, J. H. Seo, A. Garcia, M. Tantiwiwat and T.-Q. Nguyen, *Adv. Funct. Mater.*, **2009**, 19, 3063.
4. a) O. P. Lee, A. T. Yiu, P. M. Beaujuge, C. H. Woo, T. W. Holcombe, J. E. Millstone, J. D. Douglas, M. S. Chen and J. M. J. Frechet, *Adv. Mater.*, **2011**, 23, 5359; b) G. He, Z. Li, X. Wan, Y. Liu, J. Zhou, G. Long, M. Zhang and Y. Chen, *J. Mater. Chem.*, **2012**, 22, 9173; c) X. Liu, Y. Sun, L. A. Perez, W. Wen, M. F. Toney, A. J. Heeger and G. C. Bazan, *J. Am. Chem. Soc.*, **2012**, 134, 20609; d) Y. Liu, X. Du, Z. Xiao, J. Cao, S. Tan, Q. Zuo and L. Ding, *Synth. Met.*, **2012**, 162, 1665; e) E. Ripaud, D. Demeter, T. Rousseau, E. Boucard-Cetol, M. Allain, R. Po, P. Leriche and J. Roncali, *Dyes Pigm.*, **2012**, 95, 126; f) C. J. Takacs, Y. Sun, G. C. Welch, L. A. Perez, X. Liu, W. Wen, G. C. Bazan and A. J. Heeger, *J. Am. Chem. Soc.*, **2012**, 134, 16597; g) J. Zhou, X. Wan, Y. Liu, Y. Zuo, Z. Li, G. He, G. Long, W. Ni, C. Li, X. Su and Y. Chen, *J. Am. Chem. Soc.*, **2012**, 134, 16345; h) N. D. Eisenmenger, G. M. Su, G. C. Welch, C. J. Takacs, G. C. Bazan, E. J. Kramer and M. L. Chabinyc, *Chem. Mater.*, **2013**, 25, 1688; i) V. S. Gevaerts, E. M. Herzig, M. Kirkus, K. H. Hendriks, M. M. Wienk, J. Perlich, P. M√ºller-Buschbaum and R. A. J. Janssen, *Chem. Mater.*, **2013**, 26, 916; j) G. He, Z. Li, X. Wan, J. Zhou, G. Long, S. Zhang, M. Zhang and Y. Chen, *Journal of Materials Chemistry A*, **2013**, 1,

1801; k) G. He, Z. Li, X. Wan, J. Zhou, G. Long, S. Zhang, M. Zhang and Y. Chen, *J. Mater. Chem. A*, **2013**, 1, 1801; l) J. Liu, B. Walker, A. Tamayo, Y. Zhang and T.-Q. Nguyen, *Adv. Funct. Mater.*, **2013**, 23, 47; m) J.-Y. Pan, L.-J. Zuo, X.-L. Hu, W.-F. Fu, M.-R. Chen, L. Fu, X. Gu, H.-Q. Shi, M.-M. Shi, H.-Y. Li and H.-Z. Chen, *ACS Appl. Mater. Interfaces*, **2013**, 5, 972; n) M. Weidelener, C. D. Wessendorf, J. Hanisch, E. Ahlswede, G. Gotz, M. Linden, G. Schulz, E. Mena-Osteritz, A. Mishra and P. Bauerle, *Chem. Commun. (Cambridge, U. K.)*, **2013**, 49, 10865; o) G. Chen, H. Sasabe, Y. Sasaki, H. Katagiri, X.-F. Wang, T. Sano, Z. Hong, Y. Yang and J. Kido, *Chem. Mater.*, **2014**; p) Y. Kim, C. E. Song, A. Cho, J. Kim, Y. Eom, J. Ahn, S.-J. Moon and E. Lim, *Mater. Chem. Phys.*, **2014**, 143, 825; q) G. D. Sharma, M. A. Reddy, K. Ganesh, S. P. Singh and M. Chandrasekharam, *RSC Advances*, **2014**, 4, 732; r) R. Zhou, Q.-D. Li, X.-C. Li, S.-M. Lu, L.-P. Wang, C.-H. Zhang, J. Huang, P. Chen, F. Li, X.-H. Zhu, W. C. H. Choy, J. Peng, Y. Cao and X. Gong, *Dyes Pigm.*, **2014**, 101, 51.

5. A. Viterisi, F. Gispert-Guirado, J. W. Ryan and E. Palomares, *J. Mater. Chem.*, **2012**, 22, 15175.
6. a) G. Li, Y. Yao, H. Yang, V. Shrotriya, G. Yang and Y. Yang, *Adv. Funct. Mater.*, **2007**, 17, 1636; b) F.-C. Chen, C.-J. Ko, J.-L. Wu and W.-C. Chen, *Sol. Energy Mater. Sol. Cells*, **2010**, 94, 2426; c) G. Wei, S. Wang, K. Sun, M. E. Thompson and S. R. Forrest, *Adv. Energy Mater.*, **2011**, 1, 184; d) R. Hegde, N. Henry, B. Whittle, H. Zang, B. Hu, J. Chen, K. Xiao and M. Dadmun, *Sol. Energy Mater. Sol. Cells*, **2012**, 107, 112; e) E. Verploegen, C. E. Miller, K. Schmidt, Z. Bao and M. F. Toney, *Chem. Mater.*, **2012**, 24, 3923; f) H. Park, R. B. Ambade and S.-H. Lee, *J. Nanosci. Nanotechnol.*, **2013**, 13, 7975; g) B. Qu, D. Tian, Z. Cong, W. Wang, Z. An, C. Gao, Z. Gao, H. Yang, L. Zhang, L. Xiao, Z. Chen and Q. Gong, *J. Phys. Chem. C*, **2013**, 117, 3272.
7. A. Viterisi, F. Gispert-Guirado, J. W. Ryan and E. Palomares, *J. Mater. Chem.*, **2012**, 22, 15175.
8. J. Ajuria, S. Chavhan, R. n. Tena-Zaera, J. Chen, A. J. Rondinone, P. Sonar, A. Dodabalapur and R. Pacios, *Org. Electron.*, **2013**, 14, 326.
9. T. M. Clarke and J. R. Durrant, *Chem. Rev.*, **2010**, 110, 6736.
10. a) W. Shin, T. Yasuda, G. Watanabe, Y. S. Yang and C. Adachi, *Chem. Mater.*, **2013**, 25, 2549; b) V. S. Gevaerts, E. M. Herzig, M. Kirkus, K. H. Hendriks, M. M. Wienk, J. Perlich, P. Mueller-Buschbaum and R. A. J. Janssen, *Chem. Mater.*, **2014**, 26, 916.
11. The apparent decrease in crystalite size in active layers of derivative 1 upon longer annealing time is not deemed significant as the incertainty on crystalite size measurment is fairly high, 13 (+/- 3) nm and 19 (+/- 3 nm signifies that the size difference between the crystalites could be unsignificant.
12. a) D. M. DeLongchamp, R. J. Kline, D. A. Fischer, L. J. Richter and M. F. Toney, *Adv. Mater.*, **2011**, 23, 319; b) W. Chen, M. P.

Nikiforov and S. B. Darling, *Energy Environ. Sci.*, **2012**, 5, 8045; c) J. Rivnay, S. C. B. Mannsfeld, C. E. Miller, A. Salleo and M. F. Toney, *Chem. Rev.*, **2012**, 112, 5488.

13. A. Viterisi, N. F. Montcada, C. V. Kumar, F. Gispert-Guirado, E. Martin, E. Escudero and E. Palomares, *Journal of Materials Chemistry A*, **2014**, 2, 3536.
14. The packing of SQ units inside the crystallites is symbolized by the black lines. The orientation of the crystallites is depicted with the (001) and (010) (for the P-1 and P21/c phases respectively) planes parallel to the substrates as deducted from GIXRD analysis. The crystallites are shown embedded in an amorphous matrix of mixed donor and PC70BM molecules, however the ratio between amorphous and crystalline phases represented here only corresponds to a broad trend. The shape of the crystallites of derivative 2 and 4 was deduced from XRD and AFM measurements, while that of derivative 1,3 and 5 is not known.
15. a) D. S. Germack, A. Checco and B. M. Ocko, *ACS Nano*, **2013**, 7, 1990; b) Y. Vaynzof, D. Kabra, L. Zhao, L. L. Chua, U. Steiner and R. H. Friend, *ACS Nano*, **2010**, 5, 329; c) B. Ray and M. A. Alam, *Appl. Phys. Lett.*, **2011**, 99; d) W. Hu and D. Frenkel, in *Interphases and Mesophases in Polymer Crystallization III*, ed. G. Allegra, Springer Berlin Heidelberg, Editon edn., **2005**, vol. 191, pp. 1; e) G. Ruani, C. Fontanini, M. Murgia and C. Taliani, *J. Chem. Phys.*, **2002**, 116, 1713; f) D. T. W. Toolan, A. J. Parnell, P. D. Topham and J. R. Howse, *Journal of Materials Chemistry A*, **2013**, 1, 3587; g) M. A. Alam, B. Ray, M. R. Khan and S. Dongaonkar, *J. Mater. Res.*, **2013**, 28, 541; h) B. Ray and M. A. Alam, *Sol. Energy Mater. Sol. Cells*, **2012**, 99, 204.
16. R. H. Gee, N. Lacevic and L. E. Fried, *Nat. Mater.*, **2006**, 5, 39.
17. a) D. Motaung, G. Malgas, S. Nkosi, G. Mhlongo, B. Mwakikunga, T. Malwela, C. Arendse, T. G. Muller and F. Cummings, *J. Mater. Sci.*, **2013**, 48, 1763; b) G. Fang, S. Wu, Z. Xie, Y. Geng and L. Wang, *Macromol. Chem. Phys.*, **2011**, 212, 1846; c) D. E. Motaung, G. F. Malgas, C. J. Arendse and T. Malwela, *Mater. Chem. Phys.*, **2010**, 124, 208; d) S. O. Jeon, K. S. Yook and J. Y. Lee, *Org. Electron.*, **2009**, 10, 1583.
18. R. W. Balluffi, S. Allen and W. C. Carter, *Kinetics of Materials*, Wiley, **2005**.
19. a) G. De Luca, A. Liscio, P. Maccagnani, F. Nolde, V. Palermo, K. Müllen and P. Samorì, *Adv. Funct. Mater.*, **2007**, 17, 3791; b) G. De Luca, A. Liscio, F. Nolde, L. M. Scolaro, V. Palermo, K. Mullen and P. Samori, *Soft Matter*, **2008**, 4, 2064; c) E. Treossi, A. Liscio, X. Feng, V. Palermo, K. Müllen and P. Samorì, *Small*, **2009**, 5, 112; d) G. De Luca, A. Liscio, M. Melucci, T. Schnitzler, W. Pisula, C. G. Clark, L. M. Scolaro, V. Palermo, K. Mullen and P. Samori, *J. Mater. Chem.*, **2010**, 20, 71; e) G. De Luca, E. Treossi,

A. Liscio, J. M. Mativetsky, L. M. Scolaro, V. Palermo and P. Samori, *J. Mater. Chem.*, **2010**, 20, 2493.

20. L. A. Perez, K. W. Chou, J. A. Love, T. S. van der Poll, D.-M. Smilgies, T.-Q. Nguyen, E. J. Kramer, A. Amassian and G. C. Bazan, *Adv. Mater.*, **2013**, 25, 6380.
21. The pparent decrease in crystalite size in active layers of derivative 1 upon longer annealing time is not deemed significant as the incertainty on crystalite size measurment is fairly high, 13 (+/- 3) nm and 19 (+/- 3 nm signifies that the size difference between the crystalites could be unsignificant.
22. a) C. G. Shuttle, A. Maurano, R. Hamilton, B. O'Regan, J. C. de Mello and J. R. Durrant, *Appl. Phys. Lett.*, **2008**, 93, 183501; b) C. G. Shuttle, B. O'Regan, A. M. Ballantyne, J. Nelson, D. D. C. Bradley and J. R. Durrant, *Phys. Rev. B*, **2008**, 78, 113201; c) R. Hamilton, C. G. Shuttle, B. O'Regan, T. C. Hammant, J. Nelson and J. R. Durrant, *J. Phys. Chem. Lett.*, **2010**, 1, 1432; d) F. C. Jamieson, T. Agostinelli, H. Azimi, J. Nelson and J. R. Durrant, *J. Phys. Chem. Lett.*, **2010**, 1, 3306; e) A. Maurano, R. Hamilton, C. G. Shuttle, A. M. Ballantyne, J. Nelson, B. O'Regan, W. Zhang, I. McCulloch, H. Azimi, M. Morana, C. J. Brabec and J. R. Durrant, *Adv. Mater.*, **2010**, 22, 4987; f) D. Credgington, R. Hamilton, P. Atienzar, J. Nelson and J. R. Durrant, *Adv. Funct. Mater.*, **2011**, 21, 2744; g) D. Credgington, Y. Kim, J. Labram, T. D. Anthopoulos and J. R. Durrant, *J. Phys. Chem. Lett.*, **2011**, 2, 2759; h) A. Maurano, C. C. Shuttle, R. Hamilton, A. M. Ballantyne, J. Nelson, W. Zhang, M. Heeney and J. R. Durrant, *J. Phys. Chem. C*, **2011**, 115, 5947; i) D. Credgington and J. R. Durrant, *J. Phys. Chem. Lett.*, **2012**, 3, 1465; j) D. Credgington, F. C. Jamieson, B. Walker, N. Thuc-Quyen and J. R. Durrant, *Adv. Mater.*, **2012**, 24, 2135; k) G. F. A. Dibb, F. C. Jamieson, A. Maurano, J. Nelson and J. R. Durrant, *J. Phys. Chem. Lett.*, **2013**, 4, 803.
23. a) M. P. Eng, P. R. F. Barnes and J. R. Durrant, *J. Phys. Chem. Lett.*, **2010**, 1, 3096; b) C. G. Shuttle, R. Hamilton, J. Nelson, B. C. O'Regan and J. R. Durrant, *Adv. Funct. Mater.*, **2010**, 20, 698; c) C. G. Shuttle, R. Hamilton, B. C. O'Regan, J. Nelson and J. R. Durrant, *Proc. Natl. Acad. Sci. USA*, **2010**, 107, 16448; d) D. Spoltore, W. D. Oosterbaan, S. Khelifi, J. N. Clifford, A. Viterisi, E. Palomares, M. Burgelman, L. Lutsen, D. Vanderzande and J. Manca, *Adv. Energy. Mater.*, **2013**, 3, 466.
24. a) R. C. I. MacKenzie, T. Kirchartz, G. F. A. Dibb and J. Nelson, *J. Phys. Chem. C*, **2011**, 115, 9806; b) T. Kirchartz, B. E. Pieters, J. Kirkpatrick, U. Rau and J. Nelson, *Phys. Rev. B*, **2011**, 83, 115209.
25. T. Kirchartz and J. Nelson, *Phys. Rev. B*, **2012**, 86, 165201.
26. a) S. Ferdous, F. Liu, D. Wang and T. P. Russell, *Adv. Energy. Mater.*, **2014**, 4, n/a; b) B. Walker, A. Tamayo, D. T. Duong, X.-D. Dang, C. Kim, J. Granstrom and T.-Q. Nguyen, *Adv. Energy. Mater.*, **2011**, 1, 221; c) D. T. Duong, B. Walker, J. Lin, C. Kim, J.

Love, B. Purushothaman, J. E. Anthony and T.-Q. Nguyen, *Journal of Polymer Science Part B: Polymer Physics*, **2012**, 50, 1405; d) M. A. Ruderer and P. Müller-Buschbaum, in *Polymers for Energy Storage and Conversion*, John Wiley & Sons, Inc., Editon edn., **2013**, pp. 137.

27. a) S. A. Hawks, F. Deledalle, J. Yao, D. G. Rebois, G. Li, J. Nelson, Y. Yang, T. Kirchartz and J. R. Durrant, *Adv. Energy Mater.*, **2013**, 3, 1201; b) A. Baumann, T. J. Savenije, D. H. K. Murthy, M. Heeney, V. Dyakonov and C. Deibel, *Adv. Funct. Mater.*, **2011**, 21, 1687; c) A. Maurano, C. G. Shuttle, R. Hamilton, A. M. Ballantyne, J. Nelson, W. Zhang, M. Heeney and J. R. Durrant, *J. Phys. Chem. C*, **2011**, 115, 5947; d) G. F. A. Dibb, F. C. Jamieson, A. Maurano, J. Nelson and J. R. Durrant, *J. Phys. Chem. Lett.*, **2013**, 4, 803; e) F. C. Jamieson, T. Agostinelli, H. Azimi, J. Nelson and J. R. Durrant, *J. Phys. Chem. Lett.*, **2010**, 1, 3306; f) C. Deibel, T. Strobel and V. Dyakonov, *Phys. Rev. Lett.*, **2009**, 103, 036402(1); g) C. G. Shuttle, R. Hamilton, B. C. O'Regan, J. Nelson and J. R. Durrant, *Proc. Natl. Acad. Sci. U. S. A.*, 2010, 107, 16448.
28. D. Credgington, F. C. Jamieson, B. Walker, T.-Q. Nguyen and J. R. Durrant, *Adv. Mater.*, **2012**, 24, 2135.
29. a) V. Coropceanu, J. Cornil, D. A. da Silva Filho, Y. Olivier, R. Silbey and J.-L. Brédas, *Chem. Rev.*, **2007**, 107, 926; b) H. Dong, X. Fu, J. Liu, Z. Wang and W. Hu, *Adv. Mater.*, 2013, 25, 6158; c) M. Mas-Torrent and C. Rovira, *Chem. Rev.*, **2011**, 111, 4833.
30. J. Rivnay, L. H. Jimison, J. E. Northrup, M. F. Toney, R. Noriega, S. Lu, T. J. Marks, A. Facchetti and A. Salleo, *Nat. Mater.*, **2009**, 8, 952.
31. S. J. Kang, S. Ahn, J. B. Kim, C. Schenck, A. M. Hiszpanski, S. Oh, T. Schiros, Y.-L. Loo and C. Nuckolls, *J. Am. Chem. Soc.*, **2013**, 135, 2207.
32. P. Clancy, *Chem. Mater.*, **2011**, 23, 522.
33. Y. Matsuo, Y. Sato, T. Niinomi, I. Soga, H. Tanaka and E. Nakamura, *J. Am. Chem. Soc.*, **2009**, 131, 16048.

Chapter 6

Building a machine learning model for the prediction of electrical properties in small molecule organic solar cells

Table of Contents

Motivation

Early on in the development of organic solar cells it became evident that electrical device properties could not be easily derived from molecular structures.[1] Although initially some simple molecular properties like the HOMO-LUMO gap were deemed important for the achievement of high power conversion efficiencies[2], it was soon clear that this assumption was simplistic and did not account for other material properties that are fundamental for device improvement.

Computational design efforts then drifted away from the simple calculation of orbital energies and into more complicated bulk material properties, such as charge mobility.[3] Since most efforts to develop better devices were centered around the production of better donor molecules, there were some large and coordinated efforts to go deeper into the relationship between molecular structure and device properties.[4,5] These efforts finally gave birth to the Harvard Clean Energy Project[6], whose goal is to predict device properties from any given proposed molecular structure. This project had an original focus in the development of better materials for polymer solar cells, with no specific efforts towards the prediction of device properties for small molecule devices.

Through the past few years this focus in the development of predictive models for the creation of better polymer solar cells has been prevalent, with many efforts directed towards this area.[7–11] This published work has included the use of genetic algorithms with multiple filtering stages[8], molecular DFT/TD-DFT calculations[9,10] and simple 2D/3D molecular descriptors.[4] However there are no publications, to the best of our knowledge, that explicitly attempt to model the relationship between donor molecule characteristics and device electrical properties in small molecule organic solar cells.

Since single molecule entities can be obtained in pure form, have more easily tunable molecular properties, are more easily modeled using computational methods and have a wide array of available experimental results[12], we decided to design a predictive statistical model that could relate the electrical properties of organic small molecule solar cells with those of small molecule donors. Our idea is

therefore to establish a statistical model using molecular properties to yield reasonable predictions for device efficiency, open circuit potential, short circuit current and fill factor. To do this we attempted to build models using both simple 2D molecular descriptors and descriptors derived from DFT calculations.

It is also our hope that by analyzing the statistical models produced we should be able to draw some light into the relationship between different molecular properties and their relative importance in predicting device properties. In this manner we should not only be able to make predictions but we should also be able to tell which aspects of a molecule are more important and in what ways they relate to each another.

Database Building

In order to build the proposed statistical models we first constructed a database of small molecule organic donors that contained both their experimental device performance and the chemical descriptors used to make predictions. To reach this point we first built a database comprised of 198 small molecule donor structures (in SMILES format) and their Voc, Jsc, FF and PCE were taken from two published reviews[12,13] as well as several individual articles.[14–16] Care was taken so that small molecule donors were not repeated within the database. Additionally we only selected devices produced using $PC_{61}BM$ as an electron acceptor within a solution processed bulk-heterojunction structure since solar cells using a bi-layer configuration or produced through thermal evaporation might require different molecular properties to reach high efficiencies. We kept more recently published molecules[17–19] outside of the database in order to use them to test our model's predictive capacity out of sample.

To build our simple 2D descriptors from these structures we converted our SMILES connectivity files to jmol2 structure files using openBabel[20] which were then processed by the PaDEL software[21] to generate 1000 different chemical descriptors. From these descriptors we eliminated all those that did not produce information or produced inaccurate information (NaN, infinity, etc) for any given molecule within the database. We took care not to eliminate any molecule from

the database in order to avoid losing chemical diversity but instead we removed descriptors until we were left with those that could be calculated accurately for our entire donor database. By applying this filterting, 131 descriptors were kept in the database.

These descriptors include values for the number of aromatic bonds and atoms (naAromAtom, nAromBond), polarizability (bpol), hybridization (HybRatio), information content (ICN, TICN, etc), largest chain (nAtomLC), largest π system (nAtomP), largest aliphatic chain (nATomLAC), path counts (MPCN, piPCN), Petijean Number, number of rotatable bonds (nRotB, RotBFrac, nRotBt, RotBtFrac), topological radius, diameter, shape and charge (topoRadius, topoDiameter, topoShapem GGIN, JGIN), walk counts (MWCN, SRWN), Wiener numbers (WPATH, WPOL) and the Zagreb Index (Zagreb).

For the generation of 3D structures we attempted automatic generation of XYZ files from SMILES using openBabel and when this was not possible (generated files had overlapping atoms or generation was not successful) we manually generated the files using Gabedit.[22] We then proceeded to optimize the geometries in ADF 2013[23] using a standard TZP basis set with a GGA Becke-Perdew functional[24]. These geometries were then used for the calculation of electronic properties and the σ-profiles using the same basis set and function. For the calculation of the σ-profiles we used the suggested default parameters within the ADF manual. We made no efforts to optimize molecule conformations and used the default conformations produced from the automatic or manual generation process.

When generating 3D structures and electronic properties we had to eliminate molecules that were either too complex for practical calculation at the level of theory used, or that were not generated properly so convergence problems arose. This meant that our original database of 198 molecules was reduced to 91 molecules when using descriptors from DFT calculations (all molecules were kept when using 2D descriptors).

Machine Learning Model

Model selection

Many different model types can be used in the construction of quantitative relationships between chemical descriptors and experimental properties (QSPR).[25] In the area of photo-voltaics there are a few examples of machine learning where generally multi-step models with significant input preprocessing steps are needed to achieve useful results.[26,27] Simpler models with little input preprocessing such as logistic regression using simple descriptors have been used to predict electric properties of polymer solar cells[4] but these published models lacked proper out of sample validation since only results within the training set were used for the evaluation of model accuracy.

Since we wanted to use a model that allowed us to completely avoid input preprocessing steps while allowing for the large dimensionality of the problem we decided to use a random forest classifier for the prediction of device properties. We used the random forest classifier as implemented within the R[28] random forest library[29].

Random forests have been used successfully to solve a significant variety of problems in chemistry.[30–33] They have the advantage of being accurate, resistant to curve fitting, immune to the inclusion of irrelevant or correlated descriptors, immune to high dimensionality and computationally cheap.[34–36] In addition variable importance measurements can be extracted from a random forest model,[37] allowing for model interpretation beyond what can be achieved when using other classifiers such as neural networks or support vector machines.

Model Training and validation

A machine learning algorithm can only be properly validated when tested on data that was not used within the model generation process. A good model should show a very small increment in mean square error when going from training data to testing data. This means that available data must be split into two groups, a training set and a testing set, with the training set used for model construction and the testing set used for model validation.

Our database includes a wide variety of different molecular families that need to be adequately represented within the training data if any type of generalization for property prediction is to be expected from the generated models. In order to eliminate any bias that might be present from manual training set selection we used the caret package in R to randomly split our database into a training set (containing 80% of the data points) and a testing set (containing 20% of the data points) where the variable to be predicted is equally distributed across both samples. We then generated a random forest model (with 2000 trees) and measured the mean square errors within the testing sets. We repeated this process 2000 times and stayed with the database division and model that generated the least error within the testing set. This process ensured that we always produced a model that has a good capability to generalize outside of the training set, as the testing set was not used within the model construction step. Additionally we then tested the models over several molecules not included within the initial database to allow for a final cross validation of our machine learning process.

Model Results

Models based on 2D descriptors

In our first attempt to build a machine learning model we wanted to see if we could obtain accurate predictions for electric properties without the need for computationally expensive calculations or information from 3D structures. Using the 131 valid 2D chemical descriptors generated from PaDEL we constructed random forest models for the prediction of the Voc, Jsc, FF and PCE using the previously described procedure. Figure 1 shows the predicted and experimental values for the four models generated for the training set and the testing set while Table 1 shows the mean square errors for both sets within the final models.

	MSE Training Set	MSE Testing Set	MSE increase (%)
PCE (%)	0.630	1.090	73.02
Voc (V)	0.073	0.090	23.29
Jsc (mA/cm^2)	1.400	2.060	47.14
FF	0.052	0.069	32.69

Table 1. Mean square errors within the testing and training sets for random forest models built with 2D descriptors.

The plots obtained in Figure 1 already show a very low tendency of the models to over fit as we don't see an extremely low error for predictions within the training set despite the large number of predictors used. As it is expected we do see an increase in errors when going from the training set to the testing set, with the PCE testing set showing the largest increase in error at +73.02% compared to the training set. Not surprisingly the potential shows the lowest error increase when going from the training set to the testing set (+23.29%). This is to be expected as potential values have the narrowest frequency distribution and therefore even guesses towards the average are bound to get a small error. That said there is in fact a case within the testing set where the potential is predicted with a less than 10% error, even though its value is more than 20% away from the average.

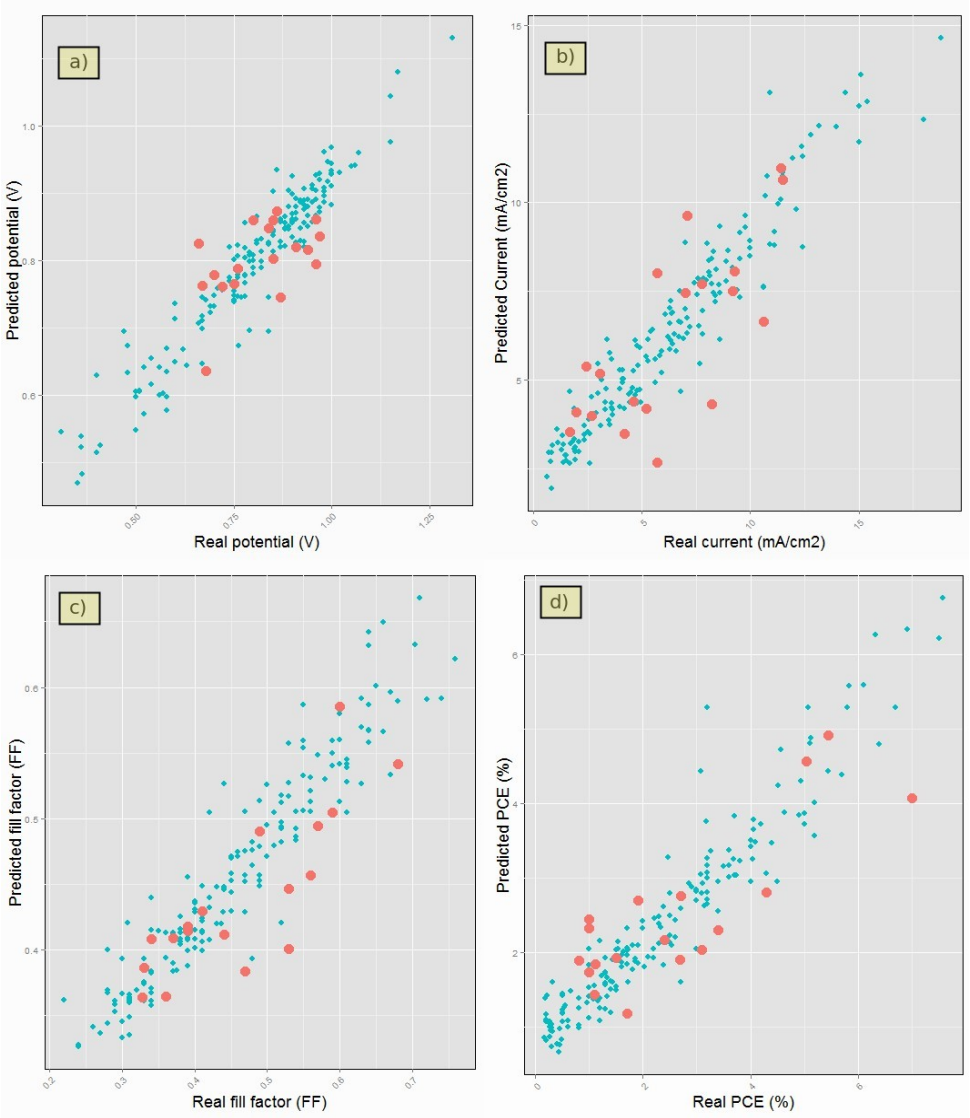

Figure 1. Predicted versus experimental values for the 4 different models created to predict Voc, Jsc, FF and PCE for the training sets (blue) and testing sets (red).

It is also interesting to study the accuracy of predictions at high PCE, fill factor and current values since these are the most interesting cases from a practical point of view. There are three cases where devices have a PCE above 5% within the testing set and model predictions are off by -9.5%, -9.5% and -41.7%. In all cases we seem to underestimate the efficiency for highly efficient devices while we overestimate for devices with low experimental efficiencies. In fact all cases where efficiencies are overestimated in the above model have an efficiency below the 2% mark. This points to an averaging effect where our results are skewed towards the average of the training set. The same effect can be observed for Jsc and FF values although we still have significantly accurate predictions for devices where high values are expected. The two highest Jsc values in the testing set are predicted with errors of -7.3% and -3.7% while the highest FF values are predicted with errors of -19.1% and -2.3%.

	PCE	Voc	Jsc	FF
1	RotBtFrac	ZMIC0	SRW9	RotBFrac
2	RotBFrac	TIC0	nAtomP	RotBtFrac
3	SRW9	RotBFrac	BIC1	nAtomP
4	CIC4	RotBtFrac	GGI6	HybRatio
5	SRW5	TIC4	RotBtFrac	nAtomLC
6	SRW7	MIC5	GGI3	GGI7
7	bpol	Kier3	BIC5	GGI6
8	HybRatio	SIC5	HybRatio	MIC1
9	JGI9	CIC3	JGI5	topoDiameter
10	IC5	SRW7	GGI10	TIC1

Table 2. Top ten descriptors ranked by importance for the 4 different models constructed to predict PCE, Voc, Jsc and FF.

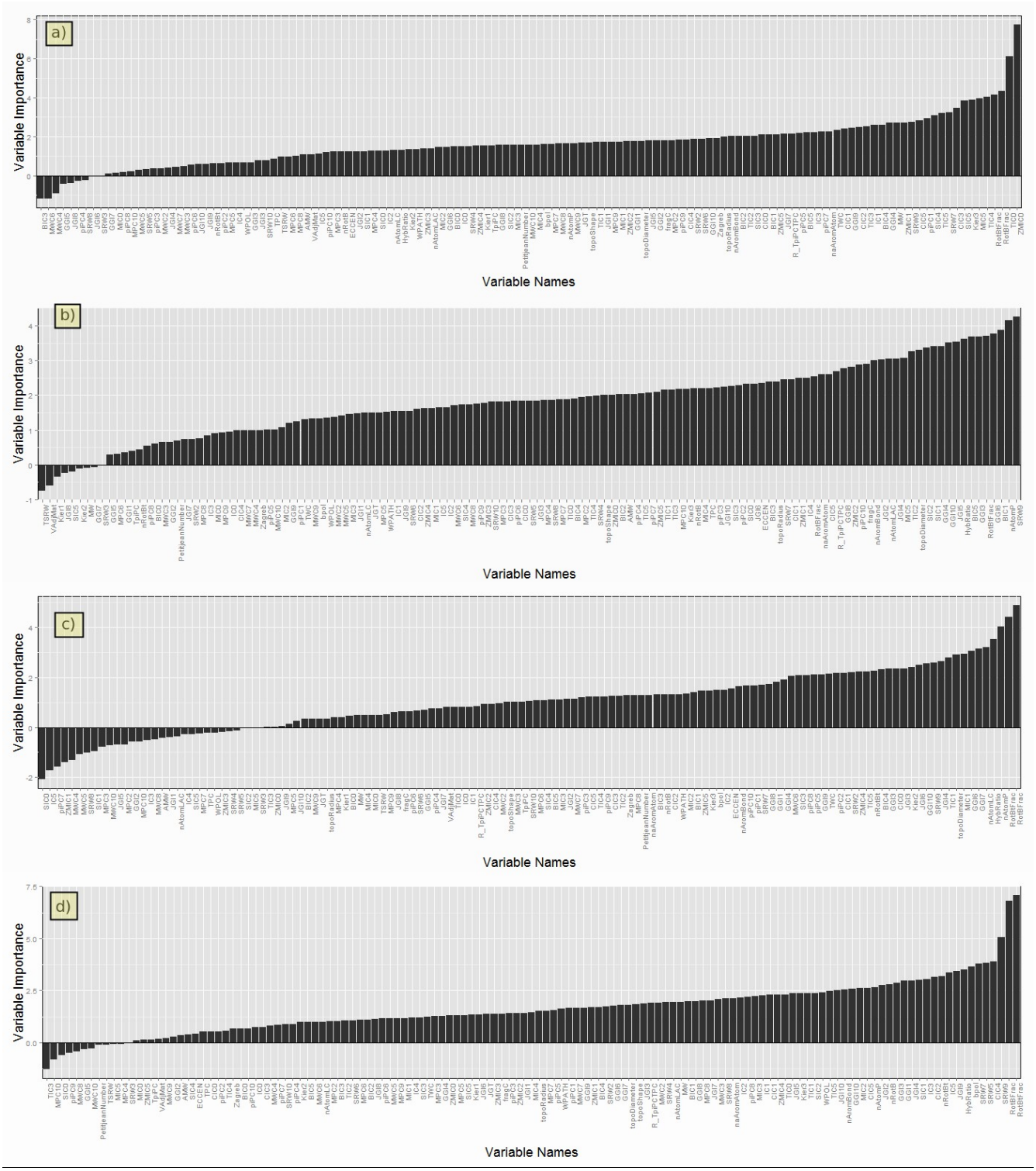

Figure 2. Descriptor importance for the 4 different models created to predict Voc(a), Jsc(b), FF(c) and PCE(d) suing 2D descriptors.

The models also give us important information about what molecular predictors

are important. Figure 2 shows the variable importance extracted from each one of the four models constructed. Table 2 shows the 10 most important variables for each model according to this ranking, where number 1 is the most important input. Variable names are those given by the PaDEL program for each descriptor.

For the PCE model we have that the most important variables are RotBtFrac and RotBFrac which describe the number of rotatable bonds within a molecule as a fraction of all bonds and all bonds except those involving hydrogen. This makes intuitive sense since we expect the size of conjugated systems and their relationships with alkyl chains to play a pivotal role in determining how well a molecule will behave within a solar cell. The SRW9, SRW5 and SRW7 variables that follows are walk count descriptors which are related in general with molecule complexity and size, more complex, less symmetric and more ramified molecules are expected to have higher values for these descriptors. The CIC4 is an information content descriptor related with the number of terminal vertices within a molecule and bpol and the HybRatio descriptors are related with molecule polarity and the hybridization ratio (the total fraction of sp2 carbons compared with the total number of carbons).

As the reader can see the overall description makes sense as it is relating variables that we would naturally consider important for a molecule within a bulk-heterojunction device. Some of these variables are also indirectly related with the HOMO/LUMO gap (those related with the extension of conjugated systems) while others are more related with aspects that would have more to do with morphological behavior (molecule complexity, ramification, vertices, etc). Some relationships between descriptor importance values also appear to make sense, for example we expect the fraction of rotatable bonds to be much more important than the absolute number of rotatable bonds, since we expect the proportion between the conjugated and non-conjugated parts of a molecule to be more relevant than the absolute size of the non-conjugated part of a molecule. We in fact observe that nRotBt is less important than RotBFRac and RobBtFrac.

In the case of the Voc model we have some different descriptors coming into play although some inputs like RotBFrac, RotBtFrac and SRW7 are shared with the PCE

model. The descriptors ZMIC0, TIC0, TIC4 and MIC5 are information content values describing topological distances although the PaDel manual is not very clear in their actual origin. Kier3 is a third order Kappa Shape index which is a descriptor designed to characterize a molecular shape by comparing it to an extreme shape (the linear molecule and the completely connected graph). In the case of a third order index, three bond paths are used to build the descriptor[38].

When looking at the Jsc we also see a significant presence of different information content descriptors (BIC1, GGI6, GGI3, BIC5, JGI5, GGI10) while we also see the SR29, RotBtFrac and HybRatio variables as we saw in the PCE model. Interestingly we also see the appearance of the nAtomP variable, which describes the number of atoms in the largest pi system within the molecule. Since charge density has a significant relationship with charge mobility and charge mobility has a significant relationship with pi system size, it makes perfect sense for the nAtomP descriptor to be of a large importance within the model that predicts Jsc.

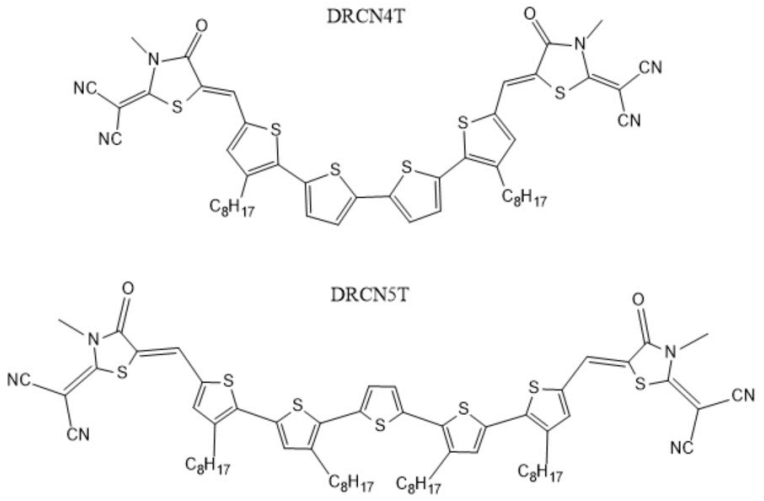

Figure 3. Chemical structure representations for the molecules used for model validation.

Interestingly the fill factor model, in terms of variable importance, looks like a mixture between the Jsc and the PCE models, as we would intuitively think would happen. The RotBFrac and RotBtFrac are the most important variables in both models while the nAtomP and HybRatio descriptors play a much more important role when predicting the FF. In this case we can also see the nAtomLC descriptor

take importance, which describes the largest chain within a molecule.

After we examined our models and how they behaved within their training and testing sets we decided to test some molecules which were not within our original database. This exercise would allow us to see how well our models are able to generalize outside of their initial training/testing universe. In order to test for this we used data for two molecules named DRCN5T and DRCN4T (Figure 3) from a recent publication[17]. Although both molecules belong to the same family of oligothiophenes, DRCN5T gives a PCE of more than 10% while DRCN4T is said to give very poor performance due to its lower conjugation length. In general any model worth using for real molecular screening should be able to easily tell that DRCN5T is a great candidate while DRCN4T is not. Our models fail to predict a high efficiency for DRCN5T (predicting a PCE of 2.3%) while they do predict a low PCE of 2.01% for DRCN4T. Current density values are also wrong by more than -50% for DRCN5T (15.66 experimental, 6.00 predicted) and fill factor values are also grossly underestimated (0.68 experimental, 0.46 predicted).

This failure to generalize comes from the fact that these first models are based on very simple descriptors that fit a rather narrow behavior within the molecules used to construct the models. As soon as you introduce donor or acceptor moieties that are not a part of the original database you get significant deviations in predictions. This is of very limited usefulness for the prediction of high PCE devices as it implies that the models are not able to generalize behavior outside of a rather narrow initial population. Since the end objective would be to predict electrical properties for devices using molecules containing previously untested moieties, being unable to do this seriously hinders the practical usefulness of the proposed models.

Models based on DFT derived descriptors

Since our first models created using 2D descriptors failed to provide enough generalization to be considered useful for the prediction of device properties using novel molecules we decided to explore the construction of new models based on information derived from DFT calculations. Since 2D descriptors fail to explicitly capture information about a molecule's electronic structure the inclusion of

descriptors that explicitly address electronic properties would in theory allow us to enhance our model performance. It is worth remembering that our database for DFT calculations includes only 91 molecules as mentioned previously.

Since device performance is related with donor/acceptor interactions and donor optoelectronic properties we decided to use DFT descriptors that were both computationally cheap to obtain and allowed us to describe the above two aspects accurately. We therefore decided to use orbital energy information (HOMO-1, HOMO, LUMO, LUMO+1) as well as the σ-profile (discretized up to 50 points) derived from COSMO calculations. The σ-profile contains information derived from the charge distribution in the molecular surface, and this is relevant to intra-molecular interactions. The σ-profiles have been used extensively for the prediction of thermodynamic properties of complex systems from the COSMO calculations of individual, independent molecules by using COSMO-RS theory.[9] We explicitly avoided the use of TD-DFT calculations that could provide additional information about donor optoelectronic properties as we wanted to avoid the high computational costs associated with the calculation of these descriptors. However it is clear that the inclusion of TD-DFT descriptors would be a viable direction for future work.

	MSE Training Set	MSE Testing Set	MSE increase(%)
PCE (%)	0.632	0.831	31.50
Voc (V)	0.087	0.097	11.49
Isc (mA/cm^2)	1.530	1.640	7.19
FF	0.052	0.089	71.15

Table 3. Mean square errors within the testing and training sets for random forest models built with DFT descriptors.

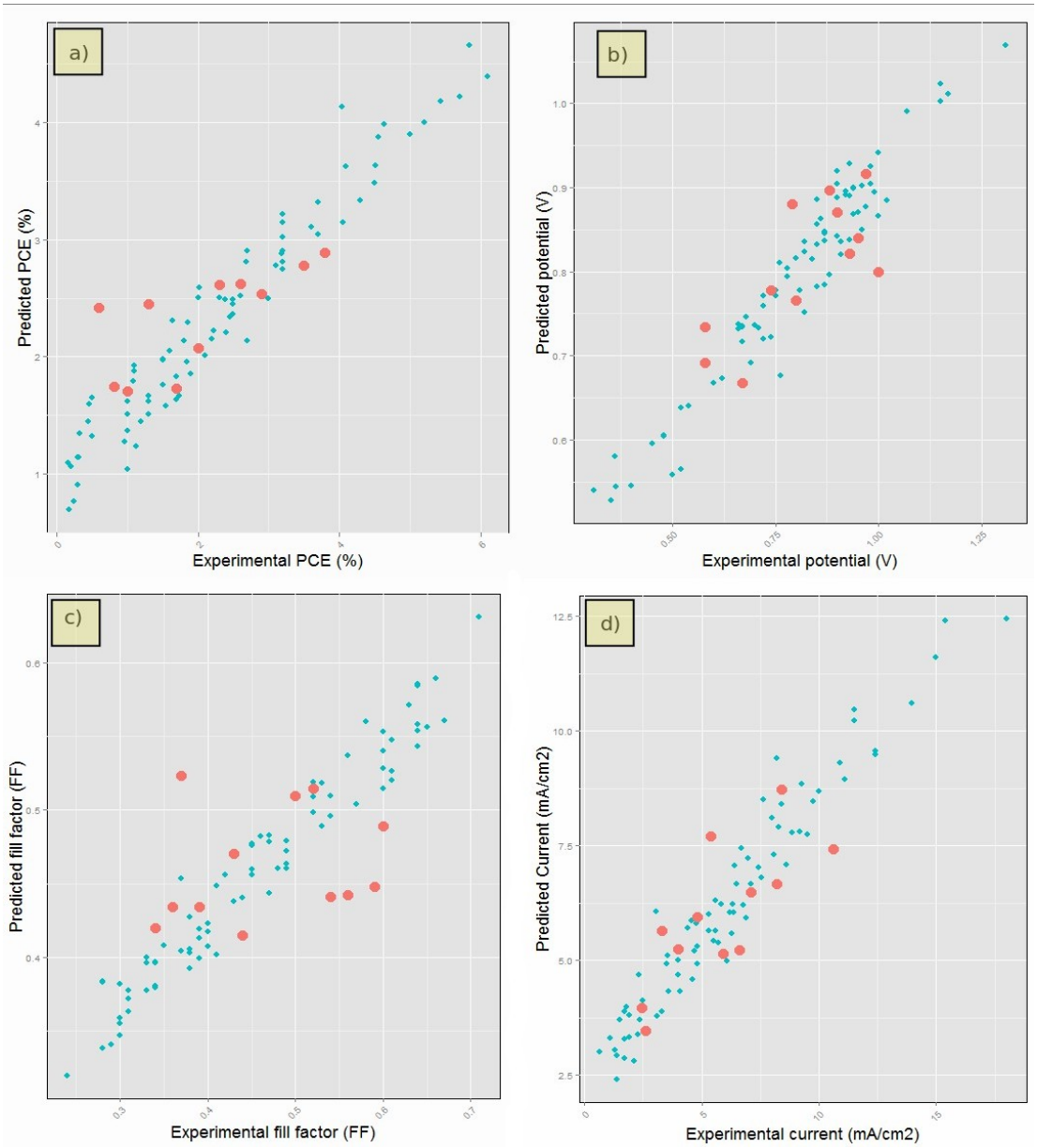

Figure 4. Predicted and experimental values for the 4 different DFT descriptor based models created to predict Voc, Jsc, FF and PCE for the training sets (blue) and testing sets (red).

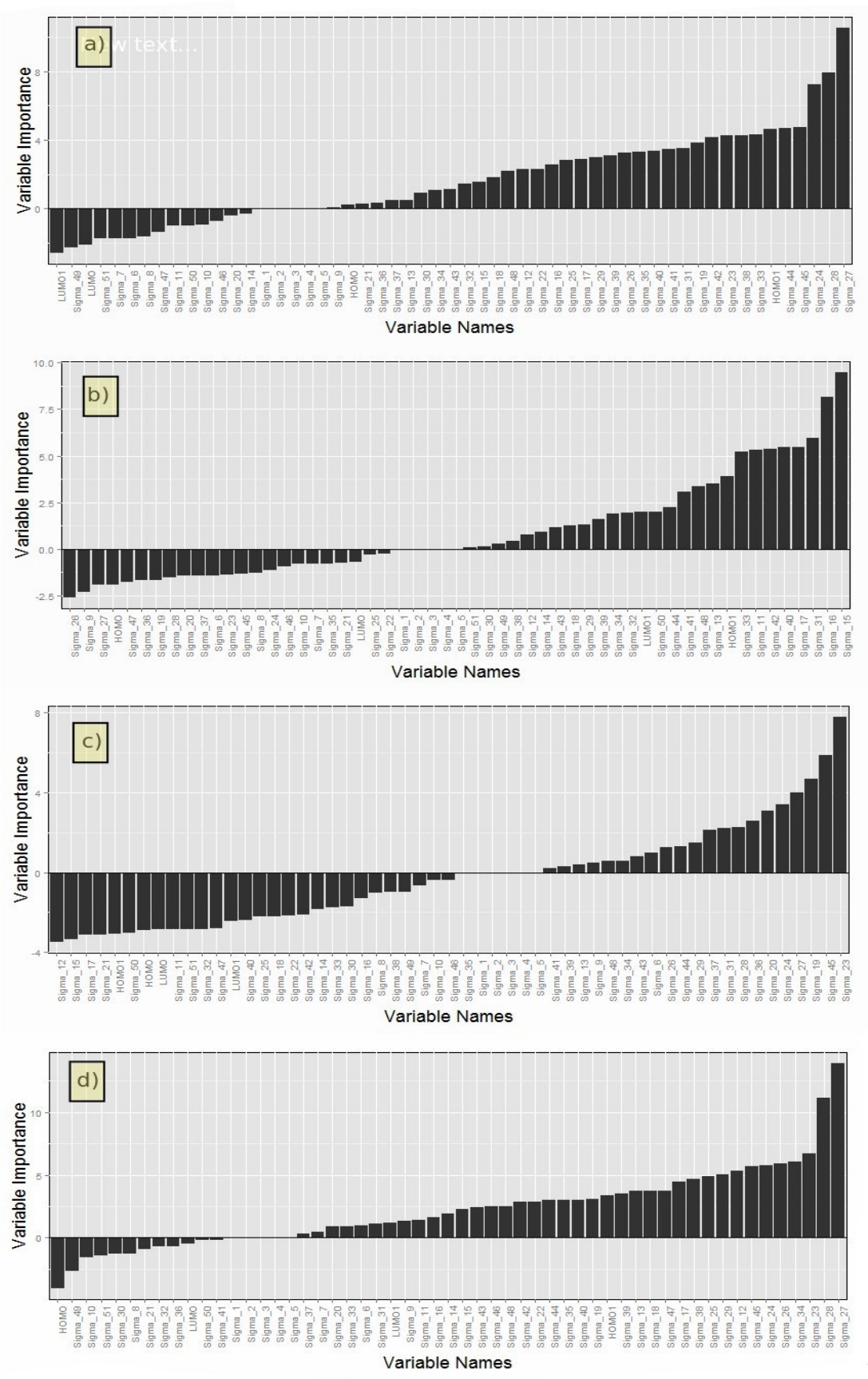

Figure 5. Descriptor importance for the 4 different models created to predict

PCE(a), Voc(b), FF(c) and Jsc(d) using DFT descriptors.

As it can be seen on Figure 4 the new models show a good ability to make predictions within the training sets and testing sets on all properties except the FF. Table 3 shows that the MSE difference between training sets and testing sets is actually much smaller than for the 2D descriptor models, with only the FF showing a dramatic increase in MSE when changing to the testing set. Absolute values for the MSE within the testing set have a lower magnitude in our DFT based models for the PCE and the Jsc, while the values are larger for the Voc and the FF. However it is important to mention here that our DFT models use only 54 variables while the 2D descriptor models used 131 variables. The size of the database is also much smaller with 91 molecules for the DFT models and 198 molecules for the 2D descriptor models. Our DFT models are therefore able to achieve similar absolute errors in the testing sets with a much lower increase between the training and the testing set using a much smaller amount of available data and a lower number of descriptors. This points to the fact that the DFT based models achieve a more important level of generalization when compared to the models based on 2D descriptors.

	PCE	Voc	Jsc	FF
1	σ-27	σ-15	σ-27	σ-23
2	σ-28	σ-18	σ-28	σ-45
3	σ-24	σ-31	σ-23	σ-19
4	σ-45	σ-17	σ-34	σ-27
5	σ-44	σ-40	σ-26	σ-24

Table 4. Top five descriptors ranked by importance for the 4 different models constructed to predict PCE, Voc, Jsc and FF using DFT derived descriptors.

In analogy with our 2D descriptor based models we can also evaluate variable importance within our models using DFT derived variables. Figure 5 shows all variable importance values while Table 4 shows the top 5 descriptors ranked by importance for the 4 different models. As you can see the orbital energy information fails to reach a very large importance within our models, even in the Voc model, which is rather interesting considering that the HOMO/LUMO gap is expected to be highly correlated with the device Voc. As a matter of fact the Voc model does show the HOMO-1 and LUMO+1 energies to be of a larger importance

than the HOMO or LUMO energies. This highlights the fact that the Voc is not a unique consequence of the difference between independent donor and acceptor frontier orbital levels but a consequence of the difference between the fermi levels of the interacting materials which depend heavily on the interaction between the donor and acceptor. This may explain why the Voc can be predicted in terms of information that is better related to molecular interactions (the σ-profile) rather than on orbital energy information.

It is also interesting to go deeper into the importance of the different σ-profile descriptors and what they may be telling us about the building of better donor molecules for organic solar cells. In order to do this it is useful to divide the σ-profile into regions that are typically populated by H-donors σ(1-18), non-polar σ(18-33) and H-acceptor σ(34-51) molecules as it has already been described in the literature.[40]

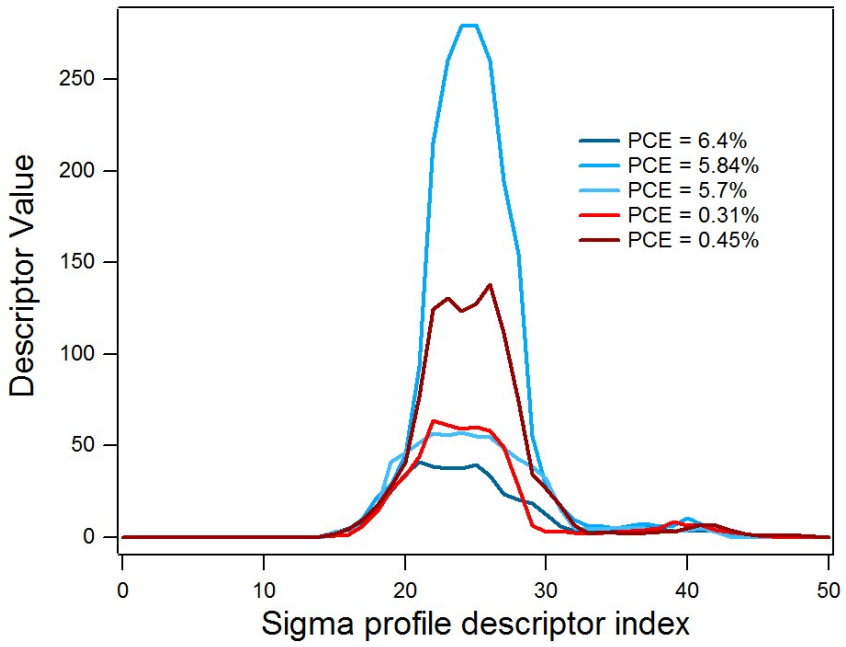

Figure 6. Sigma profile plots for donor molecules yielding devices with high and low PCE values.

In the case of the PCE, FF and Jsc the most important factors are located in the non-polar and H-acceptor regions. This makes sense if you look at the σ-profiles of the most and least efficient molecules within the DFT descriptor database (Figure

6) as the difference between these molecules is most apparent within the non-polar and H-acceptor regions while difference in the H-donor region are small since most molecules have sparse contributions within this area. This makes sense as all donors conform to some minimum common standards (such as solubility in the same organic solvents as the acceptor) which constraints the possibilities within the H-donor region of the σ-profile. Differences in efficiencies are therefore largely related with differences in the non-polar and H-acceptor regions of the σ-profile although these relationships are not linear.

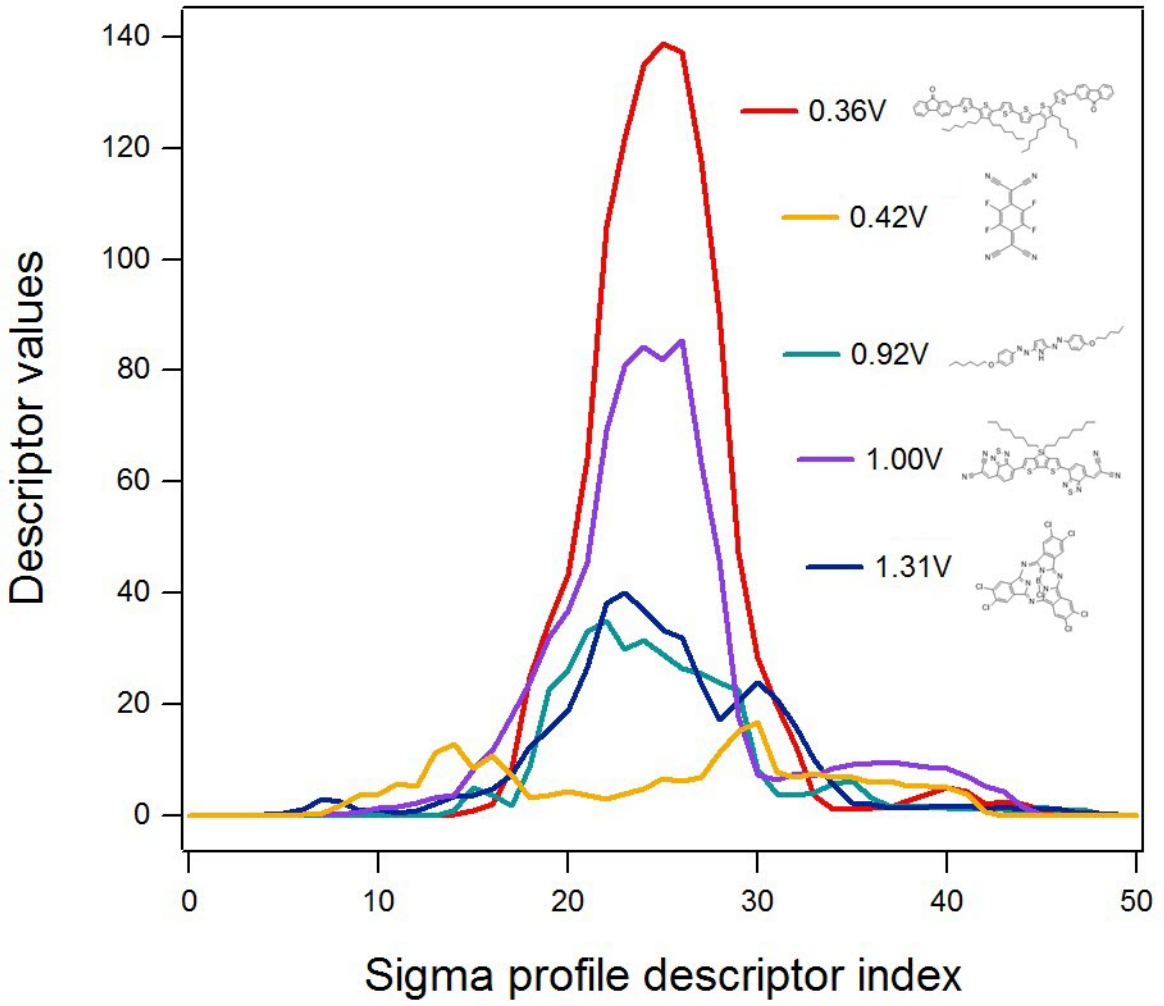

Figure 7. Sigma profile plots for donor molecules yielding devices with high and low open circuit voltages.

The Voc follow a more complicated behavior as we see that the most important variables belong to the three main regions of the σ-profile. This happens because

molecules with very different σ-profiles can lead to a similar Voc. Figure 7 shows 5 molecules σ-profiles where you can see this effect. In this case three molecules with Voc values above 0.9V have differences that are significant across the entire σ-profile. Donors leading to low Voc values also show this effect.

By looking at the importance measurements for the PCE, Jsc and FF we can also notice that the most important region within the σ-profile is the non-polar σ(18-33) descriptor region, as several descriptors within this region are shared between the three models. This also makes intuitive sense as the charge mobility and donor/acceptor domain separation properties for the molecules within our database are mainly mediated by non-polar interactions (such as pi-pi stacking).

The final test for our DFT descriptor based model is also to test it with molecules that are outside of the testing/training database used for initial model evaluation. For this purpose we also used molecules DRCN4T and DRCN5T as we did for our initial 2D descriptor based model. In this case we obtained a higher PCE prediction for DRCN5T at 3.52% although still far away from the experimentally achieved PCE of 9.8%. In the case of DRCN4T we did predict a lower efficiency of 3.14% and a lower fill factor and current in agreement with experimental results. Our fill factor and current density predictions for DRCN5T are still below experimental values by magnitudes similar to those of the 2D descriptor model predictions. However it is very interesting to note that our Voc prediction was actually very accurate, predicting a potential of 0.92V for the molecule, which is the exact experimental value.

Explaining model results

Both our 2D and DFT descriptor based models were able to predict values for PCE, FF, Jsc and Voc with good accuracy within their training sets and faced mostly acceptable increments in MSE when moving to testing sets which included molecules with similar molecular structures to those within the training set. However our models failed to predict the experimental PCE, Jsc and FF values for molecules outside of the initial molecule database, pointing to an important problem when attempting to make predictions for newer molecules.

This failure to make accurate predictions in PCE, FF and Jsc makes the models of limited usefulness for the exploration of new donor materials for organic solar cells. Since current research will aim to expand on the currently available experimental results, a model that is able to predict the outcomes of yet untested molecular families containing new donor or acceptor moieties is desirable.

There are probably many reasons why our models cannot achieve such accurate predictions and they may actually have nothing to do with our choice of statistical model or molecular descriptors. The most probable reason why we are unable to successfully predict these values may have more to do with the large variance present in device fabrication that makes the previous experimental data on old donor molecules of little usefulness to predict new donor molecule outcomes. This is evident when you look at the optimization procedures used to fabricate active layer films and how they have changed through the years and across laboratories. For example some laboratories may perform thermal and solvent annealing optimizations on donor molecules while other laboratories may not perform these procedures or may perform only one of them. Since performing one additional optimization procedure can significantly change the final efficiencies of produced devices, it becomes very difficult to judge whether the values within our database in fact correspond to the highest possible achievable PCE values for each molecule. This means that the models produced may be accurate in predicting the highest achievable PCE given the optimization constraints and fabrication techniques used within their database but have no way of accounting for improvements in optimization procedures or fabrication steps that may have surfaced through the years. In this manner it becomes impossible for a model to predict that a given donor will achieve a very high PCE when optimized through a technique that was simply not available or not commonly used before.

This is most likely what happens with DRCN5T which was optimized through both solvent and thermal annealing to achieve a PCE of nearly 10% while in our molecule database there are no examples where mixed thermal and solvent annealing techniques were used, as this mixed optimization procedure was practically not used before 2012. This means that our predicted PCE values may

be the actual maximum achievable values for this molecule under the optimization techniques most commonly carried out within our database but our models have no way of accounting for the further increase in complexity in the optimization process and fabrication techniques that now exist.

Other similar issues such as improvements in purification techniques, improvements in fabrication outcomes due to the accumulation of experience within research groups and the use of additives within active layers can cause similar effects that may hinder the ability of models to reach any useful predictive outcomes when built using old experimental results.

Since device PCE, Jsc and FF depend so strongly on device fabrication procedures it is probably not possible to build a model that is able to predict the maximum possible PCE, Jsc and FF values achievable for a given donor molecule by using old experimental data that has no way to account for improvements in these values through new fabrication techniques.

However the predictions of our models do serve as a lower-boundary through which molecules can be filtered. Even though a molecule may achieve better experimental results through improved optimization techniques, our model predictions for PCE, FF and Jsc can give low threshold to discard molecules that may not yield any type of successful result. For example a molecule with a predicted PCE lower than 1% may be readily discarded while molecules with higher predicted PCE values can be tried. In analogy if a series of molecules is to be tested the molecules can be tested in order of their predicted efficiency since the molecules with the highest predicted efficiency are bound to be better performing regardless of the optimization process used.

Conclusions

The construction of models for the accurate prediction of a solar cell's electrical properties using chemical descriptors from donor molecules proved to be a very challenging task. Our models based on simple 2D and DFT derived descriptors were able to successfully predict the FF, Voc, PCE and Jsc for devices belonging to testing sets with acceptable errors although they failed to predict the FF, PCE and

Jsc for recently fabricated devices. We attribute this failure to predict most electrical properties on newly fabricated devices to changes in device fabrication and optimization procedures between recent literature publications and those used for the construction of the database. However it is worth noting that our Voc model based on DFT derived descriptors was able to successfully predict the Voc for a recently published highly efficient molecule within experimental error. The Voc predictions are indeed expected to be more robust as the Voc is much less dependent on device fabrication procedures and much more dependent on the actual donor and acceptor combination being used.

Our models also revealed the lack of simple relationships between the donor's molecular properties and final device electrical properties, explaining why the creation of new donor structures to reach highly efficient devices is so challenging. However our 2D models did show that variables related with molecular topology, conjugation system length, alkyl chain length and hybridization have a significant importance in the determination of final device properties, pointing in the same direction as many researchers within the field.

Our models using DFT derived descriptors also gave significant insights into variable relationships, showing that orbital energies have a very secondary role in predicting device properties. This was the case even for the Voc model, where very accurate predictions were possible even with the low importance given to the HOMO/LUMO energies within the model. This further reinforces the notion that the Voc in these devices is a consequence of interactions that go beyond the simple energy difference between the HOMO of the donor and the LUMO of the acceptor. These models also showed that the non-polar σ-profile region is the most important region in the prediction of device properties, in agreement with our 2D descriptor models which often showed variables related to rotatable bond counts, conjugated system length and topology a large importance.

It is also worth mentioning that the random forest was a very good choice for the construction of the statistical models since it did not over-fit our models to the data within the training sets and provided good generalization within the testing sets. The random forest model was also exceptionally robust to the large

dimensionality of the problem, having no issue with variables that did not have any significant value in increasing prediction accuracy. Even when using 131 simple 2D descriptors the random forest was able to generate models with no over-fitting or convergence problems.

Finally it may be the case that the field of small molecule solar cells is still too young for an approach like the one we have taken to yield successful results. As the field matures and the optimization processes become more established it may become easier to test large amounts of molecules and build a database that is able to eliminate sources of variability related with differences in fabrication procedures. With variables derived from fabrication removed, it may well be possible for the approach we have followed to yield very good results in the prediction of electrical properties for solar cells based on new donor molecules. This may be especially true for our model based on DFT descriptors, where better results were achieved when compared to our 2D descriptor based models (given the smaller database used for the generation of the DFT descriptor based models).

Bibliography

(1) Brédas, J.-L.; Norton, J. E.; Cornil, J.; Coropceanu, V. *Acc. Chem. Res.* **2009**, *42* (11), 1691–1699.

(2) Scharber, M. C.; Mühlbacher, D.; Koppe, M.; Denk, P.; Waldauf, C.; Heeger, A. J.; Brabec, C. J. *Adv. Mater.* **2006**, *18* (6), 789–794.

(3) Wang, L.; Nan, G.; Yang, X.; Peng, Q.; Li, Q.; Shuai, Z. *Chem. Soc. Rev.* **2010**, *39* (2), 423–434.

(4) Olivares-Amaya, R.; Amador-Bedolla, C.; Hachmann, J.; Atahan-Evrenk, S.; Sánchez-Carrera, R. S.; Vogt, L.; Aspuru-Guzik, A. *Energy Environ. Sci.* **2011**, *4* (12), 4849.

(5) O'Boyle, N. M.; Campbell, C. M.; Hutchison, G. R. *J. Phys. Chem. C* **2011**, *115* (32), 16200–16210.

(6) Hachmann, J.; Olivares-Amaya, R.; Atahan-Evrenk, S.; Amador-Bedolla, C.; Sánchez-Carrera, R. S.; Gold-Parker, A.; Vogt, L.; Brockway, A. M.; Aspuru-Guzik, A. *J. Phys. Chem. Lett.* **2011**, *2* (17), 2241–2251.

(7) Zhou, H.; Yang, L.; You, W. *Macromolecules* **2012**, *45* (2), 607–632.

(8) Kanal, I. Y.; Owens, S. G.; Bechtel, J. S.; Hutchison, G. R. *J. Phys. Chem. Lett.* **2013**, *4* (10), 1613–1623.

(9) Salvatori, P.; Mosconi, E.; Wang, E.; Andersson, M.; Muccini, M.; De Angelis, F. *J. Phys. Chem. C* **2013**, *117* (35), 17940–17954.

(10) Zhuang, W.; Lundin, A.; Andersson, M. R. *J. Mater. Chem. A* **2014**, *2* (7), 2202–2212.

(11) Fu, Z.; Shen, W.; Tang, X.; He, M.; He, R.; Li, M. *J. Phys. Chem. A* **2015**.

(12) Lin, Y.; Li, Y.; Zhan, X. *Chem. Soc. Rev.* **2012**, *41* (11), 4245–4272.

(13) Beaujuge, P. M.; Fréchet, J. M. J. *J. Am. Chem. Soc.* **2011**, *133* (50), 20009–20029.

(14) Chen, Y.; Wan, X.; Long, G. *Acc. Chem. Res.* **2013**, *46* (11), 2645–2655.

(15) Liu, Y.; Yang, Y. M.; Chen, C.-C.; Chen, Q.; Dou, L.; Hong, Z.; Li, G.; Yang, Y. *Adv. Mater.* **2013**, *25* (33), 4657–4662.

(16) Bura, T.; Leclerc, N.; Bechara, R.; Lévêque, P.; Heiser, T.; Ziessel, R. *Adv. Energy Mater.* **2013**, *3* (9), 1118–1124.

(17) Kan, B.; Li, M.; Zhang, Q.; Liu, F.; Wan, X.; Wang, Y.; Ni, W.; Long, G.; Yang, X.;

Feng, H.; Zuo, Y.; Zhang, M.; Huang, F.; Cao, Y.; Russell, T. P.; Chen, Y. *J. Am. Chem. Soc.* **2015**, 150304052305008.

(18) Liu, C.; Yi, C.; Wang, K.; Yang, Y.; Bhatta, R. S.; Tsige, M.; Xiao, S.; Gong, X. *ACS Appl. Mater. Interfaces* **2015**, 150220090109002.

(19) Liu, Y.; Chen, C.-C.; Hong, Z.; Gao, J.; Yang, Y. M.; Zhou, H.; Dou, L.; Li, G.; Yang, Y. *Sci. Rep.* **2013**, *3*, 3356.

(20) O'Boyle, N. M.; Banck, M.; James, C. A.; Morley, C.; Vandermeersch, T.; Hutchison, G. R. *J. Cheminform.* **2011**, *3* (1), 33.

(21) Yap, C. W. *J. Comput. Chem.* **2011**, *32* (7), 1466–1474.

(22) Allouche, A.-R. *J. Comput. Chem.* **2011**, *32* (1), 174–182.

(23) Te Velde, G.; Bickelhaupt, F. M.; Baerends, E. J.; Fonseca Guerra, C.; van Gisbergen, S. J. A.; Snijders, J. G.; Ziegler, T. *J. Comput. Chem.* **2001**, *22* (9), 931–967.

(24) Becke, A. D. *Phys. Rev. A* **1988**, *38* (6), 3098–3100.

(25) Tropsha, A. *Mol. Inform.* **2010**, *29* (6-7), 476–488.

(26) Li, H.; Zhong, Z.; Li, L.; Gao, R.; Cui, J.; Gao, T.; Hu, L. H.; Lu, Y.; Su, Z.-M.; Li, H. *J. Comput. Chem.* **2015**, *36* (14), 1036–1046.

(27) Yosipof, A.; Nahum, O. E.; Anderson, A. Y.; Barad, H.-N.; Zaban, A.; Senderowitz, H. *Mol. Inform.* **2015**, n/a – n/a.

(28) R Core Team. R: A Language and Environment for Statistical Computing, 2013.

(29) Liaw, A.; Wiener, M. *R News* **2002**, *2* (3), 18–22.

(30) Polishchuk, P. G.; Muratov, E. N.; Artemenko, A. G.; Kolumbin, O. G.; Muratov, N. N.; Kuz'min, V. E. *J. Chem. Inf. Model.* **2009**, *49* (11), 2481–2488.

(31) Sheridan, R. P. *J. Chem. Inf. Model.* **2012**, *52* (3), 814–823.

(32) Jiang, P.; Wu, H.; Wang, W.; Ma, W.; Sun, X.; Lu, Z. *Nucleic Acids Res.* **2007**, *35* (Web Server issue), W339–W344.

(33) Palmer, D. S.; O'Boyle, N. M.; Glen, R. C.; Mitchell, J. B. O. *J. Chem. Inf. Model.* **2007**, *47* (1), 150–158.

(34) Svetnik, V.; Liaw, A.; Tong, C.; Culberson, J. C.; Sheridan, R. P.; Feuston, B. P. *J. Chem. Inf. Comput. Sci.* **2003**, *43* (6), 1947–1958.

(35) Breiman, L. *Mach. Learn. 45* (1), 5–32.

(36) Biau, G. *J. Mach. Learn. Res.* **2012**, *13* (1), 1063–1063 – 1095–1095.

(37) Strobl, C.; Boulesteix, A.-L.; Kneib, T.; Augustin, T.; Zeileis, A. *BMC Bioinformatics* **2008**, *9* (1), 307.

(38) Leach, A. R.; Gillet, V. J. *An Introduction to Chemoinformatics*; Springer Science & Business Media, 2007.

(39) Klamt, A. *COSMO-RS: From Quantum Chemistry to Fluid PhaseThermodynamics and Drug Design*; Elsevier, 2005.

(40) Palomar, J.; Torrecilla, J. S.; Lemus, J.; Ferro, V. R.; Rodríguez, F. *Phys. Chem. Chem. Phys.* **2010**, *12* (8), 1991–2000.

Chapter 7

Fabrication and Opto-electronic studies of hot-casted $PbCH_3NH_4I_{3-x}Cl_x$/Fullerene solar cells

Table of Contents

Motivation

Lead halide pervoskite solar cells have seen great improvements during the past few years, going from low efficiency values in 2012 to efficiencies near 20% in 2014-2015[1,2]. In particular new device architectures different from the traditional n-i-p geometry are now being explored (Figure 1). Of particular interest is the development of p-i-n architectures using fullerenes as electron acceptors as they appear to offer significantly different properties compared with devices with a mp-TiO_2 scaffold[3–8]. In general devices using fullerenes as electron acceptors without the presence of any n-type metal oxide appear to show negligible JV curve hysteresis compared with devices created using these oxides[9,10]. Since the photo physics of pervoskite devices using this geometry had not been published at the start of this project it seemed interesting to build these devices in order to explore how the photo physics of these solar cells would differ from those of perovskite devices constructed using n-type metal oxides[11].

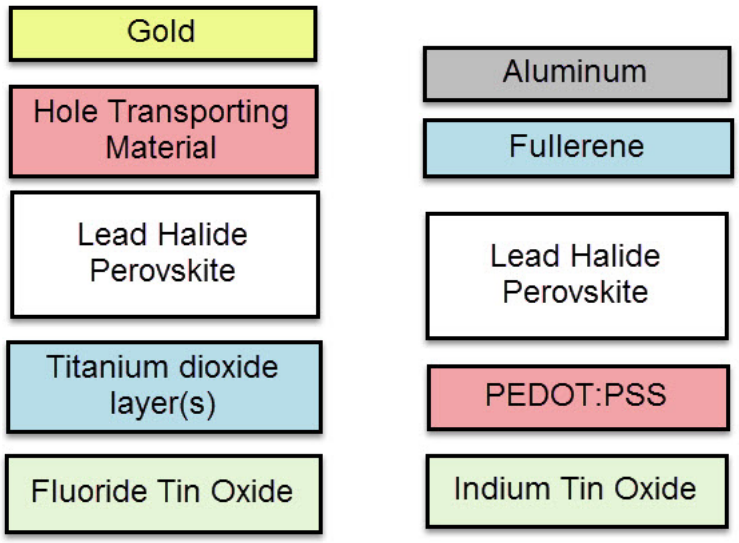

Figure 1. Layer structure commonly used for n-i-p (left) and p-i-n (right) type lead halide pervoskite solar cells.

An additional advantage of developing pervoskite devices with a p-i-n architecture using fullerenes as electron acceptors was to leverage the experience obtained

within our group in the fabrication of fullerene containing organic solar cells, which generally follow this geometry. For all these reasons we embarked on a project to standardize a p-i-n device fabrication method within our lab that could produce devices which we could use for opto-electronic studies, with the aim to compare them with our n-type metal oxide containing solar cells.

Fabrication Method

Selecting a fabrication method

There are several methods that can be used to fabricate p-i-n lead halide perovskite solar cells. These methods differ primarily in how the pervoskite is deposited and how the annealing method is carried out. The pervoskite can be deposited by using a $PbCl_2/CH_3NH_4I$ solution with temperature annealing[12], a process where the thermal annealing is replaced with ammonium chloride as an additive[13], a process where diethyl ether is used as a cosolvent[14] and two step dipping procedures[15], among others. We decided to fabricate our devices using a hot casting method[10] which can yield very high device efficiencies (>18%) as well as a high degree of control over perovskite grain size. Since the hot casting process generates the perovskite films in a very rapid manner it is also an ideal process to test the introduction of impurities or different precursor compositions without having to worry about slow crystallization kinetics that are relevant in slower pervoskite formation procedures. We also expected this faster process to be less dependent on difficult-to-control variables, such as ambient temperature and humidity, which can be critical to other perovskite fabrication techniques[16].

Our fabrication method

We fabricated devices using the p-i-n architecture showed in Figure 2. Indium tin-oxide patterned substrates were first washed and sonicated in acetone for 15 minutes, then washed and sonicated in isopropyl alcohol for 15 minutes. After this

the substrates were dried with dry air and were then ready for use. Unless otherwise noted, device fabrication starts by spin coating a film of PEDOT:PSS (Clevios 415) at 4500 rpm for 30s and then at 2500 rpm for 30 seconds. The substrates were then placed on a hot plate under ambient conditions at 120°C for 1 hour in order to eliminate all traces of water that could affect perovskite formation later on. It is very important here to note that the PEDOT:PSS covered substrates should be used without cooling between this step and the pervoskite deposition. If the substrates are cooled before proceeding the devices will not work as intended. This is most likely due to morphological changes caused in the PEDOT:PSS films by water absorption from the atmosphere when cooling[17].

Once the PEDOT:PSS has been annealed we then proceed to increase substrate temperature to the final hot casting temperature (150-250°C). After the substrate temperature has stabilized we then rapidly move each substrate to the spin coater and apply the perovskite forming solution. This solution was always preheated to 70°C. If it's not noted otherwise we used a solution comprised of PbI_2/CH_3NH_4Cl in DMF with a 1:1 molar ratio. The solution was prepared and stirred for at least 1 hour at 70°C, then filtered using a 0.45um PTFE filter and reheated to 70°C before use. The purity and quality of these precursors is fundamental to the quality and reproducibility of the devices produced. Methyl ammonium chloride should be dried at 170°C in a vacuum (<1E-2 mBar) overnight and lead iodide should be recrystallized from Milli-Q water (the effect of lead iodide purity will be discussed later on as well). Once the films are formed the contacts are cleaned with a cotton swab using deionized water and immediately placed in a globe box for the deposition of the fullerene contact (when using C60). Cleaning the contacts with DMF is less desirable as DMF vapors tend to dissolve the perovskite layer. Using water for this process allows for a more controlled cleaning process without affecting device performance. In experiments using $PC_{71}BM$ the films were placed in a low vacuum (globe box antechamber) for 5 minutes to remove any remaining solvent before spin coating the fullerene containing

solution under ambient conditions. Fullerene solutions were also stirred for at least 1 hour at 50°C before use and were also filtered with a 0.45uL PTFE filter before use. After the n-type contact has been deposited we then proceed to the metal cathode thermal evaporation. We evaporated 90-150nm Al as the back contact from tungsten boats, taking care to keep the temperature as low as possible through the entire process. For this we used 5 Al pellets (Karl Leo) per evaporation. In a similar way as with organic devices, Al covered tungsten boats should not be recycled.

Our fabrication process also differs from that implemented by researchers at Los Alamos[10]. First of all their hot casting process is carried out under an inert atmosphere, inside a globe box, while our fabrication process takes place inside a clean room under normal air and humidity conditions. Second, their temperature measurements are carried out using a heat sensing IR thermometer gun, while we measure hot plate temperatures directly using thermocouples. It is also worth noting that their device areas were measured at 3mm^2 and device properties were measured without masks, while the devices we have fabricated in our group have a larger area (9mm^2) and were always measured using masks. We did not carry out the process in the same manner as we did not have a globe box that was adequate for this procedure. Furthermore we also wanted to see if we could reproduce the same results without the need for inert atmospheric conditions. Another important factor is that the general substrate size for the Los Alamos experiments is much larger (as can be seen on this video made by their group) compared to our substrates.

Perovksite Grain Sizes

Since the Los Alamos hot casting paper does a quite comprehensive study around device performance and its relationship with crystal grain size (which in the case of this paper is in the millimeter scale), we decided to start our research by attempting to reproduce the same grain size using our own experimental

conditions. In order to do this we performed the hot casting procedure on top of PEDOT:PSS covered ITO substrates using different hot casting temperatures, precursor solution concentrations and spin coater conditions (solution volume, acceleration and final RPM). We always performed the spin coating process for 10 seconds (as described in the Los Alamos paper) and immediately analyzed films over an optical microscope to determine grain size. Figure 2 shows different characteristic grain sizes obtained at different conditions while table 1 summarizes the average grain size as a function of the different spin coating conditions.

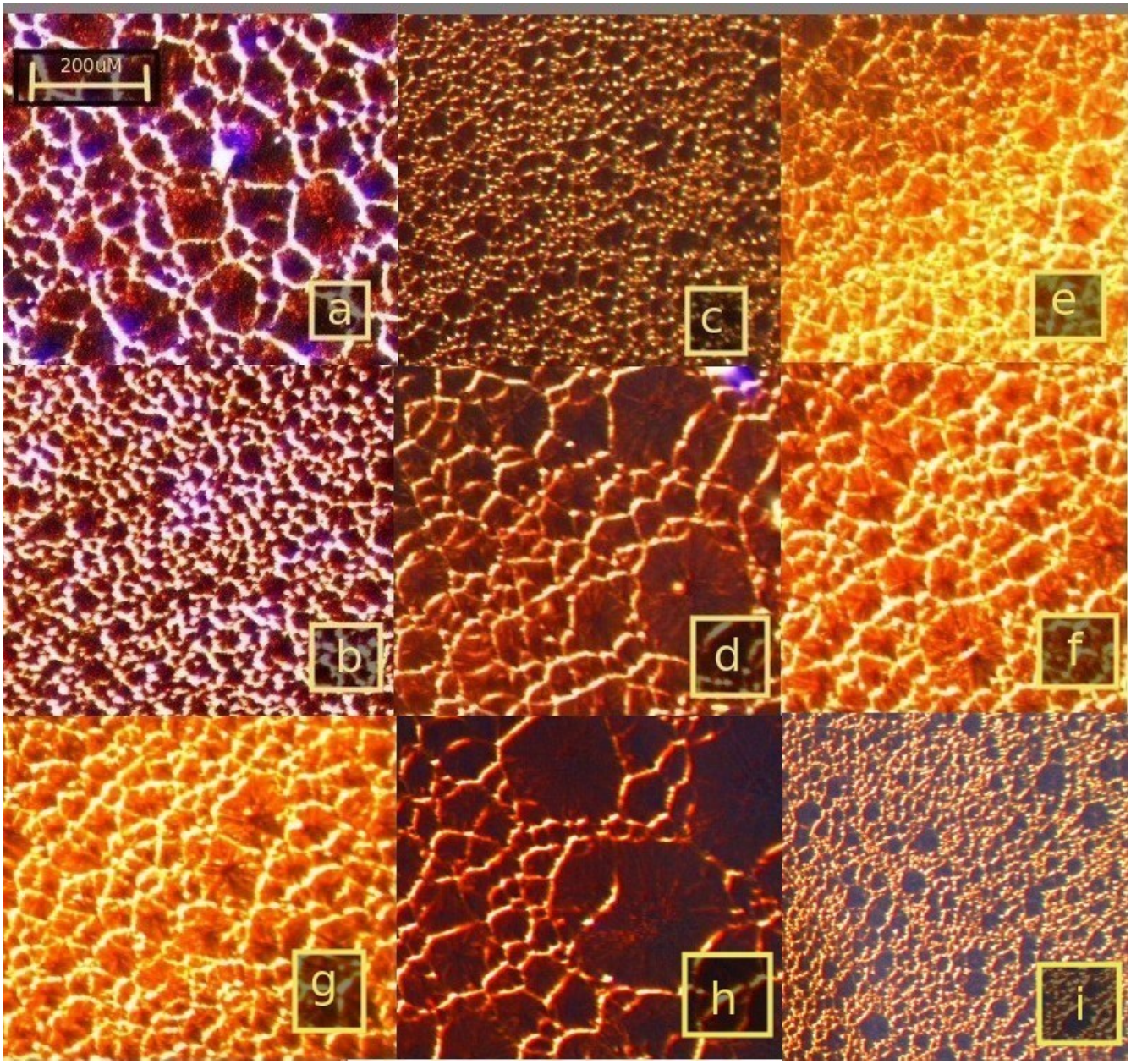

Figure 2. *Sample optical microscope images of hot-casted lead halide perovskite films deposited on PEDOT:PSS covered ITO substrates. Conditions are further detailed on Table 1.*

As in the case of the Los Alamos publication we do see an increase in the grain size as a function of the hot casting temperature but the creation of larger grains only starts to happen at much higher temperatures (approximately 200°C with low solution volumes) while in their case this happens at a much lower

temperature (180 °C). There is also a strong relationship between the crystal grain size and the volume of spin coating solution being used, with lower volumes generating larger grain sizes.

	mg/mL PbI2	accel	RPM	temp (°C)	Vol (uL)	thickness (nm)	grain size (uM)
a	200	100	4000	250	25	427	120
b	200	100	4000	250	40	411	12
c	200	20	4000	200	80	650	15
d	100	20	4000	200	80	370	113
e	200	100	6000	250	80	412	40
f	300	100	4000	250	40	642	46
g	200	100	4000	250	25	520	42
h	100	100	4000	250	40	328	175
I	200	60	4000	200	80	512	12
*	100	20	4000	200	40	657	125
*	200	40	4000	250	40	630	54
*	200	80	6000	250	100	518	16
*	100	20	4000	250	80	412	132
*	200	100	4000	180	80	490	65
*	200	80	4000	250	40	451	96

Table 1. Different conditions for the formation of lead halide pervoskite films across different experiments.

All of these effects are to be expected, since the crystal grain size depends on the crystallization speed that depends both on the total amount of solvent that comes into contact with the substrate and the thermal energy of the substrate. Note however that this dependence is not a simple dependence on the substrate's hot casting temperature – as if the substrate temperature was held constant through the process – but it's a dependence on the amount of energy that the substrate can transfer to the solution in the evaporation process that leads to the formation of the perovskite crystals. This explains why published results on much larger substrates at 180°C using a 100mg/mL PbI_2/CH_3NH_4Cl solution can yield such large crystal sizes while in our case we require either very low solution volumes or very high temperatures to obtain comparable crystal sizes at the same concentrations. Our small substrates therefore faced a considerable challenge in the hot casting process as the use of high temperatures deteriorated the PEDOT:PSS and the use of small solution volumes led to problems in substrate coverage[18]. This highlights

the fact that the substrate's geometry and heat capacity are just as important to the hot casting process as other parameters, such as the hot casting temperature, the spin coating conditions, the solution volume and the solution's concentration. Although we attempted to fabricate devices at 250°C or with low solution volumes in order to obtain crystal sizes comparable to those published in the literature, our devices under such conditions always suffered from very low efficiencies (<0.5%) and extremely poor stability. This is also the reason why we attempted to explore p-type materials different from PEDOT:PSS, as a way to attempt to circumvent this issue.

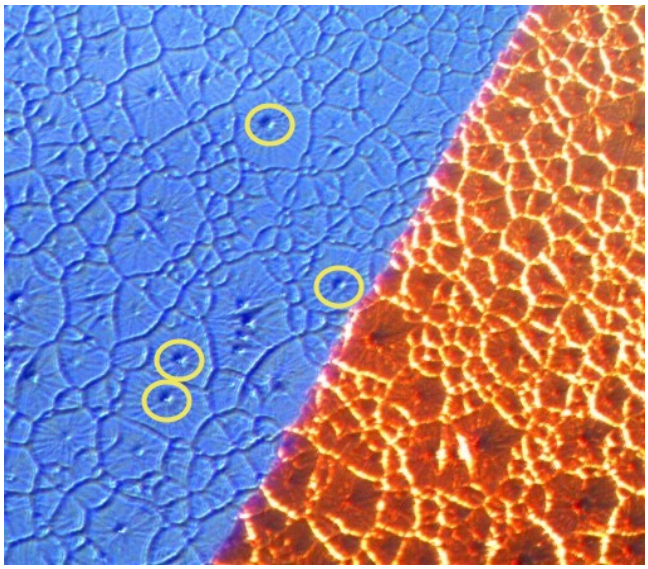

Figure 3. *Optical microscope images of a hot casted lead halide perovskite film (250°C, 100mg/mL, 20 accel, 4000 rpm, 40 uL) with 60nm $PC_{71}BM$ and Al counter electrode coverage. Al counter electrode interface shown (Al is blue). Some highly elevated peaks (200-300nm) are circled.*

We also faced a significant problem with roughness in our films, which generated problems in device stability even at lower spin coating temperatures. Mean roughness levels across linear paths (measured by surface profilometer) were usually in the 150-300nm range, with huge peaks at grain centers that even surpassed the Al counter electrode (Figure 3). It is therefore not surprising that

our devices never showed high efficiencies, as achieving homogeneous surface coverage of the fullerene over such an uneven structure is not possible. Shadowing caused by these peaks in the spin coating process is most probably the reason why our spin coated $PC_{71}BM$ devices had generally weaker performance and poorer stability compared to equally prepared devices using evaporated C_{60}. Very thick fullerene films (>150nm) to smooth the lead halide perovskite also caused strong problems with series resistance. The fact that we had always had at least some contact between the pervoskite and counter electrode probably generated leakage currents that heavily limited our device performance. Figure 2 also shows pin holes at grain boundaries under several experimental conditions that are expected to further hinder device performance. We later attempted to reduce these problems by incorporating PEG within our hot casting process.

The hot casting procedure also suffers from severe operator dependence since the speed with which the hot substrate is put on the spin coater and the hot casting solution is added is paramount in determining the final crystal sizes and device properties. If the operator is slower the substrate's initial temperature will quench more significantly – more energy will be transferred to the spin coater and surrounding atmosphere before it is transferred to the solution - and therefore smaller grain sizes will be achieved at the same initial temperature. The opposite is true if the operator is faster. This is a reason why studying film thickness and grain size systematically is so difficult as a subsequent experiment can yield different grain sizes and film thickness values depending on how fast/slow the operator is within that specific experiment. This problem seems to be more pronounced as the substrate size grows smaller as the speed of temperature quenching is faster and therefore the speed of the operator has a greater influence on device results.

As a compromise between the spin coating coverage, the largest achievable crystal sizes, the process reproducibility and the preservation of the PEDOT:PSS

layer we therefore decided to use a hot casting temperature of 200°C. In order to optimize the crystal size and thickness when using this temperature we varied solution concentrations, volumes or spin coater acceleration.

$PC_{71}BM$ as an n-type layer

PEDOT:PSS as a p-type layer

Our first attempts to build devices used the $PC_{71}BM$ fullerene as an n-type layer since several lead halide perovskite devices have already been published using this fullerene and its deposition on top of the perovskite layer can be easily carried out using a spin coating step from a dichlorobenzene solution. Most published papers use either 2 or 4% $PC_{61}BM$ or $PC_{71}BM$ solutions[12,15,19] so at first we tried to build devices using these two concentrations to see what would be the optimal PCBM concentration to use in our case (Figure 4). Table 2 shows device IV curve characteristics under these conditions (for the best devices obtained for each concentration).

Our JV Curves show very little hysteresis when compared with flat geometry devices that use mp-TiO_2 geometries, in agreement with the published literature of fullerene containing lead halide perovskite solar cells[3,9,10,13,19]. However our first devices suffered from much lower efficiencies, with the highest efficiency only reaching a PCE of 4.55%, owed primarily due to a very poor fill factor. The voltage we obtained is however larger than those commonly reported for devices containing PEDOT:PSS and PCBM which generally oscillates between 0.850-0.920 while ours reached 0.945V.

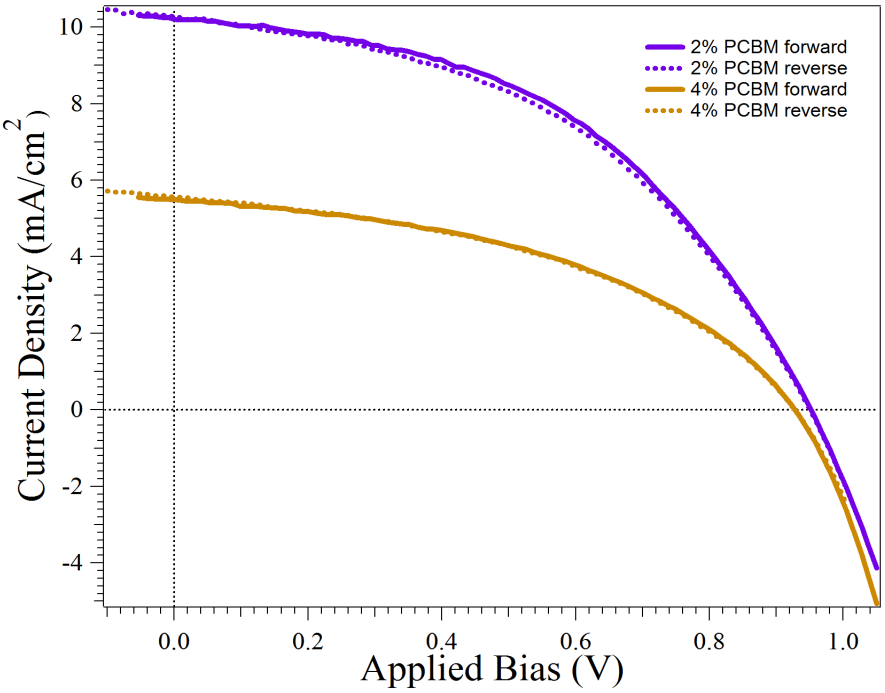

Figure 4. *JV Curves for lead halide pervoskite solar cells with a PEDOT:PSS/ PbCH3NH4I3-xClx/PC71BM/Al geometry. The pervoskite was deposited from a 1:1 PbI2/NH4Cl solution (100 mg/mL PbI2) at 200°C.*

PCBM	Voc	Jsc	FF	PCE	Rs	Rp
2% forward	0.945	10.19	0.473	4.55	355	8118
2% reverse	0.945	10.27	0.456	4.43	419	6342
4% forward	0.922	5.49	0.448	2.27	443	9806
4% reverse	0.922	5.55	0.439	2.25	632	6629

Table 2. IV curve characteristics for lead halide pervoskite solar cells constructed using different PCBM layers.

These first experiments using $PC_{71}BM$ also revealed the general lack of reproducibility inherent to the hot casting process. A subsequent experiment where all devices were fabricated in exactly the same manner as the 2% PCBM concentration champion above revealed that variations were very important between devices prepared under the same experimental conditions. Figure 45 shows all the JV Curves for this experiment and the frequency distributions for the PCE, Voc, Jsc and FF. Out of 13 different diodes that could be measured in this

experiment (out of 16) we see that results are not normally distributed as we would expect from a reproducible experimental process subject to experimental error. Plotting each diode's PCE as a function of measuring order gave us a rather enlightening curve in which it becomes obvious that device performance drops significantly as time passes. Devices are measured under a nitrogen atmosphere and are not exposed to light before measuring, meaning that the deterioration process we were seeing was caused by a process that was inherent to the devices themselves and not caused by any environmental factor. Since both the perovskite and the aluminum counter electrode are damaged by water and oxygen within the atmosphere, we could not use any characterization techniques beyond variations in fabrication procedures to help us determine what was wrong with our pervoskite devices. It is also worth noting that regular geometry lead halide pervoskite solar cells produced in our lab with an FTO/mp-TiO2/ $PbCH_3NH_4I_{3-x}Cl_x$/SpiroOMeTAD/Au structure are stable for months when stored under nitrogen. Optical microscope and profilometer analysis of the devices showed a very large roughness of the pervoskite layer (with peaks exceeding 150nm), which is what we hypothesized was causing issues with device performance. We also thought that the high temperature achieved during the hot casting process under ambient conditions could be damaging or increasing the roughness of the PEDOT:PSS layer, reason why we also wanted to test different p-type layers.

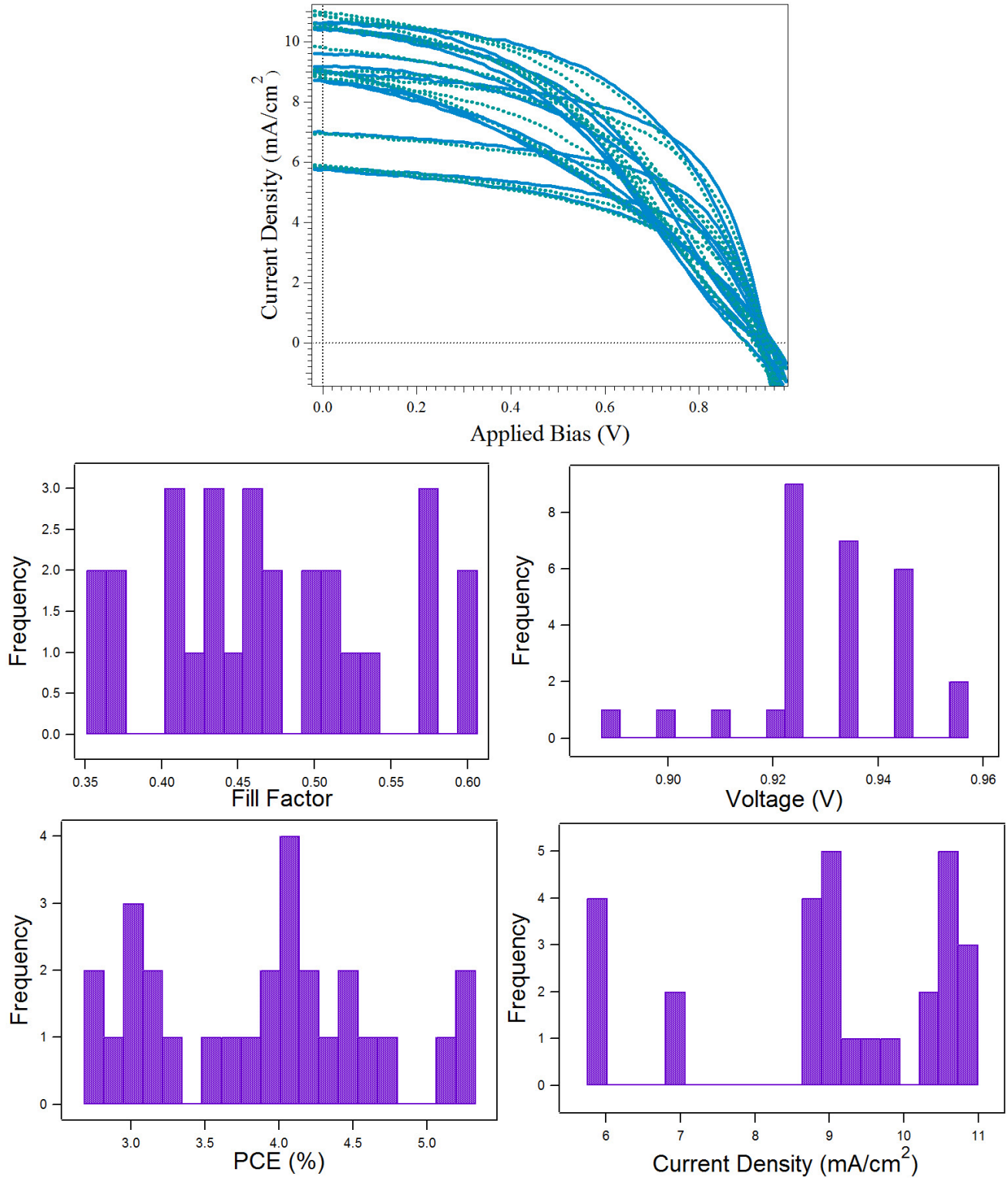

Figure 5. *JV Curves and property frequency distributions for lead halide pervoskite solar cells with a PEDOT:PSS/PbCH$_3$NH$_4$I$_{3-x}$Cl$_x$/PC$_{71}$BM/Al geometry. JV*

Curves measured in reverse bias (from positive to negative) are depicted in dotted green.

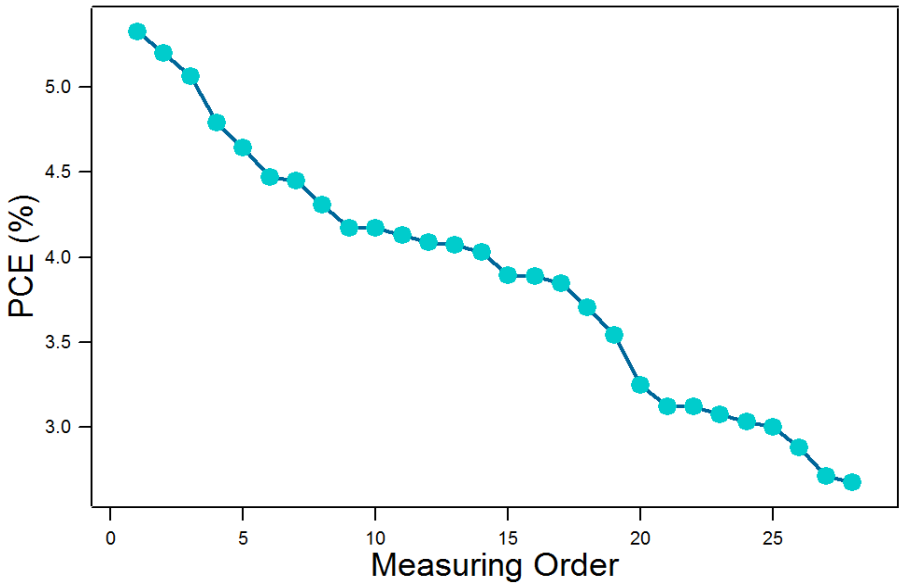

Figure 6. *Power conversion efficiency as a function of measuring order for lead halide pervoskite solar cells with a PEDOT:PSS/PbCH$_3$NH$_4$I$_{3-x}$Cl$_x$/PC$_{71}$BM/Al geometry.*

Sorbitol doped PEDOT:PSS as p-type layer

Our first attempt to increase the stability and potentially reduce the roughness of the p-type layer came from the already published use of sorbitol doped PEDOT:PSS as a way to increase the stability and conductivity of PEDOT:PSS films[17]. We therefore fabricated devices using a PEDOT:PSS layer containing sorbitol in a concentration of 2% (PEDOT:PSS(S)). The PEDOT:PSS(S) layer was spin coated under the same conditions as our regular PEDOT:PSS layer, following the exact same annealing process afterward. The perovskite film was deposited at 200°C, 20 acceleration, 4000 rpm and a concentration of 100mg/mL. The pervoskite film was then followed by a PCBM film deposited from a 2% solution as in the last devices discussed. Figure 7 shows all JV Curves for this experiment

using PEDOT:PSS(S). Table 3 shows the forward and reverse electrical properties for the champion devices.

The measured JV Curves show a higher efficiency for the PEDOT:PSS(S) solar cells when compared with our initial PEDOT:PSS devices. Thanks to this modifications to the p-type layer our efficiencies increased to +6.17% with a significant increase in the fill factor and the short circuit current. This was however accompanied by a decrease in the voltage which is expected from the changes in work function associated with the introduction of sorbitol in PEDOT:PSS [20]. It is also important to mention that device hysteresis remained minimal as we changed from PEDOT:PSS to PEDOT:PSS(S), demonstrating that hysteresis is rather independent of p-type conductivity in the case of PEDOT:PSS.

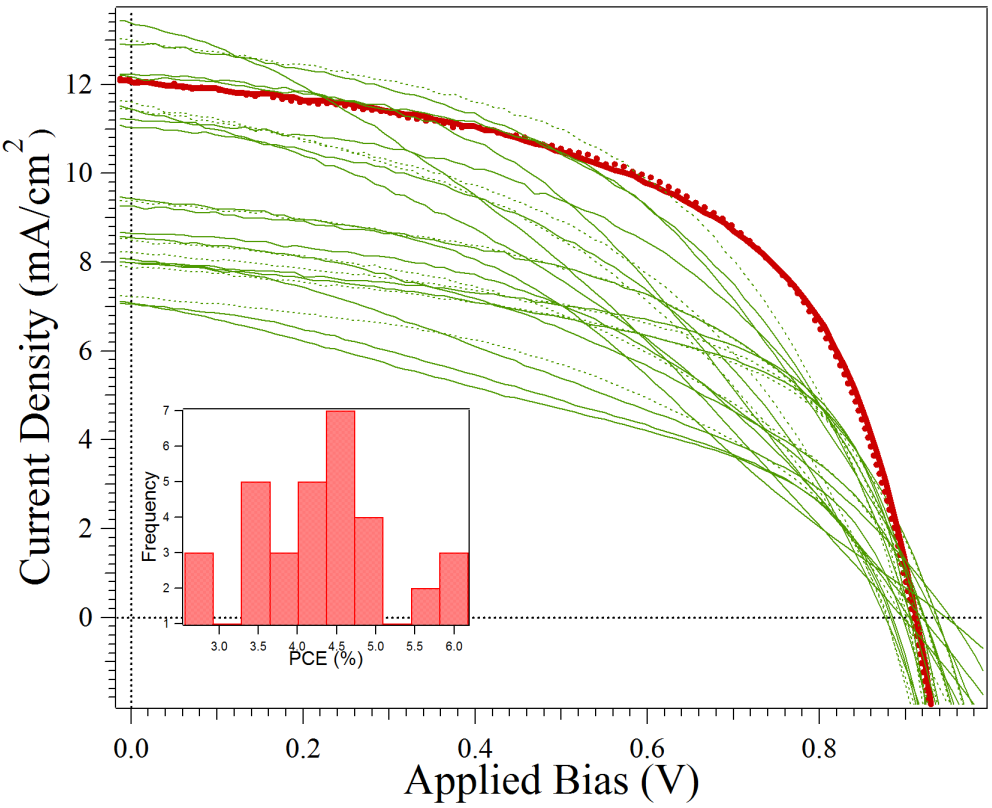

Figure 7. *JV Curves for devices fabricated using PEDOT:PSS(S). Champion device showed in red. JV Curves measured in reverse are showed in dotted green/red. A frequency distribution of all PCE values is also included as an inset plot.*

	Voc	Isc	FF	PCE	Rs	Rp
PEDOT:PSS(S) forward	0.899	12.096	0.568	6.171	107.617	4679.160
PEDOT:PSS(S) reverse	0.911	12.043	0.559	6.130	100.627	7073.460

Table 3. *Electrical properties for PEDOT:PSS(S) devices using PC71BM as a p-type layer.*

Despite the better performance of these devices we still saw significant performance degradation as a function of measuring order as showed in Figure 8. This means that although device performance could increase significantly from the use of PEDOT:PSS(S), it did not solve the problem that was causing device instability. As devices that are so unstable cannot be used for opto-electronic experiments, we decided to further experiment in order to find a device configuration that was able to yield stable results, even if such results would be less efficient. The remarkably linear behavior of device efficiency against measuring order (even though it was not perfectly timed) suggests that device performance might be relatively homogeneous upon fabrication, with differences upon measuring being largely a function of measuring time.

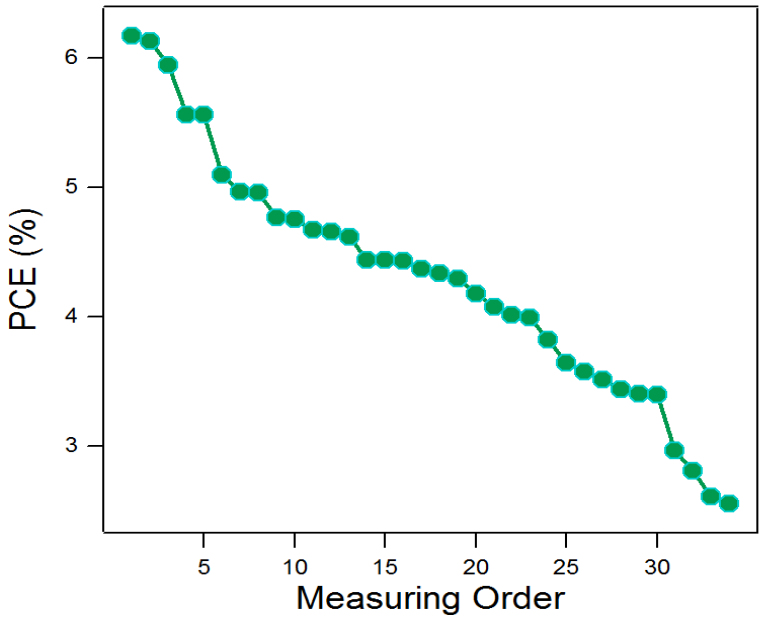

Figure 8. *Power conversion efficiency as a function of measuring order for diodes in our PEDOT:PSS(S) experiment.*

NiO and Cu doped NiO as p-type layers

At this point we thought that instability could simply be a consequence of the organic character of the PEDOT:PSS and PEDOT:PSS(S) films when heated to high temperatures in air. For this reason we decided to test NiO and Cu doped NiO as p-type films since these metal oxides have a high temperature resistance. As a matter of fact their fabrication procedure using solution processing requires high temperature annealing (+300°C) of deposited sol-gel films[21]. Since these layers had already been tested and exhibited high efficiencies on lead halide perovskite solar cells[3,21–25], we wanted to know whether we could duplicate these results using our hot casting deposition process. The first results using NiO (same hot casting conditions as for PEDOT:PSS(s)) are showed in Figure 9 (different measurements as a function of time for champion device). Table 4 shows the electrical properties for the champion device as a function of time. In this case the frequent distribution for the device properties of different NiO containing diodes is not shown as only 3 diodes within the 32 diode set could be measured.

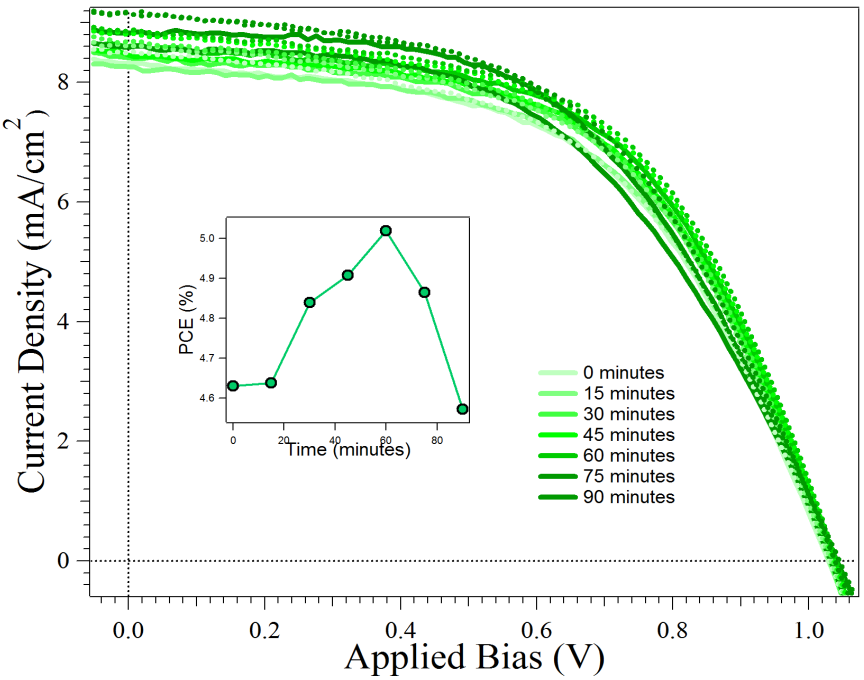

Figure 9. *JV Curves for champion device at different device measuring times in*

an experiment where NiO is used as a p-type layer. The time represents the number of minutes after the first measurement was taken. Dotted lines show the JV Curves measures in reverse.

Time (min)	Direction	Voc (V)	Jsc (mA/cm^2)	FF	PCE (%)	Rs (Ω)	Rp (Ω)
0	forward	1.027	8.319	0.54	4.63	436	9366
15	forward	1.027	8.260	0.55	4.64	429	12138
30	forward	1.027	8.401	0.56	4.84	409	12762
45	forward	1.027	8.430	0.57	4.91	405	8787
60	forward	1.027	8.620	0.57	5.02	400	16010
75	forward	1.027	8.844	0.54	4.86	441	48534
90	forward	1.039	8.601	0.51	4.57	501	13295
0	reverse	1.027	8.508	0.53	4.63	451	12354
15	reverse	1.027	8.613	0.54	4.82	430	16339
30	reverse	1.027	8.692	0.55	4.89	424	9433
45	reverse	1.027	8.816	0.56	5.07	411	11878
60	reverse	1.039	8.880	0.56	5.14	407	11504
75	reverse	1.027	9.129	0.53	5.00	443	30168
90	reverse	1.039	9.127	0.51	4.86	484	15772

Table 4. *Electrical properties for champion NiO containing device as a function of measuring time.*

Our devices containing NiO had a much larger voltage (>1V) when compared with our previous devices, something which is expected from the significantly more favorable work function of NiO compared to PEDOT:PSS[26]. This effect is accompanied by a decrease in the Jsc, which is also expected due to the lower conductivity of the NiO films. The time based experiment on the same diode also revealed that these devices are more stable, with an even slight improvement of 0.4% in their PCE after more than an hour of irradiation. There was however an important problem with these devices related with the amount of time that it took them to reach a stable Voc under illumination. These devices had to be preconditioned with 5-10 minutes of illumination at 1 sun before measuring, since otherwise the Voc would not reach a stable level. This time needed to reach steady state conditions is rather unacceptable, since it creates a very important problem when performing photo-physics experiments where dozens of measurements need to be made and both the reaching of the steady state and

the stability of the device across conditions are fundamental for the accurate interpretation of the experiments. For this reason we decided to discard the use of simple NiO devices, as they would not yield adequate conditions for the experiments we wanted to perform on our perovskite solar cell.

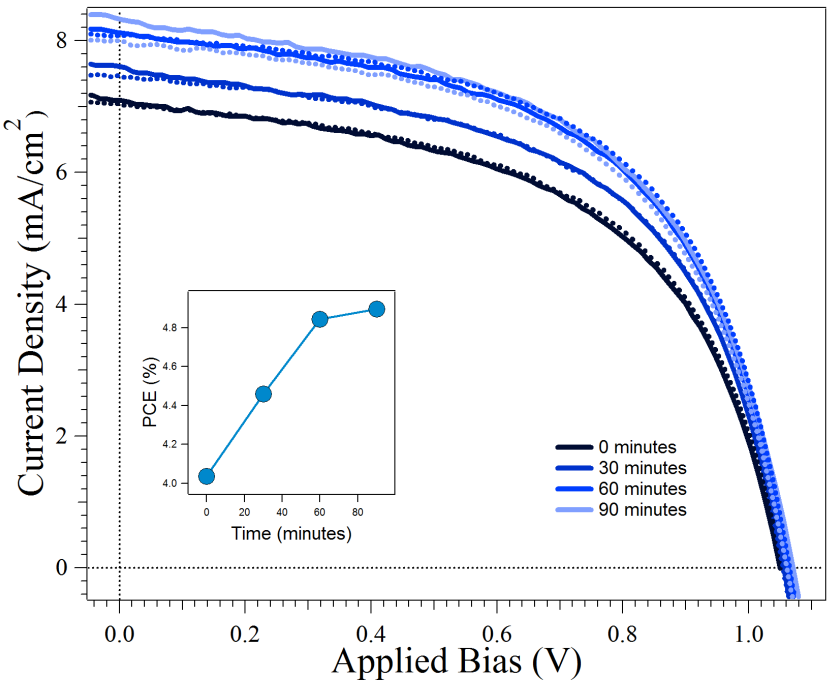

Figure 10. *JV Curves for champion device at different device measuring times in an experiment where Cu doped NiO is used as a p-type layer. The time represents the number of minutes after the first measurement was taken. Dotted lines show the JV Curves measures in reverse.*

Time	Direction	Voc (V)	Jsc (mA/cm²)	FF	PCE (%)	Rs (Ω)	Rp (Ω)
0	forward	1.038	7.088	0.55	4.04	639	7206
30	forward	1.051	7.589	0.56	4.46	428	6800
60	forward	1.051	8.108	0.57	4.84	425	7694
90	forward	1.069	8.313	0.55	4.90	256	5835
0	reverse	1.038	7.021	0.56	4.11	707	14047
30	reverse	1.051	7.435	0.57	4.46	464	18298
60	reverse	1.064	8.075	0.57	4.93	462	17854
90	reverse	1.056	7.993	0.56	4.74	273	13831

Table 5. *Electrical properties for champion NiO containing device as a function of measuring time.*

As the use of NiO increased device stability we wanted to explore further inorganic p-type layers that could improve device properties. By using a layer with a higher conductivity we hoped to increase our Jsc and FF as well as the speed with which our devices reached a stable Voc level under illumination. The Cu doped NiO layer appeared as an interesting candidate since its fabrication process was exactly the same as for our previous NiO layer, with the simple addition of a Cu containing dopant (copper (II) acetate) within the precursor solution. The JV Curves for our first Cu doped NiO experiment are shown in Figure 10 while electrical property values are showed in Table 5.

Our devices containing Cu doped NiO had an even higher voltage than our NiO devices (>1060mV). This due to the additional work function improvement generated by the Cu dopant within the NiO film[21]. However we did not see the expected increase in the Jsc from using a p-type layer with a higher conductivity and our fill factor, current and PCE values remain similar. However device stability is better than for the NiO case and the Voc response is also significantly faster, taking around half the time to achieve a stable Voc level 1 sun. We also did not see any drop in the PCE within 90 minutes while the NiO films did show this problem.

C60 as an n-type layer

Why change to C60

Our results using spin coated PC71BM as an n-type layer revealed serious problems with device performance and stability. Although our efforts to obtain better devices were initially centered around possible problems coming from the use of the PEDOT:PSS layer our results changing the p-type layer pointed out that the real problem with our devices was probably related with the interaction

between the pervoskite material and the n-type layer. As previously noted the roughness of the hot casted film was always significantly high and this generated problems with fullerene coverage when using a $PC_{71}BM$ film deposited by solution processing. In order to alleviate this issue we decided to explore the use of evaporated C_{60} as an n-type layer, since the evaporation process provides more homogeneous coverage than the spin coating process and coverage is not significantly affected by large peaks that could cause important shadowing effects in solution processing techniques.

Following this rational a C_{60} n-type layer should provide smoother coverage, a better controlled thickness and a better electron transport through the device. We hypothesized that this should generate improved device performance. We used a C_{60} thickness of 60nm through all our experiments using C_{60} as an electron transporting material.

PEDOT:PSS as a p-type layer

JV Characterization of initial devices

In order to compare with our previous results using $PC_{71}BM$ we started out our investigation of C_{60} containing devices using PEDOT:PSS as an electron blocking layer. The PEDOT:PSS deposition and annealing procedures were performed in the same manner as for our $PC_{71}BM$ tests and the hot casting process was performed using similar conditions (200°C, 200 mg/mL PbI_2, acceleration 40, RPM 4000, 80 uL). At this point we decided to move to a more concentrated Pb solution using higher volumes since these higher volumes were required to achieve proper substrate coverage in all cases while maintaining adequate active layer thickness (400-600nm). Results for $PC_{71}BM$ devices under these conditions were equivalent to results using 100mg/mL PbI2 solutions and a lower acceleration and volume at the same hot casting temperature. Our initial results with C_{60} were very encouraging (Figure 11, table 6), with a significant increase in device PCE and stability. The Jsc when using C_{60} increased very significantly when compared with

the use of $PC_{71}BM$, suggesting that the more homogeneous surface coverage did enhance electron transport properties significantly. The Fill factor also increased to a higher value when compared with our $PC_{71}BM$ devices (0.62 vs 0.47) when using C_{60}. It is also worth noting that the large voltage and general small hysteresis within our devices is also preserved when using C_{60} as an n-type layer. We can also see a linear relationship between Jsc and light intensity which is fundamental to assume negligible losses due to recombination under short circuit condition.

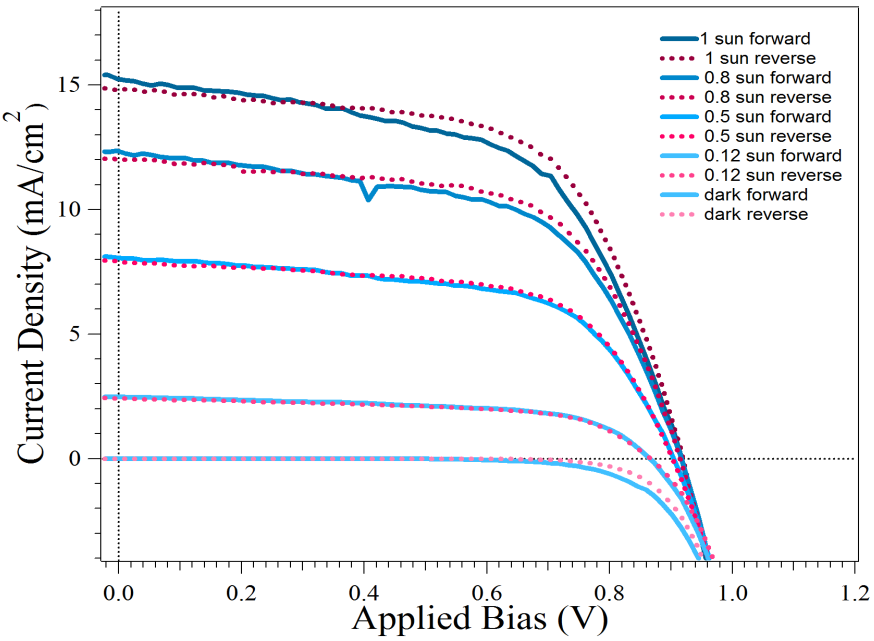

Figure 11. *JV Curves for champion C_{60} (60nm) device at different simulated light intensities.*

C60-60nm	Voc (V)	Isc (mA/cm²)	FF	PCE (%)	Rs (Ω)	Rp (Ω)
forward	0.916	15.2	0.57	7.98	104	3072
reverse	0.916	14.8	0.62	8.47	108	6499

Table 6. *Electrical properties for C_{60} champion device.*

Opto-electronic experiments for initial devices

Since our PEDOT:PSS/lead halide perovskite/C_{60} devices were finally stable and responsive enough to perform transient photo voltage, transient photo current

and photo-induced charge extraction experiments we proceeded with the photo-physical characterization of these solar cells. The device was stable enough to allow us to perform PIT-PV and TPC experiments, while we could not perform a full photo-induced charge extraction experiment due to the device being damaged by the continued laser probing within the PIT-PV and TPC experiments.

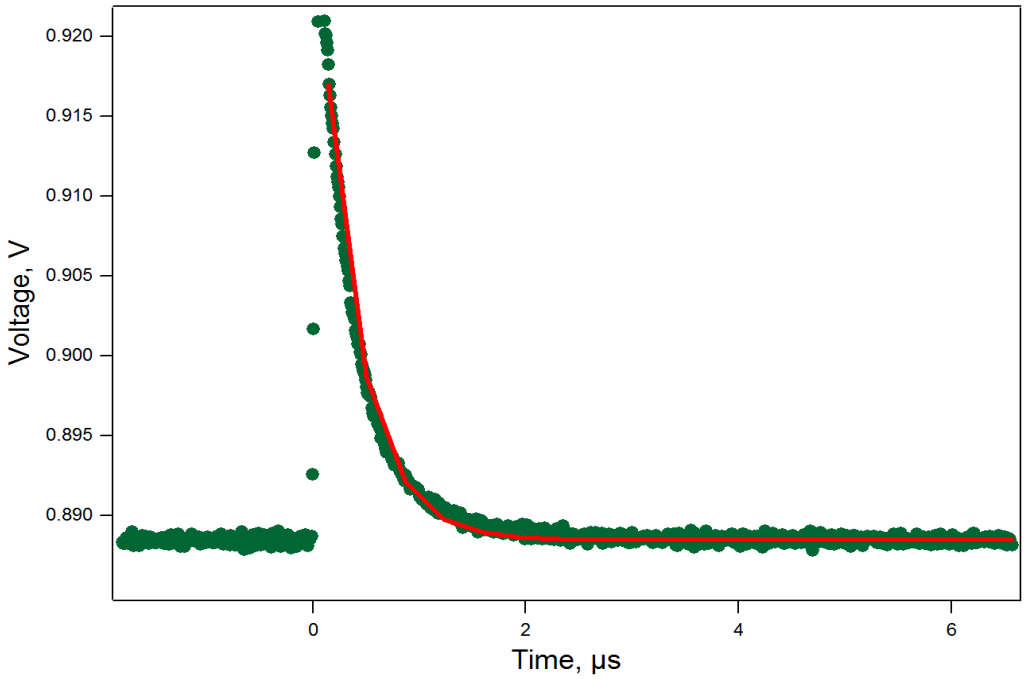

Figure 12. *PIT-PV decay at 1 Sun for a lead halide perovskite solar cell where C60 acts as an electron transporting layer. A mono-exponential fit is shown in red.*

The first interesting thing we noticed about the PIT-PV experiments is the much smaller bi-exponential character of the PIT-PV decays when compare with mp-TiO_2 containing devices. Figure 12 shows the PIT-PV decay at 1 sun with a mono exponential fit. The fit is of a good statistical quality and can be considered a good approximation when compared with a bi-exponential fit for the same curve. Since these decays are exponential we can extract single time constants using exponential regressions in order to relate charge density with decay times. We can then test the quality of this assumption by calculating the Jsc from the recombination order obtained from the charge density Vs decay time plot.

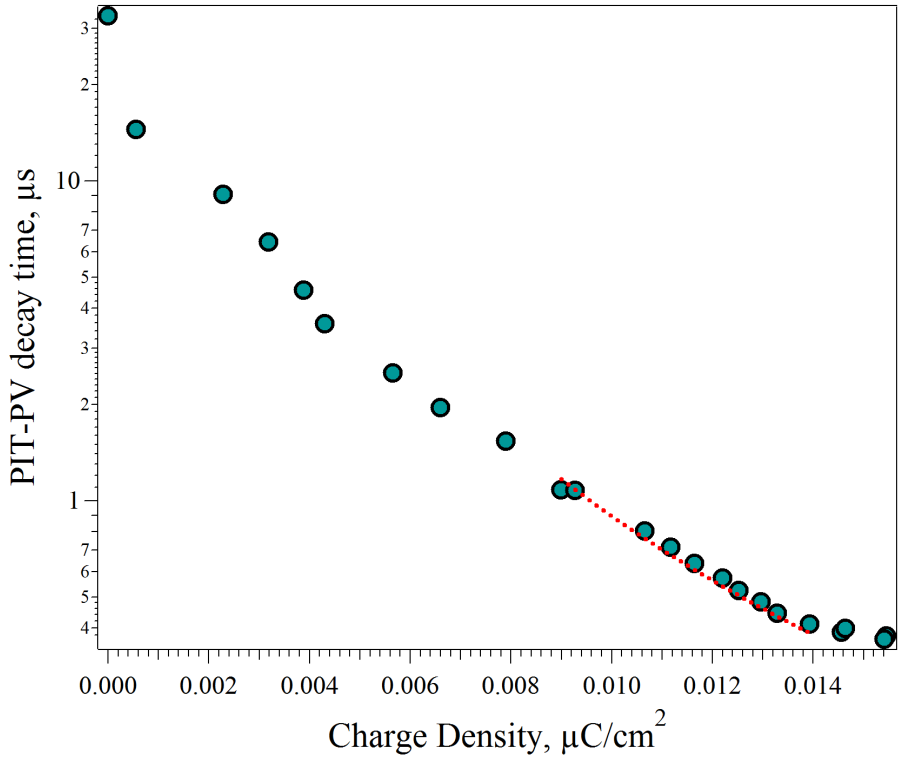

Figure 13. *PIT-PV decay time as a function of charge density for a lead halide perovskite solar cell where C_{60} acts as an electron transporting layer. A power-law fit is shown in red.*

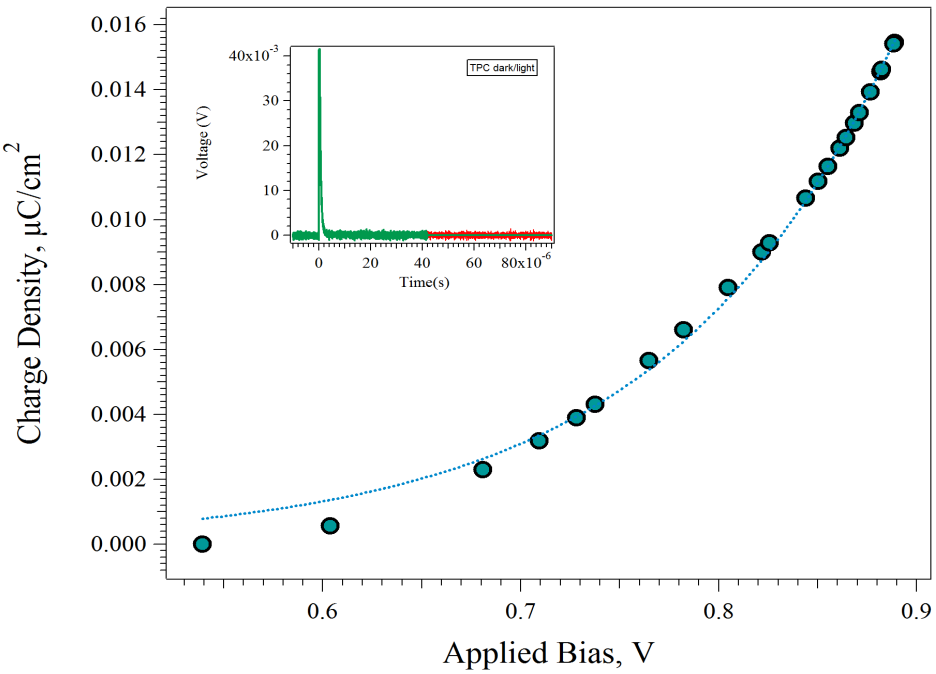

Figure

14. *Charge density as a function of applied bias for a lead halide perovskite solar cell where C_{60} acts as an electron transporting layer. A mono-exponential fit is shown in blue.*

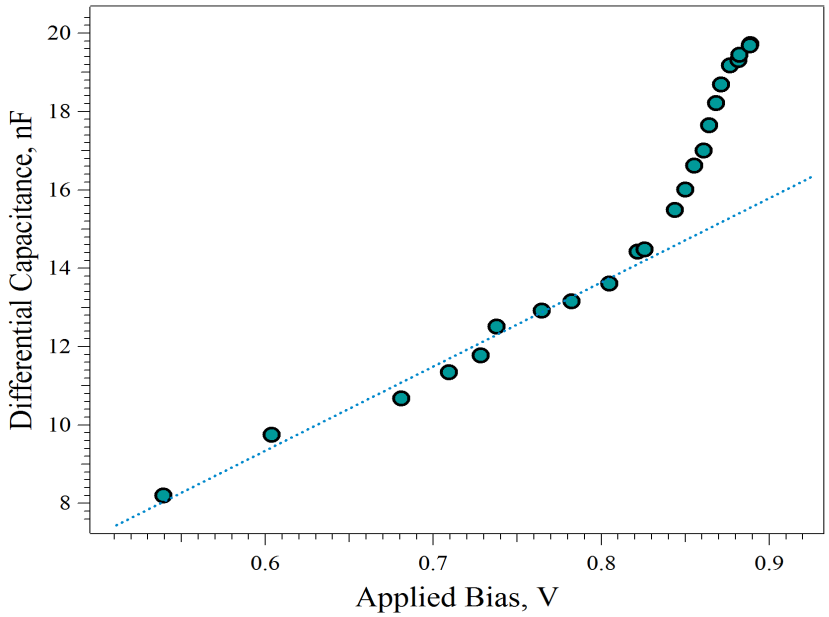

Figure 15. *Differential capacitance as a function of applied bias for a lead halide perovskite solar cell where C_{60} acts as an electron transporting layer. A linear fit representing the geometric capacitance is shown in blue.*

Figures 13, 14 and 15 display the charge density as a function decay time, differential capacitance as a function of potential and charge density as a function of applied bias plots as obtained from these experiments. We fit the PIT-PV decays using a mono-exponential function to obtain the decay times. The charge density as a function of PIT-PV decay time follows a power law function (at charge densities close to the Voc). A power law fit to this data allows us to calculate the recombination order, which is 2.53 for this device. Using this value and the charge density and decay time near the device's Voc we can estimate the device's short circuit current[11]. In this case the estimated current is 16.15 mA/cm2, which is reasonably close to the device's short circuit current at 1 sun (15.2 mA/cm2). The current might be slightly higher due to the LEDs used in the TPV experiment having a strength slightly above 1 sun and a different overall spectral composition

when compared with the solar simulator used to measure the JV curves. This match tells us that the process we are measuring does correspond to the recombination process within the device, unlike in the case of mp-TiO2 devices where a double exponential fit and a separation of the time constants was necessary in order to achieve the same result.

On Figure 15 we can also see the differential capacitance for the device as a function of applied bias. The geometric capacitance for the device is inferred from a linear fit using values far away from the Voc. As you can see the device does show a deviation from the expected geometric capacitance, which we can infer to be chemical capacitance, as the applied bias approaches the device's open circuit voltage.

It is also worth interesting to note that on this device the charge density is at least 10 times lower at equivalent decay times when compared with mp-TiO2 devices that show efficiencies near 12% in our group. This means that in order to obtain an efficiency that is only around 30% smaller these C_{60} devices should have charge mobilities at least one order of magnitude larger than on mp-TiO2 devices. The larger grain sizes within the hot casted pervoskite film may allow for this to happen.

JV Characterization of devices fabricated using lower purity PbI2 (99%)

At this point in time we had to change our PbI_2 precursor from PbI_2 99.999% to PbI2 99% since no chemical suppliers had readily available and reasonably priced higher purity PbI_2 that could be delivered within a time frame shorter than 6 months. We took this opportunity to test the effect that PbI_2 purity had on our device performance and our device photo-physics. With this in mind we prepared devices equal to the ones previously described, with the only difference being the use of the new PbI_2 precursor within the hot casting process. Figure 16 shows the JV curves and electrical properties for the best device produced.

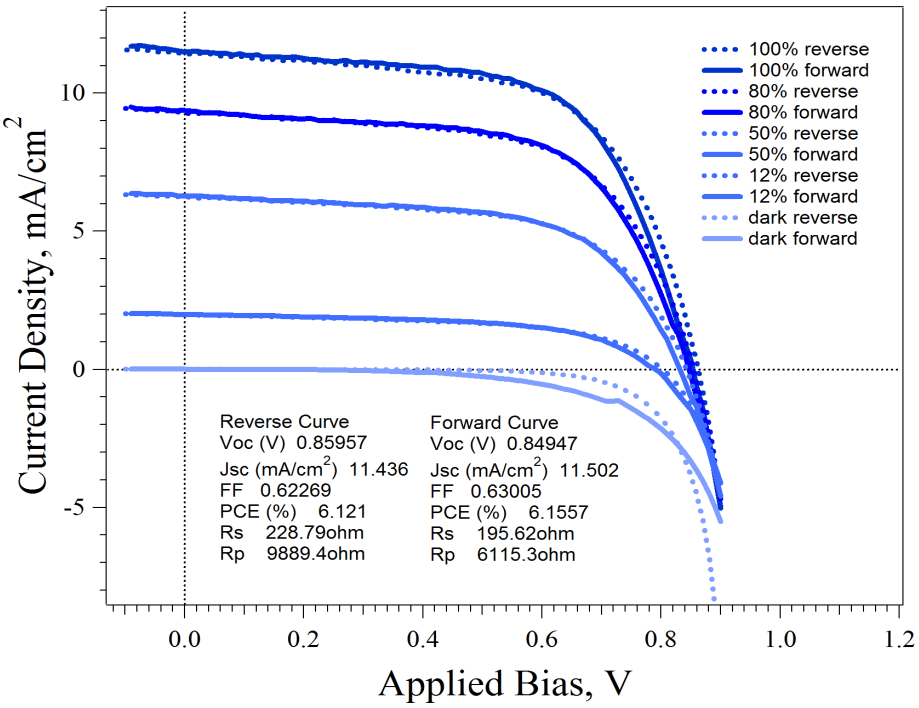

Figure 16. *JV Curves for champion device containing C60 (60nm) as an n-type layer at different simulated light intensities. This device was produced using low purity* PbI_2 *(99%).*

Through all of our experiments using this lower purity PbI2 it became clear that the lower purity PbI2 caused a drop in voltage of around 50-60 mV on all prepared devices. Fabricating a device with a Voc above 900 mV using PEDOT:PSS was not possible with the as-received lower purity PbI2. However device stability was not affected and PCE values were still higher than those that could be obtained using spin coated PC71BM. Hysteresis also remained low in our JV curves despite of the change in the lead iodide precursor. Interestingly all these devices with a lower purity PbI2 also showed a somewhat larger fill factor compared with devices produced using the higher quality reagent.

Opto-electronic experiments for devices fabricated with lower purity PbI2

Since this diode was also stable enough to perform additional experiments we took the opportunity to measure photo-physical properties. In this case we decided to perform the photo induced charge extraction measurements first, as in the previous case we could not perform this measurement due to device deterioration after laser probing during the TPV/TPC experiments.

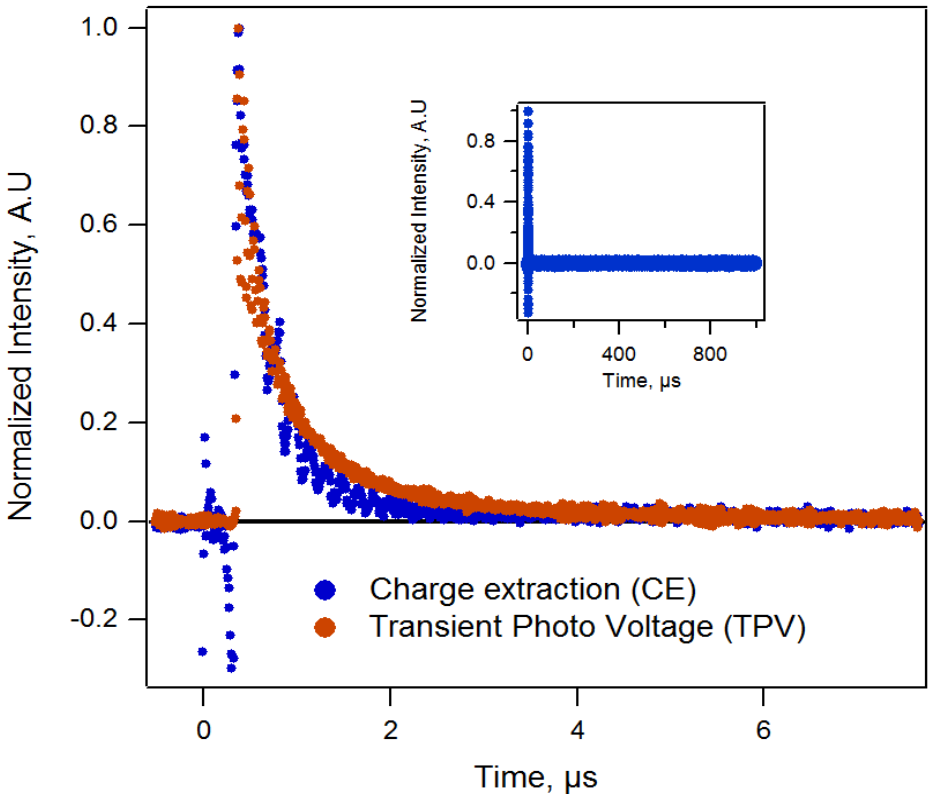

Figure 17. *.Fastest CE and TPV decays (at 1 sun simulated light intensity). An inset plot depicting a full longer term CE decay shows that it converges to 0 even at longer time scales (around 1 second).*

The CE experiments were difficult to perform due to the more than 100 seconds of illumination needed to arrive at a stable Voc before discharging the device through a resistance. This meant that the measurements took a significant

amount of time, which exposed them to deterioration throughout the experiment.

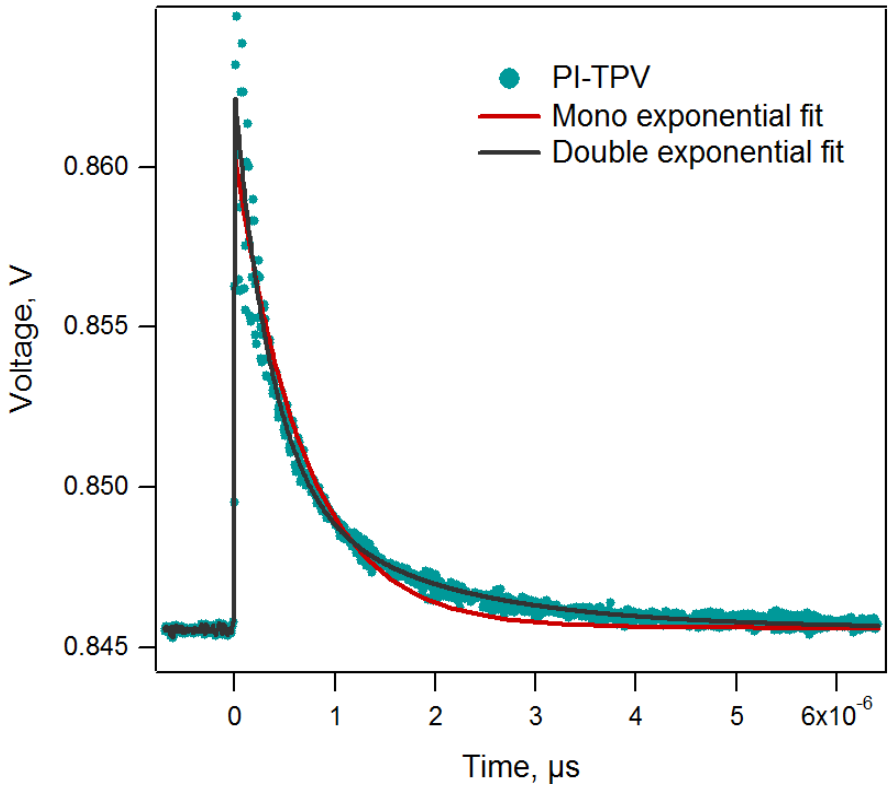

Figure 18. *Mono and bi-exponential fits on the TPV decay obtained at 1 sun simulated light intensity. Although the data shows a bi-exponential character it is far less pronounced that in the case of mp-TiO2 devices.*

The first thing we noticed about the CE decays was the much shorter decay time when compared with mp-TiO_2 devices within our group. Our mp-TiO_2 devices generally show CE decay lifetimes greater than those of the fastest TPV decays. This increased lifetime in the CE is caused by a charge accumulation source different from pure photo-induced charge separation[11]. For our hot casted devices the CE lifetime was shorter than the fastest TPV lifetime (Figure 17) which makes their photo-physical behavior analogous to that of organic solar cells, where this behavior is common.

In agreement with our previously studied devices produced with higher purity PbI2 the TPV decays show less pronounced bi-exponential behavior, further reinforcing

the hypothesis that these hot casted devices behave more alike organic solar cells than mp-TiO2 containing pervoskite solar cells.

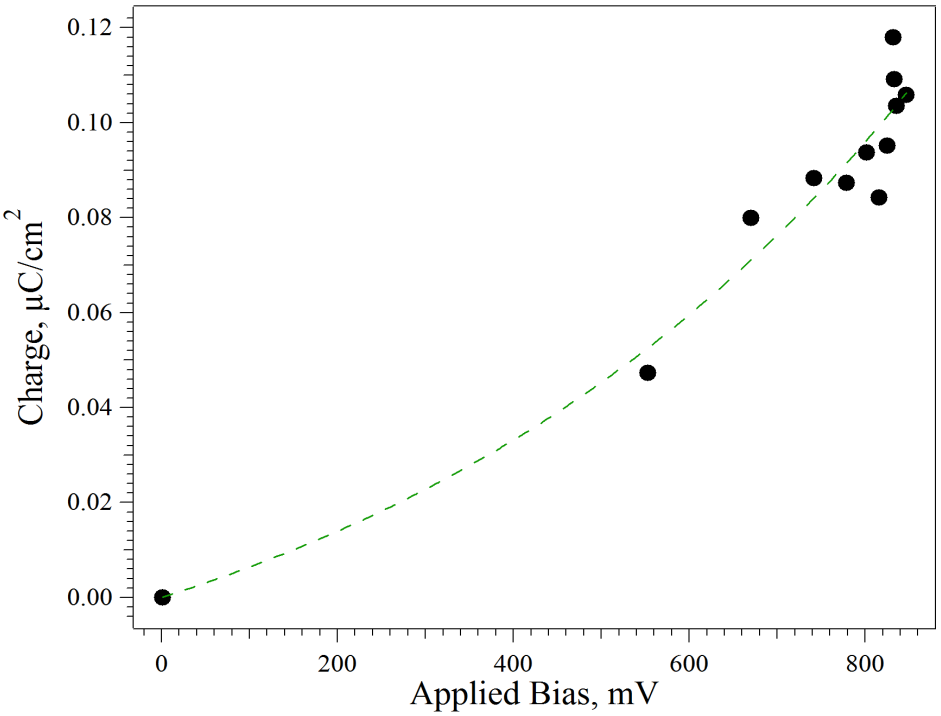

Figure 19. *Charge density Vs applied bias plot created using data from CE decays. A mono-exponential fit is shown in green.*

Given the fact that the Jsc varies linearly as a function of light intensity, that the TPV decay lifetimes can be reasonably estimated using mono-exponential function fits and that the device charge density at different levels of bias can be reasonably estimated using an exponential function from the CE data (Figure 19) we can create a plot depicting decay lifetime as a function of charge density (Figure 20).

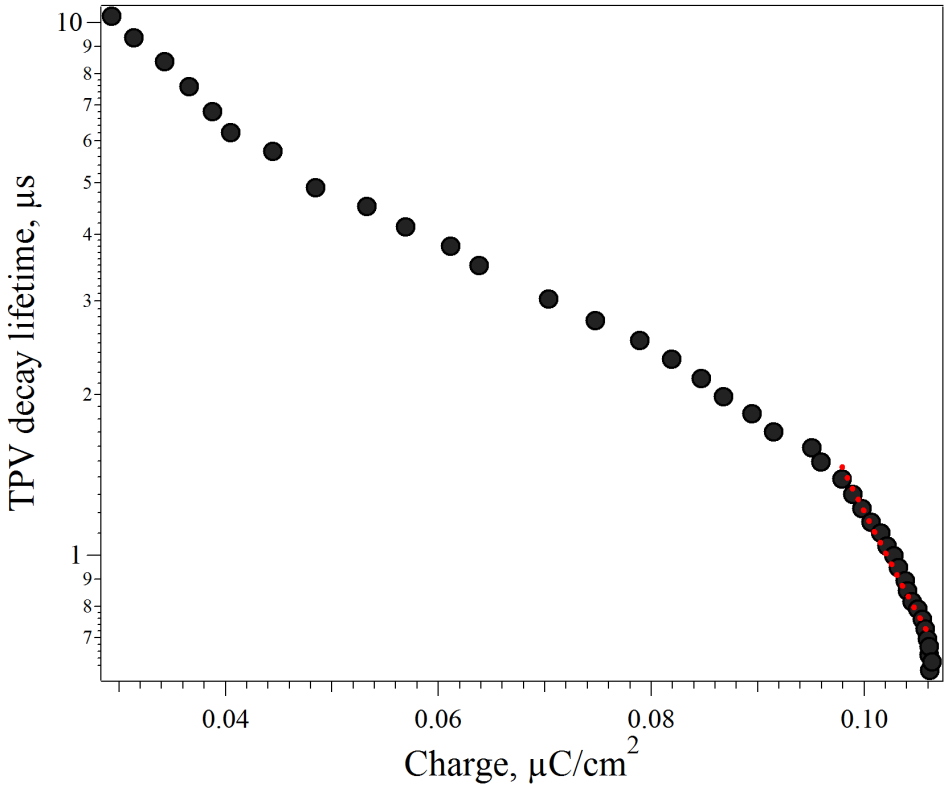

Figure 20. *TPV decay lifetime Vs charge density plot for a device produced with lower purity PbI2. A power law fit for conditions near the Voc are shown in red.*

From this plot we can make the same exercise we did for our high purity PbI2 devices where we performed a power law fit on the data near the Voc and attempted to calculate the Jsc at 1 sun from the charge density, the decay lifetime and the recombination order. With a recombination order of 10.2, a charge density of 0.1062µC/cm^2 and a decay lifetime of 0.06303µs near the Voc we can estimate the Jsc at 16.48mA/cm^2 which is close to the experimental Jsc value of 11.5mA/cm^2.

We attempted to perform TPV/TPC measurements for this device as well but the device started to deteriorate when we were making the TPV measurements. We could see this as the magnitude of the laser induced perturbation changed abnormally through the test; a clear sign that the charge density as a function of decay lifetime is changing within the device as a consequence of deterioration.

Since the key assumption of the TPC experiment is that the number of charge carriers generated by the laser induced perturbation is constant, device deterioration effectively voids the experiment.

High Purity Vs Low Purity PbI2

The use of different PbI_2 precursors has a very significant impact in device electrical and photo-physical properties. Devices fabricated with higher purity PbI_2 always had a higher Voc (about 50-60 mV higher) when compared with devices fabricated with a lower purity PbI_2 source. Additionally device efficiencies always tend to be around 1-2% lower for devices produced with the lower purity precursor .

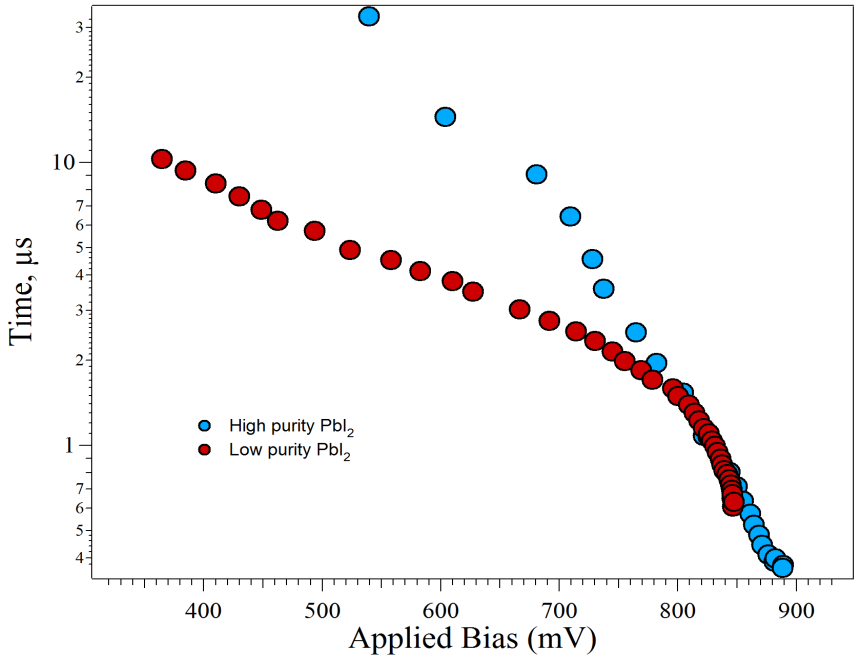

Figure 21. *TPV decay lifetime Vs applied bias for devices made with high and low purity lead iodide.*

There are also some very interesting differences in the photo-physical properties observed for both device types. Although we were never able to perform both CE and TPV/TPC experiments on the same device we could in fact observe much

faster decay lifetimes for the high purity devices near the Voc. At low bias levels the decay lifetime becomes much longer for the high purity devices while it changes behavior significantly for the low purity devices (Figure 20). This change in behavior at lower bias levels in the low purity devices may well be due to device deterioration caused by the continued laser probing during the TPV experiment.

There are also some striking differences in the charge density plots obtained for high purity devices (using TPV/TPC) and low purity devices (using CE/TPV). In the first case we have much lower charge densities of around 0.01 μC/cm^2 near the Voc while in the second case we have densities of around 0.10 μC/cm^2. This difference in 1 order of magnitude in the charge density comes from the fact that charge densities estimated from the TPV/TPC already have capacitive charges removed while charges from the CE process include total charges extracted from the device. Although in devices such as organic solar cells there tends to be good agreement between TPC/TPV and CE/TPV derived charges, the fact that geometric capacitance is of a much larger magnitude in perovskite solar cells makes the comparison between charge densities derived from TPC/TPV and those derived from CE/TPV experiments more difficult. Interestingly the estimations of Jsc from charge density, decay lifetimes and recombination order seem to agree in both cases, despite the fact that charge densities are of different magnitudes and were derived through different experimental procedures. It seems that the underestimation of the charge density is compensated by the much lower recombination order in the charge density plot obtained throuhg the TPC/TPV experiments.

It also worth mentioning that results obtained with high purity PbI2 (99.999%) can be reproduced by further purifying the low purity PbI_2 (99%) through a recrystallization process using Milli-Q water. This process is carried out by saturating a boiling solution of Milli-Q water with PbI_2, filtering and letting the

solution cool down very slowly at ambient temperature. After this crystals can be filtered from the solution and dried at 170°C for 1 day under vacuum. Note that the PbI_2 will turn orange, a normal phase transition that then reverts when the lead iodide is cooled. Although PbI_2 is not very hygroscopic it will absorb around 1% of its weight in water, reason why it is important to keep it in a globe box or desiccator. Lead iodide containing water will form a turbulent mixture when dissolved in DMF that will only become clear with heating while dry lead iodide will form a clear solution in DMF from the start. Dry lead iodide will also dissolve much faster in DMF (without any heating) while wet lead iodide will require heating and significant time to dissolve. After performing this procedure device voltage and efficiency values increase to those obtained with the high purity PbI_2.

JV Characterization of Cu doped NiO containing devices

Since devices using Cu-doped NiO as a p-type layer showed such a significant increase in voltage when using PC71BM as an n-type layer, we decided to fabricate diodes using Cu-doped NiO with C60 as an n-type layer. The devices showed similar stability and characteristics as those of Cu-doped NiO devices produced using PC71BM although their response time was faster (took less time to reach a stable Voc value). Figure 22 shows the JV curve and electrical properties for the best device built using Cu doped NiO as a p-type layer.

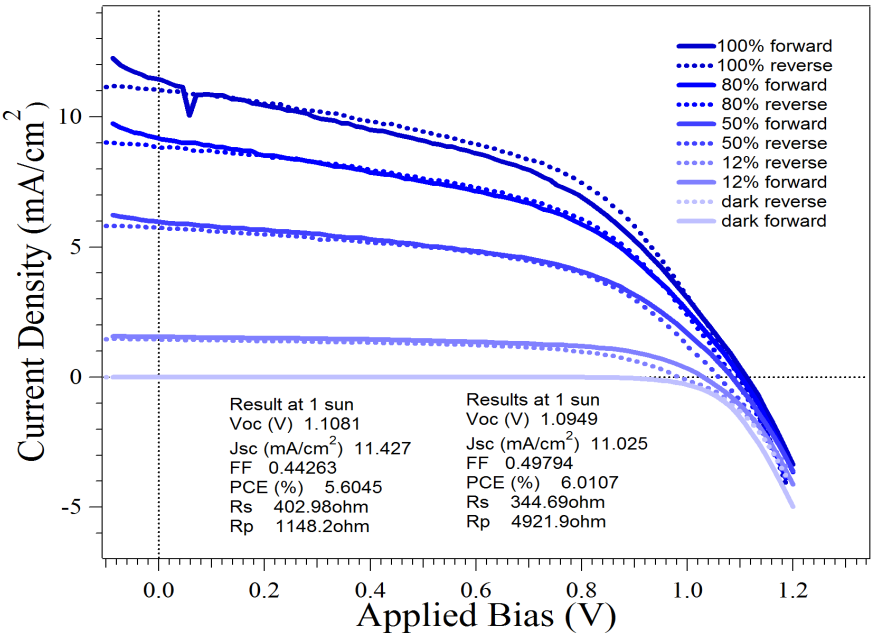

Figure 22. *JV Curve and electrical properties for the best lead halide perovskite solar cell built using Cu doped NiO as a p-type layer and C60 as an n-type layer.*

In agreement with our previous results using PC71BM as a n-type layer, our devices built using Cu doped NiO and C60 showed a significant increase in voltage towards values above 1100 mV. This voltage was the highest voltage achieve across all our experiments on pervoskite devices using hot casting. Additionally we continue to see a low hysteresis when changing to Cu doped NiO from PEDOT:PSS, also in agreement with our previous results. The PCE values achieved are better than those we reached when using PC71BM while our fill factors remain low compared to those of PEDOT:PSS based devices. Our Jsc values are also very similar to those obtained for PEDOT:PSS devices using the same PbI2 precursor.

Opto-electronic experiments for devices with Cu doped NiO as a p-type layer

In agreement with our previously showed PEDOT:PSS devices, Cu doped NiO devices have charge extraction decays that are faster than transient photo voltage decays at 1 sun and transient photo voltage decays with small bi-exponential components. For this reason we can repeat the procedure carried out for our PEDOT:PSS devices to obtain a graph where TPV decay lifetimes are plotted as a function of charge density. The results of this analysis are showed in Figure 23. In analogy with our previous devices we can estimate the Jsc by using the recombination order from the power law fit (10.908), the charge density 0.1062μC/cm^2 and the decay lifetime (1.663μs) near the Voc. This gives us a Jsc of 10.7mA/cm^2 , in agreement with the JV curve Jsc of 11.42 mA/cm^2 .

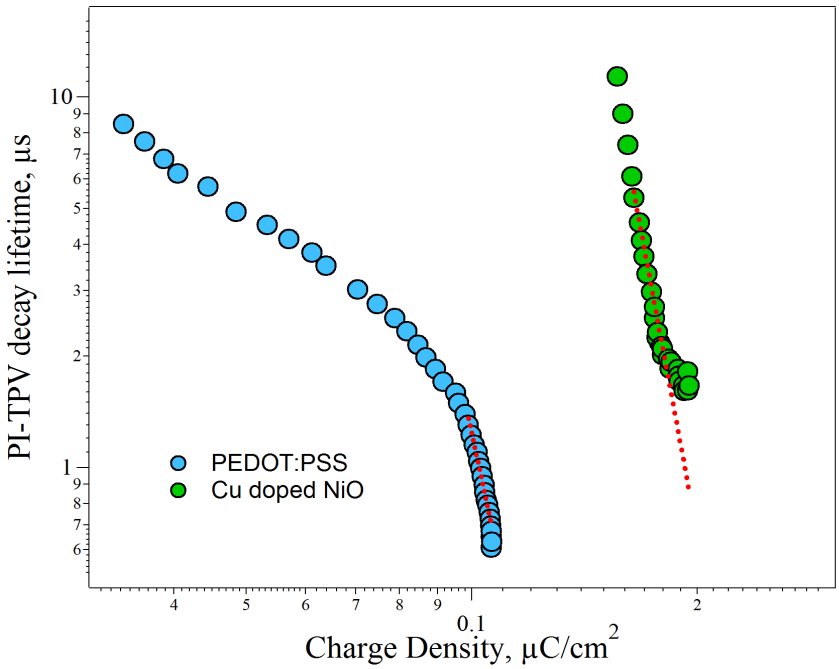

Figure 23. *TPV decay lifetime Vs charge density plot for devices where PEDOT:PSS or Cu doped NiO are used as a p-type layer. Power law fits for conditions near the Voc are shown in red.*

In Figure 23 we can also observe that the charge density accumulated for the Cu doped NiO devices is much larger than for our PEDOT:PSS device. This means that at equivalent charge densities the device using Cu doped NiO has a much longer decay lifetime. This is coherent with a shift in the density of states of the interfaces caused by the significantly more favorable work function of the Cu doped NiO contact.

Pervoskite Film Characterization

In order to better understand the composition and morphology of the lead halide pervoskite films used within the previously described devices we performed X-ray diffraction and electron microscopy analysis of films deposited on top of both PEDOT:PSS and Cu doped NiO layers. Our XRD analysis of these films (Figure 24) showed the presence of peaks characteristic of the $PbCH_3NH_4I_3$ phase while no peaks characteristic of CH_3NH_4Cl, CH_3NH_4I, PbI_2 or $PbCl_2$ phases were present

within the films. This of course does not mean that chloride is not present in the pervoskite films but merely that chloride ions did not separate into these specific crystalline phases. The X-ray fluorescence spectroscopy analysis performed inside the electron microscope does in fact reveal an almost homogeneous distribution of chloride ions within the films. This suggests that Cl is incorporated within the perovskite crystals, at least to some degree. Given the resolution of the X-ray fluorescence analysis it is not possible to know whether there are small but separated chloride and iodide rich phases within the film but we clearly don't see large chloride/iodide rich domain separations as it is observed when slow annealing processes using CH_3NH_4I and $PbCl_2$ are carried out[27]. Several published papers have also observed no chloride in the final perovskite crystals[28] when using slow deposition techniques involving methyl ammonium iodide and lead chloride but our fast hot casting technique does not allow time for chloride species to leave the film and therefore chloride phases remain trapped within the formed lead halide perovskite layer, as revealed by the fluorescence analysis.

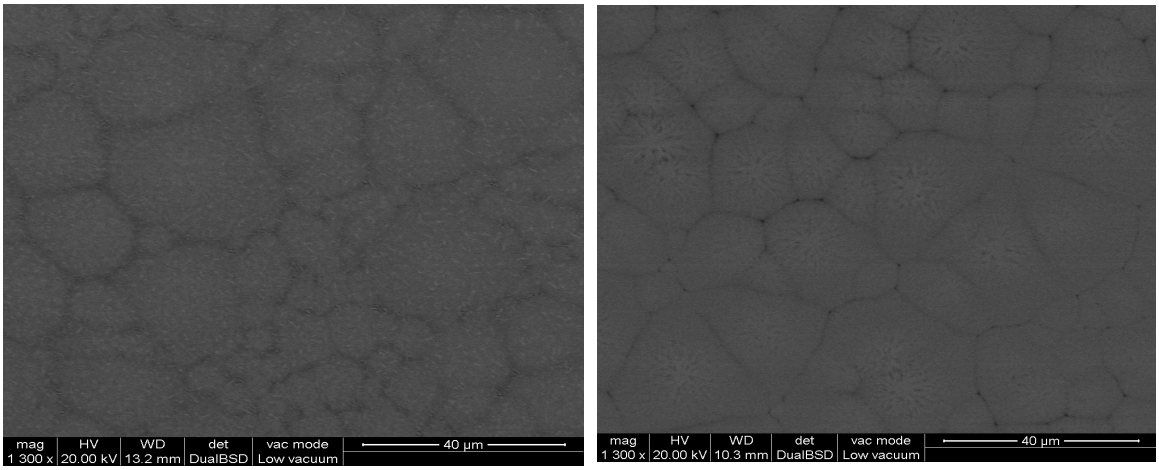

Figure 25. *Lead halide perovskite film deposited through a hot casting process over PEDOT:PSS (left) and Cu doped NiO (right). 80µL, 200mg/mL PbI_2 (99%), 200°C, 4000 rpm, 20 accel.*

Figure 25 shows that the morphology depends significantly on the layer over which the perovskite film is deposited. Although the size of the larger domains remains similar we can see a larger number of small domains in the case of PEDOT:PSS. The film deposited over PEDOT:PSS also shows many string like features on the surface while those features are absent in the case of devices deposited over Cu doped NiO. Films deposited over NiO also have a much more organized structure with better defined grain boundaries.

Conclusions

The hot casting process appeared as an attractive candidate for the fabrication of lead halide perovksite solar cells with the potential to yield fast fabrication times, limited dependence on environmental conditions, a good control over grain sizes and a good control over pervoskite composition. However the hot casting process has some important disadvantages stemming from the large amount of process variables that can affect the outcome of the hot casted films. Hot casting temperature, spin coating volume, spin coating acceleration, substrate sizes, substrate materials and operator ability are some of the most critical variables controlling the success or failure of the hot casting process. These problems are a very important deterrent to further pursue the hot casting process since something as simple as changing the person carrying out the process could have an enormous impact on its success. It was evident from our research in this area that the achievement of high efficiencies using this process is a complicated task that requires the careful optimization of many variables, some of which – like operator proficiency – cannot be easily quantified.

One of the most important problems of hot casted films involved roughness. Almost all of our efforts to generate better devices had to do with reducing the device roughness or increasing the quality of the n-type layer coverage over the hot casted film. Using an evaporated fullerene (C_{60}) instead of a solution processing step had the biggest effect in increasing device reproducibility,

stability and performance. Further reducing the roughness of the hot casted layer by including additives such as polyethylene-glycol or by changing process parameters such as the substrate size could produce better devices. Since our substrates were rather small (1.5cmx1.5cm) compared to those published in the literature[10] we could be suffering from important edge related effects that would not be present when using larger substrates. Using larger substrates also allows for lower hot casting temperatures, which could also lead to lower roughness levels.

Our use of different p-type layers also gave us important knowledge about their stability and effect over device performance. After implementing C60 we realized that PEDOT:PSS did not have any stability problems when used in hot casting under atmospheric conditions at 200°C since the poor stability of our devices came from very large roughness within the devices' active layer. However it was clear that any heating beyond 200°C damaged the PEDOT:PSS layer and greatly hindered device performance while inorganic layers, such as NiO and Cu doped NiO, could be used at much higher temperatures without any damage.

Perhaps the most interesting conclusions from this work come from our photo-physics experiments which revealed striking differences between our devices and those of mp-TiO_2 containing lead halide perovskite solar cells. Our devices without TiO_2 show an almost mono-exponential behavior within their TPV decays, while the behavior is largely bi-exponential for mp-TiO_2 devices. Our charge extraction process also shows much faster decays – in the same timescale as for organic solar cells – in great contrast with mp-TiO_2 devices were the decays do not reach the zero line after more than one second and are much slower than the TPV decays. Our devices produced through hot casting therefore show a lead halide pervoskite that behaves in a similar manner to organic solar cells, removing a lot of the complexity present when analyzing perovskite devices through photo-physic experiments.

Our work with Cu doped NiO also confirmed that the increase in potential from using this p-type layer is caused by a shift in the fermi level of the material, aligned with a significant increase in charge density at equivalent decay times when compared with devices built using PEDOT:PSS as an electron blocking layer.

Furthermore we can conclude from this work that changing the p-type layer between PEDOT:PSS, PEDOT:PSS(S), NiO or Cu doped NiO, changing the n-type layer between C_{60} and $PC_{71}BM$ or changing the hot casting conditions has no effect on the device's JV curve hysteresis. We always observed devices with very little to no hysteresis, regardless of the contacts used within the device between those mentioned above. This means that the hysteresis effect is not a property of the perovskite material but it is related with the interaction between the pervoskite and the contacts used within the device.

Bibliography

(1) Zhou, H.; Chen, Q.; Li, G.; Luo, S.; Song, T. -b.; Duan, H.-S.; Hong, Z.; You, J.; Liu, Y.; Yang, Y. *Science (80-.).* **2014**, *345* (6196), 542–546.

(2) Kim, H.-S.; Im, S. H.; Park, N.-G. *J. Phys. Chem. C* **2014**, *118* (11), 5615–5625.

(3) Chen, W.; Yongzhen, W.; Liu, J.; Qin, C.; Yang, X.; Islam, A.; Cheng, Y.-B.; Han, L. *Energy Environ. Sci.* **2014**, *8* (2), 629–640.

(4) Wen, X.; Sheng, R.; Ho-Baillie, A. W. Y.; Benda, A.; Woo, S.; Ma, Q.; Huang, S.; Green, M. A. *J. Phys. Chem. Lett.* **2014**, *5* (21), 3849–3853.

(5) Ryu, S.; Seo, J. W.; Shin, S. S.; Kim, Y. C.; Jeon, N. J.; Noh, J. H.; Seok, S. Il. *J. Mater. Chem. A* **2015**, *3* (7), 3271–3275.

(6) Wang, W.; Yuan, J.; Shi, G.; Zhu, X.; Shi, S.; Liu, Z.; Han, L.; Wang, H.-Q.; Ma, W. *ACS Appl. Mater. Interfaces* **2015**, *7* (7), 3994–3999.

(7) Kim, J.; Kim, G.; Kim, T. K.; Kwon, S.; Back, H.; Lee, J.; Lee, S. H.; Kang, H.; Lee, K. *J. Mater. Chem. A* **2014**, *2* (41), 17291–17296.

(8) Liu, X.; Yu, H.; Yan, L.; Dong, Q.; Wan, Q.; Zhou, Y.; Song, B.; Li, Y. *ACS Appl. Mater. Interfaces* **2015**.

(9) Xue, Q.; Hu, Z.; Liu, J.; Lin, J.; Sun, C.; Chen, Z.; Duan, C.; Wang, J.; Liao, C.; Lau, W. M.; Huang, F.; Yip, H.-L.; Cao, Y. *J. Mater. Chem. A* **2014**, *2* (46), 19598–19603.

(10) Nie, W.; Tsai, H.; Asadpour, R.; Blancon, J.-C.; Neukirch, A. J.; Gupta, G.; Crochet, J. J.; Chhowalla, M.; Tretiak, S.; Alam, M. A.; Wang, H.-L.; Mohite, A. D. *Science (80-.).* **2015**, *347* (6221), 522–525.

(11) O'Regan, B. C.; Barnes, P. R. F.; Li, X.; Law, C.; Palomares, E.; Marin-Beloqui, J. M. *J. Am. Chem. Soc.* **2015**, 150318153052006.

(12) You, J.; Hong, Z.; Yang, Y. M.; Chen, Q.; Cai, M.; Song, T.-B.; Chen, C.-C.; Lu, S.; Liu, Y.; Zhou, H.; Yang, Y. *ACS Nano* **2014**, *8* (2), 1674–1680.

(13) Tripathi, N.; Yanagida, M.; Shirai, Y.; Masuda, T.; Han, L.; Miyano, K. *J. Mater. Chem. A* **2015**, *3* (22), 12081–12088.

(14) Zhou, Y.; Yang, M.; Wu, W.; Vasiliev, A. L.; Zhu, K.; Padture, N. P. *J. Mater.*

Chem. A **2015**, *00*, 1–7.

(15) Wu, C.-G.; Chiang, C.-H.; Tseng, Z.-L. *J. Mater. Chem. A* **2014**, *2* (38), 15897–15903.

(16) Sheikh, A. D.; Bera, A.; Haque, M. A.; Rakhi, R. B.; Gobbo, S. Del; Alshareef, H. N.; Wu, T. *Sol. Energy Mater. Sol. Cells* **2015**, *137*, 6–14.

(17) Nardes, A. M.; Kemerink, M.; de Kok, M. M.; Vinken, E.; Maturova, K.; Janssen, R. A. J. *Org. Electron.* **2008**, *9* (5), 727–734.

(18) VITORATOS, E.; SAKKOPOULOS, S.; DALAS, E.; PALIATSAS, N.; KARAGEORGOPOULOS, D.; PETRAKI, F.; KENNOU, S.; CHOULIS, S. *Org. Electron.* **2009**, *10* (1), 61–66.

(19) Rong, Y.; Tang, Z.; Zhao, Y.; Zhong, X.; Venkatesan, S.; Graham, H.; Patton, M.; Jing, Y.; Guloy, A. M.; Yao, Y. *Nanoscale* **2015**.

(20) Park, S.; Tark, S. J.; Kim, D. *Curr. Appl. Phys.* **2011**, *11* (6), 1299–1301.

(21) Kim, J. H.; Liang, P.-W.; Williams, S. T.; Cho, N.; Chueh, C.-C.; Glaz, M. S.; Ginger, D. S.; Jen, A. K.-Y. *Adv. Mater.* **2014**, *27* (4), n/a – n/a.

(22) Hu, L.; Peng, J.; Wang, W.; Xia, Z.; Yuan, J.; Lu, J.; Huang, X.; Ma, W.; Song, H.; Chen, W.; Cheng, Y.-B.; Tang, J. *ACS Photonics* **2014**, *1* (7), 547–553.

(23) Trifiletti, V.; Roiati, V.; Colella, S.; Giannuzzi, R.; De Marco, L.; Rizzo, A.; Manca, M.; Listorti, A.; Gigli, G. *ACS Appl. Mater. Interfaces* **2015**, *7* (7), 4283–4289.

(24) Bai, Y.; Yu, H.; Zhu, Z.; Jiang, K.; Zhang, T.; Zhao, N.; Yang, S.; Yan, H. *J. Mater. Chem. A* **2014**.

(25) Wang, K.-C.; Jeng, J.-Y.; Shen, P.-S.; Chang, Y.-C.; Diau, E. W.-G.; Tsai, C.-H.; Chao, T.-Y.; Hsu, H.-C.; Lin, P.-Y.; Chen, P.; Guo, T.-F.; Wen, T.-C. *Sci. Rep.* **2014**, *4*, 4756.

(26) Greiner, M. T.; Helander, M. G.; Wang, Z.-B.; Tang, W.-M.; Lu, Z.-H. *J. Phys. Chem. C* **2010**, *114* (46), 19777–19781.

(27) Williams, S. T.; Zuo, F.; Chueh, C.-C.; Liao, C.-Y.; Liang, P.-W.; Jen, A. K.-Y. *ACS Nano* **2014**, *8* (10), 10640–10654.

(28) Grätzel, M. *Nat. Mater.* **2014**, *13* (9), 838–842.

Chapter 8

Overview and General Conclusions

Through this thesis we fabricated, tested and characterized a variety of devices as well as built statistical models in order to draw some conclusions about the relationships between molecular structure and opto-electronic properties in fullerene containing solar cells.

In our study of DPM fullerenes in **chapter 4** we constructed an in-depth picture of how changing the acceptor material affects devices built using a DPP(TBFu)2 donor. We confirmed changes in the averaged density of states distribution and the non-geminate recombination order of the devices, which were caused by changes in the crystalline structure of the donor which were in turn induced by changes in the molecular structure of the acceptor. This generated a shift in the Voc despite of the very similar LUMO level between the different acceptors used. Through this research we understood that the design of novel acceptors not only requires a favorable shifting of the LUMO level and a high electron mobility but the interaction between the acceptor and the donor must also be taken into account.

In **chapter 5** our study of a complete family of DPP derivatives revealed the great impact of subtle structural changes in the characteristics of devices built using $PC_{71}BM$ as an acceptor. Our research revealed that the donors must be able to grow mono-disperse nanometer-sized crystallites inside the D/A amorphous matrix with an orientation that matches the direction of faster transport in the crystallites. We showed that this leads to higher hole mobilities that are fundamental for better device performance. Since favorable crystallization depends on several different interaction energies we concluded that the rational design of structures that would yield optimal crystallization was very difficult. We further concluded that the use of intentionally introduced supra-molecular interactions would be useful for attempts at controlling the crystallite size and crystallization direction in small molecule solar cells.

Due to the difficulty in predicting crystal packing (even more in the presence of a

secondary acceptor phase) it seems more viable to attempt to pursue molecular structures that attempt to widen molecular absorption and increase molar absorption coefficients as these variables are more easily predicted and understood. Even though molecular packing and mobilities play a fundamental role in device performance it is probably easier to arrive at better mobilities by fine tuning motifs with optimum optical properties.

In order to see if we could surpass the small molecule donor design problem we implemented statistical models for the prediction of device electrical properties in **chapter 6**. We built an extensive database using a large array of published experimental results for small molecule donors and constructed random forest models that attempted to predict electrical properties from 2D or DFT derived descriptors. Although our models were significantly successful in predicting electrical properties within our in-database testing sets it became clear that the prediction of the Jsc, FF and PCE in newer molecules was not possible due to the evolution of device optimization techniques not present within the database. Our best results were for the prediction of Voc results, where we could achieve accurate predictions even for molecules outside of the database. From this exercise we concluded that the creation of statistical models for the prediction of organic devices will only be possible once the field reaches a higher state of maturity where much more standardized procedures for device optimization and fabrication are present.

Finally in **chapter 7** we implemented a hot casting procedure for the fabrication of perovskite solar cells using fullerenes as hole blocking layers. Our results revealed significant problems with roughness in the hot casting process which led to sub-optimal results for our device electrical properties. However our photo-physics experiments did reveal fundamental differences between mp-TiO2 perovskite solar cells and our devices produced using hot casting as our hot-casted devices showed photo-physical behavior similar to that of typical organic solar cells.

Appendix A

Additional Batch Processing Scripts

Table of Contents

RunGeometryOpt

```
#!/usr/bin/python
import subprocess
import sys
from optparse import OptionParser
import os
import re
import csv
from time import sleep
import shutil

def main():

    parser = OptionParser()

    parser.add_option("-i", "--moleculeID", dest="moleculeID",
                                        help="name of xyz file",
metavar="moleculeID")

    (options, args) = parser.parse_args()

    moleculeID = options.moleculeID
    print moleculeID

    mainFileData = """TITLE Geometry optimization
BASIS
type TZP
core Small
END

SCF
ADIIS
DIIS N=20
Iterations 300
END
Occupations KeepOrbitals=300

XC
GGA Becke Perdew
END

GEOMETRY
iterations 20000
END

ATOMS
"""

    optFileData = mainFileData

    csvfile =  open("allXYZ/" + moleculeID + ".xyz", 'rb')
    reader = csv.reader(csvfile)
```

```
        j = 0
        for row in reader:
            if j > 1:
                optFileData += row[0]
                optFileData += "\n"
            j += 1

        csvfile.close

        optFileData += "END"

        optFileData += "\n"

        if not os.path.exists("MOLECULE_"+ moleculeID):
            os.makedirs("MOLECULE_" + moleculeID)

        text_file =  open("MOLECULE_"+moleculeID + "/opt_" +  moleculeID + ".in", "w")
        text_file.write(optFileData)
        text_file.close

        print optFileData
        os.chdir("MOLECULE_" + moleculeID)

        subprocess.call("commandToSubmitAFJjob opt_"+ moleculeID + ".in", shell=True)
        print "run has been submitted by script"

    if __name__ == "__main__": main()
```

RunCOSMO

```
import subprocess
import sys
from optparse import OptionParser
import os
import re
import csv

def main():

    parser = OptionParser()

    parser.add_option("-i", "--moleculeID", dest="moleculeID",
                                        help="name of xyz file",
metavar="moleculeID")

    (options, args) = parser.parse_args()

    moleculeID = options.moleculeID
    print moleculeID
    i = moleculeID

    mainFileData = """TITLE cosmo calculation for molecule """ + str(i) +"""
    BASIS
      type TZP
      core Small
    END
    SOLVATION
      Surf Delley
      Div ndiv=4
      Solvent name=CRS cav0=1.888219 cav1=0.01014
      Charged method=CONJ conv=0.000001 iter=300 corr
      C-Mat EXACT
      SCF VAR ALL
      CSMRSP
    END
    XC
      GGA Becke Perdew
    END
    ATOMS
"""

    csvfile =  open("MOLECULE_" + moleculeID + "/opt_" + moleculeID + ".out", 'rb')
    reader = csv.reader(csvfile)
    startParsing = False
    for row in reader:
        if len(row) == 1:
            if "GEOMETRY CONVERGED" in row[0]:
                startParsing = True
        if startParsing:
            if "<" not in row[0][0:3]:
                if "C" not in row[0][0:3]:
```

```
                    if "A" not in row[0][0:5]:
                        mainFileData += "    "+ row[0][6:] + "\n"
        csvfile.close

        mainFileData += "END" + "\n"

        text_file =  open("MOLECULE_"+moleculeID + "/cosmo_" +  moleculeID + ".in",
    "w")
        text_file.write(mainFileData)
        text_file.close

        print mainFileData
        os.chdir("MOLECULE_" + moleculeID)

        subprocess.call("commandToSubmitADFjob cosmo_"+ moleculeID + ".in", shell=True)
        print "run has been submitted by script using adf13.c8m24"

    if __name__ == "__main__": main()
```

RunADFK

```
#!/usr/bin/python
import subprocess
import sys
from optparse import OptionParser
import os
import re
import csv
import shutil

def main():

    parser = OptionParser()

    parser.add_option("-i", "--moleculeID", dest="moleculeID",
                                        help="name of xyz file",
metavar="moleculeID")

    (options, args) = parser.parse_args()

    moleculeID = options.moleculeID

#in our case the “sadf” batch script was used to call the ADF tool used.
    subprocess.call("cp sadf MOLECULE_"+ moleculeID, shell=True)
    os.chdir("MOLECULE_" + moleculeID)
    subprocess.call("chmod +x sadf", shell=True)

    print "Should now run process"
    subprocess.call("./sadf cosmo_" + moleculeID, shell=True)

if __name__ == "__main__": main()
```

runSigma

```
Run#!/usr/bin/python
import subprocess
import sys
from optparse import OptionParser
import os
import re
import csv
import shutil

def main():

    parser = OptionParser()

    parser.add_option("-i", "--moleculeID", dest="moleculeID",
                                        help="name of xyz file",
metavar="moleculeID")

    (options, args) = parser.parse_args()

    moleculeID = options.moleculeID

#in our case the “sadfkf2cosmo” batch script was used to call the ADF tool used.
    subprocess.call("cp sadfkf2cosmo MOLECULE_" + moleculeID, shell=True)
    os.chdir("MOLECULE_" + moleculeID)
    subprocess.call("chmod +x sadfkf2cosmo", shell=True)

    if os.path.exists("cosmo_" + moleculeID + ".coskf") == False:
        quit()

    print "Should now run process"
    subprocess.call("./sadfkf2cosmo cosmo_" + moleculeID, shell=True)

if __name__ == "__main__": main()
```

CheckProcess

```
#!/usr/bin/python
import subprocess
import sys
from optparse import OptionParser
import os
import re
import csv
import mmap
from time import sleep
import shutil

def main():

    convergedCount = 0
    MOLECULE_COUNT = 200

    for i in range(1, MOLECULE_COUNT+1):
        if os.path.exists("allXYZ/" + str(i) + ".xyz"):
            if not os.path.exists("MOLECULE_"+ moleculeID):
                subprocess.call("python runGeometryOpt.py -i " + str(i), shell=True)
            if os.path.exists("MOLECULE_" + str(i) + "/opt_" + str(i) + ".out"):
                f = open('MOLECULE_'+ str(i)+ "/opt_" + str(i) + ".out", "r")
                if "GEOMETRY CONVERGED" in f.read():
                    print "MOLECULE " + str(i) + " HAS CONVERGED"
                    convergedCount += 1
                    if os.path.exists("MOLECULE_"+str(i)+"/TAPE21"):
                        if os.path.exists("MOLECULE_"+str(i)+"/opt_"+str(i)+".t21") == False:
                            os.rename("MOLECULE_"+str(i)+"/TAPE21","MOLECULE_"+str(i)+"/opt_" + str(i) + ".t21")
                    if os.path.exists("MOLECULE_"+str(i)+"/cosmo_"+str(i)+".out") == False:
                        subprocess.call("python runCOSMO.py -i " + str(i), shell=True)
                    else:
                        if os.path.exists("MOLECULE_"+str(i)+"/TAPE21"):
                            os.rename("MOLECULE_"+str(i)+"/TAPE21","MOLECULE_"+str(i)+"/cosmo_" + str(i) + ".t21")
                        if os.path.exists("MOLECULE_"+str(i)+"/cosmo_" + str(i) + ".t21"):

                            if os.path.exists("MOLECULE_"+str(i)+ "/cosmo_" +str(i)+".info") == False:
                                subprocess.call("python runOrbitals.py -i " + str(i), shell = True)

                            if os.path.exists("MOLECULE_"+str(i)+"/cosmo_" + str(i) + ".coskf") == False:
                                subprocess.call("python runADFK.py -i " + str(i), shell=True)
                            else:
                                if os.path.exists("allCosmo/cosmo_" + str(i) + ".cosmo") == False:
                                    subprocess.call("python runSigma.py -i " + str(i), shell=True)

                        if os.path.exists("MOLECULE_"+str(i)+"/cosmo_" + str(i) + ".cosmo"):
                            if os.path.exists("allCosmo/cosmo_" +str(i) + ".cosmo") == False:
                                os.rename("MOLECULE_"+str(i)+"/cosmo_" + str(i) + ".cosmo","allCosmo/cosmo_" + str(i)
+ ".cosmo")
                else:
                    print "MOLECULE " + str(i) + " NOT CONVERGED YET"

    print "number of converged molcules is {0}".format(convergedCount)

if __name__ == "__main__": main()
```